Science and Technology of Nuclear Installations

Computational Fluid Dynamics for Gas–Liquid Flows

Guest Editors: Dirk Lucas, Iztok Tiselj, Yassin A. Hassan, and Fabio Moretti

Computational Fluid Dynamics for Gas-Liquid Flows

Science and Technology of Nuclear Installations

Computational Fluid Dynamics for Gas-Liquid Flows

Guest Editors: Dirk Lucas, Iztok Tiselj, Yassin A. Hassan, and Fabio Moretti

Contents

Hindawi Publishing Corporation
Science and Technology of Nuclear Installations
Volume 2009, Article ID 725247, 1 page
doi:10.1155/2009/725247

Editorial
Computational Fluid Dynamics for Gas-Liquid Flows

Dirk Lucas,[1] Iztok Tiselj,[2] Yassin A. Hassan,[3] and Fabio Moretti[4]

[1] *Institute of Safety Research, Forschungszentrum Dresden-Rossendorf e.V., P.O. Box 510 119, 01314 Dresden, Germany*
[2] *Reactor Engineering Division, Institute "Jozef Stefan", Jamova 39, 1000 Ljubljana, Slovenia*
[3] *Department of Nuclear Engineering, Texas A&M University, Zachry 129, MS 3133, College Station, TX 77843-3133, USA*
[4] *Department of Mechanics, Nuclear and Production Engineering, University of Pisa, Via Diotisalvi 2, 56100 Pisa, Italy*

Correspondence should be addressed to Dirk Lucas, d.lucas@fzd.de

Received 15 December 2008; Accepted 15 December 2008

Computational fluid dynamics (CFD) codes are widely used in industrial applications for single-phase flows (e.g., in the automotive or aircraft industries). On the other hand, the application of CFD for multiphase systems is not yet mature. Safety analyses related to nuclear light water reactors require reliable simulations for different scenarios including two-phase flow situations. Prominent examples for pressurized water reactor (PWR) analyses are the prevention from departure from nucleate boiling (DNB) which is related to critical heat flux (CHF) or the pressurized thermal shock (PTS) problem which has to be considered in connection with some hypothetical loss of coolant accident (LOCA) scenarios and may also lead to two-phase flow situations in the cold leg and in the downcomer. For example, in case of boiling water reactors (BWR) analyses, the prevention from Dryout is an important issue.

The currently applied system codes based on correlations are valid for special geometries, scales, and flow patterns. This limits the transferability of small-scale experimental findings to real plant scales. On the other hand, CFD-type models depend only on local flow parameters and are for this reason much more flexible regarding geometry and scale. The increased computer power now in principle permits CFD simulations for multiphase flows and many investigations have been done in the recent years.

The problems in modeling of such gas-liquid flows using CFD codes arise from the fact that the mass, momentum, and heat transfer among the phases are strongly coupled with the complex interfacial structure. The order of magnitudes lies between the size of the smallest structures of these interfaces and the size of the typical components of nuclear reactors which finally have to be modeled. For this reason, averaging procedures are required which lead, for example, to the well-known two- or multifluid model. Due to this averaging, the primary information on the structure of the interface gets lost and has to be introduced again by the so-called closure models. Some of the physical phenomena on microscale are not yet well understood. Also, CFD-grade experimental data (i.e., data with high resolution in space and time) are often not available. Despite these open problems, there is a step-by-step progress in the simulation of gas-liquid flows in geometries and scales relevant to nuclear reactor safety (NRS).

In view of the above, it has been decided to bring out the special issue "Computational Fluid Dynamics for Gas-Liquid Flows." Two papers review and discuss the state-of-the-art of modeling and the available experimental database for the CHF and the two-phase PTS issue, respectively. Research articles focus on important topics like turbulence modeling in two-phase flows, modeling of polydispersed flows, mixing problems (including single-phase coolant flows, addressed by one paper), and jet impingement connected with bubble entrainment. Thus, this special issue provides the readers with useful information on the progress of CFD modeling for reactor-specific two-phase flows, and also on open questions, requirements for further research, modeling, and experimental data.

Dirk Lucas
Iztok Tiselj
Yassin A. Hassan
Fabio Moretti

Hindawi Publishing Corporation
Science and Technology of Nuclear Installations
Volume 2009, Article ID 214512, 14 pages
doi:10.1155/2009/214512

Review Article

Review of Available Data for Validation of Nuresim Two-Phase CFD Software Applied to CHF Investigations

D. Bestion,[1] H. Anglart,[2] D. Caraghiaur,[2] P. Péturaud,[3] B. Smith,[4] M. Andreani,[4] B. Niceno,[4] E. Krepper,[5] D. Lucas,[5] F. Moretti,[6] M. C. Galassi,[6] J. Macek,[7] L. Vyskocil,[7] B. Koncar,[8] and G. Hazi[9]

[1] *Commissariat à l'Énergie Atomique (CEA), DEN-DER-SSTH, 17 Rue des Martyrs, 38054 Grenoble, France*
[2] *Reactor Technology Division, Physics Department, Royal Institute of Technology (KTH), AlbaNova University center, 106 91 Stockholm, Sweden*
[3] *Électricité de France (EDF) R&D, Mécanique des Fluides Energie et Environnement, 6 quai Watier, 78401 Chatou, France*
[4] *Department of Nuclear Energy and Safety, Thermal-Hydraulics Laboratory, Paul Scherrer Institute (PSI), CH-5232 Villigen, Switzerland*
[5] *Forschungszentrum Dresden-Rossendorf (FZD) P.O.Box 510119, D-01314 Dresden, Germany*
[6] *Department of Mechanics, Nuclear and Production Engineering – DIMNP, Università di Pisa, 2, Via Diotisalvi, 56100 PISA, Italy*
[7] *Department of Thermal-Hydraulic Analyses, Nuclear Research Institute Rez plc (NRI), 25068 Rez, Czech Republic*
[8] *Josef Stefan Institute (JSI), Jamova 39, 1000 Ljubljana, Slovenia*
[9] *KFKI Atomic Energy Research Institute, Theoretical Thermohydraulics, Research Group, 1525 Budapest, Hungary*

Correspondence should be addressed to D. Bestion, dominique.bestion@cea.fr

Received 24 January 2008; Accepted 23 May 2008

Recommended by Iztok Tiselj

The NURESIM Project of the 6th European Framework Program initiated the development of a new-generation common European Standard Software Platform for nuclear reactor simulation. The thermal-hydraulic subproject aims at improving the understanding and the predictive capabilities of the simulation tools for key two-phase flow thermal-hydraulic processes such as the critical heat flux (CHF). As part of a multi-scale analysis of reactor thermal-hydraulics, a two-phase CFD tool is developed to allow zooming on local processes. Current industrial methods for CHF mainly use the sub-channel analysis and empirical CHF correlations based on large scale experiments having the real geometry of a reactor assembly. Two-phase CFD is used here for understanding some boiling flow processes, for helping new fuel assembly design, and for developing better CHF predictions in both PWR and BWR. This paper presents a review of experimental data which can be used for validation of the two-phase CFD application to CHF investigations. The phenomenology of DNB and Dry-Out are detailed identifying all basic flow processes which require a specific modeling in CFD tool. The resulting modeling program of work is given and the current state-of-the-art of the modeling within the NURESIM project is presented.

1. Introduction

The NURESIM Integrated Project of the 6th European Framework Programme is envisaged to provide the initial step towards a common European Standard Software Platform for modeling, recording, exchanging, and recovering data for nuclear reactors simulations. Key objectives of NURESIM include the integration of advanced physical models in a shared, open software platform, incorporating the latest advances in reactor core physics, thermal hydraulics, and coupled multiphysics modeling. The specific objectives of NURESIM are to initiate the development of the next generation of experimentally validated, "best-estimate" tools with improved prediction capabilities, standardization, and robustness to address current and future needs of industry, reactor safety organizations, academic, government, and private institutions.

The overall objective of NURESIM thermal-hydraulic subproject is to improve the understanding and the predictive capabilities of the simulation tools for key two-phase

flow thermal-hydraulic processes that can occur in nuclear reactors, focusing on two high priority issues, the critical heat flux (CHF), and the pressurized thermal shock (PTS). This overall objective has resulted from the conclusions of the EUROFASTNET [1] concerted action, which established a priority list of 44 industrial needs, and the results of the ASTAR [2], and ECORA [3] projects of the 5th Framework Programme are considered as inputs for NURESIM. The initial framework for performing the tasks is provided by the Neptune [4–6] two-phase CFD module, which is being developed by CEA and EDF, under the cosponsorship of AREVA-NP and IRSN. Other CFD tools such as CFX or FLUENT are also used within the NURESIM project. This paper focuses on the CHF investigations and primarily on the use of the two-phase CFD for both departure from nucleate boiling (DNB) and dryout investigations.

This paper presents a review of existing experimental data bases which can be used for validation of the two-phase CFD application to critical heat flux (CHF) investigations with respect to nuclear reactors. The phenomenology of DNB and dryout is detailed identifying all basic flow processes which require a specific modeling in CFD tool. The resulting programme of work is given, and the current state of the art of the modeling is presented.

2. The Multiscale Analysis of CHF

Four basic spatial scales encountered in thermal-hydraulic phenomena relevant to nuclear power plants:

(i) system scales, which are addressed by zero- and one-dimensional flow models for pipes, pumps, valves, breaks, and control systems together with CFD methods for porous media;

(ii) component-scales, which are addressed by CFD methods for porous media (typically for the core of a reactor or for the steam generators with a minimum spatial resolution in the case of the subchannel analysis);

(iii) mesoscales, which are addressed by computational fluid dynamics (CFDs) methods in open medium, including turbulence models, using either Reynolds-averaged simulations (RANSs) or large eddy simulation (LES);

(iv) microscales, which are addressed by direct numerical simulation (DNS) and interface tracking methods (ITMs) that focus on a very small domain (e.g., a domain containing a few bubbles or droplets).

In CHF investigations, the present industrial methods mainly use the component scale with 3D modeling of core assemblies using in the hot assembly the subchannel analysis. Large-scale experiments having the real geometry of the reactor assembly are used to develop empirical correlation for the CHF as function of flow variables which are averaged over the cross-section of a subchannel. The NURESIM-TH activities regarding CHF aim at using two-phase CFD as a tool for understanding boiling flow processes, in order to subsequently help new fuel assembly design and to develop better CHF predictions in both PWR and BWR. A "local predictive approach" may be envisaged for the long term where CHF correlations would be based on local (mesoscale) T/H parameters provided by CFD. If the processes leading to DNB and dryout are well understood, the CHF correlation will be physically based, but one may also develop empirical correlations if some phenomena are not clearly identified.

Considering the rather low maturity of two-phase CFD, a general methodology was proposed by a Writing Group of the OECD-CSNI (see Bestion et al. 2006 [7]) to apply it to a reactor issue with successive steps:

(i) identification of all important flow processes of the application,

(ii) selecting a basic model,

(iii) filtering turbulent scales and two-phase intermittency scales,

(iv) identification of local interface structure,

(v) modeling interfacial transfers,

(vi) modeling turbulent transfers,

(vii) modeling wall transfers,

(viii) use of finer scale simulations for modeling,

(ix) identification of validation and verification test cases with possibly some demonstration test cases.

The choice of a validation test matrix and of the basic modeling approach should be consistent with each other since there must be enough measured physical parameters to be able to validate separately each sensitive process modeled in the equations.

The identification of the basic flow processes related to both DNB and dryout and a review of available experimental data were performed before selecting a basic model and defining a development and validation programme. Next sections will present this initial work and will conclude on the present state of the art in the modeling within the NURESIM project.

3. Departure from Nucleate Boiling

3.1. The DNB Phenomenology. Departure from nucleate boiling is the main governing critical heat flux mechanism for pressurized water reactors. A huge amount of work has been devoted to the DNB in the past decades but the evaluation of the CHF still relies on fully empirical methods.

Rod bundles with spacer grids are tested in real conditions with the fuel assembly geometry and the same flow T/H conditions as in the reactor. Such experiments are very expensive and time consuming but necessary to determine the CHF behaviour of any new fuel assembly design.

The reason of this situation is that the phenomenology of convective boiling and DNB is very complex, and many small-scale processes are not well understood. It is very likely that phenomena occurring at various scales play a role; one can distinguish three scales for reactor DNB phenomenology.

(i) The *macroscale* refers to phenomena at the scale of the subchannel (e.g., about 1 cm). Macroscale phenomena are modeled in subchannel analysis codes.

(ii) The *mesoscale* refers to flow processes responsible for the profiles of the main flow parameters within subchannels (e.g., about 0.1 or 1 mm). Mesoscale flow processes can be modeled in two-phase CFD simulation tools.

(iii) *Microscale* phenomena occur at the scale of the smallest bubbles or nuclei and can only be numerically simulated by direct numerical simulation (DNS) tools and interface tracking methods (ITMs).

A nonexhaustive list of flow processes at the various scales is given here below.

MICROSCALE Phenomena

(i) Activation of nucleation sites.

(ii) Evolution of active sites density with increasing power.

(iii) Growing of attached bubbles.

(iv) Sliding of attached bubbles along heating wall.

(v) Coalescence of attached bubbles.

(vi) Extension of dry patch.

(vii) Effects of wall conductivity and heat capacity.

(viii) Detachment of bubbles.

(ix) Rewetting after detachment.

(x) Mutual influence of neighboring nucleation sites.

(xi) Influence of flow characteristics on local processes: external convective velocity.

(xii) Behaviour of detached bubbles: coalescence, migration.

(xiii) Interactions between detached bubbles.

(xiv) Forces between detached bubbles and liquid flow.

(xv) Formation of high-void layer if bubbles cannot escape due to counter current flow limitation (CCFL) type phenomenon and behaviour of the thin liquid film which vaporizes below the bubble layer.

MESOSCALE Phenomena

(i) Wall to fluid heat transfer in subcooled boiling: liquid heating, vaporization, quenching.

(ii) Transport and dispersion of bubbles.

(iii) Vaporization-condensation of bubbles.

(iv) Coalescence and breakup of bubbles.

(v) Turbulent transfers of heat and momentum within liquid.

(vi) Effects of polydispersion of bubbles on interfacial transfers

(vii) Local effects of grids: enhanced turbulence and flow rotation.

MACROSCALE Phenomena

(i) Mixing between subchannels, cross-flows, turbulence.

(ii) Grid spacers effects on mixing between sub-channels.

(iii) Effects of cross-sectional averaged pressure P, mass flux, G, and quality Xth, on DNB occurrence.

(iv) Effects of nonuniform heat flux on DNB occurrence.

(v) Effects of spacer grids on DNB occurrence.

Two-phase CFD predictions should be compared to relevant experimental data in order to validate all mesoscale flow processes, in geometrical and T/H conditions preferably representative of the industrial ones. This will bring a better understanding of the effects of the mesoscale phenomena on the CHF occurrence. Moreover, microscale flow phenomena should also be better understood for developing physically based closure laws in the CFD approach. In this purpose, any experimental information on such microscale phenomena or any DNS simulations may be used to improve the CFD simulation tool. However, this project did not bring enough information to build a physically based DNB criterion. Nevertheless, CFD simulations of boiling flowup to DNB have the potentiality to predict some mesoscale effects on flow conditions at the wall such as the development of two-phase boundary layers, or spacer grid effects, which are not seen by the subchannel analysis and current empirical CHF models. One may at least expect that the effects of nonuniform axial heat flux, which are now empirically modeled, may be simply seen by local conditions resulting from CFD predictions. Also the effects of spacer grid design on flow conditions seen by the wall may be described at the CFD scale whereas subchannel analysis can only describe the associated pressure loss, the additional mixing between neighboring subchannels and the effect on CHF when experimental data are available.

3.2. Review of the Data Basis for DNB. The following data sources were reviewed and analysed with respect to their interest for validating CFD tools used in DNB investigations. Table 2 summarizes the characteristics of the experiments, the measured parameters, and the correspondence between mesoscale phenomena and the available data. Some of these experiments provide data which may be far from flow conditions encountered in reactors when CHF occurs. However, they allow a separate effect validation with increasing complexity of the phenomenology. The "local predictive approach" requires that all local (mesoscale) T/H parameters be correctly predicted by CFD since the CHF criterion will be expressed as a function of them.

There are single phase liquid data (AGATE) which may be used as a first step in the validation of turbulence models in a rod bundle with spacer grids. Some air-water bubbly flow data (DEDALE, TOPFLOW) may be used as a first step in the validation of models for bubble transport and dispersion, coalescence and breakup, effects of polydispersion on interfacial forces, and momentum turbulent transfers. Boiling flow data in simple geometry (DEBORA, ASU,

Purdue data, KAERI data) either in steam-water of Freon (R12, R113) may then be used to further validate in more representative conditions (pressure is either atmospheric or similar to reactor conditions) the models already investigated in air-water conditions, with additional effects of wall heat transfers, turbulent heat transfers and interfacial heat, and mass transfers due to vaporization and condensation. Some DEBORA data were recorded in conditions which were very close to CHF occurrence. Effects of spacers are also validated in boiling flow conditions with the DEBORA-Promoter data. BFBT data are used to validate the void distribution of a steam-water boiling flow in a real BWR rod bundle geometry. These data are unique and can also be used to some extent for DNB investigations if one considers the low quality data. LWL data in a real-rod bundle of a WWER reactor finally allow a global validation of the boiling flowup to DNB.

3.2.1. DEDALE Air-Water Bubbly Flow Tests. DEDALE is an adiabatic air-water two-phase experimental programme performed at EDF/DER [8]. DEDALE aimed at analyzing the axial development of a bubbly flow in a vertical pipe up to the transition to slug flow and creating an accurate and reliable data base with local information for the validation of dynamics-related models in CFD tools [9, 10].

3.2.2. DEBORA Boiling Flow Tests in a Heated Pipe. The DEBORA experiment [11] was carried out at the Commissariat à l'Energie Atomique, Grenoble, France, to provide a reliable local data base on boiling phenomena (up to DNB) in PWR T/H condition ranges, in order to eventually achieve a better understanding and prediction of DNB-type boiling. Calculations and analysis with Neptune are reported in [12].

The test section is an electrically heated vertical tube with upward R12 boiling flow simulating PWR in-core T/H conditions, with local measurements along a diameter within the outlet tube cross section of both steam phase characteristics (void fraction, interfacial area concentration, bubble size, and mean axial velocity) and liquid phase parameter (temperature).

3.2.3. DEBORA Tests in a Heated Pipe with a Turbulence Promoter/Enhancer (Swirl Flows). The "DEBORA-Promoter" tests (see Figure 1) with a vane type turbulence promoter/enhancer were carried out in addition to the previous ones, to characterize the two-phase boiling flow behaviour in a complex geometry representing the industrial one. The test section is similar to the previous one, with addition of a turbulence promoter/enhancer located inside the tube either 23.5D or 10D upstream from the end of the heated length.

Validation of CFD tools on these tests provides additional information on the effect of spacer grid wake on the mixing of bubbles generated at the wall and on the effects of the flow rotation on the void repartition; simulations of such tests with Neptune_CFD were presented [13].

3.2.4. AGATE Single-Phase Tests. The AGATE experiment has been developed in CEA Grenoble. Two-test sections were used:

(i) "AGATE-Grid" consists of a 5×5 rod bundle inside a squared-section housing with a mixing vane grid;

(ii) "AGATE-Promoter" with a similar geometry as "DEBORA-Promoter" one (i.e., pipe with a 3-vane turbulence enhancer).

Nonheated water flows upwardly in the vertical test section, and velocity measurements are made using laser Doppler anemometry (LDA). Both the mean velocity and velocity fluctuations are measured in order to investigate the effects of the grid or promoter.

The data allow to validate the turbulence modeling with spacer grid (or turbulence promoter/enhancer) effects in single-phase conditions. They were used for validation of a 1D model with $k\&\varepsilon$ model [14].

3.2.5. QLOVICE Visualisation Tests. QLOVICE tests are being performed by CEA in order to investigate basic processes associated with DNB. QLOVICE is a visualization of pool boiling with high-speed video-camera.

(i) A transparent heated bottom wall allows to visualise the bubble nucleation and detachment.

(ii) A side window allows to see bubble behaviour after detachment.

First tests were performed and have clearly shown the dry patch evolutions. It was observed

(i) bubble sliding along the heating wall before detachment,

(ii) sudden large size dry patch extension observed followed by a wall rewetting,

(iii) many bubble clusters,

(iv) interactions between neighbouring nucleation sites.

Two main processes are assumed to play a significant (dominant) role on the DNB occurrence: a sudden extension of dry patch up to DNB or a CCFL type phenomenon with bubbles which cannot escape from wall after detachment. However, no conclusion can be presently drawn on the dominant process.

3.2.6. Arizona State University (ASU) Tests of Boiling Flow in a Heated Annular Channel. Experiments of turbulent subcooled flow in a vertical annular channel were carried out at the Arizona State University [15–18] to provide detailed information on average flow structure, temperature, and gas and liquid flow fields in fully developed nucleate boiling, as well as on turbulent variables controlling transport mechanisms. In the experiment, R-113 was the working fluid.

Validation of CFD tools on ASU tests provides information on the steam production at the wall in subcooled boiling, on the interfacial forces responsible for the void profiles, on interfacial heat and mass transfers, on interfacial area concentration evolution, and on turbulence in the bubbly boundary layer.

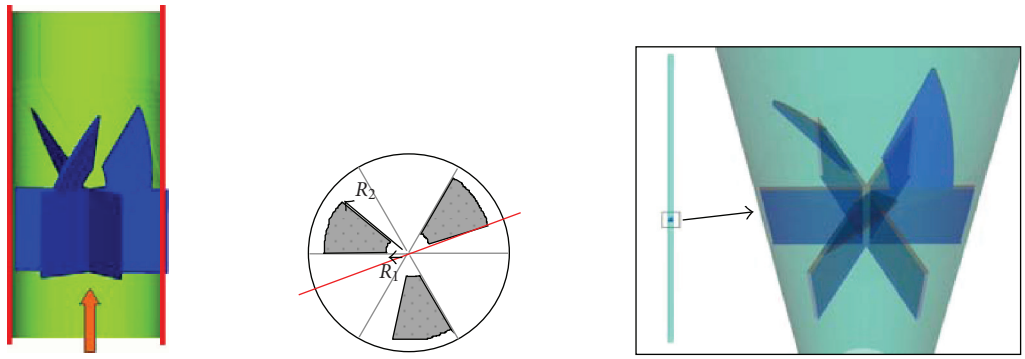

Figure 1: "DEBORA-promoter" geometry.

Measurements used simultaneously a two-component laser Doppler velocimetry for liquid velocity and a fast response cold-wire for temperature field, as well as a dual-sensor fiber optic probe for the vapour fraction and vapour axial velocity.

A comparison of Neptune simulations with the early tests was presented in [17].

3.2.7. Purdue University (PU/NE) Tests of Boiling Flow in a Heated annular Channel. Experiments have been carried out at the School of Nuclear Engineering of Purdue University in an internally heated annulus to provide local measurements of void fraction, interfacial area concentration, and interfacial velocity in subcooled boiling [19–22]. Water at atmospheric pressure was the working fluid. Influence of inlet liquid temperature, heat flux, and inlet liquid velocity on local flow parameters was specially investigated. The chosen geometry and set of conditions were aimed at scaling the conditions of a BWR. Although properties at 70 bar could not be represented, geometrical, hydrodynamic, and thermal similarities for the flow boiling processes were preserved.

Earlier tests [19, 20] include information on the axial evolution of the measured variables, and preliminary studies [19] addressed the dependence of bubble size before detachment on the axial position.

Visual observations of the boiling processes provided essential information on the displacement between the location of net vapor generation (NVG) and the location of bubble detachment [19]. More recent photographic studies of bubble lift-off diameters have been presented by Situ et al. [22–24].

A few analyses to test the validity of CFD codes have been carried out using the earlier series of test data [25, 26].

3.2.8. KAERI Tests of Boiling Flow in a Heated Annular Channel. Experiments have been carried out at the Korea Atomic Energy Research Institute (KAERI) in an internally heated annulus to provide local measurements of void fraction and phase velocities in subcooled boiling [27–29]. Water at low pressure (1 to 2 bar) is the working fluid. The aim was to provide a database for subcooled boiling modeling, including aspects such as force balances for departing vapour bubbles and bubble population balance.

Measurements of void fraction and bubble velocity were taken using a double-sensor conductivity probe. Liquid velocities were measured by a Pitot tube, correcting for the effect of bubbles [30]. Data included radial distributions of void fraction, axial liquid, and vapour velocity, interfacial area concentration (three tests only, [28]), Sauter mean diameter (three tests in [28], two more in [30]), bubble concentration (bubbles/unit volume, three tests only, [28]).

Tests have been used for assessing the CFX-4 code [27–31] especially the performance of an extension to 15 bubble classes of the MUSIG model.

3.2.9. Experimental Data on TOPFLOW Loop on Two Phase Flow in a Vertical Tube. The structure of an adiabatic air-water and of steam-water flow with reduced condensation and with slight subcooling in a vertical pipe of 195.3 mm inner diameter (DN200) was studied using wire-mesh sensors. The experiments were performed at the two-phase FLOW test facility (TOPFLOW) [32] of Safety Research of Forschungszentrum Dresden-Rossendorf e.V., which can be operated for pressure up to 7 MPa and temperature up to 286°C. Air-water data at ambient conditions and steam-water data under nearly adiabatic conditions as well as with slightly subcooled water are available for pressures of 1 and 2 MPa. Wire-mesh sensors can characterize the shape of large bubbles, since they acquire the phase distribution in the entire cross-section. By changing the injecting position of the gas supply during the next test, it is possible to study the evolution of the flow structure along the flow path in the DN200 vertical pipe.

Function and construction of wire-mesh sensors are described in [33]. Cross-section averaged gas fractions as well as radial gas fraction profiles can be calculated [34]. Radial gas velocity profiles were obtained by means of a point-to-point cross-correlation between the signals of both sensors placed in a distance of 63 mm behind each other [35]. Bubble

size distributions were extracted from the measuring data using the algorithm described by [36].

A technique to analyse the evolution of the flow structure is the calculation of radial gas fraction profiles decomposed according to bubble size classes [34]. The method was used to decompose the radial gas fraction profiles into 4 bubble size classes: class 1 from 0 to 4.8 mm equivalent diameter, class 2 from 4.8 to 5.8 mm, class 3 from 5.8 to 7.0 mm, and class 4 above 7.0 mm. Here, 5.8 mm is the critical diameter for the inversion of the lift-force according to Tomiyama [37] for air bubbles in water at ambient temperature. It decreases in case of steam-water flow with increasing pressure.

A visualisation (see Figure 2) is done by generating virtual side projections and side views of virtual central cuts from the mesh-sensor data according to the algorithms described in [38]. For each mesh-sensor data set, virtual side views and virtual centre cuts are combined in the same image. The height-to-width relation of the depicted bubbles is nearly respected in this image. It is visible how bubbles injected at the periphery move towards the centre of the pipe in case of the reference experiment without subcooling, while in the experiment with condensation the bubble density decreases with growing distance from the injection device.

The data can be used to test the complex interaction of local bubble distributions, bubble size distributions, and local heat and mass transfer. The lateral motion of the bubbles in a shear flow, bubble coalescence, and breakup and the phase transfer can be observed by measurements along the pipe. For example, the radial distribution of bubbles strongly depends on their diameter. For a vertical cocurrent upwards flow, smaller bubbles tend to move towards the wall, while large bubbles are preferably found in the centre. Details on the steam-water experiments and investigations on the modeling of such flows are presented by Lucas and Prasser [39].

3.2.10. BFBT Data on Void Fraction Distribution in BWR Fuel Assembly. Experimental tests for measuring the void fraction distribution inside boiling water reactor (BWR) fuel assemblies have been conducted by the Nuclear Power Engineering Corporation (NUPEC), Tokyo, Japan, by the use of an experimental facility referred to as BFBT (BWR Full-size Fine-mesh Bundle Tests). Data provided by such facility have been initially used for subchannel code assessment [40] and are currently being used for CFD code assessment in the framework of an OECD-NEA/US-NRC Benchmark. X-ray CT scanner and X-ray densitometers are employed to measure the void fraction distribution in a BWR full-scale fuel assembly under steady-state and transient conditions.

The test loop has a full range of steady-state void fraction testing capabilities over BWR operating conditions. Unsteady characteristics, flow changes, power changes, and complicated BWR operational transients are simulated too.

The test section consists of a full-scale BWR fuel assembly simulator, which is made of electrically heated rods able to reproduce the actual power profiles generated by nuclear fission. The instrumentation allows measurements of temperature, flow rate, pressure and, mainly, void fraction.

An X-ray CT scanner, consisting of an X-ray tube and 512 detectors, is employed to measure the void fraction in the upper part of the test section in steady-state conditions. The void fraction data have a $0.3 \times 0.3\,\text{mm}^2$ resolution. Such a high resolution makes those data useful for CFD code validation.

3.2.11. Large Water Loop Experimental Test Facility. The large water loop has been built at the NUCLEAR MACHINERY PLANT, ŠKODA, Plzen Ltd., Plzen, Czech Republic. The loop is a nonactive pressurized-water equipment with technological and thermal parameters corresponding to those of PWR. The possible parameter ranges are suitable for all types of pressurized water reactors. The CHF experimental facility (a part of large water loop) has been designed for the research of CHF in water flow through a bundle of electrically heated rods.

The test sections were formed by 7 or 19 parallel electrically heated rods with external diameters of 9 mm. Axial and radial uniform or nonuniform heat flux distribution and water up flow were used in the tests. The rods were with direct heating were specially manufactured with axially varying wall thickness while maintaining a constant outside diameter to achieve nonuniform axial heat flux. The rods (3500 mm long) were placed in regular hexagonal geometry with a pitch of 12.5–13 mm. Critical conditions were obtained under constant thermal-hydraulic conditions by gradually increasing heat input.

3.3. Development and Validation Programme of Work. Based on data and manpower availability, the following programme of validation was planed to be performed within the NURESIM project (see Table 1). Validation (V) tests allow to draw conclusions on the validity of some models whereas demonstration (D) tests check the capability of a software to simulate a complex process.

Table 2 presents the correspondence between the above data sources and the basic phenomena at the mesoscale.

The present data basis is not sufficient to validate all phenomena of interest, and the main defaults are the lack of turbulence data in high void bubbly flow and the lack of data for validation of the heat flux partitioning at the wall in convective nucleate boiling. More generally no data can provide information on microscale phenomena which makes the development of physically based models in the near wall region difficult.

3.4. State of the Art in DNB Modeling Within the NURESIM Project. The following state of the art on the modeling of two-phase flow up to DNB occurrence results from the ongoing work in NURESIM which mainly addressed flow conditions before DNB.

(1) Basic model: as boiling bubbly flows are encountered, the two-fluid model is naturally used in this flow conditions to benefit from the possibility to model all interfacial forces acting on the bubbles such as drag, lift, turbulent dispersion, virtual mass, and wall forces which control the void repartition in a boiling channel. The choice of the

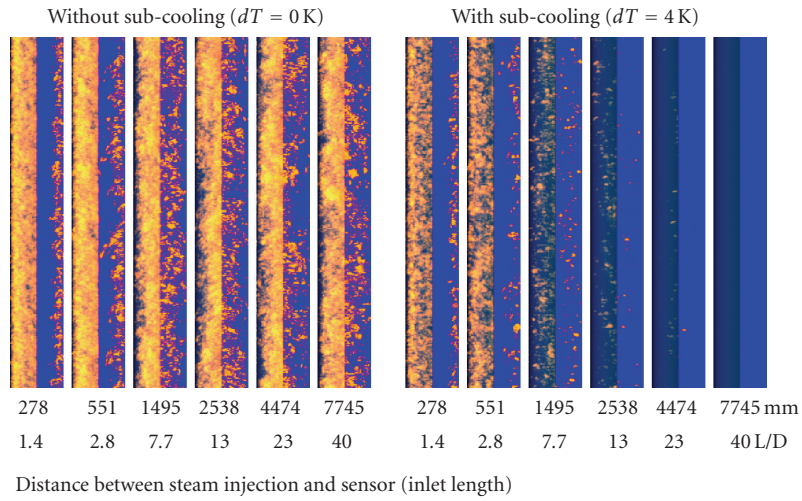

Figure 2: Virtual side projections (left halves of the columns) and side views of virtual central cuts (right halves) of the mesh-sensor data (from [39]).

Table 1: Planed validation and demonstration calculations within NURESIM project.

Validation tests and demonstration tests	Validation Demonstration	Main interest of validation
DEBORA	V	Investigations of wall heat transfer models
DEBORA tests close to CHF conditions	V	Looking for processes responsible for void accumulation close to the wall
DEBORA and/or TOPFLOW polydispersed data	V	Validation of the method of statistical moments
TOPFLOW polydispersed data	V	Validation of the MUSIG method
DEBORA polydispersed data	V	Validation of the MUSIG method
DEDALE	V	Evaluation of LES simulation of bubbly flow
ASU boiling water experiment	V	Validation of wall function Evaluation of LES simulation of boiling bubbly flow
BFBT experiments	VD	Evaluation of models controlling void distribution in actual core geometry
DEBORA	V	Investigations of wall heat transfer models
Large water loop (LWL)	VD	Evaluation of CHF prediction CFD in actual core geometry

method to model poly-dispersion effects remains partly open.

(2) Averaging or filtering equations: considering flow in a PWR core in conditions close to nominal, when boiling occurs, a high velocity steady flow regime takes place with times scales associated to the passage of bubbles being very small (10^{-4}, 10^{-3} s) and with bubble diameter being rather small (10^{-5} to 10^{-3} m) compared to the hydraulic diameter (about 10^{-2} m). These are perfect conditions to use a time average or ensemble average of equations as usually done in the RANS approach. All turbulent fluctuations and two-phase intermittency scales can be filtered since they are significantly smaller than scales of the mean flow. The use of a large eddy simulation (LES) approach may allow to simulate bubble dispersion by liquid turbulence instead of modeling it. This LES approach has been used with success in bubble plume simulations but cannot replace the RANS approach for convective boiling flows.

(3) Identification of local interface structure: there is a unique interfacial structure corresponding to a dispersed gas phase in a continuous liquid. As long as bubbly flow is encountered, there is no need to develop an identification of the local flow regime and there is no need to use an ITM. Going to DNB occurrence, a gas layer appears and a criterion must be implemented for identifying this occurrence. A very simple criterion based on the local void fraction was applied to LWL tests. However, the description of the interface structure may require addition of transport equations such as interfacial area transport (IAT) or bubble number density transport. More generally, the method of the statistical moments (MMSs) can be used to characterise the poly-dispersion of the vapour phase with a bubble

Table 2: *Correspondence between the data sources relative to DNB investigations and the basic phenomena at the mesoscale*. α: local void fraction, Ai: local interfacial area density, δ_b: local average bubble diameter, F_δ: bubble size distribution, V_{lz}: axial mean liquid velovity, v'_{lz}: rms axial liquid velovity, V_{bz}: axial mean bubble velovity, T_l: liquid temperature, T_w: wall temperature, T'_w: rms value of wall temperature, V_{lx}: radial component of mean liquid velovity, v'_{lx}: rms radial component of liquid velovity, ϕ_{crit}: critical heat flux.

	DEDALE	DEBORA	DEBORA Promoter	AGATE (&AGATE-promoter)	ASU	PURDUE boiling	KAERI boiling	TOPFLOW	BFBT	LWL
Geometry	Tube $L = 6$ m $D = 0.0381$ m	Tube $D = 0.0192$ m	Tube + promoter	Rod bundle (tube +promoter)	Annulus $Di = 15.78$ mm $De = 38.02$ m	Annulus $Di = 19.1$ m $De = 38.1$ m	Annulus $Di = 19$ mm $De = 37.5$ mm	Tube $D = 195.3$ mm	Rod bundle	Rod bundle
Fluid/flow conditions	Air-water adiabatic	R12	R12	water	R113	Steam-water	Steam-water	Air-water and steam-water	Steam/ water	Steam/ water
Local measurements	α, Ai, δ_b, F_δ, V_{lz}, v'_{lz}, V_{bz} at $Z/D = 8$, 55 & 155	α, Ai, T_l, T_w, δ_b, V_{bz},	α, Ai, T_l, T_w, δ_b, V_{bz},	V_{lz}, v'_{lz} V_{lx}, v'_{lx}	α, V_{lz}, v'_{lz}, v'_{lx}, V_{bz}, T_w, T'_w, turbulent heat fluxes	α, Ai, δ_b, V_{bz} at $z/D = 52.6$ +visual observations	α, Ai, δ_b, V_{lz}, V_{bz}	α, δ_b, V_{bz}, F_δ	α ϕ_{crit}	ϕ_{crit}
Wall to fluid heat		X			X	X	X			
Bubbles transport and dispersion	X	X			X	X	X	X		
Vaporization-condensation		X			X	X	X	X		
Coalescence and breakup of bubbles	X	X			X	X	X	X		
Turbulent Transfers of heat and momentum	X	X	X	X	X	X	X	X		
Effects of polydispersion		X						X		
Effects of grids			X	X						
Combined effects in real geometry									BWR	PWR WWER

size spectrum. Another approach of the poly-dispersion is to use a multigroup model (MUSIG method) with mass (and momentum) equations written for several bubble sizes. These two methods are being used, evaluated, and compared on both DEBORA and TOPFLOW tests. The MUSIG method with several mass equations for different bubble sizes and at least two momentum equations has shown good capabilities for capturing all qualitative effects in TOPFLOW vertical pipe tests. The MMS has been applied to a subcooled boiling DEBORA test, demonstrating a significant effect of polydispersion on the condensation predictions. MUSIG and MMS still have to be further evaluated.

(4) Momentum transfer control the void distribution and it is necessary to model all the forces acting on the bubbles. The virtual mass force is not expected to play a very important role, and rather reliable models exist for the drag force. More effort should be paid to the modeling and validation of both lift and turbulent dispersion forces since available models are still often tuned. In particular, since the lift force may depend on the bubble size, it is now necessary to model poly-dispersion to take this into account.

(5) Turbulent transfers: liquid turbulence plays a very important role in boiling flows. It influences liquid temperature diffusion, bubble dispersion, bubble detachment, bubble coalescence, and breakup which affect the interfacial area. Then, the liquid turbulent scales have to be predicted correctly to model all these processes and this will require additional transport equations. The k-epsilon or SST method was used with some success in DEBORA and TOPFLOW. A bubble column was simulated with some success using the NURESIM platform with a SGS model by Niceno et al. [41]. However, LES was not found well adapted to DEDALE test simulations or boiling flow simulations.

(6) Wall-to-fluid transfers: modeling of velocity profiles in the near-wall boiling region was improved by implementing the two-phase wall function in momentum equations. Models were validated on ASU boiling flow tests [42]. More specific wall functions need to be developed for boiling flow for energy equations. Such wall functions should be able to provide converged solution with a reasonably coarse nodalization close to a heating wall. Present versions of CFD tools provide models for heat flux partitioning into convection to liquid, vaporization, and quenching. Such models are using several correlations for density of nucleation sites, bubble departure diameter, and frequency of bubble departure, which are not separately validated by the present data basis. The comparison of void fraction close to the wall with measurements in DEBORA and ASU tests gives an indication that the amount of vaporization is reasonably predicted and the comparison of Sauter mean bubble diameter close to the wall in DEBORA tests gives an indication that the bubble departure diameter is also reasonably predicted, but more detailed experimental data in prototypical convective boiling conditions would be necessary for a more rigorous validation. The absence of a physically based DNB criterion is also a difficulty, and one may argue that microscale effects may affect the CHF even more than the mesoscale effects which are modeled. In the far future, such microscale phenomena might be clarified by microvisualisation techniques of by DNS prediction. In medium term, an empirical DNB criterion may be envisaged which will require final validation on very representative conditions. Today a simple criterion based on a limit void fraction at the wall is implemented in Neptune-CFD which allows a switch from nucleate boiling to film boiling heat transfer model but it is not satisfactory and did not predict LWL CHF tests very well.

(7) First demonstration test cases were performed with Neptune-CFD calculations of critical heat flux tests in the LWL loop which is prototypical of WWER type core assemblies. Computational grid consists of 150 000 hexahedral cells. Although the simulation is not fully successful quantitatively, Neptune showed the capability to model boiling flow in a complex industrial geometry and in reactor flow conditions up to CHF. CHF occurrence was predicted at the right location but with errors from 1% to 25% on the heat flux, which shows how far we still are from the final goal of the "local predictive approach."

4. The DryOut

4.1. The DryOut Phenomenology. Annular flow pattern usually is the predominant flow regime in upper core regions in boiling water reactors. The limitation of the total power obtained from each assembly is the occurrence of dryout. Increasing the heat flux above some critical value can lead to dryout that is associated with a sudden increase in the wall temperature, which, in turn, can destroy the cladding material and allow the radiation releases into the primary system. The phenomenology of dryout in annular mist flow was described in [43].

The liquid phase exists as a liquid film, which is attached to walls, and as droplets, which are carried in the central part of the channel by the vapour phase.

The mass flow rate in the liquid film is changing due to several mass transfer mechanisms.

(i) Due to hydrodynamic forces acting on the liquid film surface, certain amount of liquid from liquid film is entrained into the vapour core.

(ii) Another mechanism that is causing liquid film depletion is associated with evaporation due to heating applied to walls.

(iii) These two mechanisms must be counterbalanced by drop deposition from the vapour core to the liquid film surface to avoid film dryout.

There are several possible mechanisms that have been postulated for dryout (Hewitt, 1982 [44]).

(i) The liquid film dries by progressive entrainment and evaporation, which are prevailing in comparison to deposition, and dryout occurs when the film has gone.

(ii) Formation of a dry patch within the liquid film, causing such wall temperature increase that cannot be rewetted. In some situations a sudden disruption

of liquid film may occur beyond which the wall surface is dry. The disruption mechanism is not fully understood yet, however, hydrodynamic mechanisms for the disruption are postulated.

(a) For very thin liquid films. dryout occurs when the rate of evaporation at the surface exceeds the rate at which droplets arrive at the surface due to deposition.

(b) For thicker liquid films, it is postulated that dryout may occur due to vapour film formation under the liquid film. The mechanism of forming this vapour film might be of the same type as described for the DNB mechanisms.

Annular regime in boiling flow is characterized by a thin liquid film flowing on the channel walls and a gas core flowing in the central part of the channel. The droplets in the gas core represent a larger interfacial area than the liquid film and thus can dominate heat and mass transport between the phases. System pressure drop is increased by droplet acceleration in the gas core, and depositing droplets contribute to corrosion by increasing local wall friction.

To some extent, the dryout is a more simple process than the DNB since one cannot list so many microscale phenomena which may play a role. In particular, if one first focuses on the first dryout scenario with entrainment and evaporation prevailing in comparison to deposition, only mesoscale phenomena have to be considered.

The most important mesoscale phenomena and parameters in annular flow affecting the occurrence of dryout are

(1) drop size,

(2) deposition of droplets,

(3) entrainment of droplets, and

(4) film thickness.

Drop Size in Disperse Two-Phase Flow. Drop size is an important parameter which affects the deposition rates and thus the dryout phenomenon. It can be described by a size PDF, $f\,d(d)$ defined as the probability that a droplet from the distribution will have a diameter of d. It is often required that drop size distribution is represented by a single weighted mean size.

Deposition Rate. Liquid droplets carried by a turbulent gas stream will deposit on bounding walls. Clearly, deposition rate will have an important influence on the dryout occurrence.

It may depend on several unresolved issues, such as turbulence-particle interactions and drop breakup and coalescence.

Deposition rate will depend on drop dispersion in turbulent flow where particle motion is primarily governed by interactions with eddies of various scales. Depending on the ratio of the particle response time to the eddy characteristic time, the dispersion can have different characters. If this ratio is very small, particles are following the continuous flow structure. When the ratio is close to 1 (the time constants of eddies and particles are of the same range of magnitude), the dispersion of drops can be even bigger than that observed in the carrier fluid. Finally, for high values of the ratio particles remain largely unaffected by eddies.

Typically, drop deposition is associated with two mechanisms: the diffusion process and the free-flight to the wall. For proper prediction of the deposition rate of droplets, both these mechanisms have to be taken into account. In addition, impinging conditions of a drop on a liquid surface have to be considered. When a single droplet impinges a liquid film, various phenomena can occur. The droplet can bounce from the surface or merge with the liquid film. Splash can occur when the drop kinetic energy is high enough. For conditions typical for BWRs, the liquid film is thin and the velocity of droplets is high, thus splashing and mergence are the key phenomena involved.

Entrainment Rate. Several mechanisms of drop entrainment from the liquid film have been identified. The dynamic impact of gas core causes generation of waves on the film surface, with droplets being separated and entrained from the crests of these waves. The creation and breakup of the disturbance waves play important roles in the drop entrainment process. Another entrainment mechanism is associated with splashing associated with drop deposition, as already mentioned in the previous section. Finally, in a heated channel with nucleate boiling in the film, entrainment can occur due to the action of vapour bubbles which induce splashing.

Liquid Film Thickness. Calculation of the liquid film thickness is necessary to predict the occurrence of dryout. To obtain the liquid film thickness and velocity, it is necessary to solve the mass and momentum conservation equations of the film in order to determine the film flowrate and pressure drop. This requires proper modeling of deposition, entrainment, and evaporation in mass equation and of the wall friction and interfacial friction in the momentum equation which depend on the wave structure of the film interface.

4.2. DryOut Data Basis. Early experiments were focused on the measurements of the total power, which was necessary for the dryout occurrence in a heated channel. A vast number of these experiments were performed for different conduit geometries in different flow conditions. The measurements for steam-water were done in round ducts, annuli, and rod clusters. Measurements in annuli covered the pressures of 30, 50, and 70 bar (Becker and Letzer [45]; Persson [46]). For a validation of models based on the analysis of wall film flows, experimental data of pressure drops, including wall shear stress and interfacial shear stress, which characterize liquid film thickness and the onset of entrainment, respectively, are required. Also, actual measurements of film flows, film thickness, wave amplitude, frequencies, and wave velocities are needed for the validation. Moreover, because complete physical models for droplet entrainment and droplet deposition are still not available, experimental data of these are

needed to develop reliable correlations and/or computational models.

Würtz [47] has reported more than 2700 pressure drop measurements for steam-water and reviewed film flow measurements in steam-water mixtures in annular flow (see also Cousins & Hewitt [48]). The film flows were measured both in tubes and in annuli and recently, Adamson and Anglart [49] provided high-pressure steam-water data.

An extensive review of existing measurements of deposition rate has been presented by Okawa et al. [50]. The deposition rates were predominantly measured in air-water systems with low pressures (see also Govan et al. [51]). The techniques employed are the double film extraction, thermal method, and tracer method

It was experimentally proven that the mode of the deposition is dependent on the droplet size. Observations of droplet motion (Andreussi [52]) show that larger droplets travel across the gas core at about their initial velocity in a constant direction until they are deposited. This mechanism of deposition has been called direct impaction. At higher gas velocities where the droplets are comparatively smaller, the effect of the initial momentum on droplet motion becomes negligible. In this case, the eddy diffusion mechanism of deposition prevails. Bates and Sheriff [53] have presented a summary of the previous work done on droplet size/velocity in vertical annular air-water two-phase flow. The drop size distribution was investigated by Fore et al. [54] and Fore and Dukler [55]. When a gas phase is flowing over a liquid film, several different flow regimes are possible depending on the magnitude of the gas velocity. For a very small gas velocity, the interface is relatively stable, however, as the gas velocity increases the interfacial waves appear. The amplitude and irregularity of waves become pronounced as the gas velocity is further increased. At sufficiently high gas flow, the capillary waves transform into large-amplitude roll waves (disturbance waves). Near the transition to the roll wave or at a still higher gas velocity, the onset of entrainment occurs.

One way to measure entrainment is to reach a quasiequilibrium state in the system where it is considered that deposition rate is equal to the entrainment rate. Okawa et al. [50] presented a summary of existing experiments for the equilibrium entrainment rate.

Table 3 summarizes the available data base for annular-mist flow which can be used to validate CFD tools for dryout investigations.

4.3. State of The Art in DryOut Modeling Within The NURESIM Project. The following state of the art on the modeling of dryout by two-phase CFD results from the ongoing work in NURESIM.

(1) *Basic model approach:* in annular flows, the gas is a continuous phase and the liquid phase is split into a film which is continuous field and droplets as a dispersed field. The three-field model is naturally used in this flow conditions to benefit from the possibility to model separately the two liquid fields which have very different behaviours since the droplets have a high interfacial area and no wall friction whereas the film has a low interfacial area and has a friction along the wall. A simplified three-field model can be easily implemented in a two-fluid code by adding the film balance equations only in meshes along walls. The films are then treated as in a 1D model with mass momentum and energy equations written with a unique velocity component along vertical direction and a film thickness function of the vertical position only.

(2) *Filtering or averaging procedure:* considering flow in a BWR core in conditions close to nominal, a high velocity steady flow regime takes place with times scales associated to the passage of droplets being very small (10–4, 10–3 seconds) and with droplet diameter being rather small (10–5 to 10–3 m) compared to the hydraulic diameter (about 10–2 m). These are perfect conditions to use a time average or ensemble average of equations as usually done in the RANS approach. All turbulent fluctuations and two-phase intermittency scales can be filtered since they are significantly smaller than scales of the mean flow. There may be a difficulty if film waves have to be simulated since it is not clear how the averaging of the RANS approach may filter or damp the disturbance waves.

(3) *Identification of local interface structure:* is necessary to select the adequate interfacial transfer laws and to determine the interfacial area. Here, there are two interfacial structures corresponding either to a dispersed liquid phase in a continuous gas in the core flow or a film surface with waves and with droplet entrainment of deposition along walls. A simple way to identify the two situations is to consider that the latter only takes place in meshes along the walls while the former takes place everywhere else. The characterisation of the droplet field may require the use of additional transport equations for the droplet number density, or the interfacial area of any statistical moment of the droplet size distribution function. Another approach of the poly-dispersion is to use a multigroup model with mass (and momentum) equations written for several droplet sizes. A more simple characterisation of the droplet field by using an algebraic expression of an average drop diameter will be used and evaluated during the project.

(4) *Interfacial transfers:* mass transfers affect the film thickness and it is necessary to model at least the droplet deposition, the entrainment and the vaporisation. A new droplet deposition model was proposed and models for entrainment and vaporization were proposed to be evaluated. Momentum transfers affect the film thickness, and it is necessary to model gravity, wall friction, and interfacial friction. Models for these forces were proposed to be evaluated. Energy transfers also affect the film thickness, and it is necessary to model the wall heat flux, the interfacial transfer, the evaporation, and the energy transfer due to deposition and entrainment. Models for these transfers are proposed to be evaluated. Interfacial heat and mass transfer also affect the droplet field, and models are necessary for the convective heat flux from steam to droplet interface and the radiation heat flux from walls to the droplets. The mechanical behaviour of the droplets is mainly controlled by gravity and interfacial friction. Again the drop size and poly-dispersion

Table 3: *Data sources relative to dryout investigations.* Q_{film}: film flowrate, δ_f: film thickness, ΔP: pressure drop, f_w: wave frequency, C_w: wave velocity, E: fraction of entrained liquid, E_{eq}: equilibrium entrainment rate, Q_{dep}: deposition rates.

Reference	Measured value	Geometry	Fluid/heating	Flow conditions
Würtz, 1978 [47]	ΔP Q_{film} δ_f f_w C_w:	Tube test section: Di = 10 mm, Lh = 9.0 m Annulus section: Di = 17 mm De = 26 mm, Lh = 8.0 m; 3.5 m	Steam-water adiabatic and diabatic	P: 30, 50, 70, and 90 bar G: 500–3000 kg/m^2 s
Andreussi, 1983 [52]	ΔP	Plexiglass tube Di = 24 mm L = 5 m	Air-water adiabatic	P: atmospheric Gl: 9.73–200.3 g/s Gg: 17.5–50.3 g/s
Govan et al., 1989 [51]	ΔP τw τI Q_{dep}	LOTUS test rig tubular section Di = 31.8 mm L = 23 m	Air-water adiabatic	P: 2.4 bar Gl: 100, 200, 300, 500 kg/m^2 s Gg: 70–240 kg/m^2 s Temperature ambient
Cousins and Hewitt, 1968 [48]	Q_{film} C_w E	acrylic resin tube Di: 9.525 mm	Air-water adiabatic	P: 2 bar Gg: 18.14 & 31.75 kg/h Temperature ambient
Adamsson and Anglart, 2005 [49]	Q_{film}	Tube test section Di: 13.9 mm Lh: 3.65 m various power profiles	Steam-water diabatic	P: 70 bar G: 500–1750 kg/m^2 s
Okawa et al., 2005 [50]	Deposition mass transfer coefficients Droplet concentration E_{eq}	Stainless steel tube Di: 5 mm L: 3670 mm	Air-water	P: 1.4–7.6 bar Temperature ambient Gl: 201–1264 kg/m^2 s Gg: 173–627 kg/m^2 s
Fore et al., 2002 [54]	Drop size distribution	Stainless steel duct Di: 9.67 mm L: 3.4 m	Nitrogen-water	Pressure 3.4 and 17 bar Temperature 38°C Ql: 0.0157 and 0.126 kg/s Jg: 5, 7, 17 and 23 m/s
Fore and Dukler, 1995 [55]	Drop size distribution	Vertical tube Di: 50.8 mm L: 7.6 m	Air-water air-water+glycerine (50% mix) (6 cP liquid)	
Andreussi, 1983 [52]	E, Rate of liquid interchange	Plexiglass tube Di: 24 mm L: 5 m	Air-water adiabatic	Pressure: atmospheric Ql: 9.73–200.3 g/s Gg: 17.5–50.3 g/s

effects play an important role on these transfers. Models have still to be developed for these transfers on the droplet-vapour interface.

(5) *Turbulent transfers:* liquid turbulence plays a very important role in annular flows in a BWR core. It influences droplet deposition, droplet coalescence, and breakup which affects the drop size and consequently the deposition. Then, the vapour turbulent scales have to be predicted correctly to model all these processes and this will require additional transport equations to the three-field model. The k-epsilon method was used in a Eulerian-Lagrangian approach to investigate the deposition

5. Conclusion

While current industrial methods for CHF still use the subchannel analysis and empirical CHF correlations, the use of CFD already proved its potential interest in fine-scale investigations of boiling flows for a better understanding of sensitive flow processes. The "local predictive approach" where CHF empirical correlations would be based on local T/H parameters provided by CFD is not yet available but, with the present state of the modeling, CFD can already be used to subsequently help new fuel assembly design and to develop better CHF predictions in both PWR and BWR.

Acknowledgment

The NURESIM project is partly funded by the European Commission within the Sixth Framework Programme.

References

[1] D. Bestion, H. Paillère, A. Latrobe, et al., "EUROpean project for future advances in sciences and technology for nuclear engineering thermalhydraulics (EUROFASTNET)," in *Proceedings of the EU Research in Reactor Safety, Conclusion Symposium on Shared Cost and Concerted Actions (FISA '03)*, EC Luxembourg, November 2003.

[2] H. Paillère, A. Kumbaro, J. Garcia-Cascales, et al., "Advanced 3D two-phase flow simulation tool for application to reactor safety (ASTAR)," in *Proceedings of the EU Research in Reactor Safety, Conclusion Symposium on Shared Cost and Concerted Actions (FISA '03)*, EC Luxembourg, November 2003.

[3] M. Scheuerer, F. Menter, I. Tóth, et al., "Evaluation of computational fluid dynamic methods for reactor safety analyses (ECORA)," in *Proceedings of the EU Research in Reactor Safety, Conclusion Symposium on Shared Cost and Concerted Actions (FISA '03)*, EC Luxembourg, November 2003.

[4] A. Guelfi, M. Boucker, J. M. Hérard, et al., "A new multi-scale platform for advanced nuclear thermalhydraulics status and prospects of the NEPTUNE project," in *Proceedings of the 11th International Topical Meeting on Nuclear Reactor Thermalhydraulics (NURETH-11)*, Avignon, France, October 2005.

[5] D. Bestion and A. Guelfi, "Status and perspective of two-phase flow modelling in the NEPTUNE multi-scale thermal-hydraulic platform for nuclear reactor simulation," *Nuclear Engineering and Technology*, vol. 37, no. 6, pp. 511–524, 2005.

[6] D. Bestion and A. Guelfi, "Multiscale analysis of nuclear reactors thermalhydraulics—the NEPTUNE project," *La Houille Blanche*, no. 5, pp. 65–74, 2005.

[7] D. Bestion, H. Anglart, B. L. Smith, et al., "Extension of CFD codes to two-phase flow safety problems," Technical Note NEA/SEN/SIN/AMA(2006)2, OECD Nuclear Energy Agency, Paris, France, 2006.

[8] C. Grossetête, *Caractérisation expérimentale et simulations de l'évolution d'un écoulement diphasique à bulles ascendant dans une conduite verticale*, Ph.D. thesis, Ecole Centrale Paris, Paris, France, 1995.

[9] C. Morel, *Modélisation multidimensionnelle des écoulements diphasiques gaz-liquide—application à la simulation des écoulements à bulles en conduite verticale*, Ph.D. thesis, Ecole Centrale Paris, Paris, France, 1997.

[10] W. Yao and C. Morel, "Volumetric interfacial area prediction in upward bubbly two-phase flow," *International Journal of Heat and Mass Transfer*, vol. 47, no. 2, pp. 307–328, 2004.

[11] J. Garnier, E. Manon, and G. Cubizolles, "Local measurements on flow boiling of refrigerant 12 in a vertical tube," *Multiphase Science and Technology*, vol. 13, no. 1-2, pp. 1–111, 2001.

[12] C. Morel, Y. Wei, and D. Bestion, "Three dimensional modelling of boiling flow for the NEPTUNE code," in *Proceedings of the 10th International Topical Meeting on Nuclear Reactor Thermalhydraulics (NURETH-10)*, Seoul, Korea, October 2003.

[13] M. Boucker, A. Guelfi, S. Mimouni, P. Péturaud, D. Bestion, and E. Hervieu, "Towards the prediction of local thermal-hydraulics in real PWR core conditions using NEPTUNE_CFD software," in *Proceedings of the Workshop on Modelling and Measurements of Two-Phase Flows and Heat Transfer in Nuclear Fuel Assemblies*, KTH, Stockholm, Sweden, October 2006.

[14] G. Serre and D. Bestion, "Progress in improving two-fluid model in system code using turbulence and interfacial area equations," in *Proceedings of the 11th International Topical Meeting on Nuclear Reactor Thermalhydraulics (NURETH-11)*, Avignon, France, October 2005.

[15] R. P. Roy, V. Velidandla, S. P. Kalra, and P. Peturaud, "Local measurements in the two-phase region of turbulent subcooled boiling flow," *Journal of Heat Transfer*, vol. 116, no. 3, pp. 660–669, 1994.

[16] S. Kang and R. P. Roy, "Vapor phase measurements in subcooled boiling flow," *Journal of Heat Transfer*, vol. 124, no. 6, pp. 1207–1209, 2002.

[17] C. Morel, S. Mimouni, M. Lavieville, and M. Boucker, "R113 boling bubbly flow in an annular geometry simulated with the NEPTUNE code," in *Proceedings of the 11th International Topical Meeting on Nuclear Reactor Thermalhydraulics (NURETH-11)*, Avignon, France, October 2005.

[18] R. P. Roy, V. Velidandla, and S. P. Kalra, "Velocity field in turbulent subcooled boiling flow," *Journal of Heat Transfer*, vol. 119, no. 4, pp. 754–766, 1997.

[19] M. D. Bartel, *Experimental investigation of subcooled boiling*, M.S.N.E. thesis, Purdue University, West Lafayette, Ind, USA, 1999.

[20] M. D. Bartel, M. Ishii, Y. Mi, T. Masukawa, R. Situ, and M. Mori, "Experimental investigation of subcooled boiling under BWR flow conditions," in *Proceedings of the 9th International Topical Meeting on Nuclear Reactor Thermalhydraulics (NURETH-9)*, San Francisco, Calif, USA, October 1999.

[21] M. D. Bartel, M. Ishii, T. Masukawa, Y. Mi, and R. Situ, "Interfacial area measurements in subcooled flow boiling," *Nuclear Engineering and Design*, vol. 210, no. 1–3, pp. 135–155, 2001.

[22] R. Situ, T. Hibiki, X. Sun, Y. Mi, and M. Ishii, "Flow structure of subcooled boiling flow in an internally heated annulus," *International Journal of Heat and Mass Transfer*, vol. 47, no. 24, pp. 5351–5364, 2004.

[23] R. Situ, Y. Mi, M. Ishii, and M. Mori, "Photographic study of bubble behaviors in forced convection subcooled boiling," *International Journal of Heat and Mass Transfer*, vol. 47, no. 17-18, pp. 3659–3667, 2004.

[24] R. Situ, T. Hibiki, M. Ishii, and M. Mori, "Bubble lift-off size in forced convective subcooled boiling flow," *International Journal of Heat and Mass Transfer*, vol. 48, no. 25-26, pp. 5536–5548, 2005.

[25] B. Končar, I. Kljenak, and B. Mavko, "Modelling of local two-phase flow parameters in upward subcooled flow boiling at low pressure," *International Journal of Heat and Mass Transfer*, vol. 47, no. 6-7, pp. 1499–1513, 2004.

[26] B. Končar, I. Kljenak, and B. Mavko, "Nucleate boiling flow simulation with coupling of Eulerian and Lagrangian methods," in *Proceedings of the ASME Summer Heat Transfer Conference (HT '05)*, vol. 2, pp. 69–77, San Francisco, Calif, USA, July 2005.

[27] T. H. Lee, G. C. Park, and D. J. Lee, "Local flow characteristics of subcooled boiling flow of water in a vertical concentric annulus," *International Journal of Multiphase Flow*, vol. 28, no. 8, pp. 1351–1368, 2002.

[28] G. H. Yeoh and J. Y. Tu, "A bubble mechanistic model for subcooled boiling flow predictions," *Numerical Heat Transfer, Part B*, vol. 45, no. 5, part B, pp. 475–493, 2004.

[29] G. H. Yeoh and J. Y. Tu, "Thermal-hydrodynamic modeling of bubbly flows with heat and mass transfer," *AIChE Journal*, vol. 51, no. 1, pp. 8–27, 2005.

[30] J. Y. Tu, G. H. Yeoh, G.-C. Park, and M.-O. Kim, "On population balance approach for subcooled boiling flow prediction," *Journal of Heat Transfer*, vol. 127, no. 3, pp. 253–264, 2005.

[31] G. H. Yeoh and J. Y. Tu, "A unified model considering force balances for departing vapour bubbles and population balance in subcooled boiling flow," *Nuclear Engineering and Design*, vol. 235, no. 10–12, pp. 1251–1265, 2005.

[32] A. Schaffrath, A.-K. Krüssenberg, F.-P. Weiss, et al., "TOPFLOW—a new multipurpose thermalhydraulic test facility for the investigation of steady state and transient two phase flow phenomena," *Kerntechnik*, vol. 66, no. 4, pp. 209–213, 2001.

[33] H.-M. Prasser, A. Böttger, and J. Zschau, "A new electrode-mesh tomograph for gas-liquid flows," *Flow Measurement and Instrumentation*, vol. 9, no. 2, pp. 111–119, 1998.

[34] H.-M. Prasser, E. Krepper, and D. Lucas, "Evolution of the two-phase flow in a vertical tube—decomposition of gas fraction profiles according to bubble size classes using wire-mesh sensors," *International Journal of Thermal Sciences*, vol. 41, no. 1, pp. 17–28, 2002.

[35] H.-M. Prasser, J. Zschau, D. Peters, G. Pietzsch, W. Taubert, and M. Trepte, "Fast wire-mesh sensors for gas-liquid flows—visualization with up to 10 000 frames per second," in *Proceedings of the International Congress on Advanced Nuclear Power Plants (ICAPP '02)*, Hollywood, Fla, USA, June 2002, paper # 1055.

[36] H.-M. Prasser, D. Scholz, and C. Zippe, "Bubble size measurement using wire-mesh sensors," *Flow Measurement and Instrumentation*, vol. 12, no. 4, pp. 299–312, 2001.

[37] A. Tomiyama, "Struggle with computational bubble dynamics," in *Proceedings of the 3rd International Conference on Multiphase Flow (ICMF'98)*, pp. 1–18, Lyon, France, June 1998.

[38] H.-M. Prasser, M. Beyer, A. Böttger, et al., "Influence of the pipe diameter on the structure of the gas-liquid interface in a vertical two-phase pipe flow," in *Proceedings of the 10th International Topical Meeting on Nuclear Reactor Thermalhydraulics (NURETH-10)*, Seoul, Korea, October 2003.

[39] D. Lucas and H.-M. Prasser, "Steam bubble condensation in sub-cooled water in case of co-current vertical pipe flow," *Nuclear Engineering and Design*, vol. 237, no. 5, pp. 497–508, 2007.

[40] A. Inoue, T. Kurosu, T. Aoki, M. Yagi, T. Mitsutake, and S. Morooka, "Void fraction distribution in BWR fuel assembly and evaluation of subchannel code," *Journal of Nuclear Science and Technology*, vol. 32, no. 7, pp. 629–640, 1995.

[41] B. Niceno, B. Smith, and M. T. Dhotre, "Euler-Euler large eddy simulation of a square cross section bubble column using the NURESIM CFD platform," in *Proceedings of the 12th International Topical Meeting on Nuclear Reactor Thermal-hydraulics (NURETH-12)*, Pittsburgh, Pa, USA, September-October 2007.

[42] B. Končar, "Use of two-phase wall function for simulation of boiling flow," in *Proceedings of the 12th International Topical Meeting on Nuclear Reactor Thermalhydraulics (NURETH-12)*, Pittsburgh, Pa, USA, September-October 2007.

[43] D. Bestion, D. Caraghiaur, H. Anglart, et al., "Review of the existing data basis for the validation of models for CHF," NURESIM Deliverable D2.2.1, http://www.nuresim.com.

[44] G. F. Hewitt, "Burnout," in *Handbook of Multiphase Systems*, G. Hetsroni, Ed., pp. 66–141, Hemisphere, New York, NY, USA, 1982.

[45] K. M. Becker and A. Letzer, "An experimental study of the effect of the axial heat flux distribution on the dryout conditions in a 3650 mm long annulus," *International Journal of Multiphase Flow*, vol. 7, no. 1, pp. 47–61, 1981.

[46] P. Persson, "Measurements and analysis of dry out in annular geometry with two sided heating with uniform and nonuniform axial power and the influence of spacers and spacer positions," SKI/KSU/KTH Project, 2001.

[47] J. Würtz, "An experimental and theoretical investigation of annular steam-water flow in tubes and annuli at 30 to 90 bar," Risø Report 372, Risø National Laboratory, Roskilde, Denmark, 1978.

[48] L. B. Cousins and G. F. Hewitt, "Liquid phase mass transfer in annular two-phase flow: droplet deposition and liquid entrainment," UKAEA Report AERE-R 5657, Atomic Energy Research Establishment, Harwell, UK, 1968.

[49] C. Adamsson and H. Anglart, "Experimental investigation of the liquid film for annular flow in a tube with various axial power distributions," in *Proceedings of the 11th International Topical Meeting on Nuclear Reactor Thermalhydraulics (NURETH-11)*, Avignon, France, October 2005.

[50] T. Okawa, A. Kotani, and I. Kataoka, "Experiments for liquid phase mass transfer rate in annular regime for a small vertical tube," *International Journal of Heat and Mass Transfer*, vol. 48, no. 3-4, pp. 585–598, 2005.

[51] A. H. Govan, G. F. Hewitt, D. G. Owen, and G. Burnett, "Wall shear stress measurements in vertical air-water annular two-phase flow," *International Journal of Multiphase Flow*, vol. 15, no. 3, pp. 307–325, 1989.

[52] P. Andreussi, "Droplet transfer in two-phase annular flow," *International Journal of Multiphase Flow*, vol. 9, no. 6, pp. 697–713, 1983.

[53] C. J. Bates and J. M. Sheriff, "High data rate measurements of droplet dynamics in a vertical gas-liquid annular flow," *Flow Measurement and Instrumentation*, vol. 3, no. 4, pp. 247–256, 1992.

[54] L. B. Fore, B. B. Ibrahim, and S. G. Beus, "Visual measurements of droplet size in gas-liquid annular flow," *International Journal of Multiphase Flow*, vol. 28, no. 12, pp. 1895–1910, 2002.

[55] L. B. Fore and A. E. Dukler, "The distribution of drop size and velocity in gas-liquid annular flow," *International Journal of Multiphase Flow*, vol. 21, no. 2, pp. 137–149, 1995.

Hindawi Publishing Corporation
Science and Technology of Nuclear Installations
Volume 2009, Article ID 410272, 8 pages
doi:10.1155/2009/410272

Research Article

Euler-Euler Large Eddy Simulation of a Square Cross-Sectional Bubble Column Using the Neptune_CFD Code

B. Ničeno,[1] M. Boucker,[2] and B. L. Smith[1]

[1] *Thermal-Hydraulics Laboratory, Nuclear Energy and Safety Department, Paul Scherrer Institut, 5232 Villigen PSI, Switzerland*
[2] *Research & Development/MFEE, Electricité de France(EDF), 6 quai Watier, 78400 Chatou, France*

Correspondence should be addressed to B. Ničeno, bojan.niceno@psi.ch

Received 5 December 2007; Accepted 28 January 2008

Recommended by Iztok Tiselj

In this work, we report on Euler-Euler large eddy simulation (EELES) of dispersed bubbly flow in a square cross-sectional bubble column. Simulations are performed using the Neptune_CFD package, and results processed using the SALOME platform. The motivation to undertake this study is to check our implementation of the Smagorinsky subgrid-scale (SGS) model into Neptune_CFD. We outline all the physical models used, and we present instantaneous realizations of velocity and void fraction fields in order to illustrate the structure of the turbulence field, and long-time averaged results, to compare with analogous simulations performed using the CFX-4 code and experimental data. The same physical models and constants have been used in both the CFX-4 and Neptune_CFD codes, except the SGS model, which is Smagorinsky in case of Neptune_CFD and a one-equation model in CFX-4. The results obtained with EELES compare reasonably well with experiment, meaning in particular that the implementations have been successful. Some perspectives on the further use of EELES are also given.

1. Introduction

The aim of the NURESIM [1] integrated project is to provide the initial step towards a common European software platform for analysing, modelling, and exchanging data for nuclear reactor simulations. One of the main goals of the project is the integration of state-of-the-art physical models in a common, open-software platform, including the latest advances in reactor core physics, thermal-hydraulics, and coupled multiphysics modelling capabilities. The objective of the thermal-hydraulic subproject within NURESIM is the improvement of the predictive capabilities of the simulation tools for key two-phase-flow, thermal-hydraulic processes that can occur in nuclear reactors, focusing on two high-priority issues: critical heat flux (CHF) [2] and pressurized thermal shock (PTS) [3]. As a part of this activity, the Paul Scherrer Institute is investigating the potential of the EELES approach for simulating bubbly flows, which are important for understanding CHF and PTS, using the Neptune_CFD code [4], the CFD component of the NURESIM platform. In view of this, it was thought desirable to carry out EELES in a three-dimensional, square-cross-sectional bubble column, based on the experiments of Deen et al. [5], to validate the implementation of the SGS model in the code. In the present work, for reasons of simplicity, the performance of Neptune_CFD with the EELES paradigm is assessed based on the Smagorinsky SGS model. These results, and those obtained with the CFX-4 code, are compared against experimental findings [5]. We point to the potential weaknesses of the current approach, and propose directions for future research and development in the area.

Previous work on EELES (often referred to as two-fluid LES) for bubbly flows include Milelli et al. [6], who used Smagorinsky and dynamic SGS models to study the motion of a bubble plume in a cylindrical test section 50 cm in diameter, 40 cm high, for a maximum superficial gas velocity of 6.11 mm/s. A similar approach was taken by Deen et al. [7] to simulate a bubble plume in a test section with a square cross-section of 15 cm $\times$ 15 cm, a height of 45 cm, and superficial gas velocity of 4.9 mm/s. The authors compare the EELES prediction with those obtained using a $K - \varepsilon$ model and conclude that EELES results are closer to experimental measurements. Turbulent bubbly shear flows have also been analyzed [8] for a square channel 30 cm wide, 4 cm deep,

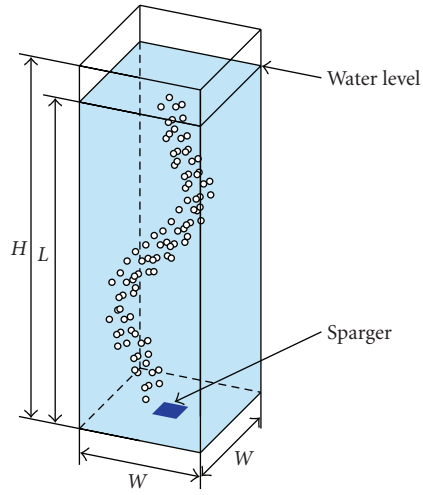

Figure 1: Geometry of the Deen bubble column experiment.

and 60 cm high. A splitter plane was used to divide the inlet channel in two equal parts. A mixture of water and air, with different velocities and void fractions, was introduced at the inlet sections. More recently, an LES calculation incorporating the Smagorinsky SGS model has been reported for a rectangular column [9]. LES predictions were compared with transient results obtained using a mixing length model and the $K-\varepsilon$ model; all three models produced similar results.

1.1. The Deen Bubble Column Experiment. In the Deen series of experiments [5], the hydrodynamics of the bubble plume is studied in the same apparatus, but for different inlet conditions. In the test to be investigated here, bubbles are created by injecting air with a superficial gas velocity of 4.9 mm/s through a central sparger at the bottom of the vessel of dimension 5 cm × 5 cm. The experiment operates at atmospheric pressure. A sketch of the Deen experiment is given in Figure 1.

2. Physical Models

2.1. Euler-Euler Approach. The governing equation for conservation of mass, with no mass exchange between the phases, takes the form:

$$\frac{\partial}{\partial t}(r\rho)_\alpha + \nabla\cdot(r\rho\mathbf{u})_\alpha = 0, \tag{1}$$

in which t is time, r is the volume fraction, ρ is the phase density, $\mathbf{u}$ the phase velocity, and α is the phase indicator. Conservation of momentum is governed by the relation:

$$\frac{\partial(r\rho\mathbf{u})_\alpha}{\partial t} + \nabla\cdot(r\rho\mathbf{u}\mathbf{u})_\alpha = -\nabla\cdot(r\tau)_\alpha - r_\alpha\nabla p + (r\rho)_\alpha\mathbf{g} + \mathbf{M}_{F,\alpha}, \tag{2}$$

where τ is shear stress, p is pressure, and $\mathbf{g}$ is the gravity vector. The last term on the right-hand side represents the momentum exchange between the phases due to interface forces and requires modelling. The models we have used are given in Section 2.3.

2.2. LES of Turbulence. Turbulence is modelled in the liquid phase of the flow. The first step in the derivation of the governing equations for LES is the decomposition of the velocity field into resolved (grid scale) and unresolved (SGS) parts. For each component, we write

$$\mathbf{u}_L = \widetilde{\mathbf{u}}_L - \mathbf{u}'_L, \tag{3}$$

where the resolved velocity on the left side is equal to the difference between the true instantaneous velocity (first term on the right) and the unresolved velocity (second term on the right). The filtering of the nonlinear advection term on the left-hand side of (2) leads to an additional stress-like term, which has to be modelled. Hence, we write

$$\tau_L = -2(\mu\mathbf{S})_L + \tau_{\mathrm{SGS},L}. \tag{4}$$

The first term represents the laminar stress, with the strain rate tensor defined as

$$\mathbf{S}_L = \frac{1}{2}\left[\nabla\mathbf{u}_L + (\nabla\mathbf{u}_L)^T\right], \tag{5}$$

and the second term derives from the turbulence effects and needs closure. In this work, we have used two closure models: Smagorinsky model (in Neptune_CFD), and a one-equation model (in CFX-4).

2.3. Smagorinsky Model. To complete (4), we use a formulation [10] for the turbulent stress:

$$\tau_{\mathrm{SGS},L} - \frac{1}{3}(\tau_{kk}\delta_{ij})_L = -2(\mu_t\mathbf{S})_L. \tag{6}$$

The second term on the left-hand side, the trace of the SGS stress tensor, is implicitly added to the pressure, while the deviatoric part is modelled by the expression on the right-hand side, that is, by the Boussinesq eddy viscosity (μ_t) concept. The Smagorinsky model is an algebraic one, with the eddy viscosity calculated from:

$$\mu_{t,L} = \rho_L(C_S\Delta)^2\,|\mathbf{S}_L|. \tag{7}$$

In (7), Δ is a filter width, associated with the cell size. In the present work, it was estimated as the cube root of the cell volume:

$$\Delta = V^{1/3}, \tag{8}$$

although other definitions are possible. C_S is the Smagorinsky constant, and was set here to 0.12 since the flow is dominated by the large-scale structures generated by the buoyancy force, as pointed out in [11]. The eddy viscosity, defined by (7), is used in the stress tensor appearing in the momentum (4), giving

$$\tau_L = -2\left[(\mu+\mu_t)\mathbf{S}\right]_L. \tag{9}$$

2.4. One-Equation SGS Model. A disadvantage of the Smagorinsky model is the loss of information resulting from use of the deviatoric part of the SGS stress tensor only. In CFX-4, we have implemented a transport equation for SGS kinetic energy (K_{SGS}), defined by

$$k_{\mathrm{SGS},L} = \frac{1}{2\rho_L}\tau_{kk,L}, \tag{10}$$

of the following transport form [12]:

$$\frac{\partial(r_L\rho_L k_{\mathrm{SGS}})}{\partial t} + \nabla\cdot(r_L\rho_L\mathbf{u}_L k_{\mathrm{SGS}}) = \nabla\left[r_L(\mu_L+\mu_{t,L})\nabla k_{\mathrm{SGS}}\right] = +r_L P_{k_{\mathrm{SGS}}} - r_L\rho_L C_\varepsilon\frac{k_{\mathrm{SGS}}^{3/2}}{\Delta}, \tag{11}$$

where $P_{k_{\mathrm{SGS}}}$ is the turbulence production term defined as:

$$P_{k_{\mathrm{SGS},L}} = (\mu_t\mathbf{S}:\mathbf{S})_L. \tag{12}$$

Using this model, the eddy viscosity is then calculated from:

$$\mu_{t,L} = C_k\rho_L\Delta k_{\mathrm{SGS},L}^{1/2}, \tag{13}$$

with model constants $C_k = 0.07$ and $C_\varepsilon = 1.05$. A detailed description of the one-equation SGS model for dispersed bubbly flows can be found in [12].

2.5. Interfacial Forces. To close the momentum equation set for the two phases, the various interphase exchange terms have to be modelled. The interphase exchange terms relevant for the configuration considered in this work are *drag*, *buoyancy*, *virtual mass,* and *lift* forces. In the framework of the EELES presented in this work, interfacial forces are applied only to the resolved field, while their SGS counterparts are neglected.

The *drag force* is modelled from the resolved velocity field as follows [13]:

$$\mathbf{M}_{D,L} = -\mathbf{M}_{D,G} = \frac{3}{4}r_G\rho_L\frac{C_D}{d_G}\left|\mathbf{u}_G-\mathbf{u}_L\right|(\mathbf{u}_G-\mathbf{u}_L), \tag{14}$$

where C_D is the drag coefficient, defined here in terms of the Eötvös number ($E_O = g\Delta\rho d_G^2/\sigma$):

$$C_D = \frac{2}{3}E_0^{1/2}. \tag{15}$$

In the present application, a bubble size of 4.0 mm is specified (the value reported in [5]), and the coefficient of surface tension $\sigma = 0.072$ N/m, giving $E_O = 2.2$ and $C_D = 1.0$.

For the *virtual mass force*, we use the model of Drew and Lahey Jr. [14]:

$$\mathbf{M}_{\mathrm{VM},L} = -\mathbf{M}_{\mathrm{VM},G} = r_G\rho_L C_{\mathrm{VM}}\left(\frac{D\mathbf{u}_G}{Dt} - \frac{D\mathbf{u}_L}{Dt}\right), \tag{16}$$

where C_{VM} is the virtual mass force coefficient, here set to 0.5.

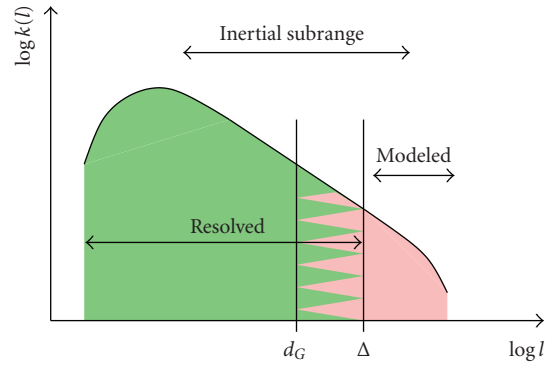

Figure 2: Bubble size larger than filter width.

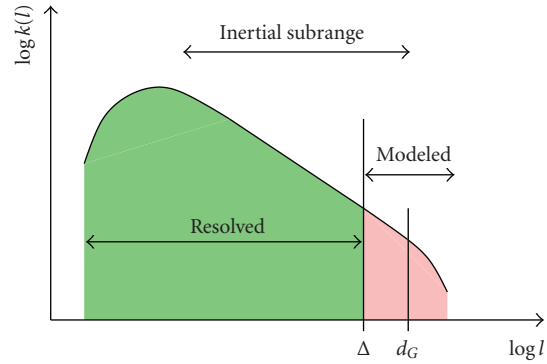

Figure 3: Bubble size smaller than filter width.

The *lift force* accounts for the transverse migration of bubbles under the influence of the liquid shear field. Following earlier work [14, 15], it is modelled here according to

$$\mathbf{M}_{L,L} = -\mathbf{M}_{L,G} = \rho_L C_L(\mathbf{u}_G-\mathbf{u}_L)\times\nabla\times\mathbf{u}_L, \tag{17}$$

in which the lift coefficient, C_L, is set to 0.5.

3. Requirements for the Numerical Grid

In the present work, we couple the Euler-Euler approach for multiphase flow with LES, and therefore have to consider the resolution requirements of both techniques simultaneously in order to choose a satisfactory grid. A basic requirement is that the control volume size should be large enough to encompass all the interface details. This is the intrinsic assumption in the derivation of the Euler-Euler model equations, and strictly has to be satisfied at the discrete level as well.

In LES, the SGS model is often very simple, and only drains energy from the resolved field without feed-back. Therefore, our goal in LES is to resolve as much of the flow field as possible, and to have as fine a grid as feasible for the available computer hardware. Since the Euler-Euler approach specifies the minimum control volume size, whereas for LES we are invariantly seeking as fine a grid as possible, the requirements for the numerical grid may sometimes

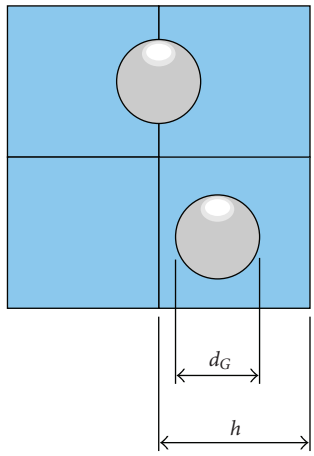

Figure 4: The Milelli condition.

be in conflict. The point is illustrated in Figures 2 and 3, which show the turbulence spectra under different modelling conditions. For a successful LES, we must have a filter width (Δ) in the inertial subrange region, and all scales of motion larger than that (left of Δ in Figures 2 and 3), must be accurately resolved on the numerical grid. If, however, we have a bubble diameter (d_G) larger than Δ (see Figure 2), it is obvious that they would induce some large-scale motions which are not properly accounted for by the EELES, since there is no information on the interface details or their influence on the resolved large-scale motions. If in addition we use a model for bubble-induced turbulence, it would drain the energy from the resolved field, further deteriorating the accuracy of the resolved field. This is illustrated by the saw-like shading in Figure 2. This influence on the resolved part of the spectra is not acceptable for LES. This is not just a conceptual consideration, as discussed in [6], and it is explained in more detail in Section 3.1 . The situation which is safe for EELES is shown in Figure 3, where d_G is smaller than Δ, and all bubble-induced scales which cannot be calculated using EELES approach fall into the SGS part of the spectra.

3.1. The Milelli Condition. The grid size considerations discussed above, are not new. In the present work, we have indicated why the bubbles must be smaller than the cell size from the point of view of the energy spectra and modelling closures for the interfacial forces. A systematic a posteriori analysis of the minimum ratio of the bubble and cell sizes for LES modelling of free bubble plumes is reported by Milelli et al. [6], which resulted in the following criterion:

$$\frac{h}{d_G} \geq 1.5. \tag{18}$$

Equation (18) states that the cell size must be at least 50% larger than the bubble diameter for accurate LES. The situation is illustrated in Figure 4. In the Deen experiment, the mean bubble size is 4 mm. Since the flow is dominated by the energetic, large-scale structures in the core of the flow, with wall effects having a smaller impact on the overall flow field, we have created a uniform grid with $30 \times 30 \times 100$ cubic cells. This results in a cell size of 5 mm, hence,

$$\frac{h}{d_G} = 1.2, \tag{19}$$

which is below the optimum value. A coarser mesh which satisfies the Milelli condition has also been used, but with no significant change in the computed results [12].

It might be argued at this point that the grid used in the present simulations is too coarse for LES, at least from the point of view of capturing all the relevant (large) scales. Judging from the flow patterns that can be expected in a square column such as this, with the bubble plume meandering from one direction to the other, it is quite conceivable that the largest, and therefore the most energetic, eddies will be of the size of the domain cross-section. Therefore, we are confident that the grid resolution we employ (30×30 cells in the cross-section) is sufficient to resolve these large structures. Should the topology of the flow be different, and should the flow be dominated by small, near-wall scales of motion, this resolution would not be adequate. The adequacy of the grid resolution used is proved in the following section.

4. Simulation Details

In this section, we briefly summarize all the relevant simulation details.

Inlet Superficial Velocities:.

for liquid: $J_L = 0.0$ m/s,

for gas: $J_G = 0.0049$ m/s.

Spatial Discretization:.

number of cells in computational domain: 90 000;

advection scheme: bounded central scheme for Neptune_CFD;

quick scheme for CFX-4.

Temporal Discretization:.

the linear backward time differencing for Neptune_CFD;

quadratic backward differencing for CFX-4;

CFL = 1.0, variable time step, approximately equal to 0.05 second for Neptune_CFD constant time step of 0.05 second for CFX-4, leading to CFL $\approx$ 1.0;

integral time of simulation: 400 seconds;

simple time-average is used in both, not weighted by volume fraction.

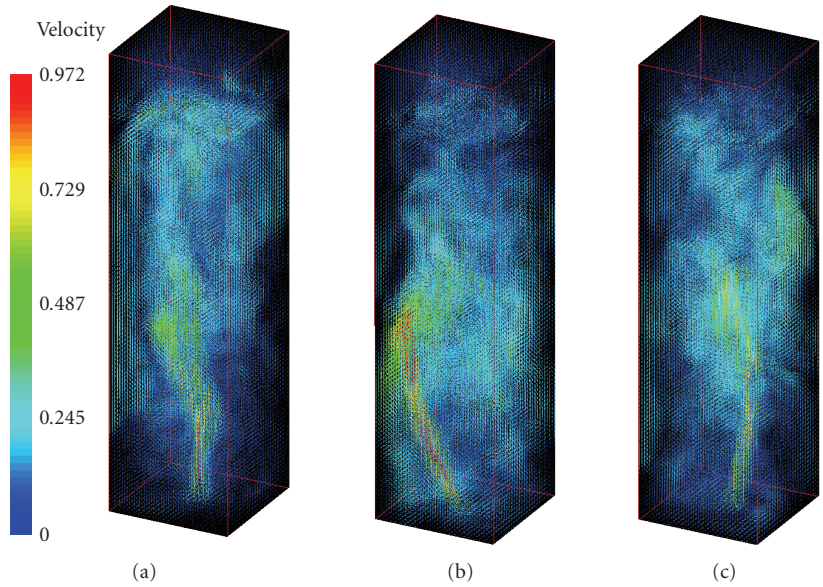

Figure 5: Instantaneous velocity vectors, calculated using Neptune_CFD, at instants: 60 seconds, 80 seconds, and 120 seconds.

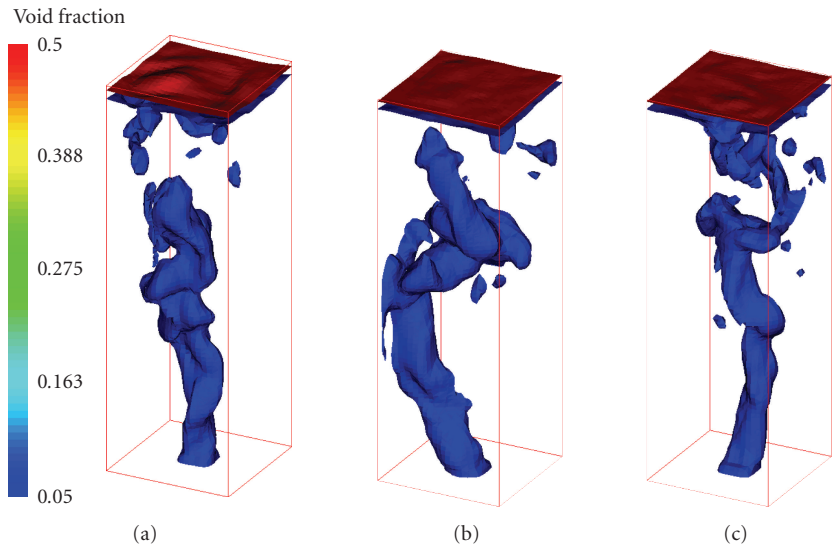

Figure 6: Isosurfaces of constant void fraction (0.05 and 0.5), calculated using Neptune_CFD, at instants: 60 seconds, 80 seconds, and 120 seconds.

5. Results

In this section, the results for our EELES with Neptune_CFD are presented. We start with the instantaneous velocity and void fraction fields to show the flow patterns in the bubble column flow, and continue with time-averaged velocity and fluctuating liquid velocity profiles. Time-averaged profiles obtained with Neptune_CFD and CFX-4 are compared with the experimental measurements of Deen et al. [5].

5.1. Instantaneous Results. Instantaneous velocity fields are shown in Figure 5. Velocity vectors are coloured with the velocity magnitude. Two things are immediately apparent. First, the velocity field does not show any signs of the growing instabilities to which LES computations are very often prone. This is not surprising, since the advection scheme is bounded. Another thing worth noting is that the velocity field pattern is changing dramatically in time. Bubbles are moving up through the large turbulent structures, driven by their buoyancy, resulting in different bubble paths at each time instant. This behaviour was also reported for bubble plume experiments [16]. Figure 6 shows two isosurfaces of constant void fraction. The blue one corresponds to the low-void fraction of $r = .05$ and the red to $r = .5$. The threshold for the blue isosurface gives a good illustration of the bubble plume shape, whereas the red one indicates the position of the free surface.

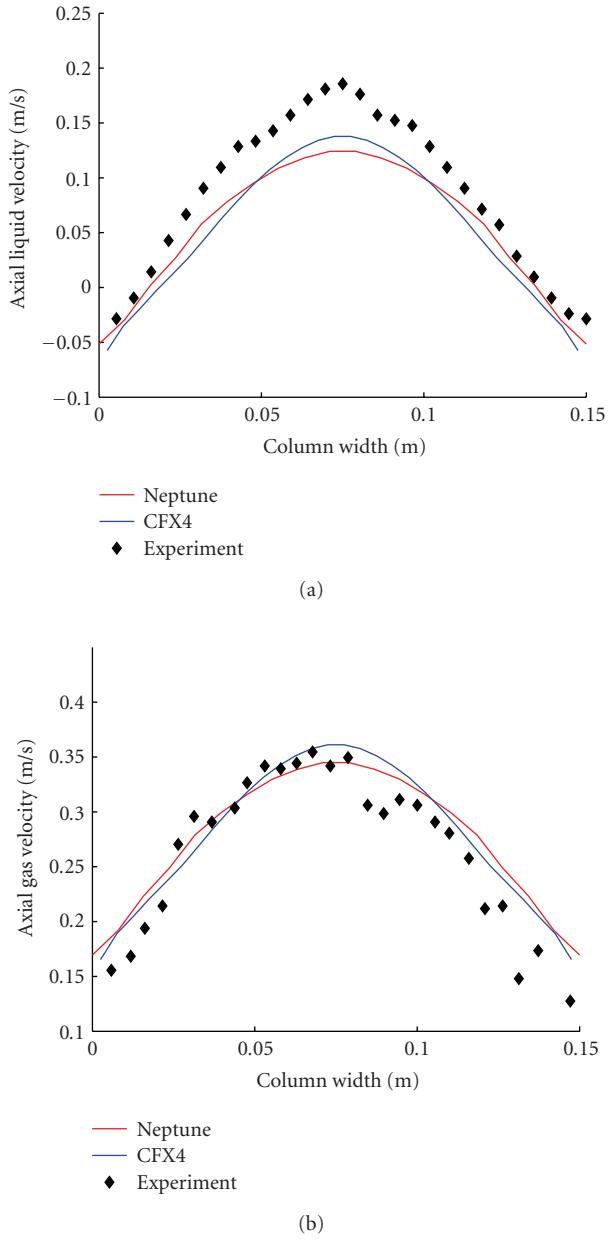

Figure 7: Comparison of (a) liquid and (b) gas velocity profiles obtained with CFX-4 using a one-equation model, Neptune_CFD with the Smagorinsky model, and experimental data.

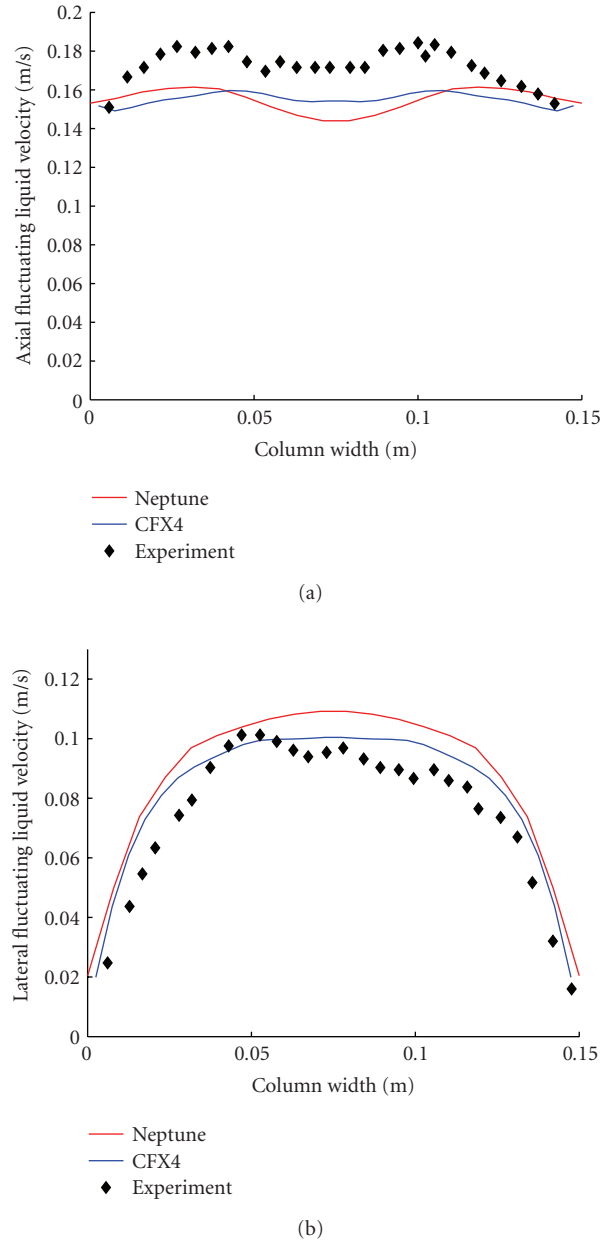

Figure 8: Comparison of (a) vertical and (b) lateral fluctuating liquid velocities, obtained using CFX-4 with a one-equation model, Neptune_CFD with the Smagorinsky model, and experimental data.

5.2. Time-Averaged Results. In this section, we compare the simulated profiles of liquid and gas vertical velocities and liquid turbulence intensities against the reported experimental data [5]. The measurements were taken along the centreline of the horizontal plane at height 25 cm.

Figure 7 shows comparisons of vertical liquid and gas vertical velocity profiles. The liquid velocity profile is somewhat under-predicted by both codes. In contrast, the gas velocity prediction compares very well with experiment in both cases. From these time-averaged results, it might be concluded that the drag force is underestimated in both codes, probably due to a wrong assumption for the drag coefficient (C_D), or for the relative velocity between the two phases [16].

The vertical component of the resolved vertical fluctuating liquid velocity is plotted in Figure 8(a). The qualitative comparison is encouraging for both codes, since the twin-peaked shape seen in the experiments is reproduced. Quantitatively, however, both codes under-predict the magnitude to some extent. Figure 8(b) shows the resolved lateral fluctuating liquid velocity, which is predicted very well. The total turbulent kinetic energy, plotted in Figure 9, in spite of the under-prediction of vertical fluctuating liquid component, is well predicted by both codes in the middle

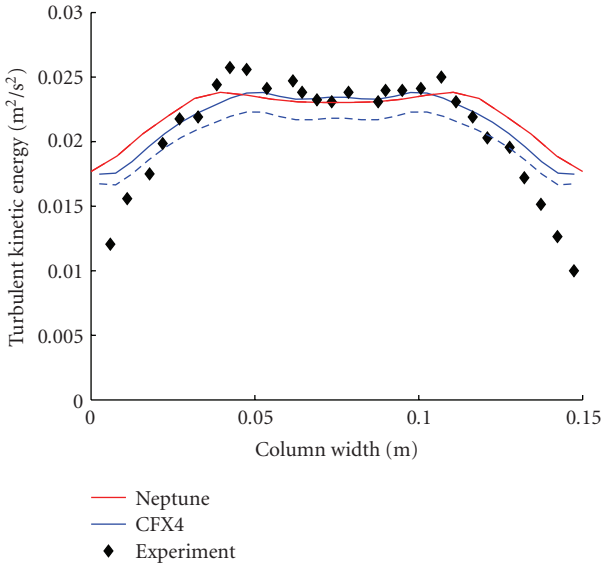

Figure 9: Comparison of liquid turbulent kinetic energy obtained with CFX-4 using a one-equation model, Neptune_CFD with the Smagorinsky model, and experimental data. The blue dashed line is the resolved, the blue continuous line is the total (resolved plus SGS) kinetic energy.

of the column and somewhat over-predicted close to the walls. This over-estimation of the near-wall kinetic energy might be attributed to insufficient resolution for the near-wall structures.

6. Conclusions and Perspectives

Implementation of the Smagorinsky SGS model in the Neptune_CFD code has been validated using data from the Deen bubble column experiment. Results have also been compared with predictions obtained from simulations performed using the code CFX-4. Generally, liquid velocity profiles are under-predicted compared with measured data, whereas the gas velocity profiles are predicted very well. This can only be attributed to a wrong assumption for the drag coefficient. The liquid velocity fluctuations predicted by both codes compare well with experiments, except for some under-prediction of the vertical component. Overall, the results obtained with the two codes are consistent, regardless of the fact that different SGS models have been used. This is a clear indication that the SGS model influences results only to a very small extent.

When envisaging the potential of LES for modelling multiphase flows in general, one should clearly distinguish between the scales at which LES might be used, since this implies the level of detail of accurate interface resolution to the degree of modelling that can be tolerated. Simulations at mesoscales imply an Euler-Euler description of the interface between the phases, such as the one described in this work. However, if LES for multiphase flows is applied at microscales, explicit interface tracking procedures would be needed. This has already been proposed in [17], and is generally referred to as large-scale simulation (LSS).

The principal advantage of EELES over LSS is that since the interface details are not calculated explicitly, the simulations may be carried out at lower cost. The principal disadvantage of EELES is that the most influential interfacial forces (lift and drag) are modelled for the large-scale field, meaning that the question of how to model these forces remains as open for EELES as it is with RANS. LSS, on the other hand, explicitly resolves the large-scale part of the interfacial forces, leaving the modelling at the SGS level, where the effects are smaller and hence less influential on the accuracy of the results. LSS modelling comes at a heavy price, due to the need to resolve all relevant interface details, imposing huge demands on computing power. Applying LSS to industrial-scale problems is beyond the current state of computing resources.

Another disadvantage of EELES stems from the different resolution requirements imposed by the Euler-Euler description of the two fluids and that of the LES approach itself, expressed in [6]. Since for an Euler-Euler description, the minimum cell size must be larger than the interface detail, accurate LES requires as fine a grid as possible. This requirement is particularly stringent in the near-wall regions, where the turbulent structures (e.g., streaks) are very small, and a very fine grid is needed to capture all relevant details. The disadvantages of EELES just outlined are not so pronounced for flows in which the bubbles are small compared to the grid size, such as for the bubble column studied in this work. Generally, one should use EELES if the flow is likely to be unsteady, with large coherent structures generated either by buoyancy or obstacles in the flow. EELES, as LES itself, should be avoided for wall-dominated flows. In other words, large eddy simulation should be used in the cases in which large eddies are present. Flows with density stratification in large channels (relevant to the PTS issue), in addition to bubble column devices, are examples where EELES has the potential to give accurate insight into the phenomena taking place and the ability to quantify them.

References

[1] D. Cacuci, "European Platform for Nuclear Reactor simulation (NURESIM)," *Integrated project NUCTECH-2004-3.4.3.1-1*. EURATOM Research and Training Programme on Nuclear Energy, 2004.

[2] D. Bestion, H. Anglart, P. Peturaud, et al., "Review of available data for validation of NURESIM two-phase CFD software applied to CHF investigations," in *Proceedings of the 12th International Topical Meeting on Nuclear Reactor Thermal Hydraulics (NURETH '07)*, Pittsburgh, Pa, USA, September-October 2007.

[3] D. Lucas, D. Bestion, E. Bodèle, et al., "On the simulation of two-phase flow pressurized thermal shock (PTS)," in *Proceedings of the 12th International Topical Meeting on Nuclear Reactor Thermal Hydraulics (NURETH '07)*, Pittsburgh, Pa, USA, September-October 2007.

[4] N. Méchitoua, M. Boucker, J. Laviéville, J. Hérard, S. Pigny, and G. Serre, "An unstructured finite volume solver for

two-phase water/vapour flows modeling based on an elliptic oriented fractional step method," in *Proceedings of the 10th International Topical Meeting on Nuclear Reactor Thermal-Hydraulics (NURETH '03)*, Seoul, Korea, October 2003.

[5] N. G. Deen, T. Solberg, and B. H. Hjertager, "Large eddy simulation of the gas-liquid flow in a square cross-sectioned bubble column," *Chemical Engineering Science*, vol. 56, no. 21-22, pp. 6341–6349, 2001.

[6] M. Milelli, B. L. Smith, and D. Lakehal, "Large-eddy simulation of turbulent shear flows laden with bubbles," in *Direct and Large-Eddy Simulation-IV*, B. J. Geurts, R. Friedrich, and O. Metais, Eds., vol. 8 of *ERCOFTAC Series*, pp. 461–470, Kluwer Academic Publishers, Dordrecht, The Netherlands, 2001.

[7] N. G. Deen, B. H. Hjertager, and T. Solberg, "Comparison of PIV and LDA measurement methods applied to the gas-liquid flow in a bubble column," in *Proceedings of the 10th International Symposium on Applications of Laser Techniques to Fluid Mechanics*, Lisbon, Portugal, July 2000.

[8] D. Lakehal, B. L. Smith, and M. Milelli, "Large-eddy simulation of bubbly turbulent shear flows," *Journal of Turbulence*, vol. 3, no. 25, pp. 1–21, 2002.

[9] B. N. Vanga Reddy, M. A. Lopez de Bertodano, E. Krepper, A. Zaruba, and H. M. Prasser, "Two-fluid model LES of a bubble column," in *Proceedings of the 11th International Topical Meeting on Nuclear Reactor Thermal-Hydraulics (NURETH '05)*, Avignon, France, October 2005.

[10] J. Smagorinsky, "General circulation experiments with the primitive equations," *Monthly Weather Review*, vol. 91, no. 3, pp. 99–165, 1963.

[11] J. B. Joshi, V. S. Vitankar, A. A. Kulkarni, M. T. Dhotre, and K. Ekambara, "Coherent flow structures in bubble column reactors," *Chemical Engineering Science*, vol. 57, no. 16, pp. 3157–3183, 2002.

[12] B. Ničeno, M. T. Dhotre, and N. G. Deen, "One-equation subgrid scale (SGS) modeling of Euler-Euler large eddy simulation (EELES) of dispersed bubbly flow," to appear in *Chemical Engineering Science*.

[13] M. Ishii and N. Zuber, "Drag coefficient and relative velocity in bubbly, droplet or particulate flows," *AIChE Journal*, vol. 25, no. 5, p. 843, 1979.

[14] D. A. Drew and R. T. Lahey Jr., "Virtual mass and lift force on a sphere in rotating and straining inviscid flow," *International Journal of Multiphase Flow*, vol. 13, no. 1, pp. 113–121, 1987.

[15] I. Žun, "The mechanism of bubble non-homogeneous distribution in two-phase shear flow," *Nuclear Engineering and Design*, vol. 118, pp. 155–162.

[16] M. Simiano, "Experimental investigation of large-scale three dimensional bubble plume dynamics," Dissertation, Swiss Federal Institute of Technology, Zurich, Switzerland, 2005.

[17] A. Alajbegovic, "Large eddy simulation formalism applied to multiphase flows," in *Proceedings of the ASME Fluids Engineering Division Summer Meeting (FEDSM '01)*, pp. 529–534, New Orleans, La, USA, May-June 2001.

Hindawi Publishing Corporation
Science and Technology of Nuclear Installations
Volume 2009, Article ID 792395, 14 pages
doi:10.1155/2009/792395

Research Article

A Second-Order Turbulence Model Based on a Reynolds Stress Approach for Two-Phase Flow—Part I: Adiabatic Cases

S. Mimouni,[1] F. Archambeau,[1] M. Boucker,[1] J. Laviéville,[1] and C. Morel[2]

[1] *Electricité de France R&D Division, 6 Quai Watier, 78400 Chatou, France*
[2] *Commissariat à l'Energie Atomique, 17 rue des Martyrs, 38000 Grenoble, France*

Correspondence should be addressed to S. Mimouni, stephane.mimouni@edf.fr

Received 14 December 2007; Revised 15 April 2008; Accepted 15 May 2008

Recommended by Dirk Lucas

In our work in 2008, we evaluated the aptitude of the code Neptune_CFD to reproduce the incidence of a structure topped by vanes on a boiling layer, within the framework of the Neptune project. The objective was to reproduce the main effects of the spacer grids. The turbulence of the liquid phase was modeled by a first-order K-ε model. We show in this paper that this model is unable to describe the turbulence of rotating flows, in accordance with the theory. The objective of this paper is to improve the turbulence modeling of the liquid phase by a second turbulence model based on a R_{ij}-ε approach. Results obtained on typical single-phase cases highlight the improvement of the prediction for all computed values. We tested the turbulence model R_{ij}-ε implemented in the code versus typical adiabatic two-phase flow experiments. We check that the simulations with the Reynolds stress transport model (RSTM) give satisfactory results in a simple geometry as compared to a K-ε model: this point is crucial before calculating rod bundle geometries where the K-ε model may fail.

1. Introduction

In a pressurized water nuclear reactor (PWR), an optimum heat removal from the surface of the nuclear fuel elements (rod bundle with spacer grids) is very important for thermal margin and safety.

One important goal is to carry out sensitivity analyses on the angle of the vanes of the fuel assembly spacer grids. In [1], the critical heat flux (CHF) experiment on the effect of the angle and of the position of mixing vanes was performed in a 2×2 rod bundle. The authors show that the mixing vanes increase the value of the CHF and the result is correlated to the magnitude of the swirl generated by the mixing vanes. If the angle of the mixing vanes is relatively small, the magnitude of the swirling flow is smaller because the rotating force created by the mixing vanes is weak. If the angle of the mixing vanes is relatively large, the mixing vanes play the role of flow obstacle under the departure from nucleate boiling (DNB) condition. Therefore, it is important that the turbulence modeling deals with rotation effects.

There have been several studies on flow mixing and heat transfer enhancement caused by a mixing-vane spacer grid in rod bundle geometry. Lee and Choi [2] simulate the flow field and heat transfer in a single-phase flow for a 17×17 rod bundle with eight spans of mixing vanes. The FLUENT commercial code is employed and a Reynolds stress transport model (RSTM) is used for turbulence. According to the authors, RSTM is helpful. Ikeda et al. [3] study an assembly consisting of a 5×5 heater rod bundle and eight specific mixing vane grids. For Ikeda et al., it might be insufficient to apply a standard K-ε model to swirl-mixing flow and narrow-channel flow conditions that include nonisotropic effects. Moreover, In et al. [4] have performed a series of CFD single-phase flow simulations to analyze the heat transfer enhancement in a fully heated rod bundle with mixing-vane spacers. For future work, In et al. recommend that a refined computational fluid dynamic (CFD) model be developed to include details of the grid structure and a higher-order turbulence model be employed to improve the accuracy of such simulations.

Additional two-phase effects like accumulation of bubbles in the center of subchannel or pockets of bubbles on the rods should be taken into account to improve the simulation of flow close to DNB. Indeed, single-phase

simulations remain insufficient and boiling flows simulations are required. In [5], the authors describe CFD approaches to subcooled boiling and investigate their capability to contribute to fuel assembly design. A large part of their work is dedicated to the modeling of boiling flows and to forces acting on the bubbles. The authors note that the size of bubbles in the bulk is correlated to the local subcooling which is an important parameter (see [1]).

Considering flow in a PWR core in conditions close to nominal, when boiling occurs, a high-velocity steady flow takes place with very small times scales associated to the passage of bubbles (10^{-4} second -10^{-3} second) and with quite small bubble diameters (10^{-5} m to 10^{-3} m) compared to the hydraulic diameter (about 10^{-2} m). According to the synthesis of the work performed in WP2.2 of the NURESIM project [6], these are perfect conditions to use a time average or ensemble average of equations as usually done in the RANS approach. All turbulent fluctuations and two-phase intermittency scales can be filtered since they are significantly smaller than the scales of the mean flow.

The large-eddy simulation is also a possible approach. In the context of the NURESIM project, several studies have been carried out with a large-eddy simulation to study the axial development of air-water bubbly flows in a pipe. But in the synthesis of the work performed in WP2.2, Bestion [6] notes that several open modeling and numerical issues still remain. So, we will focus on the RANS approach in this paper.

According to all these recommendations, a better understanding of the detailed structure of a flow mixing and heat transfer downstream of a mixing-vane spacer in a nuclear fuel rod bundle has to be investigated with an RSTM.

Moreover, the overwhelming majority of industrial CFD applications today are still conducted with two-equation eddy viscosity model, especially the standard K-ε model, while RSTM remains exceptional.

As an example of RSTM development, an RSTM model adapted to bubbly flows is studied in [7] and used to perform simulations of three basic bubbly flows (grid, uniform shear, and bubbly wake). The authors decomposed the Reynolds stress tensor of the liquid into two independent parts: a turbulent part produced by the mean velocity gradient that also contains the turbulence of the bubble wakes and a pseudoturbulent part induced by bubble displacements; each part is predicted from a transport equation. This model is interesting but has not been selected here for the following reasons. Firstly, the computation effort is doubled (turbulent and pseudoturbulent parts). Secondly, considering the flow close to nominal PWR core conditions, when boiling occurs, a high-velocity steady flow takes place and the bubble diameter is quite small (10^{-5} m to 10^{-3} m), therefore the bubbles follow the liquid streamlines and so the modeling of the pseudoturbulent part induced by bubble displacements can be omitted. Thirdly, the two-phase flow modeling proposed in [7] does not tend to a single-phase flow formulation when the void fraction tends to zero. These three arguments have imposed the choice of the higher-order turbulence model described in the paper.

A second-order moment turbulence model for simulating a bubble column is also proposed in [8]. The authors defined a Reynolds tensor for each phase. Furthermore, following a similar method used in deriving and closing the Reynolds stress equations, a modeled transport equation of two-phase velocity correlation is also solved. For the same reasons as those mentioned above for the model proposed in [7], we have not adopted the model proposed in [8]. The turbulence modeling described in the present paper takes into account the Reynolds tensor for the liquid only, while a more basic modeling is used for the vapor phase.

However, to the authors' knowledge, no industrial CFD approach for boiling flows with an RSTM approach is available in the context of the fuel assembly design. This may be due to the fact that numerical problems may occur when using an RSTM approach without caution. Furthermore, the turbulence modeling of boiling flows is not straightforward. The use of RSTM also requires finer meshes than eddy viscosity models (EVMs) and RSTM may therefore be more time and storage consuming. Developing an industrial RSTM approach is a quite challenging task but it is worth working at it: RSTM and EVM results will probably differ and it is important to determine what consequences it may have on thermal margin and safety of reactors.

In the framework of an R&D program carried out in the Neptune project (EDF, CEA, AREVA-NP, IRSN), the following strategy has been adopted:

(1) validation of the Neptune_CFD code with an RSTM approach on single-phase flow with mixing vanes and on more academic cases of air-water adiabatic bubbly flows in a pipe;

(2) validation of the Neptune_CFD code with an RSTM approach on boiling flows in a pipe and sensitivity to the angle of the vanes for fuel assembly spacer grids performed in a 2×2 rod bundle in a boiling flow configuration;

(3) validation of the Neptune_CFD code with an RSTM approach for a 5×5 rod bundle with mixing vanes currently used for commercial nuclear fuel.

Step (1) is described in this paper. The second step should be finalized by the end of 2008. The step (3) is not yet started. Our main objective in this paper is to check that the simulation with the RSTM gives satisfactory results in a simple geometry as compared to an EVM: this point is crucial before calculating rod bundle geometries where the EVM model may fail.

This paper is organized as follows. In Section 2.2, the general model we use for adiabatic bubbly flow simulations is presented in details. In Section 2.3, we underline the weaknesses of the EVM models. In Sections 3.1 and 3.2, the second-moment closure model for high Reynolds number two-phase flows is presented. In Section 2.4, we give some examples of typical PWR problems that EVM models fail to represent. In Sections 4.1 and 4.2, respectively, the Liu and Bankoff case and the sudden expansion experiment are briefly described. The comparison of the results of

Neptune_CFD calculations and the experimental data are presented. The sensitivity of the numerical results to the turbulence model for the fluid and to the most important models is studied.

Finally, conclusions are drawn about our current capabilities to simulate bubbly flows with an RSTM model and perspectives for future work are given.

2. The Neptune_CFD Solver and Physical Modeling

2.1. Introduction. Neptune_CFD is a three-dimensional two-fluid code developed more especially for nuclear reactor applications. This local three-dimensional module is based on the classical two-fluid one pressure approach, including mass, momentum, and energy balances for each phase.

The Neptune_CFD solver, based on a pressure correction approach, is able to simulate multicomponent multiphase flows by solving a set of three balance equations for each field (fluid component and/or phase) [9–12]. These fields can represent many kinds of multiphase flows: distinct physical components (e.g., gas, liquid, and solid particles), thermodynamic phases of the same component (e.g., liquid water and its vapor), distinct physical components, some of which split into different groups (e.g., water and several groups of different diameter bubbles), and different forms of the same physical components (e.g., a continuous liquid field, a dispersed liquid field, a continuous vapor field, and a dispersed vapor field). The solver is based on a finite volume discretization, together with a collocated arrangement for all variables. The data structure is totally face-based, which allows the use of arbitrary shaped cells (tetraedra, hexahedra, prisms, pyramids, etc.) including nonconforming meshes (meshes with hanging nodes).

2.2. Governing Equations and Physical modeling. The CFD module of the Neptune software platform is based on the two-fluid approach [13, 14]. In this approach, a set of local balance equations for mass, momentum, and energy is written for each phase. These balance equations are obtained by ensemble averaging of the local instantaneous balance equations written for the two phases. When the averaging operation is performed, the major part of the information about the interfacial configuration and the microphysics governing the different types of exchanges are lost. As a consequence, a certain number of closure relations (also called constitutive relations) must be supplied for the total number of equations (the balance equations and the closure relations) to be equal to the number of unknown fields. We can distinguish three different types of closure relations: those which express the interphase exchanges (interfacial transfer terms), those which express the intraphase exchanges (molecular and turbulent transfer terms), and those which express the interactions between each phase and the walls (wall transfer terms). The balance equations of the two-fluid model we use for adiabatic bubbly flows and their closure relations are described in the following subsections.

2.2.1. Main Set of Balance Equations. The two-fluid model we use for our adiabatic bubbly flow calculations consists of the following balance equations.

Two mass balance equations

$$\frac{\partial \alpha_k \rho_k}{\partial t} + \nabla \cdot (\alpha_k \rho_k \underline{V}_k) = 0, \quad k = l, g, \tag{1}$$

where t is the time, α_k, ρ_k, $\underline{V}_k$ denote the time fraction of phase k, its averaged density and velocity. The phase index k takes the values l for the liquid phase and g for gas bubbles.

Two momentum balance equations

$$\frac{\partial \alpha_k \rho_k \underline{V}_k}{\partial t} + \nabla \cdot (\alpha_k \rho_k \underline{V}_k \underline{V}_k) = -\alpha_k \underline{\nabla}_p + \underline{M}_k + \alpha_k \rho_k \underline{g} + \nabla \cdot \left[\alpha_k \left(\underline{\underline{\Sigma}}_k + \underline{\underline{R}}_k\right)\right], \quad k = l, g, \tag{2}$$

where p is the pressure, $\underline{g}$ is the gravity acceleration, $\underline{M}_k$ is the interfacial momentum transfer per unit volume and unit time, and $\underline{\underline{\Sigma}}_k$ and $\underline{\underline{R}}_k$ denote the molecular and turbulent stress tensors, the latter being also called the Reynolds stress tensor.

The interfacial transfer of momentum $\underline{M}_k$ appearing in the RHS of (2) is assumed to be the sum of four forces:

$$\underline{M}_k = \underline{M}_k^D + \underline{M}_k^{\mathrm{AM}} + \underline{M}_k^L + \underline{M}_k^{\mathrm{TD}}. \tag{3}$$

The four terms are the averaged drag, added mass, lift, and turbulent dispersion forces per unit volume. Now we will give the expressions we use for these forces and for their coefficients.

(i) Drag force

$$\underline{M}_g^D = -\underline{M}_l^D = -\frac{1}{8} A_i \rho_l C_D \left|\underline{V}_g - \underline{V}_l\right| (\underline{V}_g - \underline{V}_l), \tag{4}$$

where C_D is the drag coefficients for bubbles which can be determined experimentally. (ii) Added mass force

$$\underline{M}_g^{\mathrm{AM}} = -\underline{M}_l^{\mathrm{AM}} = -C_A^{\mathrm{lg}} \frac{1 + 2\alpha_g}{1 - \alpha_g} \alpha_g \rho_l \left[\left(\frac{\partial \underline{V}_g}{\partial t} + \underline{V}_g \cdot \underline{\underline{\nabla}} \underline{V}_g\right) - \left(\frac{\partial \underline{V}_l}{\partial t} + \underline{V}_l \cdot \underline{\underline{\nabla}} \underline{V}_l\right)\right], \tag{5}$$

where C_A^{lg} is the added mass coefficient which is equal to 1/2 for a spherical bubble and the factor $(1 + 2\alpha)/(1 - \alpha)$ takes into account the effect of the bubbles concentration [15, 16].

(iii) Lift force

$$\underline{M}_g^L = -\underline{M}_l^L = -C_L \alpha_g \rho_l (\underline{V}_g - \underline{V}_l) \wedge (\underline{\nabla} \wedge \underline{V}_l), \tag{6}$$

where C_L is the lift coefficient. This coefficient is equal to 1/2 in the particular case of a weakly rotational flow around a spherical bubble in the limit of infinite Reynolds number [17].

(iv) Turbulent dispersion force

$$\underline{M}_g^{\mathrm{TD}} = -\underline{M}_l^{\mathrm{TD}} = -C_{\mathrm{TD}} \rho_l K_l \underline{\nabla} \alpha_g, \tag{7}$$

where K_l is the liquid turbulent kinetic energy and C_{TD} is a numerical constant of order 1. This expression was proposed by Lance and Lopez de Bertodano [18]. An alternative approach is proposed by [19, 20] to model the turbulence induced by bubbles: an algebraic model developed in the framework of Tchen's theory, where the turbulent kinetic energy for the dispersed phase and the covariance are calculated from the turbulent kinetic energy of the continuous phase.

For the dispersed phase, the Reynolds stress tensor is closed using a Boussinesq-like hypothesis:

$$\underline{\underline{R}}_g = \rho_g \nu_g^T \left(\underline{\underline{\nabla}}\,\underline{V}_g + \underline{\underline{\nabla}}^T \underline{V}_g\right) - \frac{2}{3}\underline{\underline{I}}\left(\rho_g K_g + \rho_g \nu_g^T \nabla \cdot \underline{V}_g\right), \tag{8}$$

where $\underline{\underline{I}}$ is the identity tensor, with $\nu_g^T = (1/3)q_{\mathrm{lg}}(\tau_{\mathrm{lg}}^t - (C_A^{\mathrm{lg}}\tau_{\mathrm{lg}}^F/((\rho_g/\rho_l) + C_A^{\mathrm{lg}}))(\tau_{\mathrm{lg}}^F/2)) + (1/3)K_g\tau_{\mathrm{lg}}^F$, the turbulent viscosity for the dispersed phase, $K_g = K_l((b^2+\eta_r)/(1+\eta_r))$, the gas turbulent kinetic energy, $q_{\mathrm{lg}} = K_l((b+\eta_r)/(1+\eta_r))$, the covariance of the dispersed phase, $b = (1+C_A^{\mathrm{lg}})/((\rho_g/\rho_l)+C_A^{\mathrm{lg}})$, $\eta_r = \tau_{\mathrm{lg}}^t/\tau_{\mathrm{lg}}^F$, the ratio between the time scale of the continuous phase turbulence viewed by the dispersed phase (takes into account crossing trajectories effect) and the characteristic time scale of the momentum transfer rate between the liquid and dispersed phases:

$$\begin{aligned}\tau_{\mathrm{lg}}^t &= \frac{\tau_l^t}{\sigma_\alpha}\left(1 + C_\beta \xi_r^2\right)^{-1/2},\\ \tau_{\mathrm{lg}}^F &= \frac{C_A^{\mathrm{lg}} + \rho_g}{F_D^{\mathrm{lg}}},\end{aligned} \tag{9}$$

with σ_α is the turbulent Schmidt or Prandtl turbulent for the continuous phase, C_β is the crossing trajectories coefficient taken equal to 1.8, and C_A^{lg} is the added mass coefficient;

$$\xi_r = \frac{\langle |\vec{V}_r| \rangle_g}{\sqrt{(1/3)K_l}}, \qquad \tau_l^t = \frac{3}{2}C_\mu \frac{K_l}{\varepsilon_l}. \tag{10}$$

Turbulent dispersion force and Tchen's model will be compared below for bubbly flows in a straight pipe and in a sudden expansion.

2.2.2. Turbulent Transfer Terms. The K-ε model describes energy processes in terms of production and dissipation, as well as transport through the mean flow or by turbulent diffusion. The Kolmogorov spectral equilibrium hypothesis also enables one to predict a large eddy length-scale. On the other hand, the anisotropy of the stresses is quite crudely modeled. First of all the EVM model assumes the Reynolds stress tensor is aligned with the strain rate tensor (Boussinesq approximation):

$$\underline{\underline{R}}_l = \rho_l \nu_l^T \left(\underline{\underline{\nabla}}\,\underline{V}_l + \underline{\underline{\nabla}}^T \underline{V}_l\right) - \frac{2}{3}\underline{\underline{I}}\left(\rho_l K_l + \rho_l \nu_l^T \nabla \cdot \underline{V}_l\right), \tag{11}$$

where $\underline{\underline{I}}$ is the identity tensor, K_l is the liquid turbulent kinetic energy, and ν_l^T is the liquid turbulent eddy viscosity. The liquid turbulent eddy viscosity is expressed by the following relation:

$$\nu_l^T = C_\mu \frac{K_l^2}{\varepsilon_l}, \tag{12}$$

where $C_\mu = 0.09$. The turbulent kinetic energy K_l and its dissipation rate ε_l are calculated by using the two-equation K-ε approach.

2.3. EVM Weaknesses: Theoretical Approach. Flows encountered in vertical pipe are of great interest to validate the most important heat, mass, and momentum closure relations. However, some negligible effects in simple geometry sometimes become preponderant in complex geometries. For example, the modeling of two-phase flow in water-cooled nuclear reactors needs to take into account swirls and stagnation points. Applications in complex geometries also need to take into account the complex features of the secondary motions which are observed experimentally. These requirements highlight the need for meticulous turbulence modeling.

A reason for the persistent widespread use of low-level turbulence modeling in two-phase CFD is perhaps the fact that the use of two-phase CFD in complex industrial geometries is only starting. Moreover, many studies merely require "order of magnitude" or "good tendencies" answers.

However, extensive testing and application over the past three decades have revealed a number of shortcomings and deficiencies in EVM models, and among them the K-ε model, such as

(i) limitation to linear algebraic stress-strain relationship (poor performances wherever the stress transport is important, e.g., non equilibrium, fast evolving, separating, and buoyant flows),

(ii) insensitivity to the orientation of turbulence structure and stress anisotropy (poor performances where normal stresses play an important role, e.g., stress-driven secondary flows in noncircular ducts),

(iii) inability to account for extra strain (streamline curvature, skewing, rotation),

(iv) poor prediction particularly of flows with strong adverse pressure gradients and in reattachment regions.

In a plane strain situation, such as upstream of a stagnation point on a bluff body, the exact (as obtained by an RTSM) production and that obtained from an EVM are, respectively, [21]

$$\begin{aligned}P_{\mathrm{exact}} &= -\left(\overline{u_x'^2} - \overline{u_y'^2}\right)\frac{\partial V_{l,x}}{\partial x},\\ P_{\mathrm{EVM}} &= 4\nu_{l,t}\left(\frac{\partial V_{l,x}}{\partial x}\right)^2.\end{aligned} \tag{13}$$

The difference between the normal stresses actually grows slowly on the short-time scale needed for the flow to travel around the stagnation point, so the production remains moderate, and in any case is bounded, whereas P_{EVM} usually yields a severe over-prediction when the strain is high.

The simulation of swirling flow generated by the mixing vanes is our main goal since it plays an important role for the prediction of the CHF for the fuel assemblies. For this reason, the rotation effects are more specifically addressed hereafter.

It can be easily shown [22] that in the presence of an initially anisotropy turbulence, rotation will cause a redistribution of energy between normal components without affecting the value of this quantity. In fact, the angular velocity Θ does not appear explicitly in the K-equation, obtained by adding the normal stresses:

$$\frac{dK}{dt} = -\varepsilon. \tag{14}$$

Thus, the K-ε model is totally blind to rotation effects. The swirling flows can be regarded as a special case of fluid rotation with the axis usually aligned with the mean flow direction so that the Coriolis force is zero. This aspect is crucial for the simulation of hot channel of a fuel assembly. In fact, mixing vanes at the spacer grids generate a swirl in the coolant water to enhance the heat transfer from the rods to the coolants in the hot channels and to limit boiling.

In the following section, we present some examples of large-scale industrial applications, performed using eddy-viscosity models, and subsequently discuss areas of weakness of the models, highlighting some improvements that can be obtained through the use of more advances stress transport closures.

2.4. EVM Weaknesses: Illustration on the AGATE-Mixing and DEBORA-Mixing Experiment. Keeping in mind the long-term objective (two-phase CFD calculations validated under typical pressurized water reactor (PWR) geometries and thermalhydraulic conditions), we started very recently to evaluate Neptune_CFD against spacer grid type experiments. An experimental device representing three mixing blades (Figure 2) was introduced in a heated tube (diameter = 19.2 mm) and used for two different programs.

(i) *AGATE-mixing experiment* [23]. Single-phase liquid water tests, with laser-doppler liquid velocity measurements upstream and downstream the mixing blades (for each of the 15 horizontal planes, the liquid velocity is measured along 12 different diameters and there are 12 points for each radius); the velocity at inlet is 3 m/s and the pressure is 2 bar.

(ii) *DEBORA-mixing experiment* [24]. Boiling R-12 freon tests on the same geometry but the total length of the calculation domain is 3.5 m; the tube is heated and the uniform wall heat flux is 109300 W/m^2 which gives about 2% of vapor at outlet; the outlet pressure is 26.2 bar; the inlet liquid temperature is 63.3°C; the inlet liquid mass is 0.873 kg/s. The main physical phenomena to reproduce are wall boiling, entrainment of bubbles in the wakes, and recondensation. So, the prediction of the swirl is crucial.

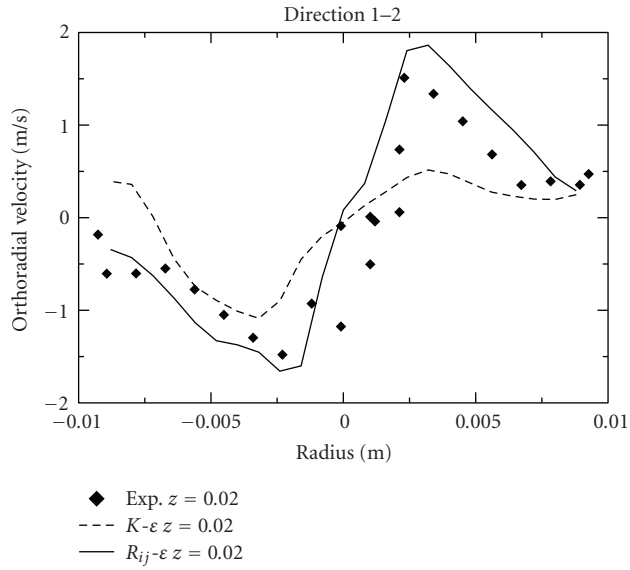

Figure 1: Orthoradial liquid velocity downstream the mixing vane (Agate-mixing experiment).

Figure 2: View of the mixing device.

For the mixing blades part (60 mm), 77000 cells are needed. This grid is considered as a reasonable compromise between the numerical accuracy and the computational effort. Figure 1 compares computed and experimental orthoradial (circular component in a horizontal plane) liquid velocity downstream the mixing vane (AGATE test). One can notice that the rotating flow is qualitatively well reproduced by Neptune_CFD although the velocity is underestimated. This is mainly due to the turbulence model (standard K-ε here) which is not optimum for this type of geometry.

The K-ε model underestimates orthoradial velocities downstream the blades, but the results remain qualitatively satisfactory. The R_{ij}-ε model gives satisfactory results (Figure 1).

In the following section, we propose a second-moment closure model to take into account the liquid turbulence in order to validate in the long-term calculations in typical

pressurized water reactor (PWR) geometries and thermalhydraulic conditions.

In the present paper, we suppose that RSTM is well known in single-phase flow [21]. Now, our objective is to test and if possible to improve our RSTM model adapted to bubbly flows as compared to experimental data and K-ε results. Indeed, we are interested by two-phase high Reynolds numbers flows, but beforehand, the mechanical models implemented in the Neptune_CFD code must be tested on the simpler cases of air-water adiabatic bubbly flows.

3. The Second-Moment Closure Model for High Reynolds Number Flows Dedicated to the Continuous Phase (Liquid)

In this section, we omit the subscript "l" for the liquid and "α" is the void fraction for the sake of simplicity.

3.1. Equation on R_{ij}. We have

$$(1-\alpha)\frac{D\rho R_{ij}}{Dt} = \frac{\partial}{\partial x_k}\left\{\left(\rho\nu + \rho C_s \frac{K}{\varepsilon}R_{ij}\right)\frac{\partial}{\partial x_k}\left((1-\alpha)\cdot R_{ij}\right)\right\} + (1-\alpha)\left(P_{ij}+G_{ij}+\Phi_{ij}+\varepsilon_{ij}\right). \tag{15}$$

In this model, the Reynolds stress tensor of the continuous phase is split into two parts, a turbulent dissipative part produced by the gradient of mean velocity and by the wakes of the bubbles and a pseudoturbulent nondissipative part induced by the displacements of the bubbles. The displacements of the bubbles should be taken into account in experiments, where air is injected at the bottom of a water pool creating a large, axisymmetric bubble plume with a large-scale recirculation flow around the plume. But swirling flows and high Reynolds number characterize our industrial applications.

Hence, we neglected, in our approach and in first analysis, the nondissipative component called "pseudoturbulent." We consider only the "turbulent" dissipative part. Within this framework, the term of production by the bubbles interfaces is written as [7]

$$\overline{-\left(\frac{p}{\rho}u_i' n_j + \frac{p}{\rho}u_j' n_i\right)\delta^I + \nu\left(\frac{\partial}{\partial x_k}u_i' u_j'\right)n_k\delta^I}, \tag{16}$$

where n indicates the normal to the interface and δ^I a Dirac function on the interface. It was omitted in [7]. Indeed, according to [7], dissipation in the wakes is balanced by the interfacial production: the equation of transport of the Reynolds stress tensor has the same form as in the single-phase case and is given by (15). When the void fraction is vanishing, the two-phase flow modeling naturally degenerates to the single-phase flow modeling.

Some terms of the equation of transport of the Reynolds stress tensor cannot be computed directly and must be modeled. A modeling resulting from [21] is proposed below.

A common way to model the viscous destruction of stresses for high Reynolds number flows is

$$\varepsilon_{ij} = \frac{2}{3}\varepsilon\delta_{ij}. \tag{17}$$

The turbulent diffusion is of diffusive nature and the most popular model is the generalized gradient diffusion:

$$D_{ij}^t = \frac{\partial}{\partial x_k}\left(C_s \frac{K}{\varepsilon}\overline{u_k' u_l'}\frac{\partial \overline{u_i' u_j'}}{\partial x_l}\right). \tag{18}$$

Pressure fluctuations tend to disrupt the turbulent structures and to redistribute the energy to make turbulence more isotropic: $\Phi_{ij} = \Phi_{ij,1} + \Phi_{ij,2} + \Phi_{ij,3} + \Phi_{ij,1}^{\omega} + \Phi_{ij,2}^{\omega} + \Phi_{ij,3}^{\omega}$ with

(i)

$$\Phi_{ij,1} = -C_1\varepsilon\left(\frac{\overline{u_i' u_j'}}{K} - \frac{2}{3}\delta_{ij}\right) \quad \text{with } C_1 = 1.8, \tag{19}$$

(ii)

$$\Phi_{ij,2} = -C_2\left(P_{ij} - \frac{2}{3}P\delta_{ij}\right), \quad \text{with } P = \frac{1}{2}P_{kk},\ C_2 = 0.6,$$

$$\Phi_{ij,3} = -C_3\left(G_{ij} - \frac{2}{3}G\delta_{ij}\right), \quad \text{with } G = \frac{1}{2}G_{kk},\ C_3 = 0.55, \tag{20}$$

(iii)

$$\Phi_{ij,1}^{\omega} = C_1^{\omega}\frac{\varepsilon}{K}\left(\overline{u_k' u_m'}\,\underline{n_k n_m}\,\delta_{ij} - \frac{3}{2}\overline{u_i' u_k'}\,\underline{n_k n_j} - \frac{3}{2}\overline{u_k' u_j'}\,\underline{n_k n_i}\right)\cdot f_{\omega}, \tag{21}$$

(iv)

$$\Phi_{ij,2}^{\omega} = C_2^{\omega}\left(\Phi_{km,2}\,\underline{n_k n_m}\,\delta_{ij} - \frac{3}{2}\Phi_{ik,2}\,\underline{n_k n_j} - \frac{3}{2}\Phi_{jk,2}\,\underline{n_k n_i}\right)\cdot f_{\omega}, \tag{22}$$

with $C_1^{\omega} = 0.5$, $C_2^{\omega} = 0.3$, $f_{\omega} = 0.4\cdot K^{3/2}/\varepsilon\cdot x_n$, where x_n is the distance to the wall and $\underline{n_k}$ the base vector normal to the wall.

(v) G is the production by body force.

3.2. Equation on ε. In the RTSM closures, the same basic form of model equation for ε is used as in the K-ε model, except that now $(\overline{u_k' u_l'})$ is available, which has the following implications.

The production of kinetic energy (P and G) in the source term of ε is treated in exact form.

The generalized gradient hypothesis is used to model turbulent diffusion.

Hence, the model equation for ε has the form

$$(1-\alpha)\frac{D\varepsilon}{Dt} = \frac{\partial}{\partial x_k}\left(C_{\varepsilon}\frac{K}{\varepsilon}\overline{u_k' u_l'}\frac{\partial(1-\alpha)\varepsilon}{\partial x_l}\right) + \left(C_{\varepsilon_1}P + C_{\varepsilon_3}G + C_{\varepsilon_4}K\frac{\partial V_k}{\partial x_k} - C_{\varepsilon_2}\varepsilon\right)\cdot\frac{(1-\alpha)\varepsilon}{K}. \tag{23}$$

The coefficients of the R_{ij}-ε model are shown in Table 2.

4. Validation on Adiabatic Bubbly Flow Cases

4.1. The LIU&BANKOFF Case [25]. In this section, we evaluate the modeling capabilities to simulate an upward bubbly flow in adiabatic conditions. We do not specifically optimize the coefficients and modeling of the momentum transfer terms to get results as good as possible. Our main objective is to validate the R_{ij}-ε turbulence model for the fluid against the K-ε one.

The test section was a $Z = 2800$ mm long, vertical smooth acrylic tubing, with inside diameter of $D = 38$ mm.

The set of physical properties is the following:

$$\begin{aligned} \rho_{\text{liquid}} &= 994.9 \text{ kg} \cdot \text{m}^{-3}, \\ \rho_{\text{gas}} &= 1.6 \text{ kg} \cdot \text{m}^{-3}, \\ \mu_{\text{liquid}} &= 7.97 \cdot 10^{-4} \text{ N} \cdot \text{s} \cdot \text{m}^{-2}, \\ \mu_{\text{gas}} &= 1.748 \cdot 10^{-5} \text{ N} \cdot \text{s} \cdot \text{m}^{-2}, \\ P_0 &= 101500 \text{ Pa}, \\ g &= 9.81 \text{ m} \cdot \text{s}^{-2}, \\ d_{\text{bubble}} &= 2.5 \cdot 10^{-3} \text{ m}. \end{aligned} \tag{24}$$

A uniform axial liquid profile is imposed at the inlet and is equal to 1.138 m/s. A uniform axial gas profile is imposed at the inlet and is equal to 1.333 m/s. The void fraction at the inlet is 0.045.

The interfacial momentum transfer term is assumed to be the sum of four different forces. The three first ones are simplified averaged expressions of the classical drag, added mass, and lift force. The fourth is the turbulent dispersion force.

The flow is assumed to be axisymmetric therefore a two-dimensional axisymmetric meshing is used. Computations have been performed on two kinds of meshing: a coarse grid (20 cells in the radial direction and 50 cells in the axial direction) and a fine grid (30 cells in the radial direction and 100 cells in the axial direction). Results are similar and computations are performed on the first grid.

At the measuring station ($Z/D = 36$), we compare numerical results against experimental data for the axial liquid velocity and the void fraction.

As recommended in [26], the lift coefficient is taken to be equal to 0.1. We have also tested the turbulent dispersion force of Davidson model [26] written as

$$F_{\text{DT}} = -\frac{3}{4}\frac{C_D}{d_b}\mu_t(1-\alpha)\left|V_g - V_l\right|\frac{\partial \alpha}{\partial x_i} \quad \text{with } \mu_t = 0.09\rho_l\frac{K_l^2}{\varepsilon}. \tag{25}$$

This expression gives values negligible with respect to the Lopez de Bertodano expression [18] (the ratio is about 1000) and the void fraction profile is observed to be similar to the profile calculated without any turbulence model for the dispersed phase. If we take the bubble fluctuation into account with the Hinze-Tchen algebraic model of bubble turbulence, we get the same results with the turbulent dispersion force.

In [27], Grossetête considers that bubbles are deformed near the wall. To take into account this effect, the author proposes to put a negative lift coefficient near the wall and otherwise a positive one. Nevertheless, calculations

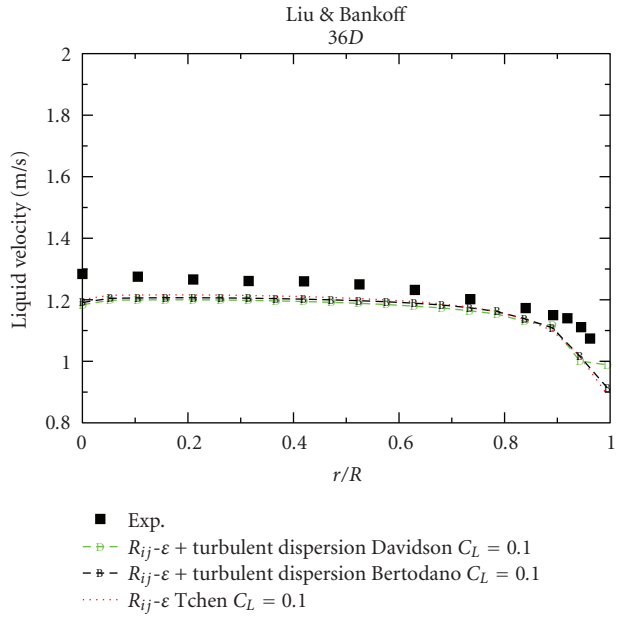

Figure 3: Radial profile of the liquid velocity, comparisons of turbulent dispersion forces with $CL = 0.1$.

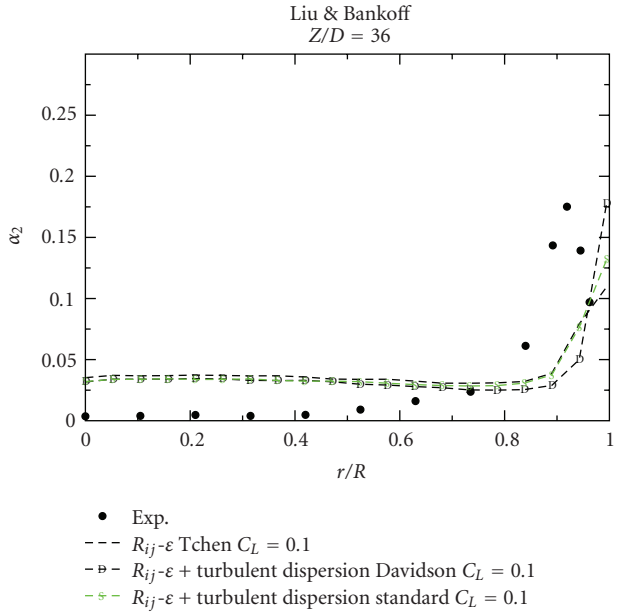

Figure 4: Radial profile of void fraction, comparisons of turbulent dispersion forces with $CL = 0.1$.

Table 1: Simulated test case.

I.D.* (mm)	J_L (m/s)	J_G (m/s)	$\langle\alpha\rangle_2$
50	1.57	0.3	0.12
100	0.39	0.075	0.0903

* internal diameter.

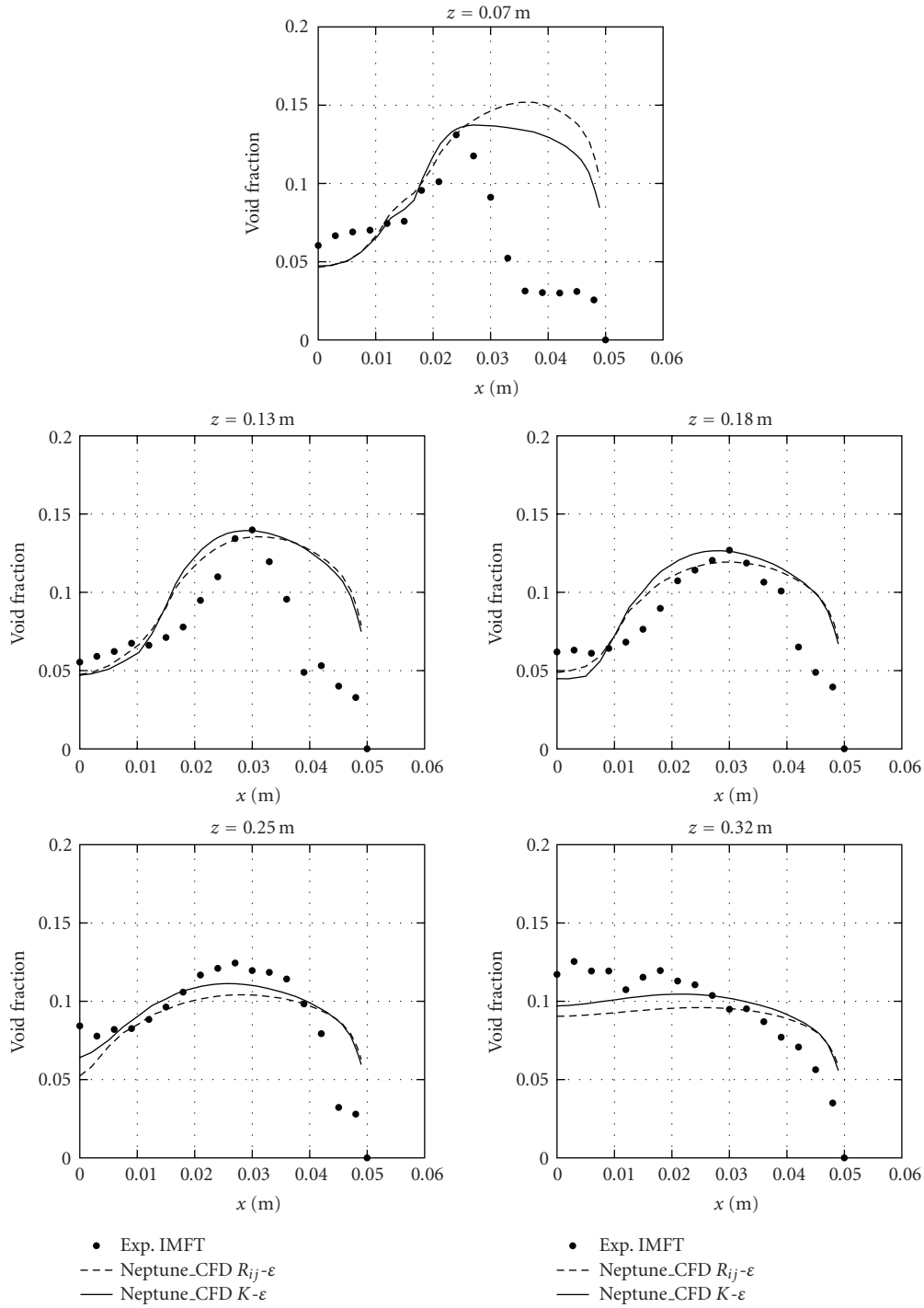

Figure 5: Void fraction profiles.

(not presented in this paper) show a peak of void fraction at the wall. We have also tested the Tomiyama lift force [28, 29], but results are not improved. Moreover, a wall lubrification force [30] can push the bubbles away from the wall and improve the results.

Figures 3 and 4 show that the simulation results are in quite good agreement with the experimental data. In [31], computations performed with a K-ε turbulence model for the liquid produced comparable results. Our main objective in this paper is to check that the simulation with the R_{ij}-ε turbulence model gives satisfactory results in a simple geometry, which is crucial before calculating industrial geometries, where the K-ε turbulence model is susceptible to fail.

But improvement of the modeling of the interfacial forces exerted on bubbles by the surrounding liquid is required. A

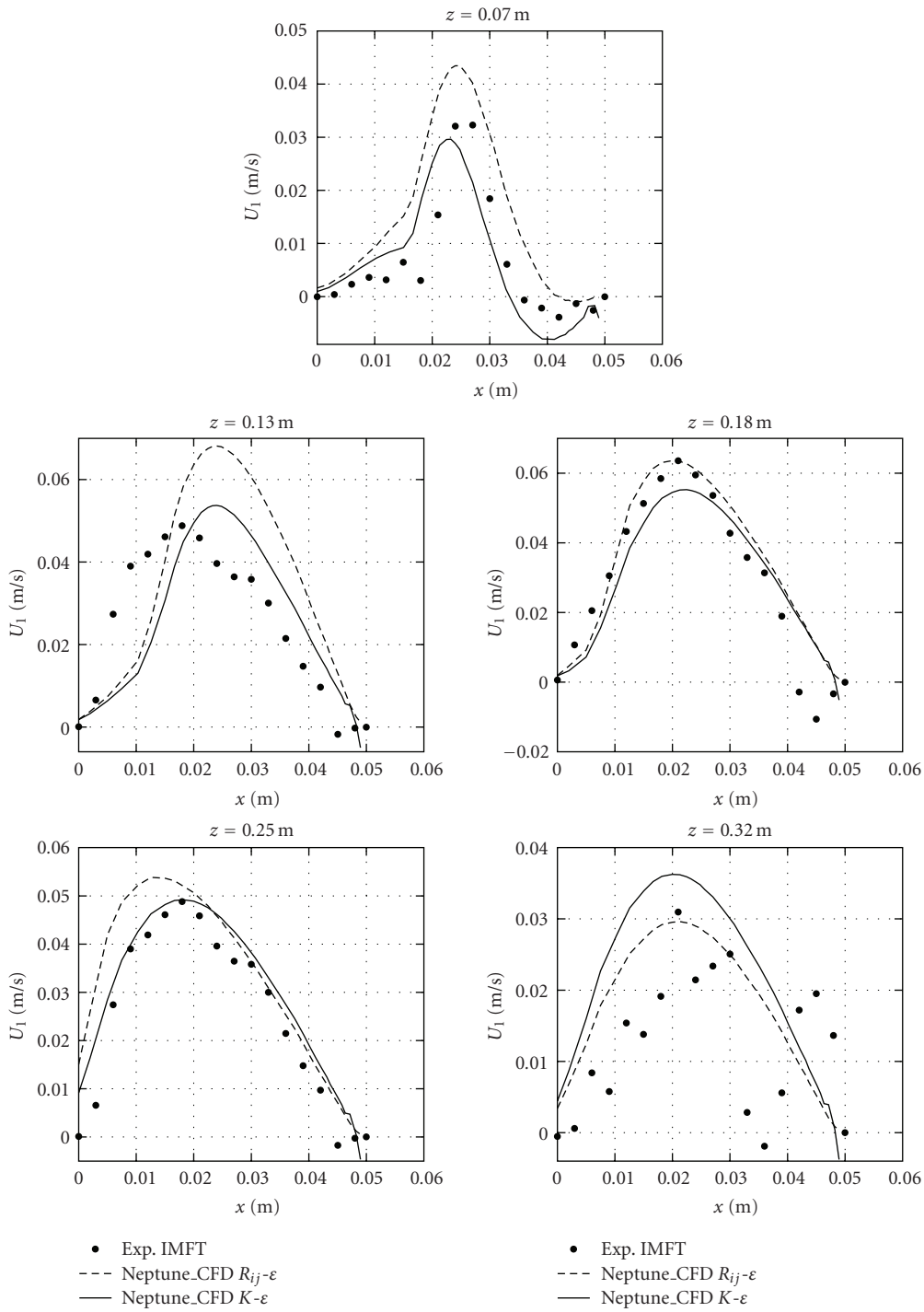

Figure 6: Liquid mean radial velocity profiles.

strong sensitivity to the lift coefficient has been found in our calculations. Other forces, like the turbulent dispersion force, have also a crucial effect on the void fraction distribution. These forces depend on uncontrolled parameters like the bubble shape, the liquid turbulence, the bubbles collective effects, and so on [31].

4.2. Sudden Expansion Experiment. Bel Fdhila [32] investigated experimentally several upwards bubbly flows in a vertical pipe with a sudden expansion. The total length of the pipe was equal to 14 meters. The bottom part of the tube had a length equal to 9 meters and an internal diameter equal to 50 mm, the top part of the tube (5 m length) having an internal diameter equal to 100 mm. The fluids used were water and air under atmospheric pressure and ambient temperature. Six measuring sections were located upstream and downstream of the singularity. The first measuring section was located two centimetres before the singularity,

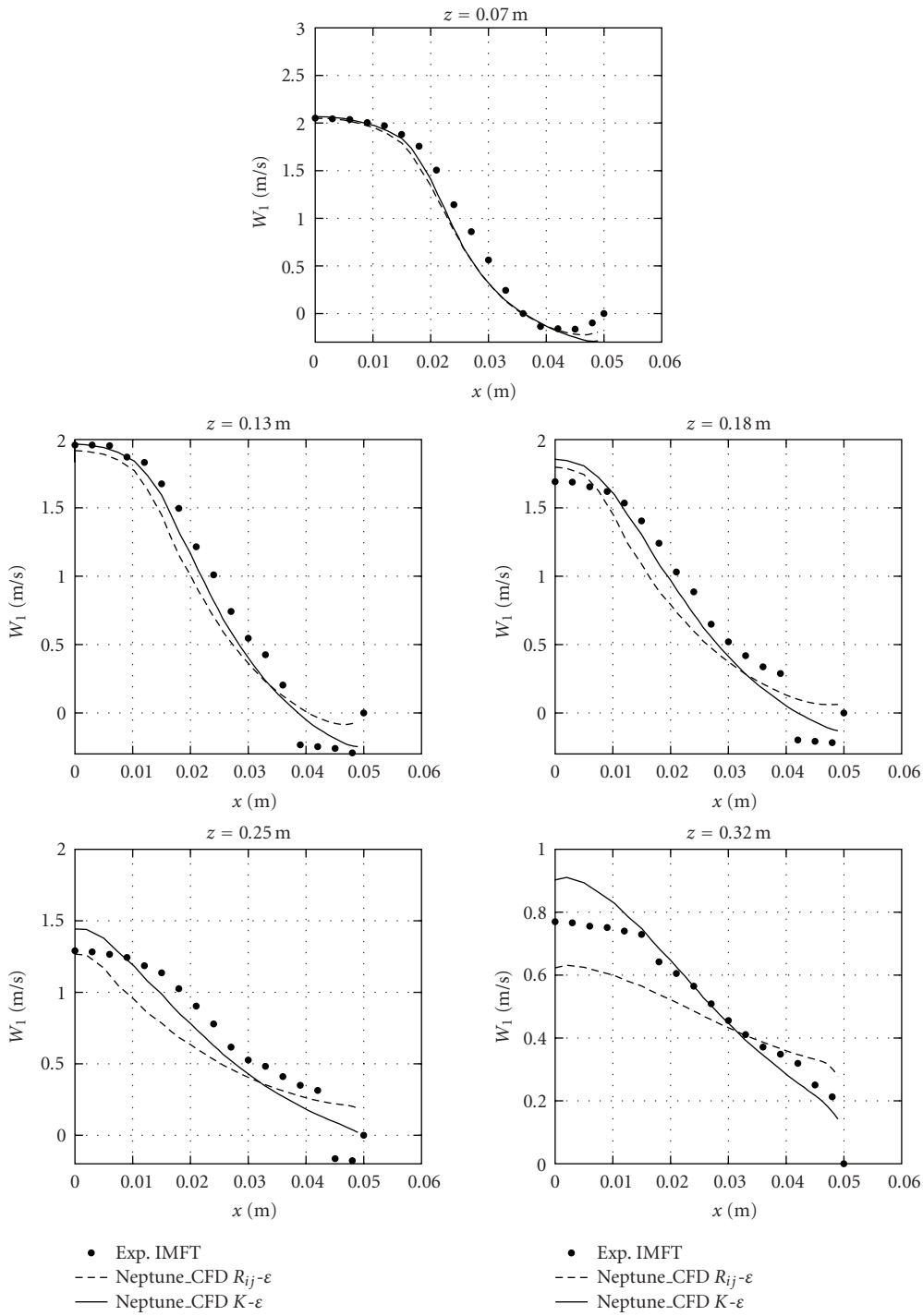

Figure 7: Liquid mean axial velocity profiles.

the other five were located at 7, 13, 18, 25, and 32 cm above the singularity. In each measuring section, the radial profile of the void fraction was measured by means of a single optical probe, and two components of the liquid velocity were measured by means of a hot film anemometer. The time-averaged components of this velocity field and three components of the liquid Reynolds stress tensor were deduced (the flow being assumed axisymmetric). The bubble size was not measured in the experiment. According to the author, the observed bubble diameter was equal to a few millimetres, the bubbles remaining relatively small due to the strong turbulence existing in the liquid phase.

In our calculations, only a small part of the tube, containing the singularity and the six measuring sections,

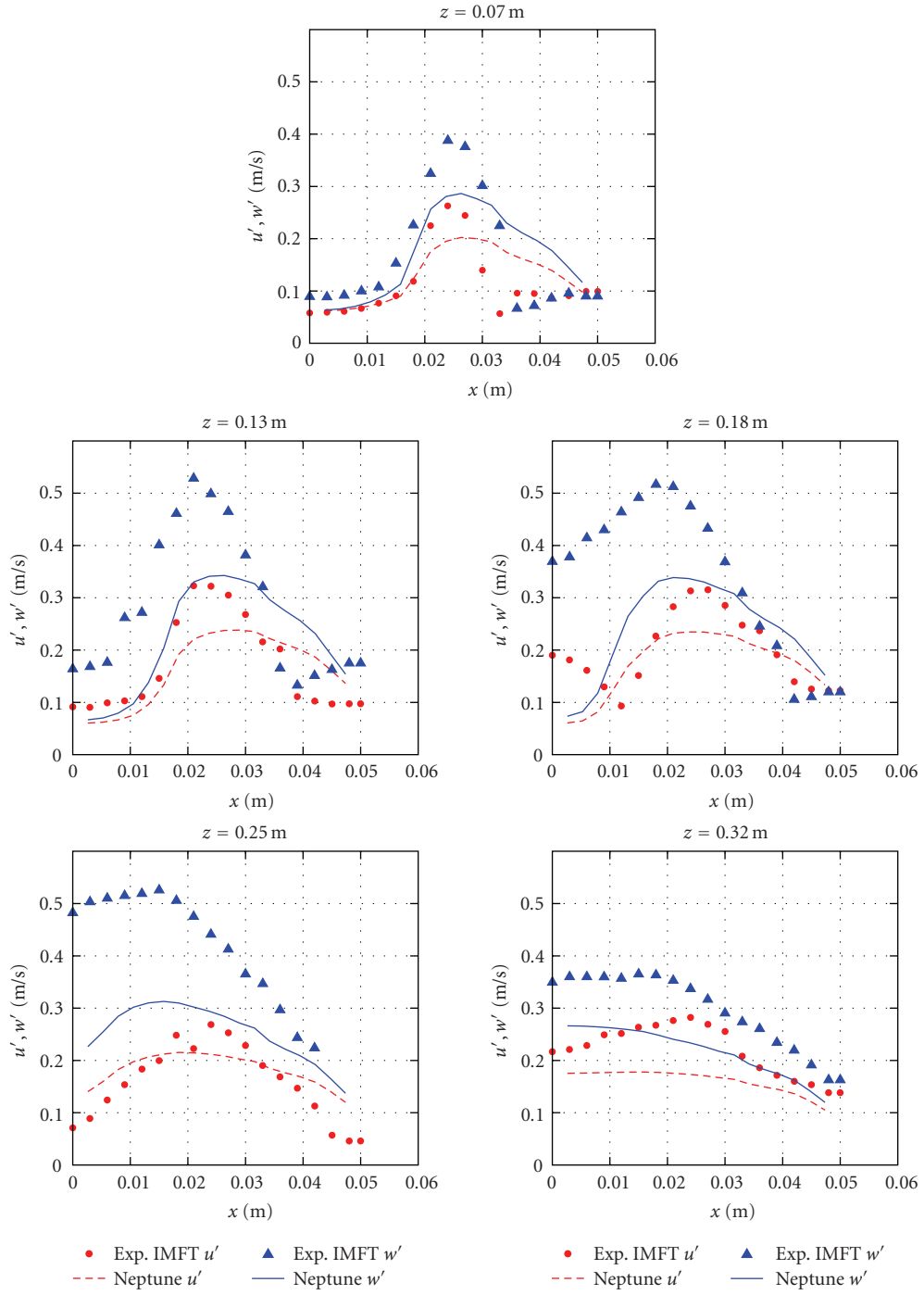

Figure 8: Liquid r.m.s. radial (u') and axial (w') velocity profiles (R_{ij}-ε).

Table 2

C_s	C_1	C_2	C_1^{ω}	C_2^{ω}	C_{ε}	C_{ε_1}	C_{ε_2}	C_{ε_3}	C_{ε_4}
0.2	1.8	0.6	0.5	0.3	0.18	1.44	1.92	1.44	0.33

was reproduced. The radial profiles of the void fraction and the liquid mean and fluctuating velocities measured upstream of the singularity were used as inlet conditions. The length of the calculation domain is equal to 38 cm. The flow is assumed to be axisymmetric therefore a two-dimensional axisymmetric meshing is used. Several calculations have been done in order to test the sensitivity to the axial and radial grids. Four different grids have been tested in [33], the number of radial meshes in the largest section multiplied by the number of axial meshes being 10∗38, 20∗76, 20∗152, and 40∗152, respectively. The comparison of different calculations of the same two-phase flow, realized on these four different grids show that the calculations performed with the finest grid can be considered as converged. All the calculations presented here have been done on the finest 40∗152 calculation grid. The flow studied here is characterized by the liquid and gas superficial velocities and the area-averaged void fraction in the two sections given in Table 1. It can be noted that the averaged void fraction has important values for this test (12%).

Cokljat [34] performed calculations of the sudden expansion experiment with the FLUENT code. Predictions were obtained using the standard K-ε model as well as an RSTM for the continuous phase, while the turbulence closure for the dispersed phase is achieved by the algebraic model of Tchen [19, 20]. With this approach, similar as ours, the authors indicate that both models produce similar results for the axial velocity but void fraction results are improved with the RSTM model.

We only consider the classical drag, added mass, and dispersion turbulent force. The dispersion force coefficient is equal to 2 in the computations. The bubble diameter is equal to 2 mm. Following [18, 33, 34], we underline the necessity to discard the lift force. In fact, the effect of the lift force is to produce sharp peaks near the wall because the classical modeling of the lift force seems not well adapted to this case.

The simulation results are in reasonable agreement with the experimental data for the void fraction profiles (Figure 5) and have been improved as compared to [33, 34]. But the profiles at $z = 7$ cm and $z = 13$ cm show that the void fraction is underestimated which mean that a better understanding of the physical mechanisms is still needed.

Especially for the axial and radial mean liquid velocity profiles(Figure 6,7), we have obtained a good agreement which means that the recirculation zone is well captured.

We have obtained only qualitatively good results for the RMS quantities (Figure 8) because the turbulence mechanisms in a bubbly flow are far from being fully understood [18]. But the turbulence modeling of the dispersed phase in a PWR core in conditions close to nominal is less crucial than the liquid turbulence modeling.

Finally, results with the R_{ij}-ε turbulence model for the fluid are similar to the K-ε one, which is our main objective in this case, before calculating rod bundle geometries, where the K-ε model may fail.

5. Conclusion and Perspectives

An analysis of turbulence modeling for two-phase flows has been proposed. Indeed, the use of eddy viscosity models is widespread and may be sufficient for parallel flows in vertical pipes, but that type of model does not account for effects that are preponderant in complex geometries, especially when swirling flows are involved, for example, in pressurized water reactor cores downstream of mixing vanes and spacer grids. In accordance with the theory, it is demonstrated in the case of a flow downstream of a mixing vane that using a Reynolds stress model is an efficient way to improve the simulation of such complex flows. To demonstrate that the use of a Reynolds stress model is not bound to deteriorate the classical results obtained with an eddy viscosity model, a validation step on more analytical experiments is detailed (bubbly flows in a straight pipe and in a sudden expansion): the study shows that the Reynolds Stress model implemented in the multiphase 3D code Neptune_CFD satisfactorily reproduces the results obtained with the standard eddy viscosity model and both compare reasonably well with the experiments.

As concern the computational cost, we note that in the case of the DEBORA-mixing test which is under process, the time required by iteration is, respectively, 3.09 seconds and 2.81 seconds for RSTM and EVM. The time step is, respectively, 5 milliseconds and 5.4 milliseconds with a CFL equal to 1. In this particular case, the RSTM over-cost is about 18.8%.

Moreover, among the developments planned in the medium term, we have identified the need for a polydispersion model.

Besides, the Neptune project has set up a medium and long-term experimental program to acquire detailed measurements in simplified and real geometries, both in adiabatic and real conditions [9, 10].

Nomenclature

A_i: Interfacial area concentration
C_d: Drag coefficient
dt: Numerical time step
g: Gravity acceleration
K_l: Liquid turbulent kinetic energy
$\underline{M}_k$: Interfacial momentum transfer per unit volume and unit time
p: Pressure
Pr_l: Liquid Prandtl number
$\underline{\underline{R}}_k$: Reynolds stress tensor
Re_b: Bubble Reynolds number
t: Time
u_i': Fluctuation of the liquid velocity
$\underline{V}_k$: Averaged velocity of phase k
$\underline{V}_{ki}$: Interfacial-averaged velocity
α_k: Denotes the time fraction of phase k
ε_l: Dissipation rate
μ_g: Gas molecular viscosity
ν_l: Liquid kinematic viscosity
ν_l^T: Liquid turbulent eddy viscosity
ρ_k: Averaged density of phase k
σ: Surface tension
τ_w: Wall shear stress
$\underline{\underline{\Sigma}}_k$: Molecular stress tensor.

Subscripts/Superscripts

l: Liquid state
g: Gas bubbles
k: Phase $k = l$ or g.

Acknowledgments

This work has been achieved in the framework of the Neptune project, financially supported by CEA (Commissariat à l'Energie Atomique), EDF (Electricité de France), IRSN (Institut de Radioprotection et de Sûreté Nucléaire), and AREVA-NP.

References

[1] B. S. Shin and S. H. Chang, "Experimental study on the effect of angles and positions of mixing vanes on CHF in a 2×2 rod bundle with working fluid R-134a," *Nuclear Engineering and Design*, vol. 235, no. 16, pp. 1749–1759, 2005.

[2] C. M. Lee and Y. D. Choi, "Comparison of thermo-hydraulic performances of large scale vortex flow (LSVF) and small scale vortex flow (SSVF) mixing vanes in 17×17 nuclear rod bundle," *Nuclear Engineering and Design*, vol. 237, no. 24, pp. 2322–2331, 2007.

[3] K. Ikeda, Y. Makino, and M. Hoshi, "Single-phase CFD applicability for estimating fluid hot-spot locations in a 5×5 fuel rod bundle," *Nuclear Engineering and Design*, vol. 236, no. 11, pp. 1149–1154, 2006.

[4] W.-K. In, T.-H. Chun, C.-H. Shin, and D.-S. Oh, "Numerical computation of heat transfer enhancement of a PWR rod bundle with mixing vane spacers," *Nuclear Technology*, vol. 161, no. 1, pp. 69–79, 2008.

[5] E. Krepper, B. Končar, and Y. Egorov, "CFD modelling of subcooled boiling—concept, validation and application to fuel assembly design," *Nuclear Engineering and Design*, vol. 237, no. 7, pp. 716–731, 2007.

[6] D. Bestion, "Synthesis of work performed in WP2.2," 6th Euratom Framework Program NURESIM, deliverable D2.2.1.1b, 2007.

[7] J. Chahed, *Forces interfaciales et turbulence dans les écoulements à bulles: modélisation et étude de cas de référence*, Ph.D. thesis, L'Université des Sciences et Techniques de Tunis, Tunis, Tunisia, 1999.

[8] L. X. Zhou, M. Yang, C. Y. Lian, L. S. Fan, and D. J. Lee, "On the second-order moment turbulence model for simulating a bubble column," *Chemical Engineering Science*, vol. 57, no. 16, pp. 3269–3281, 2002.

[9] A. Guelfi, M. Boucker, J. M. Hérard, et al., "A new multi-scale platform for advanced nuclear thermal-hydraulics status and prospects of the NEPTUNE project," in *Proceedings of the 11th International Topical Meeting on Nuclear Reactor Thermal-Hydraulics (NURETH-11)*, Avignon, France, October 2005.

[10] A. Guelfi, D. Bestion, M. Boucker, et al., "NEPTUNE: a new software platform for advanced nuclear thermal hydraulics," *Nuclear Science and Engineering*, vol. 156, no. 3, pp. 281–324, 2007.

[11] S. Mimouni, A. Archer, J. Laviéville, M. Boucker, and N. Méchitoua, "Modeling and computation of cavitation flows: a two-phase flow approach," *La Houille Blanche*, no. 6, pp. 121–128, 2006 (French).

[12] S. Mimouni, M. Boucker, J. Laviéville, A. Guelfi, and D. Bestion, "Modelling and computation of cavitation and boiling bubbly flows with the NEPTUNE_CFD code," *Nuclear Engineering and Design*, vol. 238, no. 3, pp. 680–692, 2008.

[13] M. Ishii, *Thermo-Fluid Dynamic Theory of Two-Phase Flow*, Collection de la Direction des Etudes et Recherches d'Electricité de France, no. 20, Eyrolles, Paris, France, 1975.

[14] J. Delhaye, M. Giot, and M. Riethmuller, *Thermal-Hydraulics of Two-Phase Systems for Industrial Design and Nuclear Engineering*, Hemisphere, New York, NY, USA, 1981.

[15] N. Zuber, "On the dispersed two-phase flow in the laminar flow regime," *Chemical Engineering Science*, vol. 19, no. 11, pp. 897–917, 1964.

[16] M. Ishii, "Two-fluid model for two-phase flow," *Multiphase Science and Technology*, vol. 5, no. 1–4, pp. 1–63, 1990.

[17] T. R. Auton, "The lift force on a spherical body in a rotational flow," *Journal of Fluid Mechanics*, vol. 183, pp. 199–218, 1987.

[18] M. Lance and M. Lopez de Bertodano, "Phase distribution phenomena and wall effects in bubbly two-phase flows," *Multiphase Science and Technology*, vol. 8, no. 1–4, pp. 69–123, 1994.

[19] E. Deutsch and O. Simonin, "Large eddy simulation applied to the motion of particles in stationary homogeneous fluid turbulence," in *Proceedings of the International Symposium on Turbulence Modification in Multiphase Flows*, vol. 110, pp. 35–42, ASME FED, Portland, Ore, USA, June 1991.

[20] E. Deutsch, *Dispersion de particules dans une turbulence homogène isotrope stationnaire calculée par simulation numérique directe des grandes échelles*, Ph.D. thesis, Electricité de France, Clamart, France, 1992.

[21] K. Hanjalic and D. Laurence, *Introduction to Turbulence Modelling*, Lecture series 2002-02, von Karman Institute for Fluid Dynamics, Sint-Genesius-Rode, Belgium, 2002.

[22] P. Chassaing, *Turbulence en mécanique des fluides*, Cépaduès, Toulouse, France, 2000.

[23] F. Falk and A. Giacommelli, "Rapport d'essais AGATE PROMOTEUR de MELANGE," CEA DTP/SETEX/LTAC/03-191. Internal report, 2003.

[24] F. Falk and R. Hugonnard, "Rapport d'essais DEBORA PROMOTEUR de MELANGE, essais de BO et de topologie, campagne 4800–4900–5000," CEA DTP/SETEX/LTAC/02-158. Internal report, 2002.

[25] T. J. Liu and G. Bankoff, "Structure of air-water bubbly flow in a vertical pipe—II: void fraction, bubble velocity and bubble size distribution," in *Proceedings of ASME Winter Annual Meeting*, Dallas, Tex, USA, November 1990.

[26] R. Zboray and F. de Cachard, "Simulating large-scale bubble plumes using various closure and two phase turbulence models," *Nuclear Engineering and Design*, vol. 235, no. 8, pp. 867–884, 2005.

[27] C. Grossetête, *Caractérisation expérimentale et simulations de l'évolution d'un écoulement diphasique à bulles ascendant dans une conduite verticale*, Ph.D. thesis, École Centrale de Paris, Paris, France, 1995.

[28] A. Tomiyama, "Struggle with computational bubble dynamics," in *Proceedings of the 3rd International Conference on Multiphase Flow (ICMF '98)*, pp. 1–18, Lyon, France, June 1998.

[29] A. Tomiyama, K. Sakoda, G. P. Celata, and I. Zun, "A simple method for evaluating fluctuating bubble velocity and its application to a hybrid bubble tracking method," in *Proceedings of the 3rd International Symposium on Two-Phase*

Flow Modelling and Experimentation (ISTPME '04), Pisa, Italy, September 2004.

[30] S. P. Antal, R. T. Lahey Jr., and J. E. Flaherty, "Analysis of phase distribution in fully developed laminar bubbly two-phase flow," *International Journal of Multiphase Flow*, vol. 17, no. 5, pp. 635–652, 1991.

[31] S. C. P. Cheung, G. H. Yeoh, and J. Y. Tu, "On the numerical study of isothermal vertical bubbly flow using two population balance approaches," *Chemical Engineering Science*, vol. 62, no. 17, pp. 4659–4674, 2007.

[32] R. Bel Fdhila, *Analyse expérimentale et modélisation d'un écoulement vertical à bulles dans un élargissement brusque*, Ph.D. thesis, Institut National Polytechnique de Toulouse, Toulouse, France, 1991.

[33] C. Morel, J. Pouvreau, J. Laviéville, and M. Boucker, "Numerical simulations of a bubbly flow in a sudden-expansion with the NEPTUNE code," in *Proceedings of the 3rd International Symposium on Two-Phase Flow Modelling and Experimentation (ISTPME '04)*, Pisa, Italy, September 2004.

[34] D. Cokljat, M. Slack, S. A. Vasquez, A. Bakker, and G. Montante, "Reynolds-stress model for Eulerian multiphase," *Progress in Computational Fluid Dynamics*, vol. 6, no. 1/2/3, pp. 168–178, 2006.

Hindawi Publishing Corporation
Science and Technology of Nuclear Installations
Volume 2009, Article ID 950536, 12 pages
doi:10.1155/2009/950536

Research Article

Two-Phase Flow Simulations for PTS Investigation by Means of Neptune_CFD Code

Maria Cristina Galassi,[1] Pierre Coste,[2] Christophe Morel,[2] and Fabio Moretti[1]

[1] *Department of Mechanical, Nuclear, and Production Engineering (DIMNP), University of Pisa, Via Diotisalvi n. 2, 56126 Pisa, Italy*
[2] *DEN/DER/SSTH/LMDL, CEA/Grenoble, 17 Rue des Martyrs, 38054 Grenoble Cedex 9, France*

Correspondence should be addressed to Maria Cristina Galassi, mc.galassi@ing.unipi.it

Received 31 January 2008; Revised 3 June 2008; Accepted 18 August 2008

Recommended by Dirk Lucas

Two-dimensional axisymmetric simulations of pressurized thermal shock (PTS) phenomena through Neptune_CFD module are presented aiming at two-phase models validation against experimental data. Because of PTS complexity, only some thermal-hydraulic aspects were considered. Two different flow configurations were studied, occurring when emergency core cooling (ECC) water is injected in an uncovered cold leg of a pressurized water reactor (PWR)—a plunging water jet entering a free surface, and a stratified steam-water flow. Some standard and new implemented models were tested: modified turbulent k-ε models with turbulence production induced by interfacial friction, models for the drag coefficient, and interfacial heat transfer models. Quite good agreement with experimental data was achieved with best performing models for both test cases, even if a further improvement in phase change modelling would be suitable for nuclear technology applications.

1. Introduction

The Integrated Project, European Platform for Nuclear Reactor Simulations (NURESIM), financially supported by the European Commission, aims at developing a common European standard software platform for modelling, recording, and recovering computer simulation data for current and future nuclear reactor system [1–3]. Neptune_CFD [4–6] is the thermal-hydraulic two-phase CFD tool of NURESIM and is designed to simulate most of two-phase flow configurations encountered in nuclear reactor power plants. Neptune_CFD is developed within the framework of the NEPTUNE project, financially supported by Commissariat à l'Énergie Atomique (CEA), Électricité de France (EDF), Institut de Radioprotection et de Sûreté Nucléaire (IRSN), and AREVA-NP.

One task of the NURESIM Project [7] is the prediction of PTS phenomena through computational fluid dynamics' (CFDs) codes, in order to improve the operational safety and remnant life assessment of the PWRs.

A PTS scenario limiting to the reactor pressure vessel lifetime is the cold water ECC injection into the cold leg during a small-break loss of coolant accident (SBLOCA) [8]; rapid wall cooling can lead to strong thermal gradients and consequently to high stresses in the pressurized components, while local reduction of fracture toughness occurs due to temperature decrease. Complex phenomena take place when cold water is transported from injection nozzle to the downcomer, such as

(i) turbulent mixing of momentum and heat in the jet region and downstream of the impingement zone,

(ii) stratified two-phase flow with condensation at the free surface.

The two flow configurations considered in this paper are likely to share common physical features with these scenarios and represent challenging cases for multiphase models validation. As a matter of fact, they were identified as relevant PTS scenarios [9] and selected as test cases for CFD codes validation [10] within the ECORA Project.

The first concerns a jet flow impinging on a free surface, with air carry under and subsequent bubble dispersion in the water bath. Since turbulence strongly influences the

condensation and the diffusion of heat within the water, it also influences the temperature field and plays a major role in the severity of the PTS Scenario. CFD models have to capture this turbulence production by jet kinetic energy in order to provide reliable predictions, and the Iguchi tests [11] are used as separate effect tests for code validation.

The second one relates to a turbulent stratified steam-water flow with interfacial heat and mass transfers. Simulating such a problem involves many critical aspects for the successful validation of CFD models: turbulence should be accurately predicted near the interface, and turbulence models should account for anisotropy effects; all interphase transport source terms have to be accurately represented in the solved equations, needing a numerically stable and robust solver. Numerical results are compared with experimental data from the cocurrent LAOKOON test case at high Reynolds number of steam [12–14].

2. Modelling

In this paper, a local 3D two-fluid approach [15] for turbulent flows with/without condensation is presented. In this approach, a set of local balance equations of mass, momentum, and energy is written for each phase. These balance equations are obtained by time averaging (or ensemble averaging) the local instantaneous balance equations written for the two phases. When the averaging operation is performed, most of the information about the interfacial configuration and exchanges is lost. As a consequence, a certain number of constitutive relations are needed for the closure of the equations system.

Three different types of closure relations can be identified: those which express the intraphase exchanges (molecular and turbulent transfer terms), those which express the interphase exchanges (interfacial transfer terms), and those which express the interaction between each phase and the walls (wall transfer terms) [16].

Together with Neptune_CFD standard models, various modified models developed at CEA/Grenoble are tested regarding the turbulence production induced by interfacial friction, the drag coefficient, and the interfacial heat transfer [17]. In the following will be presented the balance equations together with the closure laws of the most important terms used to simulate the considered two-phase problems.

2.1. Mass, Momentum, and Energy Averaged Balance Equations. The Neptune_CFD code is based on the classical two-fluid model, which consists of the following six balance equations.

(i) Two mass-balance equations are

$$\frac{\partial \alpha_k \rho_k}{\partial t} + \nabla \cdot (\alpha_k \rho_k \underline{V}_k) = \Gamma_k, \quad k = L, G, \tag{1}$$

where the quantities α_k, ρ_k and $\underline{V}_k$ are the averaged fraction of presence, the averaged density, and the averaged centre of mass velocity for phase k, with the phase index k being equal to L for the liquid phase and to G for the gaseous phase. The right-hand side (RHS) of (1), denoted by Γ_k, is the rate of phase change (evaporation or condensation) per unit volume of mixture.

(ii) Two momentum balance equations are

$$\frac{\partial \alpha_k \rho_k \underline{V}_k}{\partial t} + \nabla \cdot (\alpha_k \rho_k \underline{V}_k \underline{V}_k) = -\alpha_k \underline{\nabla} p + \underline{M}_k + \alpha_k \rho_k \underline{g} + \nabla \cdot \left[\alpha_k \left(\underline{\underline{\tau}}_k + \underline{\underline{\tau}}_k^T\right)\right], \quad k = L, G, \tag{2}$$

where p is the averaged pressure, common to the two phases, and g is the gravity acceleration vector. The two tensors $\underline{\underline{\tau}}_k$ and $\underline{\underline{\tau}}_k^T$ are the averaged molecular and turbulent Reynolds stress tensors, respectively, and the vector $\underline{M}_k$ is the averaged interfacial momentum transfer between phases.

(iii) Two total enthalpy balance equations are

$$\frac{\partial}{\partial t}\left[\alpha_k \rho_k \left(h_k + \frac{V_k^2}{2}\right)\right] + \nabla \cdot \left(\alpha_k \rho_k \left(h_k + \frac{V_k^2}{2}\right) \underline{V}_k\right) = \alpha_k \frac{\partial p}{\partial t} + \alpha_k \rho_k \underline{g} \cdot \underline{V}_k + \Gamma_k \left(h_{ki} + \frac{V_k^2}{2}\right) + q''_{ki} a_i + q'''_{wk} - \nabla \cdot \left[\alpha_k \left(\underline{q}_k + \underline{q}_k^T\right)\right], \quad k = L, G, \tag{3}$$

where h_k is the bulk-averaged enthalpy of phase k and h_{ki} is the interfacial-weighted averaged enthalpy. The two vectors $\underline{q}_k$ and $\underline{q}_k^T$ are the molecular and turbulent heat fluxes. The term $q''_{ki} a_i$ is the heat flux exchanged between phase k and the interface per unit volume, where a_i is the interfacial area concentration (or interfacial area per unit volume), and the term q'''_{wk} is a possible heat exchange term between phase k and the wall.

2.2. Turbulent Transfer Terms. In the Neptune_CFD code [5], for each phase k, the Reynolds stress tensor is closed using a Boussinesq-like hypothesis [18].

A two-equation k-ε model for the calculation of the turbulent eddy viscosity is used, which is an extension to multiphase flows of the classical model used in single phase flows. The two equations for the turbulent kinetic energy and the turbulent dissipation rate are written in the following nonconservative form:

$$\rho_k \left[\frac{\partial K_k}{\partial t} + V_{k,i} \frac{\partial K_k}{\partial x_i}\right] = \frac{1}{\alpha_k} \frac{\partial}{\partial x_j}\left[\alpha_k \frac{\mu_k^T}{\sigma_K} \frac{\partial K_k}{\partial x_j}\right] + \rho_k (\mathrm{PROD}_k + G_k - \varepsilon_k) + P_K^i, \tag{4}$$

$$\rho_k \left[\frac{\partial \varepsilon_k}{\partial t} + V_{k,i} \frac{\partial \varepsilon_k}{\partial x_i}\right] = \frac{1}{\alpha_k} \frac{\partial}{\partial x_j}\left[\alpha_k \frac{\mu_k^T}{\sigma_\varepsilon} \frac{\partial \varepsilon_k}{\partial x_j}\right] + \rho_k \frac{\varepsilon_k}{K_k} (C_{\varepsilon 1} \mathrm{PROD}_k + C_{\varepsilon 1} \max(G_k, 0) - C_{\varepsilon 2} \varepsilon_k) P_\varepsilon^i, \tag{5}$$

where the turbulent viscosity is given by $\mu_k^T = C_\mu \rho_k (K_k^2/\varepsilon_k)$ with $C_\mu = 0.09$.

PROD_k represents the (positive) production due to the mean velocity gradients, and G_k is a stratification attenuation term modelling the correlation between fluctuating densities and velocity (more details are available in [5]). $C_{\varepsilon 1} = 1.44$ and $C_{\varepsilon 2} = 1.92$ are the two classical constants taken from the single-phase model.

By the k-ε models being primarily valid only for turbulent core flows, the near-wall region will be modelled with the standard wall function approach [18].

The two terms P_K^i and P_ε^i take into account the additional turbulence production (or destruction) due to the influence of each phase on the other one.

2.2.1. Various Options for Bubbly Flows Tested in the Jet Experiment Calculations

"ke liq + TRC". TRC stands for turbulence reverse coupling. For the liquid phase of a bubbly flow, the two terms P_K^i and P_ε^i are given by

$$P_K^i = -\left(\underline{M}_G^D + \underline{M}_G^{\mathrm{AM}}\right) \cdot (\underline{V}_G - \underline{V}_L),$$
$$P_\varepsilon^i = C_{\varepsilon 3} \frac{P_K^i}{\tau}, \quad \tau = \left(\frac{{d_{32}}^2}{\varepsilon_L}\right)^{1/3}, \tag{6a}$$

where $\underline{M}_G^D$ and $\underline{M}_G^{\mathrm{AM}}$ are, respectively, the averaged drag and added mass forces, $C_{\varepsilon 3}$ is a constant parameter equal to 0.6 in our calculations, and τ is the characteristic time defined as a function of the imposed bubble diameter d_{32} and the turbulence dissipation rate ε_L. It represents the time scale of liquid eddies having the same size as the bubble diameter d_{32}.

"ke EDF". The difference to notice with the previous one is that the dissipation production term is

$$P_\varepsilon^i = C_{\varepsilon 4} \frac{\varepsilon_k}{K_k} P_K^i. \tag{6b}$$

"ke liq". Means that the influence of these interfacial turbulence effects of (6a), (6b) was not considered in the calculations.

"laminar". Means in the jet experiment calculations that the k-ε transport equations were not used for the gas phase.

2.3. Interfacial Transfer Terms

2.3.1. Heat and Mass Transfers. If the mechanical terms are neglected in comparison to the thermal terms in the averaged form of the energy jump condition, it reduces to [15]

$$\sum_k \left(\Gamma_k h_{ki} + q''_{ki} a_i\right) \approx 0. \tag{7}$$

This important relation (together with the mass jump condition $\Gamma_G = -\Gamma_L$) allows to compute the mass-transfer term as a function of the two volumetric heat fluxes $q''_{ki} a_i$ and the interfacial-averaged enthalpies h_{ki}. We assume that the interfacial-averaged enthalpies are identical to the phase-averaged enthalpies ($h_{ki} = h_k$). Each interfacial heat transfer term $q''_{ki} a_i$ is the product of the interfacial heat flux density which is expressed as

$$q''_{ki} = C_{ki}(T_{\mathrm{sat}}(p) - T_k), \tag{8}$$

where C_{ki} is a heat transfer coefficient, T_k and $T_{\mathrm{sat}}(p)$ are, respectively, the averaged temperature of phase k and the saturation temperature, and α is the void fraction (or vapour void fraction).

The interfacial area concentration in bubbly flow is

$$a_i = \frac{6\alpha_G}{d_{32}}. \tag{9a}$$

In stratified flow, with the "continuous approach," it is

$$a_i = \left|\nabla \alpha_G\right|. \tag{9b}$$

In stratified flow, with the "discrete approach," it is

$$a_i = \frac{1}{h_{\vec{n}}}, \tag{9c}$$

where $h_{\vec{n}}$ is the cell size equal to the length of the segment which includes the gravity centre of the cell and which has the direction $\vec{n}$ normal to the free surface.

A two-phase liquid-vapour flow is considered, where the liquid is identified by index "L" and the vapour by index "G". q''_{Gi} model is not relevant for tests presented here: air-water or saturated vapour. q''_{Li} is calculated with

$$q''_{Li} = C_{Li}(T_{\mathrm{sat}} - T_L). \tag{10}$$

Two models for the heat exchange coefficient C_{Li}, as follows, are used in the present calculations. They are selected amongst the different choices available in the standard version of the code because they are dedicated for PTS applications. Both models can be applied either with a discrete approach, where the heat transfer is calculated only in interface cells and is zero elsewhere, using (9c), or with a continuous approach, where the heat transfer is calculated in all the grid cells of the domain, using (9b) at each time step. In practice, the liquid volume fraction gradient which gives the interfacial area a_i is nonzero only near the interface, and consequently the calculated heat transfer tends rapidly to zero elsewhere.

Neptune_CFD 2004 [19] (HD1).

$$C_{Li} = \frac{2}{\pi} \frac{\lambda_L}{\mu_L} \rho_L V_L^* \sqrt{\mathrm{Pr}}, \tag{11}$$

with

$$V_L^* = \max\left(V_L, 0.001\right),$$
$$V_L = \min\left(|\underline{V}_L|, C_\mu^{0.25}\sqrt{K_L}\right). \tag{12}$$

Since this model takes into account only condensation effects at the water-steam interface, it has been completed by a residual droplet contribution (in the upper zone where $\alpha_L < 0.1$) taken as a "return to saturation" term, with a constant time scale τ_L arbitrary equal to 1 second, and the weighting function $f(\alpha_L) = 1 - \alpha_L = \alpha_G$.

Coste ICMF'2004 (HD2). This model was implemented by CEA/Grenoble. Like many others, it is based on the old concept of surface renewal (Higbie, 1935 [20]). It differs in the definition of the characteristic renewal frequency scale. As discussed in [17, 21], the assumption of renewal by Kolmogorov eddies gives rise to a theoretical contradiction when the Prandtl number approaches unity, that is generally true for water. An alternative was then proposed [21], called *HD2* hereafter, where the frequency is calculated with the Kolmogorov eddies length scale and velocity fluctuation due to turbulence. The validity domain of the surface renewal model framework is then

$$\Pr\left(\mathrm{Re}_t\right)^{7/16} \gg 1. \tag{13a}$$

The heat transfer coefficient is

$$C_{Li} = \rho_L C_{pL}\sqrt{a_L}\left(\frac{\varepsilon_L}{\nu_L}\right)^{1/4}\left(\frac{\delta^4\varepsilon_L}{\nu_L^3}\right)^{1/24}, \quad a_L = \frac{\lambda_L}{\rho_L C_{pL}}, \tag{13b}$$

where δ represents the large eddies length. This model has been validated with Simmer and Neptune_CFD codes on about twenty test cases of COSI experiment. From this point of view, its validity domain is given by the characteristic nondimensional numbers of this experiment.

2.3.2. Momentum Transfer. In the case of a bubbly flow, the interfacial transfer of momentum $\underline{M}_k$ appearing in (2) is assumed to be the sum of five forces:

$$\underline{M}_k = \Gamma_k \underline{V}_k + \underline{M}_k^D + \underline{M}_k^{\mathrm{AM}} + \underline{M}_k^L + \underline{M}_k^{\mathrm{TD}}, \tag{14}$$

where we have assumed that the interfacial-averaged velocity is equal to the phase-averaged velocity ($\underline{V}_{ki} = \underline{V}_k$), the first term on the right-hand side of (14) represents the interfacial transfer of momentum associated to the interfacial transfer of mass. The other terms are, respectively, the averaged drag, added mass, lift and turbulent dispersion forces per unit volume.

Standard Models

Drag force is.

$$\underline{M}_G^D = -\underline{M}_L^D = -\frac{1}{8}a_i\rho_L C_D\,|\,\underline{V}_G - \underline{V}_L\,|\,(\underline{V}_G - \underline{V}_L), \tag{15}$$

where C_D is the nondimensional drag coefficient.

Concerning the drag coefficient closure law, the *separated phases*' model and the *Ishii* correlation were considered. The separated phases' model, used for liquid-gas separated flows, is a Simmer-like model [22] which considers either dispersed gas bubbles in a continuous liquid flow, or dispersed liquid droplets in a continuous gas flow with regard to the volumetric fraction.

The Ishii's empirical correlation, used in case of bubbly flow, provides the automatic calculation of the drag coefficient based on the local regime:

$$C_D = \frac{2}{3}d_{32}\sqrt{\frac{g\,|\,\rho_G - \rho_L\,|}{\sigma}}\left\{\frac{1 + 17.67\,|\,f(\alpha_G)\,|^{6/7}}{18.67 f(\alpha_G)}\right\}^2, \tag{16}$$
$$f(\alpha_G) = (1-\alpha_G)^{1.5},$$

where σ is the surface tension. Equation (16) assumes that we are in the distorted bubble regime.

Added mass force is

$$\underline{M}_G^{\mathrm{AM}} = -\underline{M}_L^{\mathrm{AM}} = -C_{\mathrm{AM}}\frac{1+2\alpha_G}{1-\alpha_G}\alpha_G\rho_L\left[\left(\frac{\partial \underline{V}_G}{\partial t} + \underline{V}_G.\underline{\underline{\nabla}}\,\underline{V}_G\right) - \left(\frac{\partial \underline{V}_L}{\partial t} + \underline{V}_L.\underline{\underline{\nabla}}\,\underline{V}_L\right)\right], \tag{17}$$

where C_{AM} is the added mass coefficient which is equal to 0.5 in the case of spherical bubbles.

Lift force is

$$\underline{M}_G^L = -\underline{M}_L^L = -C_L\alpha_G\rho_L(\underline{V}_G - \underline{V}_L)\wedge(\underline{\nabla}\wedge\underline{V}_L), \tag{18}$$

where C_L is the lift coefficient. This coefficient is equal to 0.5 in the particular case of a weakly rotational flow around a spherical bubble in the limit of infinite Reynolds number.

Turbulent dispersion force is

$$\underline{M}_G^{\mathrm{TD}} = -\underline{M}_L^{\mathrm{TD}} = -C_{\mathrm{TD}}\rho_L K_L \underline{\nabla}\alpha_G, \tag{19}$$

where C_{TD} is a numerical constant of order 1.

New Implemented Models

Drag force. This model too was inspired by the Simmer code but differs from the separated phases in the definition of the drag coefficient for $\alpha_G < 0.7$ (mixing case, defined previously). In fact, the separated phases' model in this case considers that in every cell is present different percentage of liquid with bubbles inclusion and gas with drops inclusion, depending on the value of α_G. In free surface flows with a flat surface, bubbles and droplets are not present, and such a model will be not coherent with physical reality. In fact, this model will lead to an overestimation of the friction due to high bubble drag coefficient, which depends on the fluid density. In order to account roughly for this, as a first step towards the adaptation of drag force closure law to the free surface case, *Dev* model [21, 23] multiplies the bubble drag coefficient for bubbly flows ($\alpha_G < 0.7$) by a factor of 10^{-4}. A second step is to use a wall law type approach but it has been implemented too recently [24] to be tested in the present work.

3. Calculations Discussion and Results

Neptune_CFD is based on a fully unstructured finite volume meshing, together with a collocated arrangement for all flow variables [16]. The solver, based on an elliptic oriented fractional step approach, is able to simulate multifield and multiphase flows. The nonlinear behaviour between pressure and the phase fractions and the symmetric treatment of the fields are taken into account in an iterative procedure, within the time step.

3.1. Prediction of Turbulence Distribution below a Plunging Jet. Experimental data of Iguchi et al. [11] for a plunging

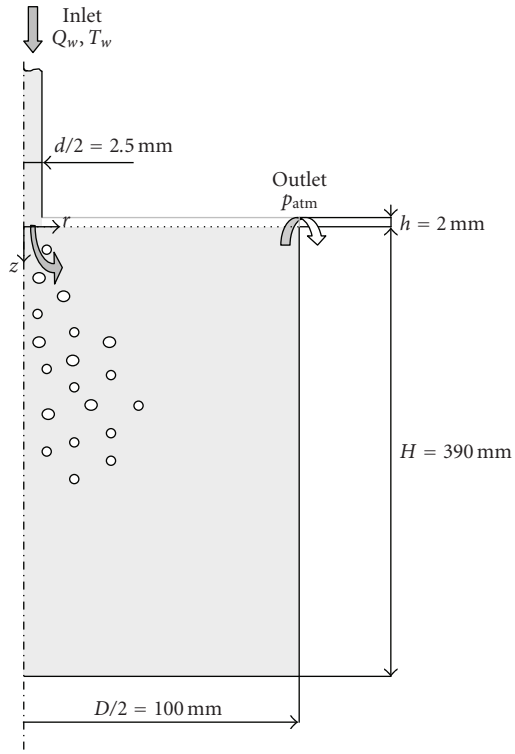

Figure 1: Iguchi's experiment: fluid domain.

Table 1: Geometry and flow conditions.

(a) Geometry of test section

Circular injector, vertical downward flow	
Vessel diameter	$D = 200$ mm
Vessel height	$H = 390$ mm
Injector diameter	$d = 5$ mm
Height of the injector above free surface	$h = 2$ mm

(b) Flow conditions

Turbulent nonfragmented jet entering a free surface	
Fluids	Air-water
Heating	no
Pressure	1 bar
Jet velocity	2.54 m/s
Jet turbulence intensity	5–15%

water jet entering a free surface (see Figure 1) are considered to evaluate prediction capabilities of the two-phase models implemented in the code.

The considered experimental conditions and measurements are summarised in Table 1.

From the experiments, the authors found that in this configuration the jet produces a significant amount of small bubbles ($d < 0.001$ m or 1 mm) in the entire water bath.

In all calculations presented in this section, the fluid domain was represented by nonuniform 2D spatial grids,

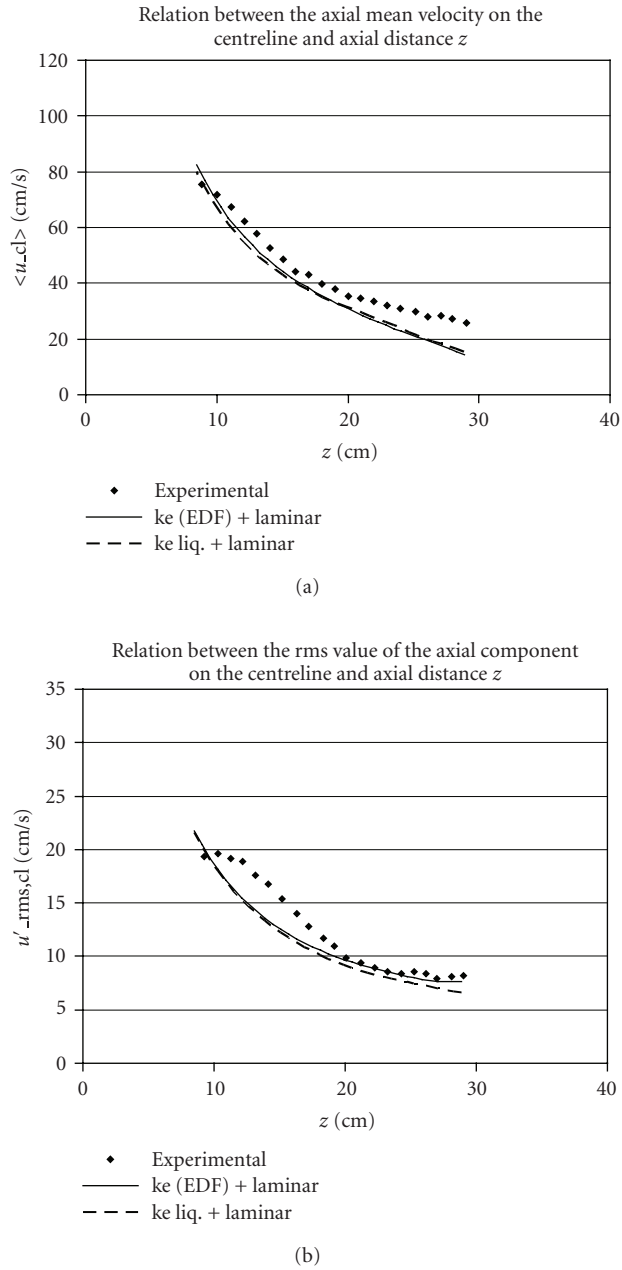

Figure 2: Calculated and measured values on the centreline.

adequately refined in the near wall regions. All boundary conditions were taken as suggested by the NURESIM Programme specifications [8].

Preliminary calculations testing different grids showed that the predicted flow reaches a steady-state configuration in a physical time of 4 seconds, and resulted in the selection of a reference spatial meshing (with 74×214 cells in the vessel and 5×102 in the pipe).

First results showed that the numerical simulation effectively accounts for air entrainment near the bath surface ($z = 10$ cm) and bubble dispersion in the whole water vessel ($z = 20$ and 30 cm), but with very small void fraction values ($\alpha \sim 10^{-3}$).

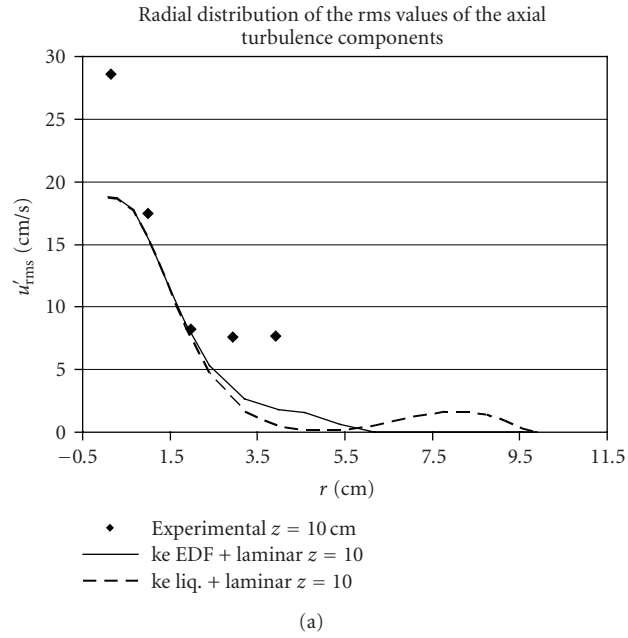

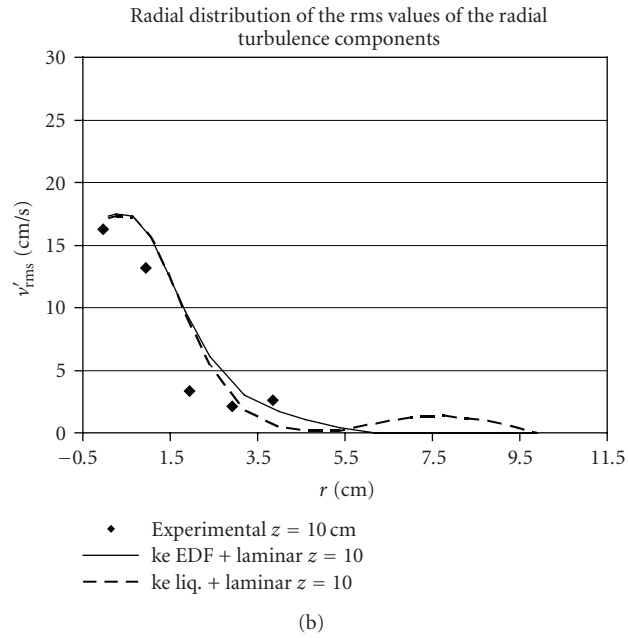

FIGURE 3: Radial distribution of the root-mean-square values of turbulence components.

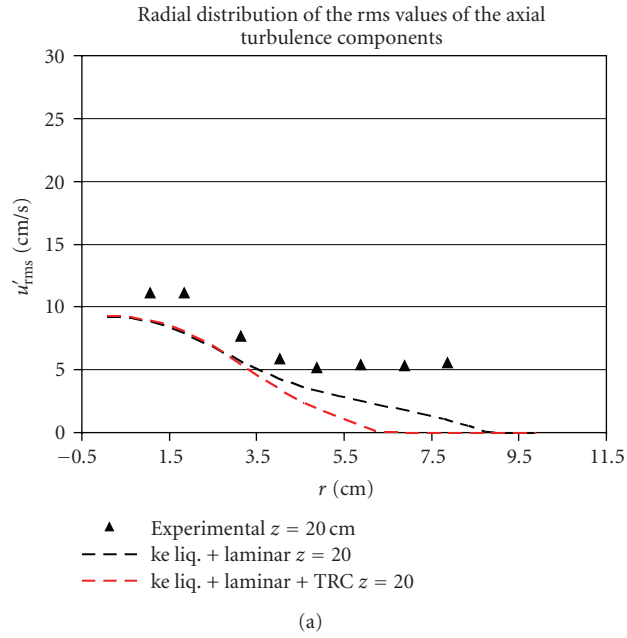

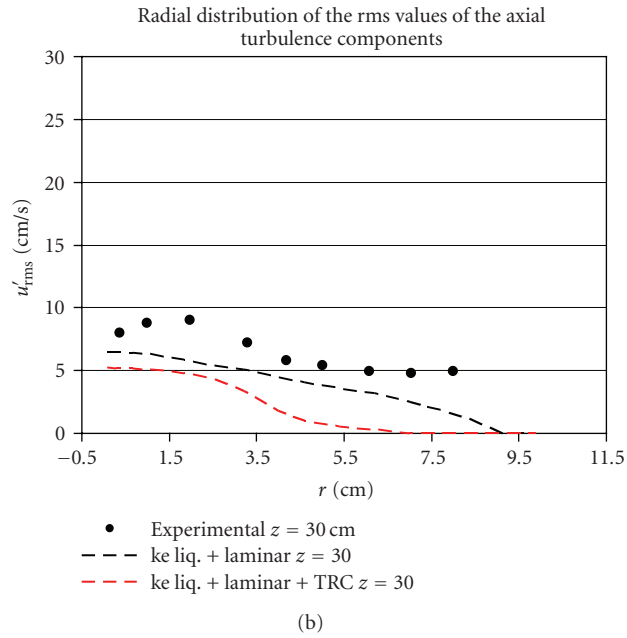

FIGURE 4: Radial distribution of the root-mean-square values of the axial turbulence component (TRC term sensitivity analysis).

Various two-phase turbulence models described in Section 2.2 were tested together with the separated phases model for the drag coefficient also evaluating the influence of interfacial turbulence effects. Predicted results [25] for the axial mean velocity and the root-mean-square value of axial fluctuation on the centreline along the vertical direction were generally in quite good agreement with experimental data (available for $10\,\text{cm} < z < 30\,\text{cm}$), with some underestimation (see Figure 2).

Both the k-ε models considered for water (the standard and modified versions) underestimated the turbulence production and predicted almost the same radial profiles for the turbulence components u'_{rms} and v'_{rms}, failing to catch the anisotropy of the problem (see Figure 3).

This is a classical feature of the k-ε model; important differences are observed especially near the bath surface ($z = 10\,\text{cm}$) for the u'_{rms} prediction. Nevertheless, moving downstream ($z > 20\,\text{cm}$), the flow decelerates and the calculated values better match the experimental data.

Considering the "*TRC*" contribution (see (6a)) in the "*ke liq*" model brings worst results; contrary to what expected, it generally caused a further reduction in turbulence

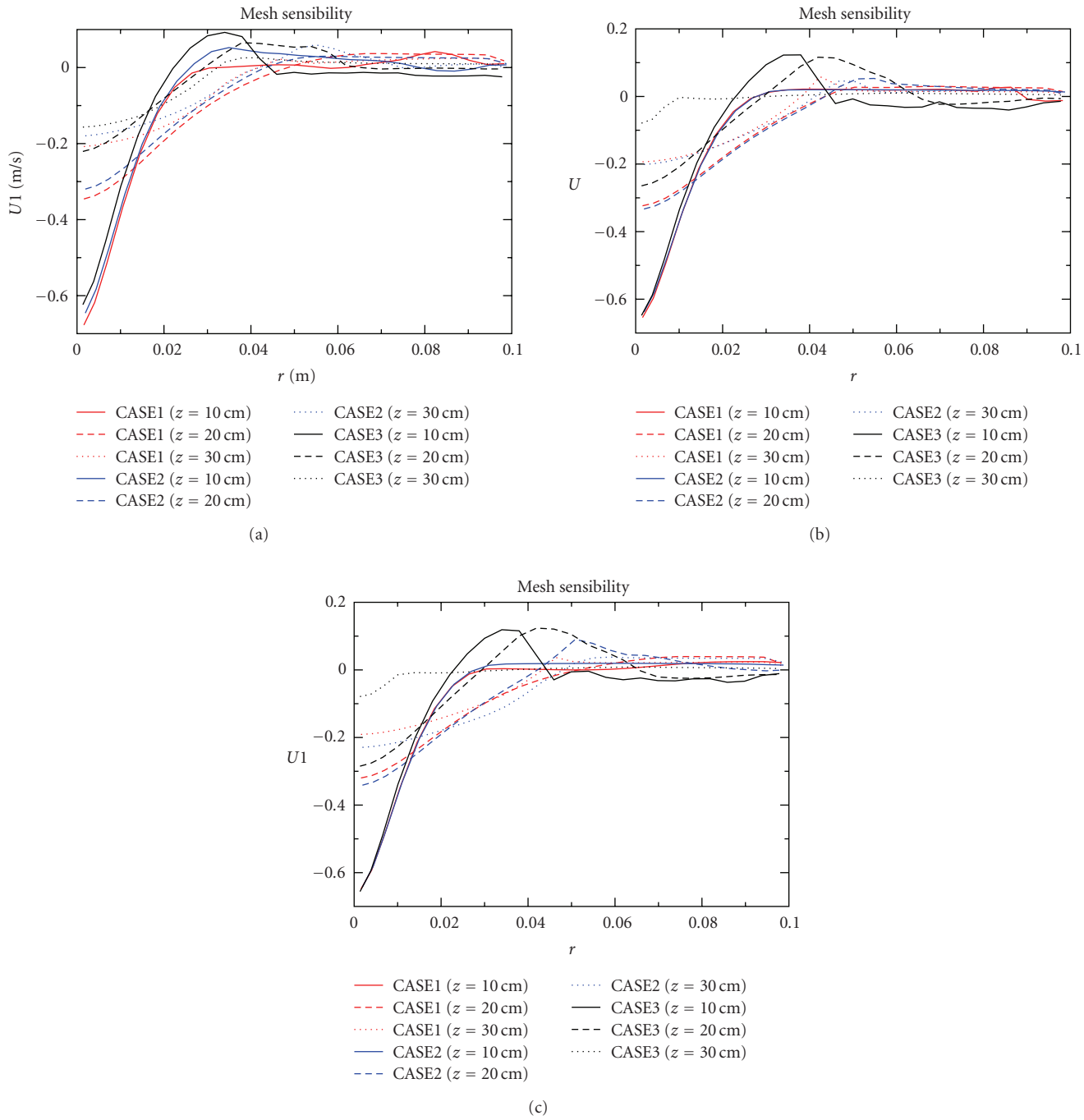

Figure 5: Mesh sensitivity study (CASE1 = finer mesh, CASE2 = mean mesh, CASE3 = coarser mesh): radial velocity profiles considering the modified k-ε model together with (a) separated phases model or (b) the Ishii's correlation for C_D, and (c) adding the nondrag forces (AM, L, TD) contribution.

estimation, especially far from the surface (see Figure 4). Looking at (4), it can be observed that the additional turbulence production terms (the "*TRC*" contribution), P_K^i and P_ε^i, act on both turbulence kinetic energy and turbulence dissipation equation, so that the overall effect can be either an increase or a decrease of turbulence. Trying to modify the relative importance of production and dissipation terms in the turbulent kinetic energy equation (4), by means of changing the values of bubble diameter, d_{32}, and the parameter $C_{\varepsilon 3}$, did not lead to better results. Probably, a more accurate study is needed to clarify the relation between these parameters and TRC term effects.

A sensitivity analysis to mesh refinement was conducted for the best performing turbulence model, considering three successively refined grids (CASE1, 104 × 212 cells; CASE2, 52 × 106 cells; CASE3, 26 × 53 cells). At first, the separated

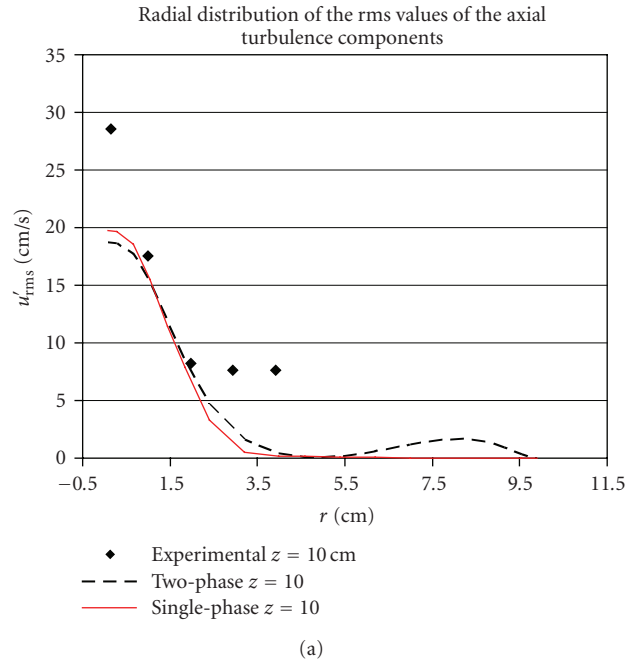

Figure 6: Radial distribution of rms values of the turbulence components-comparison between single- and two-phase results.

phases' model was adopted for the drag coefficient (see Figure 5(a)); then the Ishii's correlation given in (16) was tested (see Figure 5(b)), and finally the added mass (AM), lift (L), and turbulent dispersion (TD) force contributions (see Figure 5(c)) described in Section 2.3.2 above were taken into account. The dependence of numerical results from grid refinement is strongly reduced but the convergence on spatial meshing is not reached. Moreover, the void fraction prediction always seems to change without coherence considering

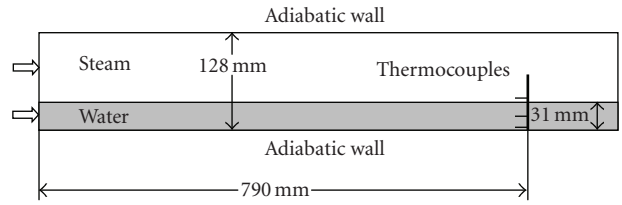

Figure 7: 2D simulation domain.

the different grids; this fact probably depends on the air entrainment modelling at the free surface.

Iguchi [11] presented a comparison between experimental measurements for the two-phase case and theoretical values for the single-phase free jet, showing that the mean velocity and turbulence characteristics were not affected by the bubbles, and agreed well with those for the single-phase case.

An analogous single-phase study was carried out finding that turbulence prediction was not considerably influenced by bubble entrainment, according to experimental evidence (see Figure 6).

Even if there is some confidence in the predicting capabilities of k-ε models on water jet impact effect, some uncertainties are left regarding the prediction of turbulent parameters near the free surface (important to determine the interfacial transfers) because experimental data are not available. Moreover, the effects of water jet on gas entrainment need to be clarified.

3.2. Prediction of Direct Contact Condensation in Turbulent Steam-Water Stratified Flow. This test case concerns a horizontal stratified flow of subcooled water and saturated dry steam along a rectangular straight channel with adiabatic walls. Available experimental data have been measured in the Technical University of Munich using the LAOKOON test facility [14]. The correspondent two-dimensional geometry recommended in [9] for CFD simulations is presented in Figure 7.

One experimental test was simulated, namely, the cocurrent case at high Reynolds number of steam. The regime parameters and the water temperature profile at the measurement section are listed in Table 2. The fluid domain was represented by uniform 2D grids, with different refinement. All boundary conditions were taken as suggested by the NURESIM Program specifications in [8].

Calculations were generally run for 40 seconds, since steady-state conditions were typically reached after 30 to 40 seconds. In all CFD simulations, small surface waves were observed, causing values of flow characteristics calculated near the interface to oscillate, so that presented results are time averaged between $t = 30$ seconds and $t = 40$ seconds.

Simulations were run testing at first standard two-phase models (see Figure 8(a)) and then the new implemented models (see Figure 8(b)).

Results showed that modified k-ε turbulence model and drag coefficient Dev model perform better than the standard

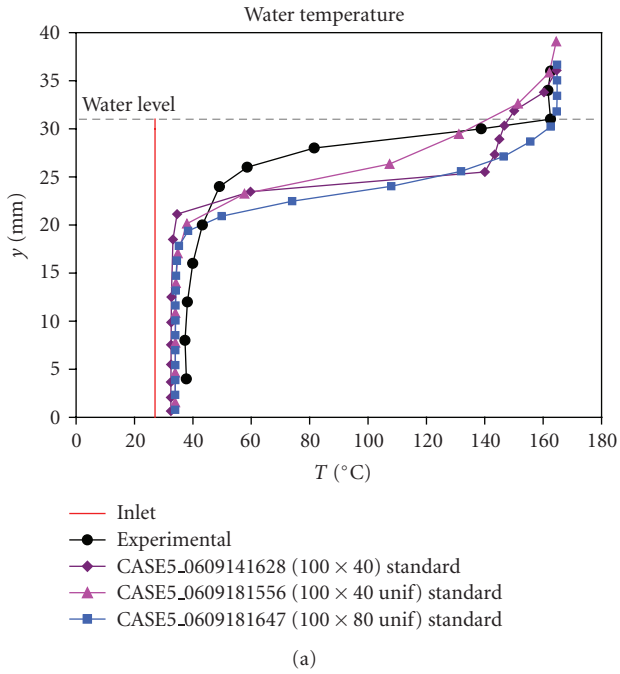

Figure 8: Water temperature profiles for (a) standard ("St") and (b) modified condensation models ("cont" = continue approach, "rt" = relaxation time, "discr" = discrete approach).

versions, so they were chosen for the sensitivity study of the interface transfers models.

The two models *HD1* and *HD2* were compared. Predicted temperature profiles were qualitatively correct, and calculated condensation rates were all around 40%, according to experimental data (the dimensionless condensation rate (CR) is given by the ratio between the overall calculated

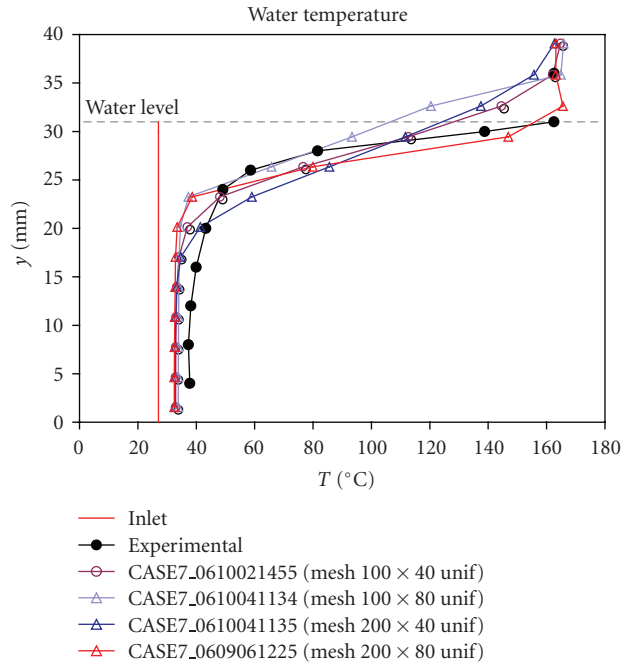

Figure 9: Water temperature profiles for *HD2* model (discreet approach) mesh sensitivity study.

mass transfer [kg/s] and the vapour mass-flow rate entering at inlet [kg/s]).

The *HD2* (discrete approach) model resulted as the best performing model and was chosen as reference to develop a mesh sensitivity study (see Figure 9) (the discreet approach represents the free surface as a sharp discontinuity and allows to consider condensation only in surface cells; in the continuous approach, the free surface is smeared for few grid cells, and the flow variables are distributed continuously with high gradients at the phase separation surfaces).

As a result, temperature profiles seemed not very sensitive to mesh refinement in the bottom part of the channel, while some differences are observed near the interface. Concerning the condensation rate, calculated values were strongly influenced by mesh refinement: increasing axial refinement caused a rise in condensation (~70%), while increasing mesh refinement in height direction caused a reduction (~15%); for mesh refinement in both directions the sensitivity was reduced (~30%).

The configuration is subject to the Kelvin-Helmotz instability. In physical reality, the surface tension is opposed to it at length scales which can be compared with the typical cells size of our meshes. In the calculations, no surface tension is taken into account on interfaces larger than cells size. Then, the instabilities tend to be overestimated with small cells. This is what happens in present calculations; when refining axially the mesh, the sensitivity on the condensation rate is clear. Such instabilities generate a higher microscale turbulence which in turn generates a higher condensation rate, so it is not possible to quantify how much can be attributed to one or the other. With large enough cells, the instabilities growth cannot be simulated, and therefore the

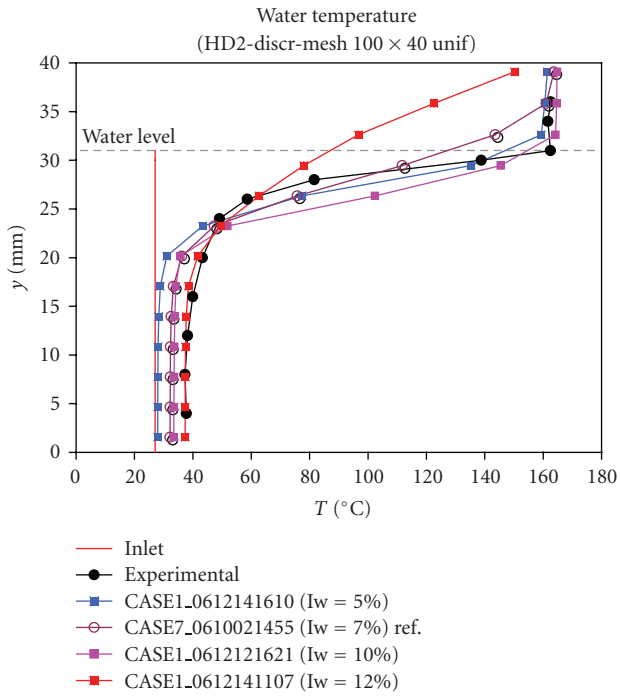

(a)

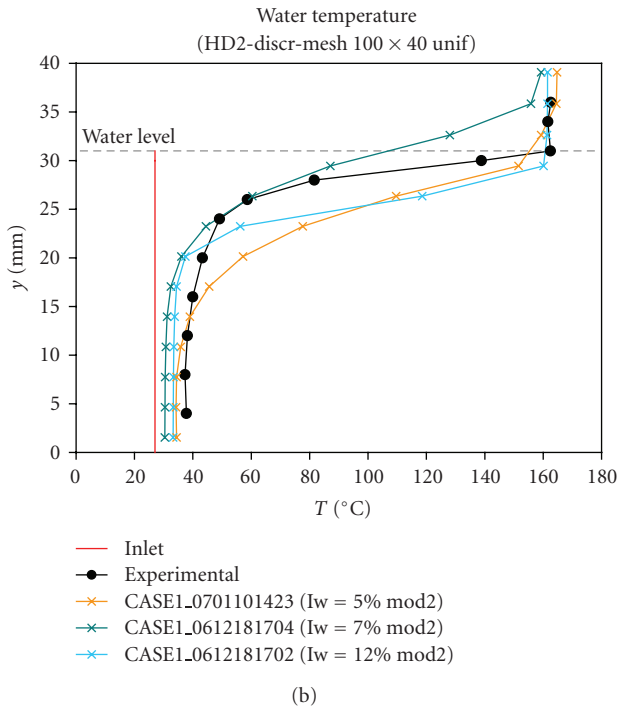

(b)

Figure 10: Water temperature profiles: inlet turbulence sensitivity study.

calculated large interfaces are more stable. When refining radially, as the axial length is kept the same and remains quite large, the effect on the calculation is much less coming from an increase of the instabilities than from the modelling sensitivity to the mesh. This sensitivity rather due to the models is not satisfactory, and future work will be dedicated to it.

Table 2: Flow regime parameters and measured temperature profiles.

(a)

Flow regime parameters	
Inlet flow rate velocity of water	0.28
Inlet flow rate velocity of steam	3.2 m/s
Inlet water temperature	300.2 K
Measured mean water temperature	324.43 K
Pressure	0.697 MPa
Height of water layer	0.031 m
Measured steam velocity	1.94 m/s
Condensation rate	~40%

(b)

y [mm]	T [K]
4	310.94
8	310.48
12	311.31
16	313.14
20	316.42
24	322.26
26	331.79
28	354.73
30	411.97
31	435.67
34	434.77
36	435.74

Moreover, since no exhaustive information is available about the water inlet turbulence, numerical experiments were carried out to investigate the results sensibility to turbulence boundary conditions.

At first only the water turbulence intensity was changed (see Figure 10(a)). Then, the equation which governs the relationship between the turbulence kinetic energy k and the turbulent dissipation rate ε was also modified (see Figure 10(b)). In both cases, water temperature profiles and condensation rate showed a strong dependence on turbulence boundary conditions, so that it seems necessary to carry on a close examination on this point.

4. Conclusions

This study presents a validation of Neptune_CFD against plunging jet data of Iguchi [11] and DCC on stratified steam-water flow for the LAOKOON experiment [14], with an extensive performance comparison of different two-phase models in predicting flow characteristics in PTS scenarios.

One test of Iguchi's experiment is simulated, where small bubbles are entrained below the free surface. Numerical simulations effectively account for air entrainment and bubble dispersion but with very small void fraction values (less than

0.5%), which is qualitatively consistent with experimental observations (quantitative comparison is not possible since void fraction measurement is not available). Predictions of the mean velocity field were always in a rather good agreement with experimental data. Calculated turbulence was generally not bad but significant underestimation is obtained far from the jet axis region. Big differences are also observed in the prediction of turbulent velocities components near the free surface. In fact, none of the used turbulence models succeeded in predicting the anisotropy of the problem; however the main objective of the turbulence model is here to predict turbulent diffusion of heat in the liquid layer and a k-ε model may be sufficient. Considering the interfacial turbulence effects, in contrast to what expected, brought a further reduction in turbulence estimation. Normally, due to the small size of bubbles, there should not be a significant influence of bubbles on the turbulence as mentioned by Iguchi. It is then recommended to further consider the formulation of the interfacial production and dissipation terms in case of small bubbles. Anyway, an under prediction of turbulence would, in real PTS applications, lead to an overestimation of the scenario severity, since steam condensation in the bulk liquid is strongly enhanced by the turbulence level.

For the considered case of LAOKOON experiment, calculations were run at first with standard models for both drag coefficient and interface transfers. Recent models for free surfaces developed at CEA/Grenoble were also tested—a method for interfacial friction and two methods for interfacial heat transfers. In all CFD simulations, small surface waves were observed, causing flow characteristics calculated near the free surface to oscillate. Calculated condensation rates were often higher than measured value, probably because of a turbulence overestimation at the interface. Most of numerical predictions gave correct qualitative water temperature profiles at probe location, while some performance dissimilarities were found in the near surface region, and temperatures are underestimated in the bottom part of the channel. Considering recent free surface models allowed calculated values to better match experimental data, but as well as for standard models, numerical predictions were found to be mesh dependent.

Improving considered models, reducing grid sensitivity, and increasing accuracy in calculating turbulence and interface transfers would then be advantageous.

As a conclusion, we can state that the present work contributed to the assessment of CFD code applicability to PTS scenarios; presented simulations of Iguchi's jet test demonstrated that k-ε models could predict reasonably well the jet induced turbulence and that it is important to consider also the coupling of the turbulence fields. LAOKOON study showed that the two-fluid approach is appropriate to study a stratified steam-liquid flow with condensation, even if further improvement on heat transfer modelling is required.

Acknowledgments

Understanding the code and clearing up the encountered problems would not be possible without the precious collaboration of CEA and University of Pisa colleagues. Special thanks are also due to the NEPTUNE Project team for their continuous support.

References

[1] A. Guelfi, M. Boucker, J. M. Hérard, et al., "A new multi-scale platform for advanced nuclear thermal-hydraulics status and prospects of the NEPTUNE project," in *Proceedings of the 11th International Topical Meeting on Nuclear Reactor Thermal Hydraulics (NURETH 11)*, Avignon, France, October 2005.

[2] D. Bestion and A. Guelfi, "Status and perspective of two-phase flow modelling in the NEPTUNE multi-scale thermal-hydraulic platform for nuclear reactor simulation," *Nuclear Engineering and Technology*, vol. 37, no. 6, 2005.

[3] A. Guelfi, D. Bestion, M. Boucker, et al., "NEPTUNE: a new software platform for advanced nuclear thermal hydraulics," *Nuclear Science and Engineering*, vol. 156, no. 3, pp. 281–324, 2007.

[4] N. Méchitoua, M. Boucker, J. Laviéville, J. Hérard, S. Pigny, and G. Serre, "An unstructured finite volume solver for two-phase water-vapour flows based on an elliptic oriented fractional step method," in *Proceedings of the 11th International Topical Meeting on Nuclear Reactor Thermal Hydraulics (NURETH 11)*, Avignon, France, October 2005.

[5] J. Laviéville, E. Quémérais, S. Mimouni, and N. Méchitoua, NEPTUNE CFD V1.0 theory manual, EDF, 2006.

[6] J. Laviéville, E. Quémérais, M. Boucker, and L. Maas, NEPTUNE CFD V1.0 User Guide, EDF, 2005.

[7] V. Riikonen and M. Ilvonen, "Deliverable D2.1.1: identification of relevant PTS-scenarios, state of the art of modelling and needs for model improvement," in *European Commission 6th Euratom Framework Programme 2005-2008, Integrated Project (IP): NURESIM, Nuclear Reactor Simulations, Sub-Project 2: Thermal Hydraulics*, D. Lucas, Ed., pp. 27–34, 2006.

[8] J. Vihavainen and M. Puustinen, "Deliverable D2.1.2: review of the existing data basis for the validation of models for PTS," in *European Commission 6th Euratom framework programme 2005-2008, Integrated Project (IP): NURESIM, Nuclear Reactor Simulations, Sub-Project 2: Thermal Hydraulics*, D. Lucas, Ed., pp. 51–58, 2006.

[9] M. Scheuerer, F. Menter, Y. Egorov, et al., "Selection of PTS-relevant test cases," 5th Euratom Framework Programme 1998–2002, *EVOL-ECORA-D05a*, December 2002.

[10] Y. Egorov, M. Boucker, A. Martin, S. Pigny, M. Scheuerer, and S. Willemsen, "Validation of CFD codes with PTS-relevant test cases," 5th Euratom Framework Programme 1998–2002, *EVOL-ECORA-D07*, September 2004.

[11] M. Iguchi, K. Okita, and F. Yamamoto, "Mean velocity and turbulence characteristics of water flow in the bubble dispersion region induced by plunging water jet," *International Journal of Multiphase Flow*, vol. 24, no. 4, pp. 523–537, 1998.

[12] H. Ruile, Direktkontaktkondensation in geschichteten Zweiphasenströmungen [thesis], VDI Verlag, Düsseldorf, Germany, 1996.

[13] D. Hein, H. Ruile, and J. Karl, Kühlmittelerwärmung bei Direktkontaktkondensation an horizontalen Schichten und vertikalen Streifen zur Quantifizierung des druckbelasteten Thermoschocks, BMFT Forschungsvorhaben 1500906, Abschlußericht, Lehrstuhl für Thermische Kraftanlagen, TU München, 1995.

[14] M. Goldbrunner, J. Karl, and D. Hein, "Experimental investigation of heat transfer phenomena during direct contact

condensation in the presence of non condensable gas by means of linear raman spectroscopy," in *Proceedings of the 10th International Symposium on Applications of Laser Techniques to Fluid Mechanics*, Lisbon, Portugal, July 2000.

[15] M. Ishii, *Thermo-Fluid Dynamic Theory of Two-Phase Flow*, Collection de la Direction des Etudes et Recherches d'Electricite de France, no. 22, Eyrolles, Paris, France, 1975.

[16] C. Morel, S. Mimouni, J. M. Laviéville, and M. Boucker, "R113 boiling bubbly flow in an annular geometry simulated with the NEPTUNE code," in *Proceedings of the 11th International Topical Meeting on Nuclear Reactor Thermal Hydraulics (NURETH 11)*, Avignon, France, October 2005.

[17] W. Yao, D. Bestion, P. Coste, and M. Boucker, "A three-dimensional two-fluid modeling of stratified flow with condensation for pressurized thermal shock investigations," *Nuclear Technology*, vol. 152, no. 1, pp. 129–142, 2005.

[18] J. H. Ferziger and M. Peric, *Computational Method for Fluid Dynamics*, Springer, Berlin, Germany, 3rd edition, 2002.

[19] M. Boucker, J. Laviéville, A. Martin, C. Béchaud, D. Bestion, and P. Coste, "Preliminary applications of the new NEPTUNE two-phase CFD solver to pressurized thermal shock investigations," in *Proceedings of the 12th International Conference on Nuclear Engineering (ICONE '04)*, vol. 2, pp. 745–751, Arlington, Va, USA, April 2004.

[20] R. Higbie, "The rate of absorption of a pure gas into a still liquid during a short time of exposure," *Transactions of the American Institute of Chemical Engineers*, vol. 31, pp. 365–389, 1935.

[21] P. Coste, "Computational simulation of multi-D liquid-vapour thermal shock with condensation," in *Proceedings of the 5th International Conference on Multiphase Flow (ICMF '04)*, Yokohama, Japan, May-June 2004.

[22] S. Kondo, Y. Tobita, K. Morita, and N. Shirakawa, "SIMMER-III : an advanced computer program for LMFBR severe accident analysis," in *Proceedings of the International Conference on Design and Safety of Advanced Nuclear Power Plants (ANP '92)*, Tokyo, Japan, October 1992.

[23] P. Coste, "An approach of multidimensional condensation modeling for ECC injection," in *Proceedings of the 41st European Two-Phase Flow Group Meeting*, Trondheim, Norway, May 2003.

[24] P. Coste, J. Pouvreau, C. Morel, J. Laviéville, M. Boucker, and A. Martin, "Modeling turbulence and friction around a large interface in a three-dimension two-velocity Eulerian code," in *Proceedings of the 12th International Topical Meeting on Nuclear Reactor Thermal Hydraulics (NURETH 12)*, Pittsburgh, Pa, USA, September-October 2007.

[25] M. C. Galassi, C. Morel, D. Bestion, J. Pouvreau, and F. D'Auria, "Validation of NEPTUNE CFD module with data of a plunging water jet entering a free surface," in *Proceedings of the 12th International Topical Meeting on Nuclear Reactor Thermal Hydraulics (NURETH 12)*, Pittsburgh, Pa, USA, September-October 2007.

Hindawi Publishing Corporation
Science and Technology of Nuclear Installations
Volume 2009, Article ID 320738, 12 pages
doi:10.1155/2009/320738

Research Article

CFD Simulation of Polydispersed Bubbly Two-Phase Flow around an Obstacle

E. Krepper,[1] P. Ruyer,[2] M. Beyer,[1] D. Lucas,[1] H.-M. Prasser,[3] and N. Seiler[2]

[1] *Institute of Safety Research, Forschungszentrum Dresden-Rossendorf (FZD), P.O. Box 510119, 01314 Dresden, Germany*
[2] *Institut de Radioprotection et de Sûreté Nucléaire, CE Cadarache, Bât. 700, BP 3, 13 115 Saint Paul lez Durance Cedex, France*
[3] *Institute of Energy Technology, ETH-Zürich, Sonneggstrasse 3, 8092 Zürich, Switzerland*

Correspondence should be addressed to E. Krepper, e.krepper@fzd.de

Received 10 January 2008; Accepted 18 February 2008

Recommended by Iztok Tiselj

This paper concerns the model of a polydispersed bubble population in the frame of an ensemble averaged two-phase flow formulation. The ability of the moment density approach to represent bubble population size distribution within a multi-dimensional CFD code based on the two-fluid model is studied. Two different methods describing the polydispersion are presented: (i) a moment density method, developed at IRSN, to model the bubble size distribution function and (ii) a population balance method considering several different velocity fields of the gaseous phase. The first method is implemented in the Neptune_CFD code, whereas the second method is implemented in the CFD code ANSYS/CFX. Both methods consider coalescence and breakup phenomena and momentum interphase transfers related to drag and lift forces. Air-water bubbly flows in a vertical pipe with obstacle of the TOPFLOW experiments series performed at FZD are then used as simulations test cases. The numerical results, obtained with Neptune_CFD and with ANSYS/CFX, allow attesting the validity of the approaches. Perspectives concerning the improvement of the models, their validation, as well as the extension of their applicability range are discussed.

1. Introduction

Many flow regimes in Nuclear Reactor Safety Research are characterized by multiphase flows, with one phase being a liquid and the other phase consisting of gas or vapor of the liquid phase. The flow regimes found in vertical pipes are dependent on the void fraction of the gaseous phase, which varies, as void fraction increases, from bubbly flow to slug flow, churn turbulent flow, annular flow, and finally to droplet flow at highest void fractions. In the regimes of bubbly and slug flows, a spectrum of different bubble sizes is observed. While dispersed bubbly flows with low gas volume fraction are mostly monodispersed, an increase of the gas volume fraction leads to a broader bubble size distribution due to breakup and coalescence of bubbles. The exchange area for mass, momentum, or heat between continuous and dispersed phases thus cannot be simply modeled based on the knowledge of just the void fraction and a mean diameter. Moreover, the forces acting on the bubbles may depend on their individual size which is the case not only for drag but also for nondrag forces. Among the forces leading to lateral migration of the bubbles, that is, acting in normal direction with respect to the main drag force, bubble lift force was found to change the sign as the bubble size varies. Consequently, in the context of pipe flows, this leads to a radial separation between small and large bubbles and to further coalescence of large bubbles migrating toward the pipe center into even larger Taylor bubbles or slugs.

An adequate modeling approach must consider all these phenomena. The paper presents two different approaches both being based on the Eulerian modeling framework. On one hand, a generalized inhomogeneous multiple size group (MUSIG) model was applied, for which the dispersed gaseous phase is divided into N inhomogeneous velocity groups (phases), each of these groups being subdivided into M_j bubble size classes. On the other hand, a moment density method is used to model the evolution of the bubble size distribution function along the flow, where main statistics of the distribution being described with a reduced set of transport equations. For both models, bubble breakup and

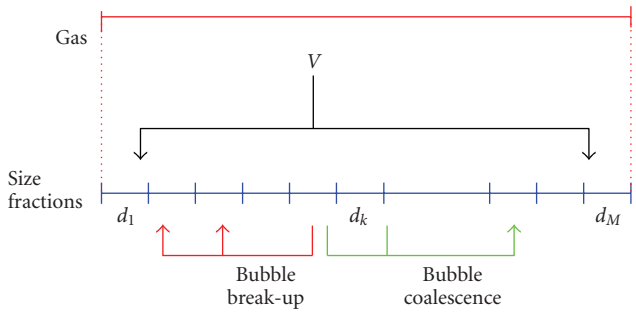

Figure 1: Scheme of the standard MUSIG model: all size fractions representing different bubble sizes move with the same velocity field.

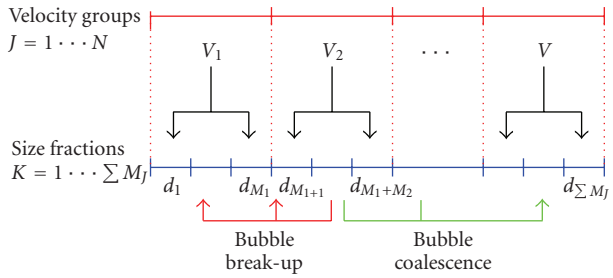

Figure 2: Improvement of the MUSIG approach: the size fractions M_j are assigned to the velocity field V_j.

coalescence processes are taken into account by appropriate models.

2. Model for the Local Size Distribution of a Bubble Population

2.1. Closure Models for Momentum Exchange and for Bubble Coalescence and Breakup. While modeling a two-phase flow using the Euler/Eulerian approach, the momentum exchange between the phases has to be considered. Apart from the drag acting in flow direction, the so-called nondrag forces acting mainly perpendicularly to the flow direction must be considered. Namely, the lift force, the turbulence dispersion force, the virtual mass force, and the wall force play an important role.

The turbulent dispersion force acts on smoothing the gas volume fraction distribution and can be evaluated either from a single expression related to drag turbulent contribution, [1] or deduced from a model for dispersed phase agitation contribution to the momentum balance, for example, the Tchen model [2]. To avoid the maximum gas fraction at the wall, Tomiyama et al. [3, 4] propose a wall force.

The lift force $\vec{F_L}$ considers the interaction of the bubble with the shear field of the liquid. For a single bubble, it reads

$$\vec{F_L} = -C_L \rho_l \frac{\pi d^3}{6} (\vec{w_g} - \vec{w_l}) \times \mathrm{rot}(\vec{w_l}), \tag{1}$$

where ρ_l is the liquid density, d the bubble diameter, and $\vec{w_g}$ and $\vec{w_l}$ are the bubble and liquid velocities, respectively.

The classical lift force, which has a positive coefficient C_L, acts in the direction of decreasing liquid velocity. In case of cocurrent upwards pipe flow, this is the direction towards the pipe wall. Numerical [5] and experimental [3] investigations showed that the direction of the lift force changes its sign if a substantial deformation of the bubble occurs. Tomiyama [4] investigated single bubble motion and derived the following correlation for the coefficient of the lift force from these experiments:

$$C_L = \begin{cases} \min\left[0.288 \tanh(0.121\,\mathrm{Re}), f(\mathrm{Eo}_d)\right], & \mathrm{Eo}_d < 4 \\ f(\mathrm{Eo}_d), \quad \text{for } 4 < \mathrm{Eo}_d < 10 \\ -0.27 \quad \mathrm{Eo}_d > 10 \end{cases}$$

with

$$f(\mathrm{Eo}_d) = 0.00105\mathrm{Eo}_d^3 - 0.0159\mathrm{Eo}_d^2 - 0.0204\mathrm{Eo}_d + 0.474. \tag{2}$$

This coefficient depends on the modified Eötvös number Eo_d, which is formulated for the maximum horizontal bubble size in flow direction [6] and on the Reynolds number Re based on bubble size. The sign of the lift coefficient, and, consequently, the direction of the lift force, depends, thus, on the bubble size diameter. This behavior, originally found for single bubbles of air in glycerol, was also established by different experiments for gas-water polydispersed flows (e.g., [7]) and for different fluids too.

For several flow configurations, this bubble size dependency of the lift force direction can lead to the separation between small and large bubbles. This effect has been shown to be a key phenomenon for the development of the flow regime.

The bubble coalescence model takes into account the random collision processes between two bubbles. The applied model is based on the work of Prince and Blanch [8]. The bubble breakup model considers the collision between a liquid turbulent eddy of a certain characteristic size and a bubble (see [9]). Coalescence and breakup mechanistic models are common to both methods for taking into account the polydispersion in size of the bubble population. We introduce corresponding "breakup" and "coalescence" numerical coefficients F_B and F_C used to scale the original correlations.

2.2. Population Balance Approach

2.2.1. The MUSIG Model by Lo. In principle, the Eulerian two-fluid approach can be extended to simulate a continuous liquid phase and several gaseous dispersed phases solving the complete set of balance equations for each phase. The investigations, however, showed that for an adequate description of the gas volume fraction profile including a population balance model decades of bubble size classes would be necessary. In a CFD code, such a procedure is limited by the increased computational effort to obtain converged flow solutions. To solve this problem, the multiple size group model first implemented by the code developers in CFX-4 solves only one common momentum equation for all bubble size classes (homogeneous MUSIG model, see [10],

Figure 1). Mathematically, the multiple size group model (MUSIG) is based on the population balance method and the two-fluid modeling approach. The dispersed phase is divided into M size fractions. The population balance equation is applied to describe the mass conservation of the size fractions taking into account the interfraction mass transfer resulting from bubble coalescence and breakup. This model approach allows a sufficient number of size fraction groups required for the coalescence and breakup calculation to be used and has found a number of successful applications to large-scale industrial multiphase flow problems.

Nevertheless, the assumption also restricts its applicability to homogeneous dispersed flows, where the slip velocities of particles are almost independent of particle size and the particle relaxation time is sufficiently small with respect to inertial time scales. Thus, the asymptotic slip velocity can be considered to be attained almost instantaneously. The homogeneous MUSIG model described above fails to predict the correct phase distribution when heterogeneous particle motion becomes important. One example is the bubbly flow in vertical pipes, where the nondrag forces play an essential role on the bubble motion. The lift force was found to change its sign, when applied for large deformed bubbles, which are dominated by the asymmetrical wake ([3], see Section 2.1). The lift force in this case has a direction opposite to the shear-induced lift force on a small bubble. For this reason, large bubbles tend to move to the pipe core region resulting in a core void maximum, whereas a near-wall void peak is measured for small bubbles. The radial separation of small and large bubbles cannot be predicted by the homogeneous MUSIG model. This has been shown to be a key mechanism for the establishment of a certain flow regime.

2.2.2. New Strategy: the Inhomogeneous MUSIG Model. A combination of the consideration of different dispersed phases and the algebraic multiple size group model was proposed to combine both the adequate number of bubble size classes for the simulation of coalescence and breakup and a limited number of dispersed gaseous phases to limit the computational effort [11]. The inhomogeneous MUSIG model was developed in cooperation with ANSYS CFX and is implemented in CFX since the version CFX-10 ([12–14] see Figure 2).

In the inhomogeneous MUSIG model, the gaseous dispersed phase is divided into a number N of the so-called velocity groups (or phases), where each of the velocity groups is characterized by its own velocity field. Further, the overall bubble size distribution is represented by dividing the bubble diameter range within each of the velocity groups j in a number M_j, $j = 1, \ldots, N$, bubble subsize fractions. The population balance model, considering bubble coalescence or bubble breakup is applied to the subsize groups. Hence the mass exchange between the subsize groups can exceed the size ranges assigned to the velocity groups resulting in mass transfer terms between the different phases or velocity groups.

The lower and upper boundaries of bubble diameter intervals for the bubble size fractions can be controlled by either an equal bubble diameter distribution, an equal bubble mass distribution, or can be based on user definition of the bubble diameter ranges for each distinct bubble diameter fraction. The subdivision should be based on the physics of bubble motion for bubbles of different size, for example, different behavior of differently sized bubbles with respect to lift force or turbulent dispersion. Extensive model validation calculations have shown that in most cases, $N = 2$ or 3, velocity groups are sufficient in order to capture the main phenomena in bubbly or slug flows [15, 16].

2.3. The Moment Density Method Approach. The moment density method proposes an alternative way to model polydispersion. This method allows to model the time and space evolution of a realistic distribution with the help of a very reduced number of transport equations, for example, Kamp et al. [17], Hill [18]. This is an interesting property, especially from a numerical point of view, with regard to alternative methods like population balance methods. In the present study, we restrict our attention to adiabatic bubbly flows of an incompressible gas inside a continuous liquid phase, and only consider a dispersion in bubbles size. We here present the basic formalism of the moment density method.

2.3.1. A Distribution Function Parameterized by Its Statistical Moments. The moment density method requires the use of an approximate representation of the bubble population thanks to a presumed shape continuous function for the bubble size distribution function f, the one being thus totally determined by a finite number of parameters. The moment densities are intensive physical quantities characterizing mean properties of the population, like the density of bubble area or volume, the so-called volumetric interfacial area a_i, and the volumetric fraction α of the dispersed phase. Bubbles being assumed as spherical and of diameter d, it yields

$$\begin{aligned} a_i &= \int \pi d^2 f \partial d, \\ \alpha &= \int \frac{\pi d^3}{6} f \partial d. \end{aligned} \tag{3}$$

In this work, we introduce f as being simply quadratic in the bubble size d,

$$f = \begin{cases} \dfrac{3\ n(\vec{x},t)\ d}{4\ d_1^3(\vec{x},t)}(2d_1(\vec{x},t) - d) & \text{if } d \le 2d_1, \\ 0 & \text{elsewhere,} \end{cases} \tag{4}$$

where n is the local density number of bubbles (m^{-3}) and d_1 is the mean diameter of the distribution. It is easy to show that n, d_1, a_i, and α are related through:

$$\begin{aligned} 2d_1 a_i &= 9\alpha, \\ 243\pi\, n\, \alpha^2 &= 10\, a_i^3. \end{aligned} \tag{5}$$

The knowledge of the two moment densities a_i and α is thus sufficient to reconstruct the whole distribution function f. The choice for these two parameters is dictated by their importance in the description of the two-phase flow, especially concerning the transfers between the phases.

2.3.2. Transport Equations for the Size Distribution. The transport of the distribution function f obeys a Liouville-Boltzmann equation from which one can derive transport equations for the main moment densities as well as for their transport velocities [19]. The main idea of the method consists in solving a finite number of moment densities transport equations in the framework of the two-fluid model. This solving allows to determine the distribution parameters and thus the whole population evolution. Thus we consider the solving of the following transport equations:

$$\begin{aligned}\frac{\partial a_i}{\partial t} + \nabla\left(a_i\langle\vec{w}\rangle_{a_i}\right) &= \int 2\pi d\left(\frac{\underline{d}d}{\underline{d}t}\right) f\,\partial d + \int \pi d^2 \dot{F}_{c,b}\,\partial d,\\ \frac{\partial \alpha}{\partial t} + \nabla\cdot\left(\alpha\langle\vec{w}\rangle_{\alpha}\right) &= \int \frac{\pi d^2}{2}\left(\frac{\underline{d}d}{\underline{d}t}\right) f\,\partial d,\end{aligned} \tag{6}$$

where $\dot{F}_{c,b}$ is the source term of the Liouville-Boltzmann equation. The transport velocities $\langle\vec{w}\rangle_{a_i}$ and $\langle\vec{w}\rangle_{\alpha}$ of a_i and α, respectively, are assumed to be equal to the mean transport velocity of the bubbles $\vec{w}_g$ (no correlation between dispersions in velocity and in size is taken into account at the current stage of development of the model). $\langle\vec{w}\rangle_{\alpha}$ is defined by

$$\alpha\langle\vec{w}\rangle_{\alpha} = \int \frac{\pi d^3}{6}\,\vec{w}\,f\,\partial d, \tag{7}$$

where $\vec{w}$ is the velocity of a bubble of size d. It satisfies the transport equation:

$$\begin{aligned}&\frac{\partial \alpha\langle\vec{w}\rangle_{\alpha}}{\partial t} + \nabla\cdot\left(\alpha\langle\vec{w}\rangle_{\alpha}\langle\vec{w}\rangle_{\alpha}\right)\\ &\quad= -\nabla\cdot\left(\alpha\,\langle\vec{w}'\,\vec{w}'\rangle_{\alpha}\right) + \int \frac{\pi d^3}{6}\left(\frac{\underline{d}\vec{w}}{\underline{d}t}\right) f\,\partial d.\end{aligned} \tag{8}$$

2.3.3. Closure Relations. The closure of the system of (3)–(8) concerns models (i) for coalescence and breakup events through $\dot{F}_{c,b}$, (ii) for the bubble size evolution along its trajectory $\underline{d}d/\underline{d}t$, (iii) for the hydrodynamic forces acting on individual bubbles, through $d\vec{w}/\underline{d}t$, as well as (iv) for the kinetic stress tensor $\nabla\cdot(\alpha\,\langle\vec{w}'\,\vec{w}'\rangle_{\alpha})$. The closure issue is based on the mechanistic model of all these phenomena at the scale of a single bubble. Source terms of the equations are then evaluated from the integral of individual contributions over the whole bubble population, whose size distribution function is known. The simplicity of the analytical expression (4) for f allows to easily derive expressions for the integrals from the classical models described in Section 2.1. In this study, since the dispersed phase is considered as incompressible and incondensable, the bubble size evolution along its trajectory is zero. Detailed expressions for the source terms can be found in [20].

It is worth pointing out that solving the system of (3)–(8), coupled with the system of balance equations for the continuous phase, is sufficient to describe the evolution of a broad spectrum of bubble sizes. This simplicity of the formulation is advantageous especially in terms of computational cost. Further extension of the model, taking into account the dispersion in velocity, can be considered using a similar formalism. For example, size-related velocity distribution can be introduced to model size-dependent bubble migration due to lift force, like it is done for the inhomogeneous MUSIG model. Moreover, this method has already been successful to consider more general particles velocity dispersion, for example, the work of Fox [21] concerning crossing trajectories.

Table 1: Water and gas superficial velocities J_L and J_G of the tests investigated in this paper.

	J_G [m/s]		
	—	0.0368	0.0898
J_L [m/s]	1.611	—	Run n° 097
	1.017	Run n° 074	Run n° 096

3. The Experiment–Bubbly Flow Around an Obstacle

In the presented experiment performed at the TOPFLOW facility of Research center Dresden-Rossendorf (FZD), the large test section with a nominal diameter of DN200 was used to study the flow field around an asymmetric obstacle (see Figure 3). This is an ideal test case for CFD code validation, since the obstacle creates a pronounced three-dimensional two-phase flow field. Curved stream lines, which form significant angles with the gravity vector, a recirculation zone in the wake and a flow separation at the edge of the obstacle are common in industrial components and installations.

The wire-mesh technology was applied to measure the gas volume fraction and the gas velocity in different distances up- and downstream the obstacle [22]. The sensor provides detailed data on the instantaneous flow structure with a high resolution in space and time. In particular, they allow visualizing the structure of the gas-liquid interface [23].

The tests were performed both for air/water and for steam/water. In the current paper, only adiabatic air/water tests were considered. The parameters are summarized in Table 1.

4. Numerical Settings

4.1. CFX and Population Balance Method. Pretest calculations using ANSYS/CFX and applying a monodispersed bubble size approach were performed for the conditions of test run 074 (J_L = 1.017 m/s, J_G = 0.0368 m/s) (see [24–26]). In the calculation, a fluid domain was modeled 1.5 m upstream and downstream the obstacle. Half of the tube including a symmetry boundary condition set at the xz-plane of the geometry was simulated. In the present paper, the inhomogeneous MUSIG model approach was applied to air/water obstacle experiments run 096 (J_L = 1.017 m/s, J_G = 0.0898 m/s) and run 097 (J_L = 1.611 m/s, J_G = 0.0898 m/s). In the presented calculations for run 096 and run 097, 25, and 20, respectively, subsize gas fractions representing equidistant bubble sizes up to 25 mm and 20 mm, respectively, were simulated, assigned to 2 dispersed

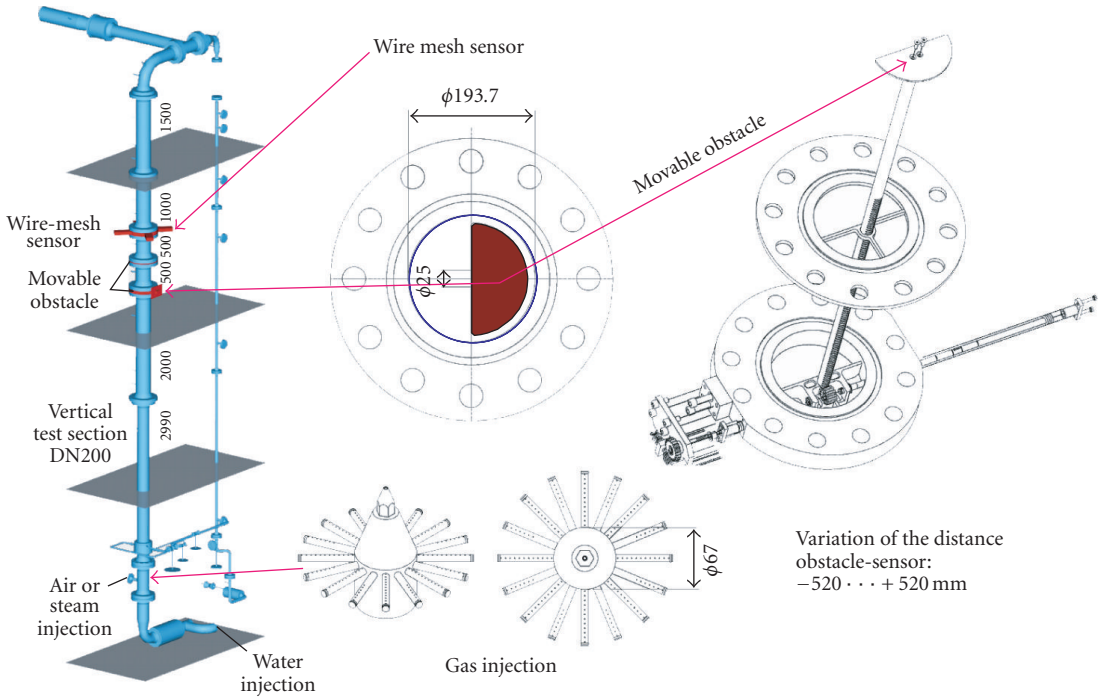

Figure 3: Sketch of the movable obstacle with driving mechanism—a half-moon shaped horizontal plate mounted on top of a toothed rod.

gaseous phases. The first 6 size groups were assigned to the first gaseous phase (or velocity group) and the remaining size groups were assigned to the second gaseous phase. The bubble size distribution measured at the largest upstream position was set as an inlet boundary condition for the calculation.

4.2. Neptune_CFD and Moment Density Method. Neptune_CFD code [27], which is based on the two-fluid model formulation, has been used to perform numerical simulations using the moment density method. The test run 074 has been simulated using a calculation domain corresponding to a 1 m long half pipe centered on the obstacle of around 150 000 cells that takes benefit of the symmetry of the experimental setup. Neptune_CFD calculations of test 074 are based on a k-ε model for the liquid flow, the Tchen correlation being used to model the fluctuations related to bubbles turbulent motion. Bubble hydrodynamics model include both laminar and turbulent evaluations of drag, lift, and virtual mass forces, thanks to a drift model for the relative velocity. Inlet boundary conditions correspond to flat profiles for α, a_i, and the velocities, allowing to recover the experimental surface averaged values for superficial velocities and mean bubble diameter. The surface averaged volumetric fraction and mean diameter are used to reconstruct the inlet bubble size distribution function. The numerical method is based on a pressure-based method. Mass, momentum, and energy equations are coupled by an iterative procedure within a time step. Spatial discretization is based on finite volume framework on unstructured meshes, all the variables being computed at the center of cells.

5. Comparison of Measured and Calculated Results

5.1. The Main Observed Phenomena. Both the steady-state ANSYS CFX calculations applying the inhomogeneous MUSIG model, and the Neptune_CFD calculations applying the moment density method, could reproduce all qualitative details of the flow structure of the two-phase flow field around the diaphragm. The structure of the flow for the here considered test cases 074, 096, and 097 are essentially similar. These different tests have been selected for the purpose of investigating certain phenomena which are more or less pronounced.

The numerical results have been compared to three-dimensional wire-mesh sensor data in Figure 4 (ANSYS CFX for the run 096) and Figure 5 (Neptune_CFD for the run 074). The water velocity and the total gaseous void fraction are represented. All qualitative details of the structure of the two-phase flow field around the obstacle could be reproduced.

Shortly, behind the obstacle a strong vortex of the liquid combined with the accumulation of gas is observed. The measured and calculated shape and extension of the recirculation area agree very well. Upstream the obstacle, a stagnation point with lower gas content is seen in experiment and calculation. Details, like the velocity and void fraction maxima above the gap between the circular edge of the obstacle and the inner wall of the pipe, are also found in a good agreement between experiments and calculations. In the unobstructed cross sectional part of the tube a strong jet is established. Main discrepancies between experimental and Neptune_CFD results concern the volumetric fraction

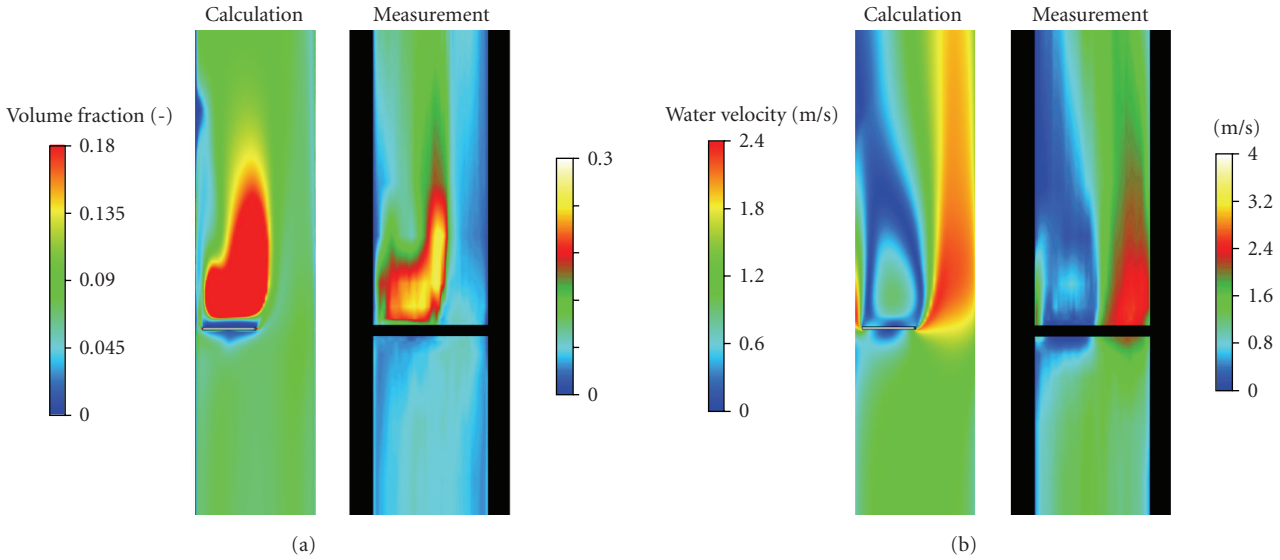

Figure 4: Comparison of time averaged values calculated by CFX (left) and measured (right) up- and downstream of the obstacle in the air-water test run 096, $J_L = 1.017$ m/s, $J_G = 0.0898$ m/s, ($F_B = F_C = 0.05$).

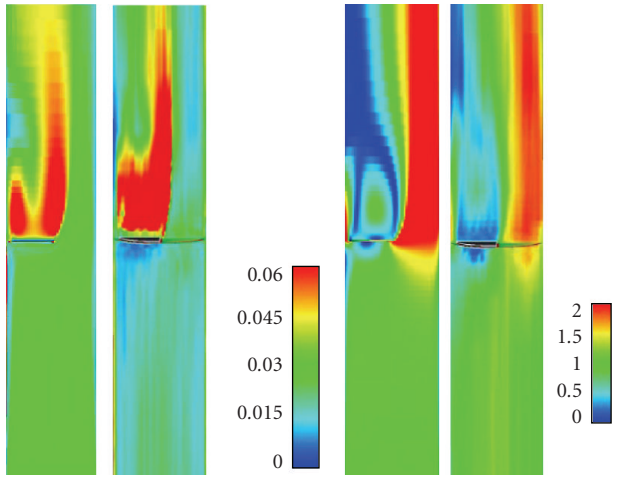

Figure 5: Neptune_CFD numerical (left-hand side of each pair) versus TOPFLOW experimental (right-hand side of each pair) results for run 074. The two left-hand side pictures represent the dispersed phase volume fraction (scale from 0 to $6 \cdot 10^{-2}$) across the symmetry plane of the pipe and the two right-hand side pictures the liquid velocity norm (scale from 0 to 2 ms^{-1}).

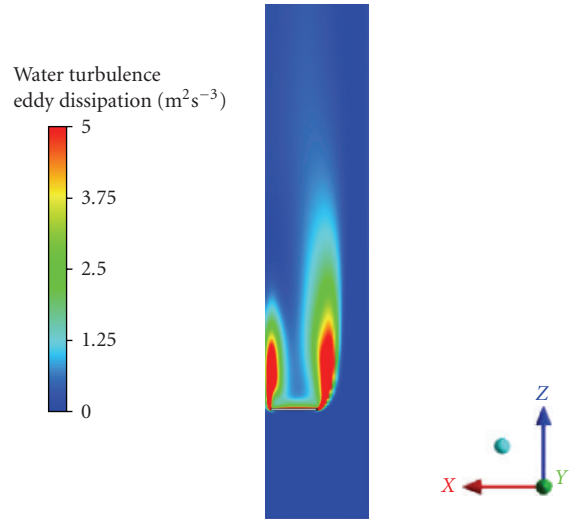

Figure 6: Turbulence eddy dissipation (run 096) (CFX).

upward (below) the obstacle and can be associated to the flat profiles used as inlet bottom boundary conditions.

The structure of the flow is studied in more detail in the following sections.

5.2. Phenomena in the Wake of the Obstacle

5.2.1. Size Distribution of the Bubble Population. More detailed understanding of the flow situation can be gained, considering the bubble size distribution. According to the applied bubble breakup model of Luo and Svendsen [9], bubble breakup can be expected in regions showing high-turbulent eddy dissipation. Figure 6 presents maximum values of the numerically evaluated turbulent eddy dissipation at the edges of the obstacle. At the same time, the applied bubble coalescence model of Prince and Blanch [8] indicates strong importance of coalescence in regions of bubble accumulation, that is, in the wake behind the obstacle. Both bubble coalescence (see gas accumulation shown in Figures 4 and 5) and bubble breakup (see distribution of turbulence dissipation Figure 6), which might partially compensate each other, are expected shortly behind the obstacle.

Figure 7 presents measured cross-sectional averaged bubble size distributions upstream ($z = -0.52$ m), shortly behind ($z = 0.08$ m) and downstream the obstacle ($z = 0.52$ m) for the run 096. The measurements show in the

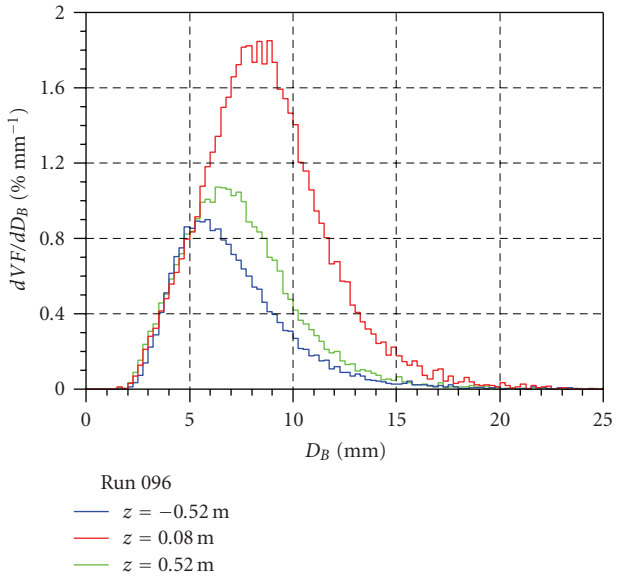

Figure 7: Measured bubble size distribution for run 096.

bubble accumulation zone at $z = 0.08$ m the cross-sectional average shows a shift toward larger bubbles. The experimentally measured bubble size distribution of run 074 is essentially similar to the run 096. It can be seen on the volumetric fraction maps, Figure 8. Above the obstacle, where turbulent intensity is strong, breakup is not experimentally attested, contrarily to the Luo and Svedsen [9] model prediction, but coalescence occurs, leading to the formation of big bubbles (over 7 mm) that concentrate thereafter in the central part of the pipe.

Both ANSYS CFX and Neptune_CFD calculated bubble size distributions, however, show a shift of the mean bubble diameter toward smaller bubbles shortly behind the obstacle when both coalescence and breakup are taken into account. In the calculations, the bubble breakup is overestimated. The corresponding results are provided by Figure 9 for the run 096 and on Figure 10 for run 097. This disagreement was found not solvable by simple changes of breakup or coalescence coefficients, which were set here to $F_B = F_C = 0.05$. Similar deviations would arise at other locations of the flow domain. Neptune_CFD results for the run 074 with standard coefficients $F_B = F_C = 1$ are shown in Figure 11 (the details can be found in [20]).

This suggests to perform computations for which breakup is neglected, but that still consider the Prince and Blanch [8] coalescence model with standard coefficient. The corresponding Neptune_CFD results show that both bubble size repartition and order of magnitude are consistent with experimental results: big bubbles of more than 7 mm are created and accumulate in the recirculation zone just above the obstacle (see Figure 14). Big bubbles stay in the LHS of the pipe, the unobstructed cross-sectional part of the pipe is free of big bubbles, that is consistent with the experimental observation.

As partial conclusions, (i) the Luo and Svendsen breakup model tends to overestimate the breakup of TOPFLOW experimental tests, whereas (ii) the use of the Prince and Blanch model for coalescence within the framework of the moment density method allows to predict satisfying evolution of bubble size across the flow.

5.2.2. Bubbles Streamlines. More detailed effects of lateral motion of small and large bubbles can be revealed by studying bubble streamlines and by analyzing lift forces acting on bubbles of different size. On one hand, the liquid velocity flow carries the small bubbles into the region behind the obstacle (see Figures 12 and 14, right-hand side for the bubble streamlines). Lateral deviation due to lift force is illustrated on Figure 13 for the lift force arrows with the population balance method and Figure 14, right-hand side for the lift coefficient with the moment density method. On the other hand, the air accumulation in the wake region leads to bubble coalescence and the generation of large bubbles as revealed by the analysis of experimental results. This phenomenon is underestimated in the calculations taking breakup into account.

Caused by the lift force, large bubbles are redirected into the downstream jet (see Figure 13) once they can be formed in the wake by coalescence. The streamline representation (see Figure 12) clearly shows this phenomenon for large bubbles already present in the upstream flow.

In the actual version of the moment density method used in Neptune_CFD, dynamics of the bubble population is estimated using a single transport velocity. The averaged lift contribution takes into account both the bubble size distribution and the Tomiyama correlation. When a majority of bubbles are locally above the critical Eötvös number, the lift coefficient changes its sign. In this case, the direction of the lift force is changed, as it can be seen on Figure 14. As a consequence, the bubble streamlines above the obstacle deviate to the center of the pipe. This explains the low value of the dispersed phase volumetric fraction near the left-hand side part of the pipe wall above the obstacle for Neptune_CFD numerical results (see Figure 5). This result is fully consistent with experimental results.

As a partial conclusion concerning the bubble streamlines calculations, both methods showed their ability to consider the effect of bubble size on the lateral deviation of bubble streamlines due to lift force. This provides a more precise understanding and a more accurate prediction of bubbles repartition across the flow.

5.3. Phenomena in the Jet. In the cross-sectional area beside the obstacle, a strong jet is established creating strong shear flow. The resulting phenomena are more pronounced with increasing water velocity, like in run 097, where the liquid velocity was increased to $J_L = 1.611$ m/s. Figure 16 represents measured and ANSYS CFX calculated cross-sectional gas fraction distributions for this run. In the most downstream cross section of the measurements an almost gas bubble free region in the centre of the jet is found. Bubbles are collected at the edges of the jet in regions of largest water velocity gradient.

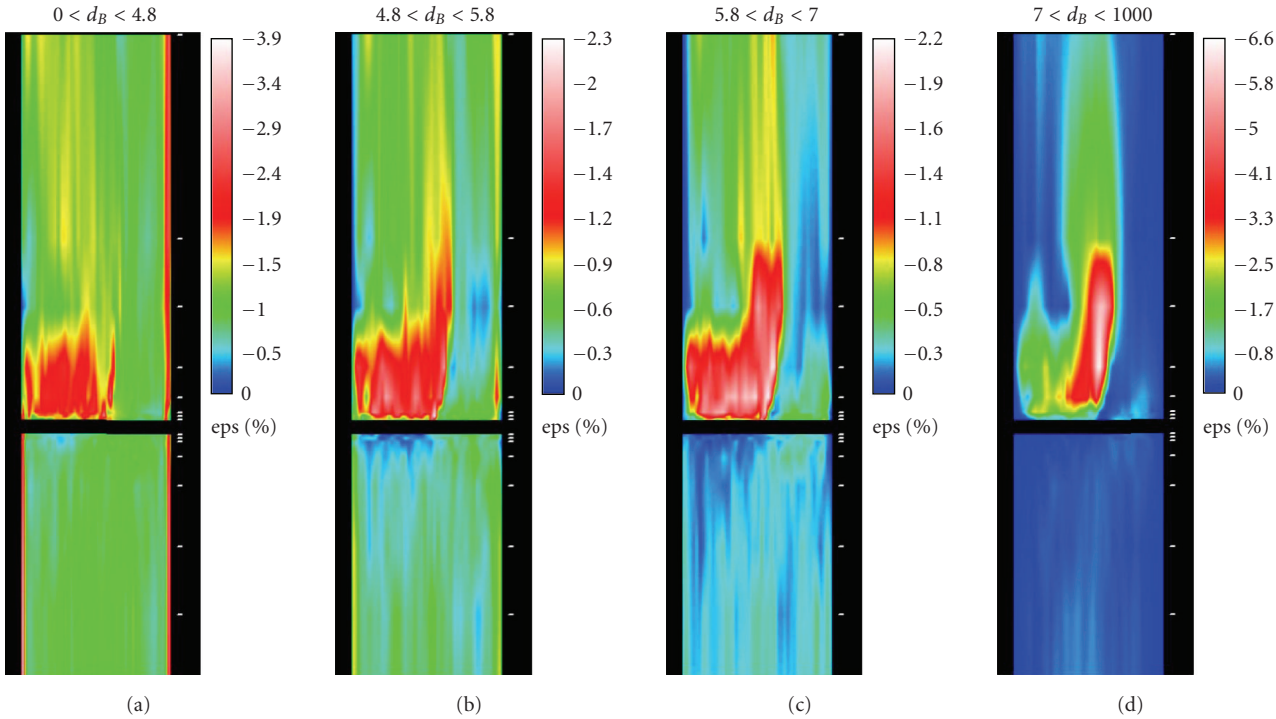

Figure 8: TOPFLOW experimental volumetric fractions of air bubbles according to different size classes, extracted from [24].

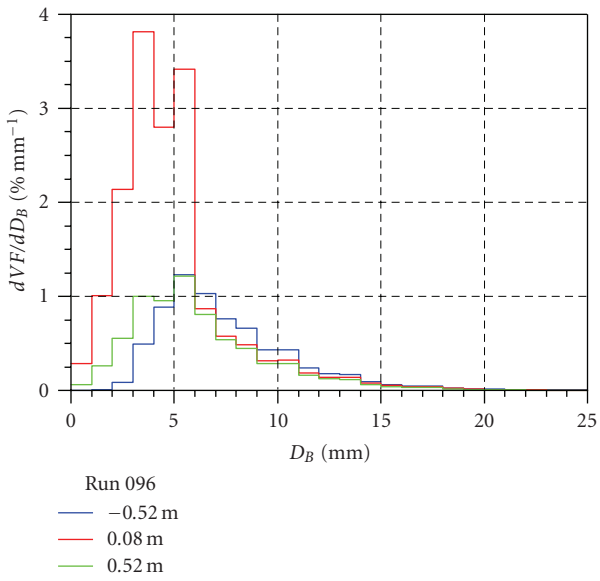

Figure 9: Bubble size distributions for run 096 (J_L = 1.017 m/s, J_G = 0.0898 m/s) (CFX) ($F_B = F_C = 0.05$).

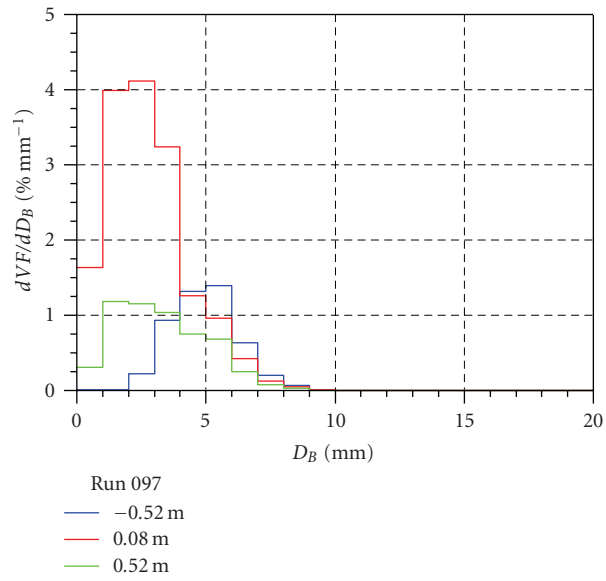

Figure 10: Bubble size distributions for run 097 (J_L = 1.611 m/s, J_G = 0.0898 m/s) (CFX) ($F_B = F_C = 0.05$).

The streamline representation of the ANSYS CFX calculations, however, (Figure 12 for run 096, which is fairly similar to run 097) indicates large bubbles being directed into the jet caused by the lift force. This discrepancy between experiment and ANSYS CFX calculations can possibly be explained by the strong water velocity gradient near the jet. This strong shear flow induces bubble breakup which is not yet considered in the model of Luo and Svendsen [9]. In the tests, the big bubbles could migrate toward the jet, but be fragmented at the relatively sharp boarder of this jet. Only a small fraction of the small bubbles created by this breakup process can enter the jet by action of the turbulent dispersion force.

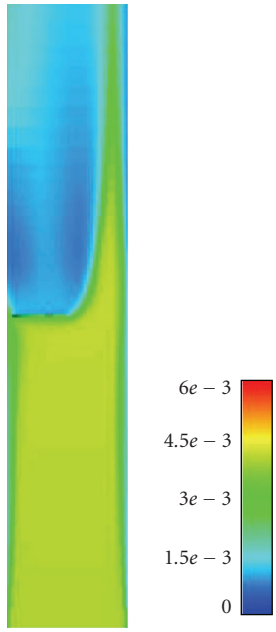

Figure 11: Neptune_CFD result for mean Sauter bubble diameter (m), both breakup and coalescence being taken into account ($F_B = F_C = 1$) run 074.

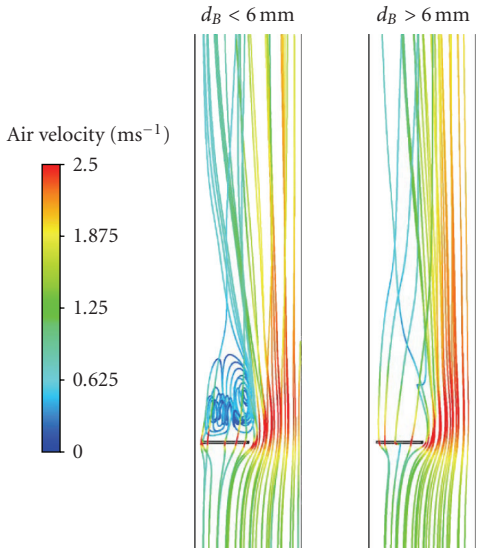

Figure 12: Streamlines for small (left) and large (right) bubbles (run 096) (CFX).

The gas distribution resolved by bubble size classes (see Figure 15) shows clearly the deviations between measurements and calculations. In the experiment, the gas accumulation behind the obstacle leads to a strong coalescence and the creation of large bubbles. In the CFX-calculations, this effect is underestimated.

In Neptune_CFD calculations based on the moment density method the bubble breakup was neglected. As attested by Figure 14, left-hand side, in this case the bubbles present in the jet are small bubbles. Big bubbles created

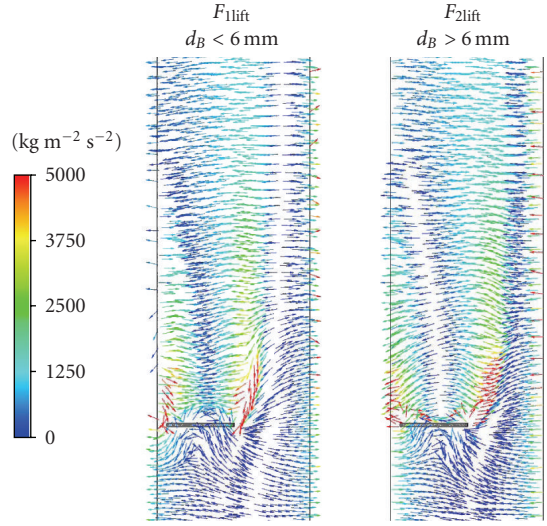

Figure 13: Bubble lift force vectors for the different gas velocity groups (run 096) (CFX).

are concentrated in the center of the pipe where the largest value of volumetric fraction can be found (Figure 5). The structure of the gas repartition in the jet for both calculation and experiments is represented on Figure 17. In the upper part, the structure of the flow of the numerical calculation is consistent with experimental results. The most important deviation is observed in the region just above the obstacle ($z = 0.08$m). A gain in accuracy of these results could be achieved by considering size-dependent velocity dispersion within the moment density method, in particular for bubble size-dependent lateral migration in the regions where there exists a strong mixing of different bubble sizes (mainly just above the obstacle as far as run 074 is concerned, see Figure 8).

Nevertheless, the main trends of the bubble dynamics downward the obstacle are in agreement with experimental results (see Figure 16 for CFX and Figure 17 for Neptune_CFD).

6. Summary and Perspectives

In this study, we focused on the model of the bubble size distribution in the numerical simulation of bubbly flows. More deep understanding of the flow structure is possible when considering a more accurate characterization of the polydispersion. For upward two-phase flow in vertical pipes the core peak in the cross-sectional gas fraction distribution could be reproduced very well both by the moment density and by the MUSIG population balance methods. For complex flows, the general three-dimensional structure of the flow could be well reproduced in the simulations.

These test cases of pipe flow with internal obstacle demonstrate the complicated relationship and interference between size-dependent bubble migration, bubble coalescence, and breakup effects for real flows. With an appropriate given distribution function, the numerical effort of the moment density method is lower compared to the multiple

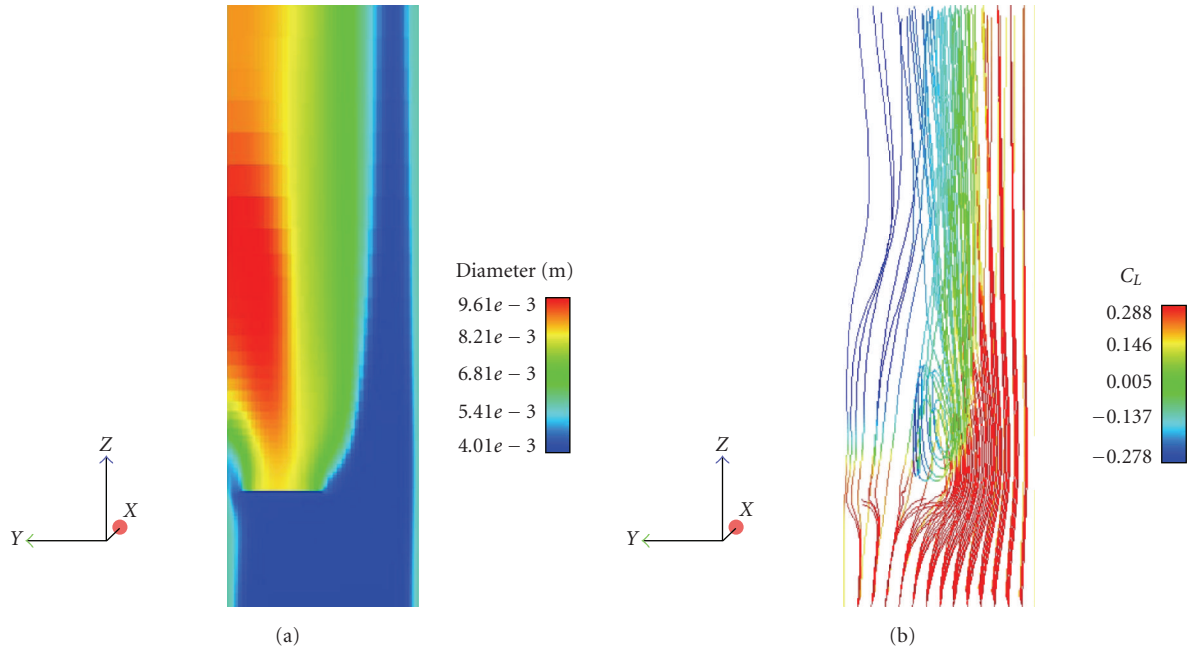

Figure 14: Neptune_CFD numerical results for local mean bubble diameter and corresponding streamlines colored by the equivalent mean lift coefficient (run 074) ($F_B = 0; F_C = 1$).

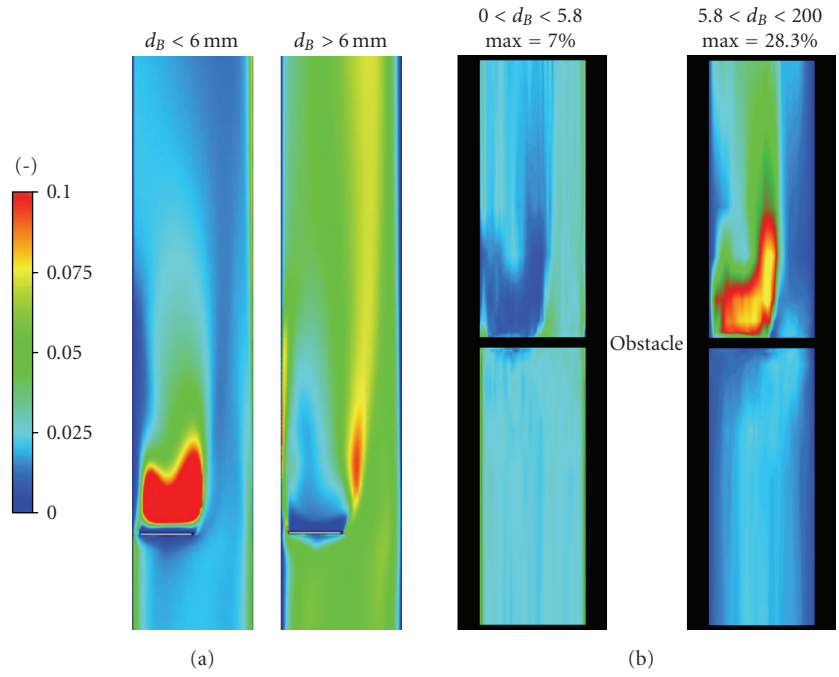

Figure 15: Calculated by CFX (left) and measured (right) gas distributions up- and downstream of the obstacle resolved to bubble size classes (run 096 $J_L = 1.017$ m/s, $J_G = 0.0898$ m/s, $F_B = 0, F_C = 0.05$).

bubble size group method (MUSIG). On the other hand, applying the MUSIG method the simulation of a flow situation allows to deal with more general shapes for the distribution function. Both methods enable to consider the effect of polydispersion in size on the bubble population dynamics, in particular on the evaluation of interphase momentum transfers associated with lift and drag. The inhomogeneous population balance model, using several velocity fields for the bubbly phase, is able to deal with size separation of a locally polydispersed in size population, whereas the moment density method accounts for local diversity in bubble hydrodynamics thanks to a single-averaged contribution

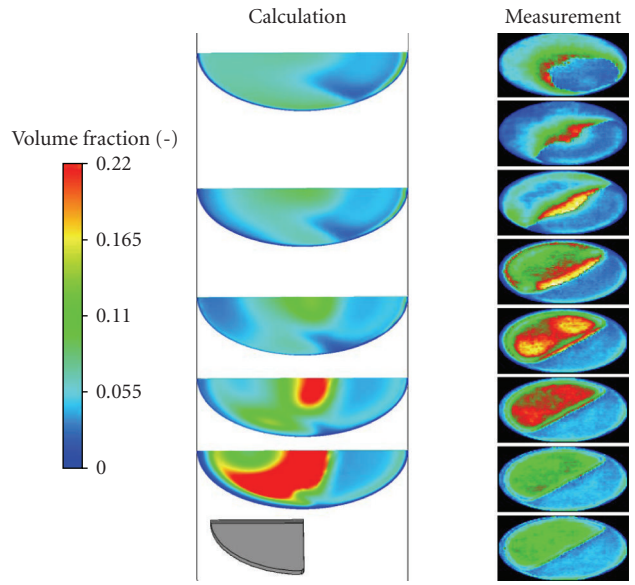

Figure 16: Calculated by CFX (left) and measured (right) gas cross-fractional distributions downstream the obstacle (run 097 J_L = 1.611 m/s, J_G = 0.0898 m/s, $F_B = F_C = 0.05$). Calculations (obstacle shown), distances at z = 0.08 m, 0.16 m, 0.25 m, 0.37 m, and 0.52 m. Measurements (obstacle in the upper left area). distances at z = 0.01 m, 0.015 m, 0.02 m, 0.04 m, 0.08 m, 0.16 m, 0.25 m, and 0.52 m.

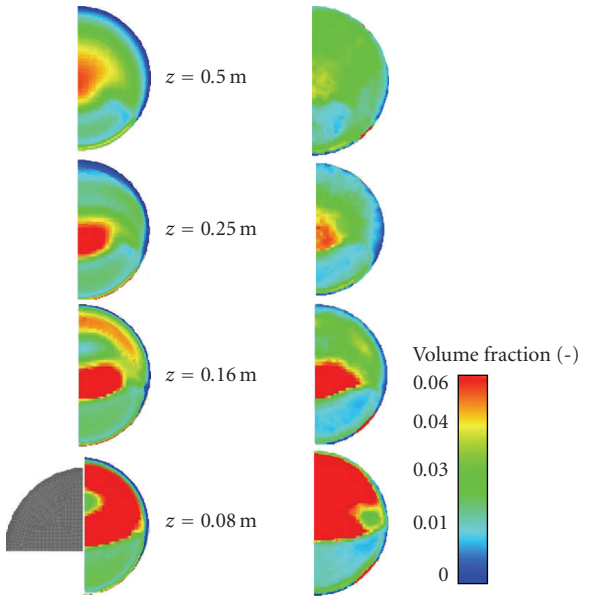

Figure 17: Calculated by Neptune_CFD (left) and measured (right) gas volumetric fraction run 074 for different elevations (obstacle, symbolized in gray, is at z = 0 m and covers the "upper" part of the half-pipe cross-section representation).

of interphase transfers. These two promising refinements of the two-fluid model for bubbly flows have shown their ability to recover consistent description of the lift force in the upper part of the flow, where complex flow structures are observed.

While the closure models on bubble forces, which are responsible for the simulation of bubble migration, allow to explain the bubbles hydrodynamic behavior observed experimentally, clear deviations occur for bubble coalescence and breakup. Both methods based on similar coalescence and breakup models lead to the same conclusion: in the simulations of the TOPFLOW experiments, the Luo and Svendsen model leads to an overestimation of the breakup that appears as negligible in the experiments. On the other hand, the coalescence model of Prince and Blanch seems able to recover the correct bubble size, if used solely, as attested by corresponding Neptune_CFD calculations. For both methods, the presently applied models describing bubble breakup and coalescence could be proven as weak points in numerous CFD analyses. These bubble breakup and coalescence models depend to a large extent on the turbulence properties of the two-phase flow, which were not measured and could not be validated in the pipe flow test cases. Therefore, further investigations are necessary to determine whether the currently used multiphase flow turbulence models deliver appropriate and verifiable quantities that can be used for the description of bubble dynamics processes.

Extensions of both the moment density method and the MUSIG method to nucleate boiling regime numerical simulation are in progress. This includes the phenomena of compressibility, phase-change, and wall nucleation. To model the bubble size-dependent lateral migration phenomenon, the moment density method should also include a model for the bubble velocity distribution. This can be done using a similar formalism to the present model for bubble size distribution function.

Nomenclature

a_i: Specific interfacial area [m^{-1}]
C_L: Lift force coefficient [-]
d: Bubble diameter [m]
$\underline{d}$: Lagrangian derivative
Eo: Eötvös number [-]
f: Size distribution function [m^{-4}]
$\dot{F}_{c,b}$: Breakup and coalescence related variations of f [$m^{-4}s^{-1}$]
$F_{B/C}$: Breakup, coalescence coefficients [-]
F_L: Lift force [kg m s^{-2}]
J: Superficial velocity [m s^{-1}]
n: Bubbles number density [m^{-3}]
N: Number of velocity groups [-]
M: Number of sub-size groups [-]
Re: Reynolds number [-]
V: Velocity [m s^{-1}]
w: Bubble velocity [m s^{-1}]
z: Axial coordinate [m]
l: Liquid
g: Gas
α: Volumetric fraction [-]
ρ: Density [kg m^{-3}].

Acknowledgments

Part of this study is carried out at the Institute of Safety Research of the FZD as a part of current research projects

funded by the German Federal Ministry of Economics and Labour, Project nos. 150 1265 and 150 1271. The other part of this study carried out at the Institut de Radioprotection et de Sûreté Nucléaire (IRSN) has been achieved in the framework of the Neptune project, financially supported by CEA (Commissariat à l'Énergie Atomique), EDF (Électricité de France), IRSN, and AREVA-NP. The authors express their gratitude to the technical TOPFLOW (FZD) team.

References

[1] A. D. Burns, T. Frank, I. Hamill, and J.-M. Shi, "The favre averaged drag model for turbulent dispersion in Eulerian multiphase flows," in *Proceedings of the 5th International Conference on Multiphase Flow (ICMF '04)*, pp. 1–17, Yokohama, Japan, May-June 2004, paper no. 392.

[2] E. Deutsch and O. Simonin, "Large eddy simulation applied to the motion of particles in stationary homogeneous fluid turbulence," in *Turbulence Modification in Multiphase Flows*, vol. 110, pp. 35–42, ASME FED, Portland, Ore, USA, 1991.

[3] A. Tomiyama, I. Sou, I. Zun, N. Kanami, and T. Sakaguchi, "Effects of Eötvös number and dimensionless liquid volumetric flux on lateral motion of a bubble in a laminar duct flow," in *Advances in Multiphase Flow*, pp. 3–15, Elsevier Science, Amersterdam, The Netherlands, 1995.

[4] A. Tomiyama, "Struggle with computational bubble dynamics," in *Proceedings of the 3rd International Conference on Multiphase Flow (ICMF '98)*, pp. 1–18, Lyon, France, June1998.

[5] E. A. Ervin and G. Tryggvason, "The rise of bubbles in a vertical shear flow," *Journal of Fluids Engineering*, vol. 119, no. 2, pp. 443–449, 1997.

[6] R. M. Wellek, A. K. Agrawal, and A. H. P. Skelland, "Shapes of liquid drops moving in liquid media," *AIChE Journal*, vol. 12, no. 5, pp. 854–862, 1966.

[7] H.-M. Prasser, M. Beyer, H. Carl, et al., "Evolution of the structure of a gas-liquid two-phase flow in a large vertical pipe," *Nuclear Engineering and Design*, vol. 237, no. 15–17, pp. 1848–1861, 2007.

[8] M. J. Prince and H. W. Blanch, "Bubble coalescence and break-up in air-sparged bubble columns," *AIChE Journal*, vol. 36, no. 10, pp. 1485–1499, 1990.

[9] H. Luo and H. F. Svendsen, "Theoretical model for drop and bubble break-up in turbulent flows," *AIChE Journal*, vol. 42, no. 5, pp. 1225–1233, 1996.

[10] S. Lo, Application of the MUSIG model to bubbly flows, AEAT-1096, AEA Technology, June 1996.

[11] E. Krepper, D. Lucas, and H.-M. Prasser, "On the modelling of bubbly flow in vertical pipes," *Nuclear Engineering and Design*, vol. 235, no. 5, pp. 597–611, 2005.

[12] J.-M. Shi, P.-J. Zwart, Th. Frank, U. Rohde, and H.-M. Prasser, "Development of a multiple velocity multiple size group model for poly-dispersed multiphase flows," Annual Report of Institute of Safety Research. Forschungszentrum Rossendorf, Dresden, Germany, 2004.

[13] P. A. Zwart, A. Burns, and C. Montavon, "Multiple size group models," Tech. Rep. CFX-5.7, AEA Technology plc, Oxfordshire, UK, November 2003.

[14] T. Frank, P. J. Zwart, J.-M. Shi, E. Krepper, D. Lucas, and U. Rohde, "Inhomogeneous MUSIG model—a population balance approach for polydispersed bubbly flows," in *Proceedings of the International Conference on Nuclear Energy for New Europe*, Bled, Slovenia, September 2005.

[15] E. Krepper, Th. Frank, D. Lucas, H.-M. Prasser, and P. J. Zwart, "Inhomogeneous MUSIG model-a population balance approach for polydispersed bubbly flows," in *Proceedings of the 6th International Conference on Multiphase Flow (ICMF '06)*, Leipzig, Germany, July 2007, paper no. 375.

[16] E. Krepper, M. Beyer, Th. Frank, D. Lucas, and H.-M. Prasser, "Application of a population balance approach for polydispersed bubbly flows," in *Proceedings of the 6th International Conference on Multiphase Flow (ICMF '06)*, Leipzig, Germany, July 2007, paper no. 378.

[17] A. M. Kamp, A. K. Chesters, C. Colin, and J. Fabre, "Bubble coalescence in turbulent flows: a mechanistic model for turbulence-induced coalescene applied to microgravity bubbly pipe flow," *International Journal of Multiphase Flow*, vol. 27, no. 8, pp. 1363–1396, 2001.

[18] D. P. Hill, "The computer simulation of dispersed two-phase flows," Ph.D. thesis, Imperial College of Science, Technology and Medecine, University of London, London, UK, 1998.

[19] O. Simonin, "Continuum modelling of dispersed two-phase flows," in *Combustion and Turbulence in Two Phase Flows*, VKI Lecture Series 1996-02, Von Karman Institute for Fluid Dynamics, Brussels, Belgium, 1996.

[20] P. Ruyer, N. Seiler, M. Beyer, and F. P. Weiss, "A bubble size distribution model for the numerical simulation of bubbly flows," in *Proceedings of the 6th International Conference on Multiphase Flow (ICMF '06)*, Leipzig, Germany, July 2007, paper no. 484.

[21] R. O. Fox, "Introduction and fundamentals of modelling approaches for polydisperse multiphase flows," in *Multiphase Reacting Flows: Modelling and Simulation*, D. L. Marchisio and R. O. Fox, Eds., vol. 492 of *CISM Courses and Lectures*, pp. 1–40, Springer, New York, NY, USA, 2007.

[22] H.-M. Prasser, A. Böttger, and J. Zschau, "A new electrode-mesh tomograph for gas-liquid flows," *Flow Measurement and Instrumentation*, vol. 9, no. 2, pp. 111–119, 1998.

[23] H.-M. Prasser, E. Krepper, and D. Lucas, "Evolution of the two-phase flow in a vertical tube—decomposition of gas fraction profiles according to bubble size classes using wire-mesh sensors," *International Journal of Thermal Sciences*, vol. 41, no. 1, pp. 17–28, 2002.

[24] H.-M. Prasser, T. Frank, M. Beyer, H. Carl, H. Pietruske, and P. Schütz, "Gas-liquid flow around an obstacle in a vertical pipe experiments and CFD simulation," in *Proceedings of the Annual Meeting on Nuclear Technology*, vol. 16, Aachen, Germany, May 2005.

[25] Th. Frank, P. J. Zwart, E. Krepper, H.-M. Prasser, and D. Lucas, "Validation of CFD models for mono- and polydisperse air-water two-phase flows in pipes," in *OECD/NEA International Workshop on The Benchmarking of CFD Codes for Application to Nuclear Reactor Safety (CFD4NRS '06)*, Garching, Germany, September 2006, paper no. B6-32.

[26] Th. Frank, H.-M. Prasser, M. Beyer, and S. Al Issa, "Gas-liquid flow around an obstacle in a vertical pipe—CFD simulation and comparison to experimental data," in *Proceedings of the 6th International Conference on Multiphase Flow (ICMF '06)*, Leipzig, Germany, July 2007, paper no. 135.

[27] A. Guelfi, D. Bestion, M. Boucker, et al., "NEPTUNE: a new software platform for advanced nuclear thermal hydraulics," *Nuclear Science and Engineering*, vol. 156, no. 3, pp. 281–324, 2007.

Hindawi Publishing Corporation
Science and Technology of Nuclear Installations
Volume 2009, Article ID 387020, 10 pages
doi:10.1155/2009/387020

Research Article

Mechanistic Multidimensional Modeling of Forced Convection Boiling Heat Transfer

Michael Z. Podowski[1] and Raf M. Podowski[2]

[1] *Center for Multiphase Research, Rensselaer Polytechnic Institute, Troy, NY 12180, USA*
[2] *SeeqPod, Inc., Emeryville, CA 94608, USA*

Correspondence should be addressed to Michael Z. Podowski, podowm@rpi.edu

Received 1 June 2008; Accepted 22 August 2008

Recommended by Iztok Tiselj

Due to the importance of boiling heat transfer in general, and boiling crisis in particular, for the analysis of operation and safety of both nuclear reactors and conventional thermal power systems, extensive efforts have been made in the past to develop a variety of methods and tools to evaluate the boiling heat transfer coefficient and to assess the onset of temperature excursion and critical heat flux (CHF) at various operating conditions of boiling channels. The objective of this paper is to present mathematical modeling concepts behind the development of mechanistic multidimensional models of low-quality forced convection boiling, including the mechanisms leading to temperature excursion and the onset of CHF.

1. Introduction

Because of the complexity of phenomenagoverning boiling heat transfer in general, and subcooled boiling inparticular, the predictions of CHF have traditionally been based on correlating data obtained from numerous experimental measurements. At the same time, our understanding of the local physical mechanisms governing thenear-wall phase change and transport has been steadily improving. Given the progress made in the computational fluid dynamics methods, the possibility of using complete multidimensional models to predict boiling heat transfer before, and up to, the onset of CHF becomes an attractive option complementing the traditional phenomenological approach used in the past.

The objective of this paper is to discuss various physical and mathematical modeling concepts for local heat transfer phenomena in boiling systems, and to show that the proposed approach can be combined with mechanistic multidimensional models of two-phase flow and used to predict various parameters characterizing low-quality forced-convection boiling, including the mechanisms leading to temperature excursion and the onset of CHF.

2. Multidimensional Multifield Model of Forced-Convection Boiling

The multifield modeling concept is based on coupling a complete mechanistic multidimensional model of two-phase flow with the models governing local heat transfer and phase change phenomena in heated channels. The major components of the overall model are the following:

(a) conservation equations for the individual fields,

(b) the model of turbulence,

(c) closure laws for the interfacial mass transfer,

(d) closure laws for the interfacial momentum transfer,

(e) closure laws for the interfacial energy transfer,

(f) kinematic boundary conditions for phasic velocities and turbulence,

(g) thermal boundary conditions for the near-wall heat transfer.

2.1. Multifield Conservation Equations. The multifield model of two- and multiphase flows assumes that each phase can be

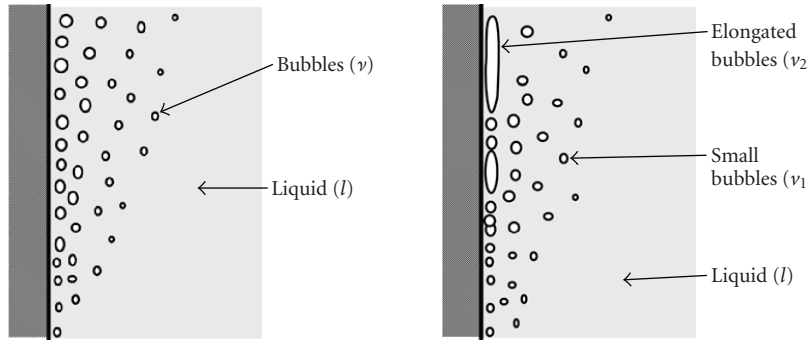

(a) Two-field model (b) Three-field model

Figure 1: An illustration of the multifield model of two-phase flow in a boiling channel.

represented by either one or several fields. In the latter case, the individual fields represent topologically different flow structures within a given phase (such as liquid film and liquid droplets or groups of gas bubbles of different sizes). Typical ensemble-averaged conservation equations for a multifield model can be written as follows:

Mass

$$\frac{\partial(\alpha_k\rho_k)}{\partial t} + \nabla\cdot(\alpha_k\rho_k\mathbf{u}_k) = \Gamma_k, \tag{1}$$

Momentum

$$\frac{\partial(\alpha_k\rho_k\mathbf{u}_k)}{\partial t} + \nabla\cdot(\alpha_k\rho_k\mathbf{u}_k\mathbf{u}_k) = -\nabla(\alpha_k p_k) + \nabla\cdot(\alpha_k\boldsymbol{\tau}_k^{\text{tot}}) + \alpha_k\rho_k\mathbf{g} + \widehat{\mathbf{M}}_k^i, \tag{2}$$

Energy

$$\frac{\partial(\alpha_k\rho_k e_k)}{\partial t} + \nabla\cdot(\alpha_k\rho_k\mathbf{u}_k e_k) = -\nabla\cdot(\alpha_k\mathbf{q}_k^{\text{tot}}) + \nabla\cdot[\alpha_k(-p_k\mathbf{I} + \boldsymbol{\tau}_k^{\text{tot}})\cdot\mathbf{u}_k] + \alpha_k\rho_k\mathbf{g}\cdot\mathbf{u}_k + \widehat{E}_k^i, \tag{3}$$

where α_k, ρ_k, $\mathbf{u}_k$, and e_k are the volume fraction, density, velocity, and specific internal energy, respectively, of field-k, Γ_k is the net mass transfer rate (this and all other terms are per unit volume) of field-k, $\boldsymbol{\tau}_k^{\text{tot}}$ is the total shear stress, $\widehat{\mathbf{M}}_k^i$ is the total interfacial force, $\mathbf{q}_k^{\text{tot}}$ is the local heat flux, and $\widehat{E}_k^i$ is the interfacial heat transfer rate, all for field-k. Details concerning the various terms in (1)–(3) can be found in [1].

In the modeling of low-quality nucleate boiling flows, a two-field model can normally be used, which accounts for the continuous liquid (l) and dispersed vapor (v) fields. This is shown in Figure 1(a), where upon departing from the heated wall, bubbles move into the subcooled liquid region and condense.

For high wall heat fluxes, vapor concentration near the heated wall increases, so that the individual departing bubbles may coalesce and form elongated bubbles, as shown in Figure 1(b). Since the mechanisms governing the motion and heat transfer of elongated bubbles may be quite different from those for small spherical bubbles (field-v_1), it is appropriate to use a separate field for the former, denoted here as field-v_2.

The multidimensional multifield conservation equations, (1)–(3), must be complemented by appropriate boundary conditions and closure laws. The boundary conditions of particular interest to this work are associated with the effect of heated channel wall on local flow and phase change in the near-wall region. The necessary closure laws and models are those for turbulence, interfacial forces, interfacial mass transfer, and heat transfer. A brief description of the major closure laws and boundary conditionspertinent to low-quality two-phase flows in boiling channels is given below.

2.2. Multifield Model of Turbulence Model. Two-phase flow turbulence is normally modeled using the κ-ε model [2] for the continuous liquid field ($k = l$), modified to include the effect of bubble-induced turbulence. The turbulent kinetic energy, κ_l, and the energy dissipation, ε_l, of the liquid field are, respectively, given by

$$\frac{\partial(\alpha_l\kappa_l)}{\partial t} + \nabla\cdot(\alpha_l\mathbf{u}_l\kappa_l) = \nabla\cdot\left(\alpha_l\frac{\mu_l^t}{\rho_l\sigma_\kappa}\nabla\kappa_l\right) + S_l^\kappa,$$
$$\frac{\partial(\alpha_l\varepsilon_l)}{\partial t} + \nabla\cdot(\alpha_l\mathbf{u}_l\varepsilon_l) = \nabla\cdot\left(\alpha_l\frac{\mu_l^t}{\rho_l\sigma_\varepsilon}\nabla\varepsilon_l\right) + S_l^\varepsilon. \tag{4}$$

For given $\kappa_l\varepsilon_l$, the turbulent viscosity, μ_l^t, can be expressed as

$$\mu_l^t = C_\mu\rho_l\frac{\kappa_l^e}{\varepsilon_l} + \mu_B^t, \tag{5}$$

where the bubble-induced turbulence can be written as [3]

$$\mu_B^t = C_{\mu B}\alpha_l\rho_l\sum_{k=1}^{2}(\mathbf{u}_{v_k} - \mathbf{u}_l). \tag{6}$$

2.3. Interfacial Mass Transfer. Since in nucleate boiling, evaporation occurs only at (or near) the heated wall; the interfacial mass transfer between the liquid and vapor fields is practically only due to vapor condensation in contact

with subcooled liquid. In addition, after elongated bubbles start forming, another possible interfield mass exchange mechanism is due to small bubble coalescence. Hence, the volumetric mass transfer terms can be expressed as

$$\Gamma_l = -\Gamma^{\text{evap}} + \Gamma^{\text{cond}} = -(\Gamma_{v_1} + \Gamma_{v2}), \tag{7}$$

$$\Gamma_{v_1} = \Gamma_{v_1}^{\text{evap}} - \Gamma_{v_1}^{\text{cond}} - \Gamma_{v_1}^{\text{clsc}}, \tag{8}$$

$$\Gamma_{v_2} = \Gamma_{v_2}^{\text{evap}} - \Gamma_{v_2}^{\text{cond}} + \Gamma_{v_1}^{\text{clsc}}. \tag{9}$$

In (7), $\Gamma^{\text{evap}} = \Gamma_{v_1}^{\text{evap}} + \Gamma_{v_2}^{\text{evap}}$ and $\Gamma^{\text{cond}} = \Gamma_{v_1}^{\text{cond}} + \Gamma_{v_2}^{\text{cond}}$ are the total evaporation and condensation rates per unit volume, respectively, and $\Gamma_{v_1}^{\text{clsc}}$ is the coalescence rate of small bubbles per unit volume (which becomes a source term for the elongated bubble field).

2.4. Interfacial Momentum Transfer. In general, the total interfacial force on phase-k can be expressed as a superposition of several component forces:

$$\widehat{\mathbf{M}}_k^i = p_k^i \nabla \alpha_k - \boldsymbol{\tau}_k^i \cdot \nabla \alpha_k + \Gamma_k \mathbf{u}_k^i + \sum_j \mathbf{M}_{k,j}^i. \tag{10}$$

In dispersed bubbly flows, the major interfacial forces are the following (for details and source references, see [1]):

Drag Force

$$\mathbf{M}_{l,v_k}^D = -\mathbf{M}_{v_k,l}^D = -\frac{1}{8} C_{D,k} A_{v_k}''' \rho_l (\mathbf{u}_{v_k} - \mathbf{u}_l) \left| \mathbf{u}_{v_k} - \mathbf{u}_l \right|, \tag{11}$$

Virtual Mass Force

$$\mathbf{M}_{l,v_k}^{\text{VM}} = -\mathbf{M}_{v_k,l}^{\text{VM}} = -C_{\text{VM},k} \alpha_{v_k} \rho_l \left(\frac{D_{v_k} \mathbf{u}_{v_k}}{Dt} - \frac{D_l \mathbf{u}_l}{Dt} \right), \tag{12}$$

Lift Force

$$\mathbf{M}_{l,v_k}^L = -\mathbf{M}_{v_k,l}^L = -C_{L,k} \alpha_{v_k} \rho_l (\mathbf{u}_{v_k} - \mathbf{u}_l) \times \nabla \times \mathbf{u}_l, \tag{13}$$

Turbulent Dispersion Force

$$\mathbf{M}_{l,v_k}^{\text{TD}} = -\mathbf{M}_{v_k,l}^{\text{TD}} = C_{\text{TD},k} \alpha_{v_k} \rho_l \nabla (\alpha_l \kappa_l) \tag{14}$$

for $k = 1, 2$, where $\alpha_l = 1 - (\alpha_{v_1} + \alpha_{v_2})$.

As it can be seen from (11)–(14), direct momentum exchange occurs between the continuous liquid and each vapor field, whereas bubble-bubble interactions are due to the coalescence of small bubbles to form elongated bubbles (see Section 2.5 below) and they mainly involve mass and energy transfers.

2.5. Interfacial Energy Transfer. Given a very low-vapor superheat, the interfacial volumetric condensation rates can be expressed as

$$\Gamma_k^{\text{cond}} = \frac{q_k''^i}{h_{fg}} \quad (k = v_1, v_2), \tag{15}$$

where the interfacial energy transport from vapor field-k to the continuous liquid field is given by

$$q_k''^i = H_{k-l}^i (T_{\text{sat}} - T_l) A_k''' \quad (k = v_1, v_2). \tag{16}$$

In (16), A_k''' is the interfacial area density for vapor field-k, and H_{k-l}^i is the local interfacial heat transfer coefficient that can be obtained from

$$H_{k-l}^i = \frac{k_l}{d_k} \left[2 + 0.6 \left(\frac{\rho_l d_k v_{r,k}}{\mu_l} \right)^{0.5} \left(\frac{c_{pl} \mu_l}{k_l} \right)^{0.33} \right], \quad (k = v_1, v_2). \tag{17}$$

Equations (16) and (17) imply

$$q_l''^i = q_{v_1}''^i + q_{v_2}''^i = \left[H_{v_1-l}^i A_{v_1}''' + H_{v_2-l}^i A_{v_2}''' \right] (T_{\text{sat}} - T_l). \tag{18}$$

The rate of bubble coalescence can be obtained from

$$\Gamma_{v_1}^{\text{clsc}} = b_{v_1-v_1} \alpha_{v_1}^2 + b_{v_1-v_2} \alpha_{v_1} \alpha_{v_2}, \tag{19}$$

where $b_{v_1-v_1}$ and $b_{v_1-v_2}$ are the corresponding rate coefficients.

3. Near-Wall Heat Transfer in Nucleate Boiling

In the nucleate subcooled boiling in a heated channel, the wall heat is partially used to form bubbles and the remaining portion is transferred to the liquid. The heat transfer from the wall in the vicinity of a nucleation site occurs during two distinct periods: the bubble growth time and the waiting time. The total convective heat flux from the wall is the sum of three models [4]:

$$q_{\text{NB}}'' = q_{1\phi}'' + q_e'' + q_Q'', \tag{20}$$

where $q_{1\phi}''$ is the single-phase convective heat flux, q_e'' is the heat flux associated with phase change (evaporation), and q_Q'' is the so-called quenching heat flux, which is transferred to the liquid phase during the waiting time.

Outside of the influence area of the bubbles, the heat transfer from wall to the liquid can be determined from

$$q_{1\phi}'' = A_{1\phi}'' \text{St}_P \rho_l c_{pl} u_{l,P} (T_w - T_{l,P}), \tag{21}$$

where $A_{1\phi}''$ is the fraction of the wall unaffected by the nucleation sites, St_P is the Stanton number calculated from a heat transfer correlation in terms of the local liquid velocity and Prandtl number, T_w, is the wall temperature, and $T_{l,P}$ is the local liquid temperature near the heated wall. In numerical calculations, the local fluid properties are normally determined at the center of the near-wall computational cell. As long as a consistent turbulence model is used (see Section 2.2), the calculated single-phase heat flux component is independent of the distance between point-P and the wall, or, in other words, is grid-independent.

The evaporation heat flux is given by

$$q_e'' = \frac{\pi}{6} d_{\text{det}}^3 \rho_v f_{\text{det}} N'' h_{fg}, \tag{22}$$

where d_{det} is the critical bubble diameter at detachment, f_{det} is the frequency of nucleation, and N'' is the number of nucleation sites per unit area (nucleation site density).

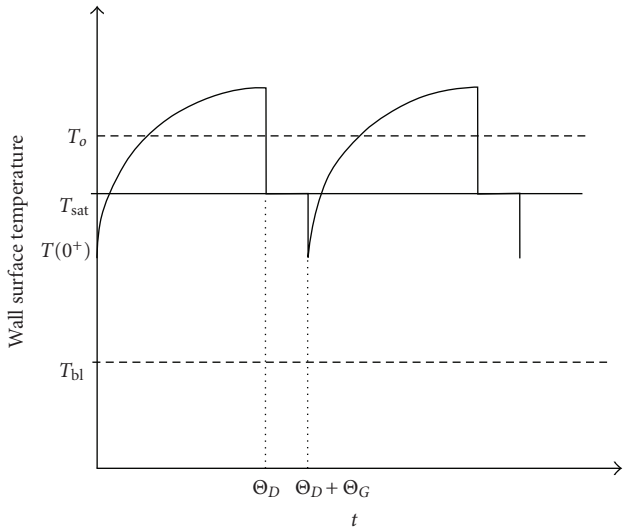

Figure 2: Surface temperature oscillations in the wall during the ebullition cycle.

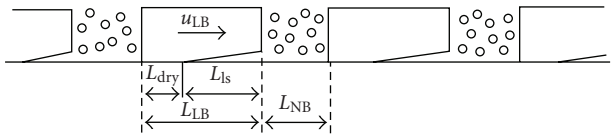

Figure 3: Phase distribution in the near-wall region.

The quenching heat flux has been analytically calculated by Del Valle and Kenning [5] as

$$q''_Q = \Theta_D f_{\text{det}} A''_{2\phi} \frac{2k_l(T_w - T_l)}{\sqrt{\pi \Theta_D k_l/(\rho_l c_{pl})}}, \tag{23}$$

where Θ_D is the waiting (or dwell) time elapsed between the detachment of a bubble and the nucleation of a subsequent one. The term $A''_{2\phi}$ is the fraction of the wall area participating in the quenching heat flux.

Additional relationships needed to close the model include the following [6].

(i) Bubble diameter at departure [7]

$$d_{\text{det}} = 0.0014 \cdot \text{Exp}\left(- \frac{\Delta T_{\text{sub}}}{45} \right), \tag{24}$$

where ΔT_{sub} is in °C, and d_{det} is in m. It is known that the liquid velocity has a significant effect on the bubble diameter at detachment.

(ii) Nucleation site density [8]

$$N'' = 185(T_w - T_l)^{1.805}. \tag{25}$$

Two very important terms in the model described above are the bubble waiting time and the nucleation frequency. A mechanistic approach to determine both parameters is described in Section 4 based on the analysis of the bubble ebullition cycle.

4. Bubble Ebullition Cycle

The mechanisms of nucleation at a cavity on a heated wall and the subsequent bubble growth have been investigated very extensively before. However, most existing results are normally given in the form of relationships between selected parameters, rather than as complete analytical models. It turns out that using a rigorous analytical approach to combine transient heat transfer solutions for the heated wall and for the liquid filling the space vacated by departing bubbles, a consistent model can be derived for bubble ebullition in forced convection-subcooled boiling. A schematic of the ebullition cycle is shown in Figure 2. The cycle consists of two major stages: the quenching period and the bubble growth period.

The quenching (or dwell) period is initiated when the subcooled liquid fills the space near the heated wall vacated by the departing bubble. During that time, the space inside a given cavity is gradually filled with vapor which eventually forms a hemispherical bubble on the top of the cavity. The quenching period is followed by a bubble growth period during which the bubble quickly expands forming a thin liquid sublayer separating the bubble from the heated surface. Since the liquid sublayer is very thin, the temperature drop across this layer is very small, so that the local wall temperature quickly drops to the saturated vapor temperature which itself only exceeds slightly the saturation temperature corresponding the system pressure.

Accounting to the periodic nature of the process, a closed-form solution can be obtained for the parameters characterizing the timing of bubble ebullition. The model is based on using coupled solutions to the transient heat conduction equations for the heated wall and the fluid laminar sublayer near the wall:

$$\frac{\partial T}{\partial t} = a\nabla^2 T, \tag{26}$$

where $a = k/\rho c_p$ is the thermal diffusivity of the respective material.

Since the characteristic time of surface temperature fluctuations during nucleation is very short and, thus, the distance across the wall affected by a change in the surface temperature is small compared to the size of the surface area exposed to quenching by cold water, the wall heat conduction can be approximated by a one-dimensional model. Using a steady-state as a reference, the time-dependent temperature distribution across the heated wall during the quenching period (i.e., between 0 and Θ_D in Figure 2) becomes [9]

$$T_w(y,t) = T_o + \frac{q''_H}{k_w} y + \frac{a_w}{2\sqrt{\pi}} \int_0^t \frac{y}{[a_w(t-t')]^{1.5}} \text{Exp}\left[- \frac{y^2}{4a_w(t-t')} \right] \times [T_i(t') - T_o]dt', \tag{27}$$

where $q''_H > 0$ is the constant heating rate per unit surface area of the heated wall, T_o is the average (constant) temperature

of the heated wall surface in contact with the fluid, and y is the distance across the heater away from the wetted surface.

Using (27), the following expression can be derived for the time-dependent surface heat flux during the quenching (dwell) period

$$q_w''(t) = -q_H'' + \frac{k_w}{\sqrt{\pi a_w}}\left\{\int_0^t \frac{dT_i}{dt'}\frac{dt'}{\sqrt{t-t'}} + \left[\frac{T_i(0^+) - T_o}{\sqrt{t}}\right]\right\}, \tag{28}$$

where $T_i(0^+)$ is the wall temperature at the beginning of the dwell period (the "+" superscript is used to indicate that a temperature discontinuity occurs at $t = 0$, as shown in Figure 2).

Since the near-wall space vacated by the departing bubble is immediately filled by subcooled liquid, the liquid temperature starts quickly increasing in contact with the heated wall. The time- and position-dependent liquid temperatures across the laminar boundary layer (where the effect of flow-driven convection is negligible) can be determined by solving the transient heat conduction equation, (26). Assuming that the liquid temperature outside the boundary layer is constant, $T_{\mathrm{bl}} = \text{constant}$, whereas the liquid temperature in contact with the heated wall is $T_i(t)$, yields the following expression:

$$T_l(y,t) = T_{\mathrm{bl}} + \frac{a_l}{2\sqrt{\pi}}\int_0^t \frac{y}{[a_l(t-t')]^{1.5}}\mathrm{Exp}\left[-\frac{y^2}{4a_l(t-t')}\right][T_i(t') - T_{\mathrm{bl}}]dt' \tag{29}$$

In a manner similar to that used for the wall, the following expression is obtained from (29) for the instantaneous time-dependent surface heat flux into the fluid:

$$q_w''(t) = -k_w\left.\frac{\partial T_w}{\partial y}\right|_{y=0} = -\frac{k_l}{\sqrt{\pi a_l}}\left\{\int_0^t \frac{dT_i}{dt'}\frac{dt'}{\sqrt{t-t'}} + \frac{T_i(0^+) - T_{\mathrm{bl}}}{\sqrt{t}}\right\}. \tag{30}$$

Combining (28) and (30) and taking the limit as $t \to 0^+$ yields the surface temperature at the beginning of the quenching (or dwell) period:

$$T_i(0^+) = \left(\frac{k_w T_o}{\sqrt{a_w}} + \frac{k_l T_{\mathrm{bl}}}{\sqrt{a_l}}\right)\left(\frac{k_w}{\sqrt{a_w}} + \frac{k_l}{\sqrt{a_l}}\right)^{-1}. \tag{31}$$

Substituting (31) back into the combined (28) and (30), one obtains

$$\int_0^t \frac{dT_i(t')}{dt'}\frac{dt'}{\sqrt{t-t'}} = \frac{q_H''}{k_w/\sqrt{\pi a_w} + k_l/\sqrt{\pi a_l}}. \tag{32}$$

Solving (32) for $T_i(t)$ with the initial condition $T_i(t) = T_i(0^+)$ yields

$$T_i(t) = T_i(0^+) + \frac{2q_H''}{\sqrt{\pi}\left(k_w/\sqrt{a_w} + k_l/\sqrt{a_l}\right)}\sqrt{t}. \tag{33}$$

Substituting (33) into (29) and rearranging yield the following expression for the instantaneous surface heat flux during the dwell period:

$$q_w''(t) = -k_l\left.\frac{\partial T_l}{\partial y}\right|_{y=0} = -k_l\frac{T_i(0^+) - T_{\mathrm{bl}}}{\sqrt{\pi a_l t}} - \frac{q_H''}{1 + (k_w/k_l)\sqrt{a_l/a_w}}. \tag{34}$$

4.1. Dwell Time Θ_D. The time of transition from the dwell period to the growth period is reached when the bubble radius becomes equal to the wall cavity radius. At this time instant, the steam temperature inside the hemispherical bubble outside the cavity must be equal to the temperature of the surrounding liquid at a distance from the wall equal to the cavity radius. Using the Clausius-Clapeyron equation to determine the steam superheat, and combining the resultant expression with (34), one arrives at the following relationship:

$$\frac{2q_H''/\sqrt{\pi}}{k_w/\sqrt{a_w} + k_l/\sqrt{a_l}}\sqrt{\Theta_D} - \frac{[T_i(0^+) - T_{\mathrm{bl}}]r_c}{\sqrt{\pi a_l \Theta_D}} + T_i(0^+) - T_{\mathrm{sat}} - \frac{q_H'' r_c/k_l}{1 + (k_w/k_l)\sqrt{a_l/a_w}} - \frac{2\sigma}{r_c}\frac{T_{\mathrm{sat}}\upsilon_{fg}}{h_{fg}} = 0, \tag{35}$$

where r_c is the cavity radius and σ is the surface tension.

As can be seen, for given fluid and wall properties and thermal conditions, (35) becomes an algebraic (quadratic) equation for the bubble dwell time, Θ_D.

Interestingly, if the dwell time is known, (35) can be used to determine the average surface heat flux during the quenching period. Specifically, integrating (34) from 0 to Θ_D yields

$$|\overline{q}_D''| = \frac{2k_l[T_i(0^+) - T_{\mathrm{bl}}]}{\sqrt{\pi a_l \Theta_D}} + \frac{q_H''}{1 + (k_w/k_l)\sqrt{a_l/a_w}}. \tag{36}$$

4.2. Growth Time Θ_G. As soon as the bubble starts growing outside the cavity, the vapor is produced mainly from the evaporating liquid sublayer between the wall and the bubble. Since the temperature drop across the thin sublayer is very small, the local surface temperature during this period remains close to the saturation temperature. The energy balance for the growing bubble can be written as

$$\frac{\rho_g h_{fg}}{2}\frac{d(d_B)}{dt} = |q_w''(t)|. \tag{37}$$

The time-dependent wall heat flux during the bubble growth time can be obtained from (28) by noticing that during this period, that is, for $\Theta_D < t < \Theta_D + \Theta_G$, the wall temperature remains approximately constant and equal to the saturation temperature:

$$q_w''(t) = -q_H'' - k_w\frac{T_i(\Theta_D) - T_{\mathrm{sat}}}{\sqrt{\pi a_w(t - \Theta_D)}}. \tag{38}$$

Substituting (38) into (37) and integrating between Θ_D and $\Theta_D+\Theta_G$ yield the following expression for the maximum bubble diameter at detachment:

$$d_{\text{det}} = \frac{2}{\rho_v h_{fg}} \int_{\Theta_D}^{\Theta_D+\Theta_G} |\, q_w''(t)\,|\, dt = \frac{2}{\rho_v h_{fg}} \left[q_H'' \Theta_G + 2k_w \frac{T_i(\Theta_D) - T_{\text{sat}}}{\sqrt{\pi a_w}} \sqrt{\Theta_G} \right], \tag{39}$$

where (see (33))

$$T_i(\Theta_D) = T_i(0^+) + \frac{2q_H''/\sqrt{\pi}}{k_w/\sqrt{a_w} + k_l/\sqrt{a_l}} \sqrt{\Theta_D}. \tag{40}$$

The bubble diameter at detachment can be evaluated using one of several different models that have been developed to date. In particular, using the force balance for a single bubble, Staub [10] developed the following expression:

$$d_{\text{det}} = 0.5 \left\{ \sqrt{\left[\frac{3\tau_w}{2(\rho_l - \rho_v)g} \right]^2 + \frac{3\sigma F(\beta_c)}{(\rho_l - \rho_v)g}} - \frac{3\tau_w}{2(\rho_l - \rho_v)g} \right\}, \tag{41}$$

where τ_w is the wall shear stress and $F(\beta_c)$ is an experimentally determined function of the contact angle.

For given bubble diameter at detachment and bubble dwell time, (39) can be readily solved for the bubble growth time Θ_G.

Interestingly, if the bubble growth time is known, (39) can be used again, this time to determine the average wall heat flux during the bubble growth period:

$$|\, \overline{q}_G''\,| = \frac{1}{\Theta_G} \int_{\Theta_D}^{\Theta_D+\Theta_G} |\, q_w''(t)\,|\, dt = q_H'' + 2k_w \frac{T_i(\Theta_D) - T_{\text{sat}}}{\sqrt{\pi a_w \Theta_G}}. \tag{42}$$

Finally, the bubble frequency of detachment and the total detachment time can be obtained from

$$f_{\text{det}} = \frac{1}{\Theta_{\text{det}}} = \frac{1}{\Theta_D + \Theta_G}. \tag{43}$$

Naturally, summing up (34) and (42) yields

$$|\, \overline{q}_D''\,| + |\, \overline{q}_G''\,| = q_H'', \tag{44}$$

where q_H'' is the surface heat flux of the heater (see (27)).

5. Wall Temperature Excursion (CHF)

5.1. Physical Concept. The wall temperature excursion (or CHF) in low-quality boiling is associated with the ability of the bubbles formed at the nucleation sites to depart from the wall, so that the vacated space can be filled with fresh liquid, so that the quenching and bubble growth processes can continue [9, 11]. Thus, two conditions must be satisfied simultaneously to avoid wall temperature excursion, one concerned with dispersed bubble concentration in the near-wall region, the other with the velocity at which the bubble departs from the wall to make room for the next generation bubble formed at the same nucleation site. Since the size of bubbles departing from the nucleation sites is normally very small (of the order of 1 mm or less), their shape is nearly spherical. Thus, the two conditions mentioned above can be formulated as follows.

(1) The bubble maximum void fraction of dispersed bubbles in the near-wall region cannot exceed the maximum packing factor for spherical particles, the theoretical value of which (obtained from geometrical considerations) is

$$\alpha \le \alpha_{\max} = \frac{\pi}{3\sqrt{2}} \approx 0.74. \tag{45}$$

(2) Taking into account that to form a new undeformed bubble at a given cavity at the time of detachment, the distance between the previously formed bubble at the same cavity and the heated wall at the same time instant must be at least equal to the bubble diameter, the maximum evaporation heat flux to avoid temperature excursion must satisfy the following condition:

$$\frac{q_e''}{h_{fg}} = \frac{\pi}{6} d_{\text{det}}^3 \rho_v f_{\text{det}} N'' \le \rho_v u_{\text{det,min}} \alpha, \tag{46}$$

where

$$u_{\text{det,min}} = m d_{\text{det}} f_{\text{det}}. \tag{47}$$

The coefficient, $m \ge 1$, reflects the fact that in reality the axial motion of bubbles may require a distance from the wall larger than one bubble diameter to avoid the coalescence with other bubbles formed in the adjacent upstream cavities.

It is interesting to notice that (46) can be rewritten as

$$\frac{\pi}{6} d_{\text{det}}^2 N'' \le m\alpha. \tag{48}$$

5.2. Near-Wall Heat Transfer in the Presence of Elongated Bubbles. A schematic illustrating the near-wall conditions in the presence of elongated bubbles is shown in Figure 3. It follows from the previous discussion that at any axial location along the channel the time-dependent wall temperature fluctuates periodically, increasing in the poor heat transfer (elongated bubble) region and decreasing, where heat transfer is more efficient (in the nucleate boiling region).

According to Figure 3, averaging the local wall heat flux over both regions always yields the given constant heating rate of the heater per unit surface area. In particular, the overall average heat flux can be partitioned into the following terms:

$$q_H'' = q_{v_1}'' + q_{v_2}''. \tag{49}$$

In (49), q_{v_1}'' is the nucleate boiling component corresponding to small dispersed bubbles:

$$q_{v_1}'' = q_{\text{NB}}'' A_{v_1}'', \tag{50}$$

where q_{NB}'' is given by (20), and A_{v_1}'' is the area density (wall area fraction) for the small bubble region.

Table 1: Predicted bubble diameter at detachment.

d_{det} [mm] (23)	d_{det} [mm] Current model at $p = 5$ MPa	d_{det} [mm] Current model at $p = 7$ MPa	d_{det} [mm] Current model at $p = 10$ MPa
1.1	1.16	1.02	0.68

The heat flux component corresponding to elongated bubbles, q''_{v_2}, is given by[9, 11]

$$q''_{v_2} = q''_{\text{ls}} A''_{\text{LB}} \frac{L_{\text{ls}}}{L_{\text{LB}}} + q''_{\text{dry}} A''_{\text{LB}} \left(1 - \frac{L_{\text{ls}}}{L_{\text{LB}}}\right), \tag{51}$$

where A''_{LB} is the wall area density for elongated bubbles, L_{ls} is the length of the liquid sublayer underneath an elongated bubble, q''_{ls} is the corresponding average heat flux across the liquid layer, and q''_{dry} is the heat transfer rate per unit wall in the dry region.

The length of large bubbles has been measured by Gersey and Mudawar [12] and found to agree very well with the critical wavelength of the Helmholtz instability vapor/liquid interface. This length can be calculated from

$$L_{\text{LB}} = \frac{2\pi\sigma}{\rho_l (v_v - v_l)^2} \left(1 + \frac{\rho_l}{\rho_v}\right). \tag{52}$$

Another parameter characterizing elongated bubbles is their distance from the wall. Assuming that the initial distance (at the tip of the bubbles) corresponds to the viscous sublayer thickness [13], we obtain

$$L_{\text{LB}} = 10 v_l \sqrt{\frac{\rho_l}{\tau_w}}, \tag{53}$$

where τ_w is the wall shear stress.

5.3. Wall Temperature Excursion Criterion. It can be readily noticed that as the total wall heat flux increases, the elongated bubble area density will also increase and so will the dry region under the elongated bubbles. Consequently, the local heat flux in the elongated bubble region, q''_{v_2}, will go down and that in the dispersed bubble region, q''_{v_1}, will go up. With the corresponding area density decreasing, nucleate boiling in the region between elongated bubbles will intensify, eventually leading to a situation when replenishment of the near-wall region with liquid will be no longer possible. As a result, a sudden wall temperature excursion will occur. The critical condition beyond which small bubbles cannot be removed away from the wall and replaced by fresh liquid can be written as

$$\frac{\pi}{6} d^2_{\text{det}} N'' \le m\alpha_{\text{NB}} = m \frac{\alpha_{v_1}}{A''_{v_1}}, \tag{54}$$

where α_{NB} is the volumetric fraction of dispersed bubbles in the nucleate boiling region and α_{v_1} is the local near-wall volume fraction (per unit volume of the channel) of the dispersed bubbles.

Naturally, the local near-wall void fraction is the sum of the partial vapor volume fractions of the dispersed bubbles and the elongated bubbles:

$$\alpha = \alpha_{v_1} + \alpha_{v_2}. \tag{55}$$

Table 2: Predicted nucleation frequency.

Pressure [MPa]	$f_{\text{det}}\sqrt{d_{\text{det}}}$ [m$^{1/2}$/s] Ceumern-Lindenstjerna [12]	$f_{\text{det}}\sqrt{d_{\text{det}}}$ [m$^{1/2}$/s] Current model
5	3.67	3.62
7	3.54	3.24
10	3.47	2.67

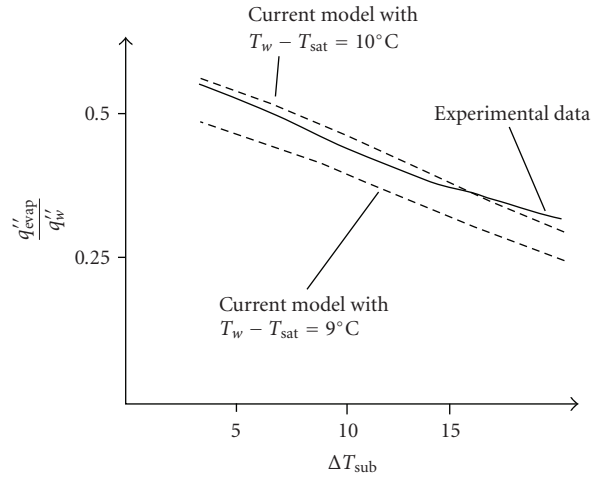

Figure 4: A comparison between the predicted and experimental evaporation heat flux [14].

6. Model Testing and Validation

6.1. Nucleate Boiling. The theoretical model of bubble ebullition discussed in Sections 3 and 4 was used to evaluate various parameters characterizing nucleate boiling, and compare the result of predictions against the results of measurements. Typical results are shown in Tables 1 and 2 and in Figure 4.

The predictions for the bubble diameter at departure and the nucleation frequency are shown in Tables 1 and 2. First, the predicted bubble diameter has been compared against the expression given by (24), obtained for a liquid velocity of 0.2 m/s. The calculations using the present models have been performed for a wall heat flux of $q''_w = 4.73 \cdot 10^3$ kW/m^2, a subcooling of 10°C, and three different pressures. The results are shown in Table 1 [9].

As can be seen, whereas the predicted bubble diameter at detachment compares well against the simple correlation of Tolubinsky and Kostanchuk [7], the current model also allows for quantifying the effect of system pressure (and other parameters, such as velocity) which is ignored in the expression given by (24).

Next, the calculated bubble departure frequency was compared against the correlation of Ceumern-Lindenstjerna [15]. The calculations were performed for $q''_w = 1.4 \cdot 10^3$ kW/m^2. The results forthree different pressures are shown in Table 2.

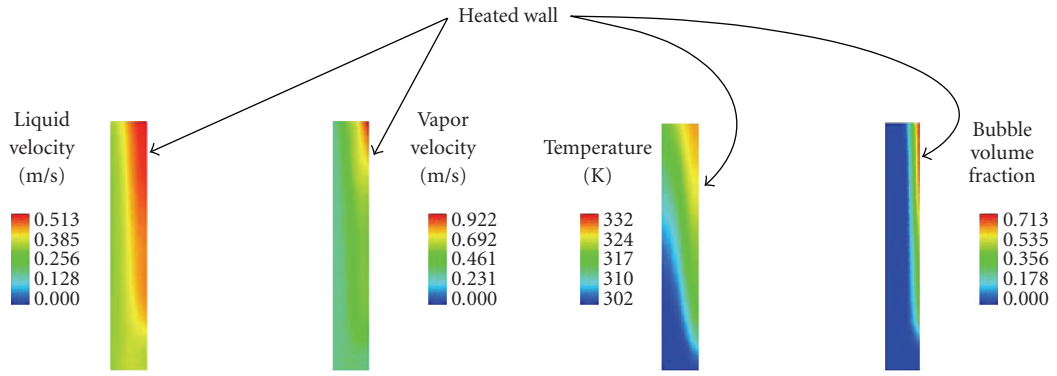

FIGURE 5: Color contours of the calculated phasic velocities, temperature, and void fraction in subcooled boiling: mass flux = 512 kg/m^{2}s, heat flux = 241 kW/m^2, inlet subcooling = 30 K.

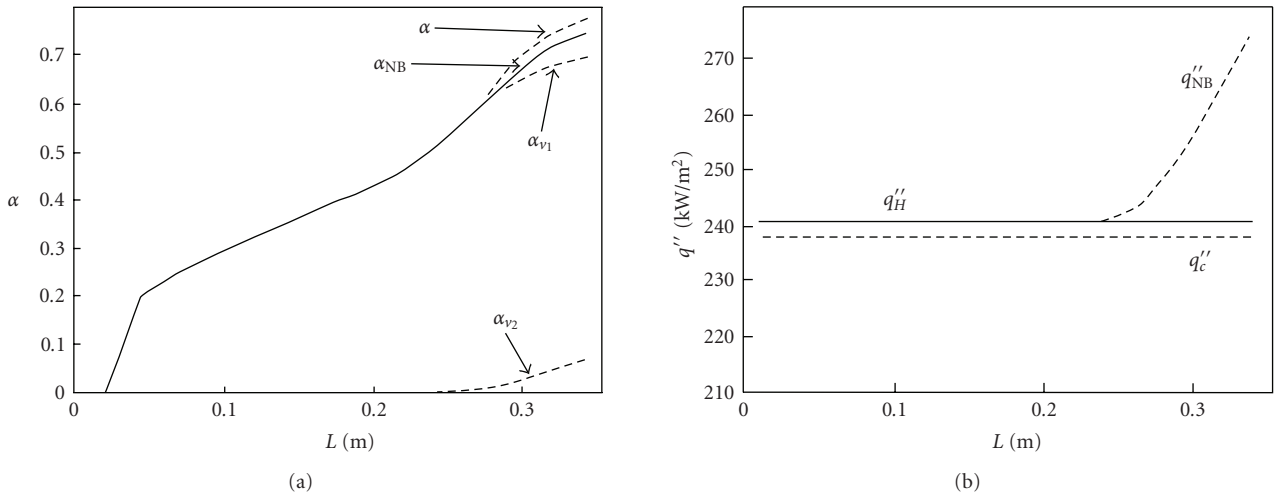

FIGURE 6: Axial distributions of near-wall channel parameters for the conditions shown in Figure 5: (a) the concentrations of small bubbles and elongated bubbles, (b) a comparison between the heat transfer removal rate in the elongated bubble region, average wall heat flux, and critical heat flux.

The predicted evaporation heat flux in a boiling channel used by Bartolomei and Chanturia [13] is shown in Figure 4. In this comparison, the nucleation sites density was obtained from the expression proposed by Lemmert and Chawla [8] (see (25)). The measured wall superheat was about 9.5°C but changed slightly along the channel. In order to account for the uncertainties in the wall temperature measurements, the results for two fixed values are shown in Figure 4. As can be seen, a very good agreement has been obtained, especially for liquid subcooling between 5°C and 15°C.

It can be noticed that the current model is capable of quantifying the effect of various physical parameters which are normally not accounted for when a phenomenological approach, based solely on correlating experimental data, is used.

6.2. Temperature Excursion. To perform predictions of the temperature excursion, the three-dimensional three-field model of two-phase flow discussed in Section 2 has been combined with both models discussed in Sections 3–5. The calculations have been performed for the experimental conditions of Hino and Ueda [16], in which R113 was used at a pressure of 147 kPa. The heated test section was 0.357 m long and 0.018 m ID tube, with a centrally located heated rod, 0.008 m diameter. The outer tube wall was insulated, and there was an unheated section installed upstream of the annulus-shaped heated section, allowing the flow to reach fully developed conditions at the entrance to the heater.

Typical radial and axial distributions of various local flow parameters are shown in Figure 5. The axial distributions of the near-wall concentrations of both small bubbles and elongated bubbles are shown in Figure 6. As it can be seen, the rate of bubble concentration increase in the dispersed-bubble region accelerates as the elongated bubbles start being formed. This is due to a dramatic reduction inthe heat transfer removal rate in the elongated bubble region, which in turn increases the local heat flux in the nucleate-boiling region. As it can be seen in Figure 6, whereas the average wall heat flux is fixed at a level of 241 kW/m^2, the nucleate boiling heat flux experiences a dramatic growth as the

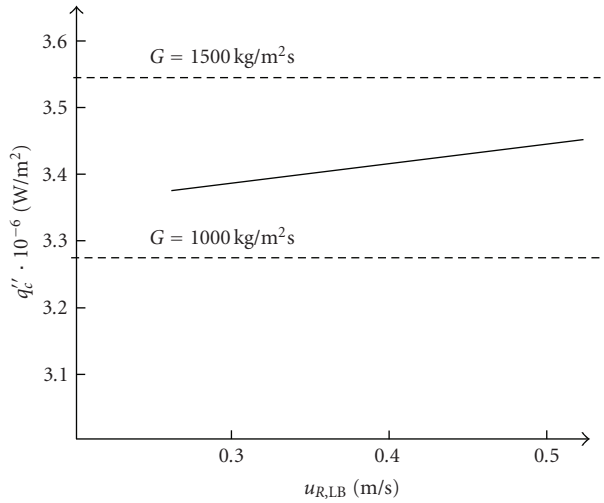

Figure 7: Typical calculated values of critical heat flux, compared against experimental data for subcooled and low-quality boiling of water at 4.5 MPa [17].

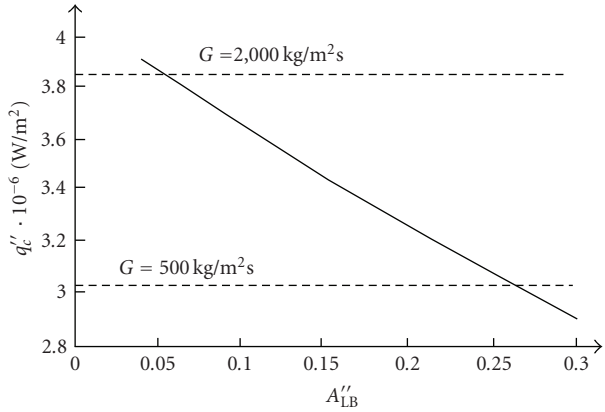

Figure 8: Typical calculated values of critical heat flux, compared against experimental data for subcooled and low-quality boiling of water at 4.5 MPa [17].

concentration of elongated bubbles stars increasing. Indeed, due to the combined effects of increasing evaporation rate and increasing fraction of the wall area occupied by elongated bubbles, the local void fraction approached the value, $\alpha = 0.75$, which already exceeded the limit given by (44). This, in turn, stopped the wall replenishment by liquid phase and caused a sudden temperature excursion. Thus, one concludes that the assumed wall heat flux was just beyond the onset of CHF. Converting the difference between the actual volume fraction value of 0.75 and the critical value of 0.74 into the corresponding power level difference yields the critical heat flux (CHF) of about 238 kW/m^2. Since the uniform heat flux of the heater used in the calculations (241 kW/m^2) corresponded to the experimental onset of temperature excursion, the estimated prediction error in the present case was less than 2%. Similar calculations performed for other conditions produced errors of the order of ±15%.

Figures 7 and 8 show the calculated CHF for various flow conditions, in comparison with typical data based on experimental correlations. The predicted critical heat flux is within the range of the measured values for heated channels operating at subcooled boiling or low-quality boiling conditions. What is particularly important is that the predicted trends in the critical heat flux agree well with the existing experimental evidence. Specifically, q_c'' gradually decreases with increasing velocity (and, thus, flow rate) and decreases with increasing vapor concentration (flow quality).

7. Conclusions

Several aspects of mechanistic multidimensional modeling and computer simulations of two-phase flows and boiling heat transfer have been discussed. The specific models included the mechanisms of local-subcooled boiling heat transfer in forced convection flows, a mechanistic approach to bubble ebullition cycle, and criteria for temperature excursion (CHF) in low-quality flows.

The results of model testing indicate that the proposed physical mechanisms are consistent with the existing experimental evidence regarding the phaseand temperature distributions, and wall temperature excursion. The current approach is particularly suitable for implementation in general CFD computational models using a multifield concept of two-phase flow.

References

[1] M. Z. Podowski, "On the mechanistic modeling of interfacial phenomena in gas/liquid two-phase flows," in *Proceedings of the 6th International Conference on Multiphase Flow (ICMF '07)*, Leipzig, Germany, July 2007.

[2] B. E. Launder and D. B. Spalding, "The numerical computation of turbulent flows," *Computer Methods in Applied Mechanics and Engineering*, vol. 3, no. 2, pp. 269–289, 1974.

[3] Y. Sato, M. Sadatomi, and K. Sekoguchi, "Momentum and heat transfer in two-phase bubble flow—I. Theory," *International Journal of Multiphase Flow*, vol. 7, no. 2, pp. 167–177, 1981.

[4] N. Kurul and M. Z. Podowski, "On the modeling of multidimensional effects in boiling channels," in *Proceedings of the 27th National Heat Transfer Conference*, Minneapolis, Minn, USA, July 1991.

[5] V. H. Del Valle and D. B. R. Kenning, "Subcooled flow boiling at high heat flux," *International Journal of Heat and Mass Transfer*, vol. 28, no. 10, pp. 1907–1920, 1985.

[6] A. Alajbegovic, N. Kurul, M. Z. Podowski, D. Drew, and R. T. Lahey Jr., "A new mechanistic model of critical heat flux in forced-convection subcooled boiling," in *Proceedings of the 8th International Topical Meeting on Nuclear Reactor Thermal-Hydraulics (NURETH-8)*, pp. 973–980, Kyoto, Japan, September-October 1997.

[7] V. I. Tolubinsky and D. M. Kostanchuk, "Vapour bubbles growth rate and heat transfer intensity at subcooled water boiling," in *Proceedings of the 4th International Heat Transfer Conference*, vol. 5, Paris, France, August 1970, paper no. B-2.8.

[8] M. Lemmert and L. M. Chawla, "Influence of flow velocity on surface boiling heat transfer coefficient," in *Heat Transfer in Boiling*, E. Hahne and U. Grigull, Eds., Academic Press and Hemisphere, New York, NY, USA, 1977.

[9] R. M. Podowski, D. A. Drew, R. T. Lahey Jr., and M. Z. Podowski, "A mechanistic model of the ebullition cycle in forced-convection subcooled boiling," in *Proceedings of the 8th International Topical Meeting on Nuclear Reactor Thermal Hydraulics (NURETH-8)*, vol. 3, pp. 1530–1537, Kyoto, Japan, September-October 1997.

[10] F. W. Staub, "The void fraction in subcooled boiling: prediction of the initial point of net vapor generation," *Journal of Heat Transfer*, vol. 90, pp. 151–157, 1968.

[11] M. Z. Podowski and S. P. Antal, "CFD predictions of temperature excursion (CHF) in low-quality boiling in heated channels," in *Proceedings of the 12th International Heat Transfer Conference*, Grenoble, France, August 2002.

[12] C. O. Gersey and I. Mudawar, "Effects of heater length and orientation on the trigger mechanism for near-saturated flow boiling critical heat flux—I. Photographic study and statistical characterization of the near-wall interfacial features," *International Journal of Heat and Mass Transfer*, vol. 38, no. 4, pp. 629–641, 1995.

[13] E. Moursali, J. L. Marié, and J. Bataille, "An upward turbulent bubbly boundary layer along a vertical flat plate," *International Journal of Multiphase Flow*, vol. 21, no. 1, pp. 107–117, 1995.

[14] G. G. Bartolomei and V. M. Chanturia, "Experimental study of true void fraction when boiling subcooled water in vertical tubes," *Thermal Engineering*, vol. 14, pp. 123–128, 1967.

[15] W.-C. B. Ceumern-Lindenstjerna, "Bubble departure diameter and release frequencies during nucleate pool boiling of water and aqueous NaCl solution," in *Heat Transfer in Boiling*, E. Hahne and U. Grigull, Eds., Academic Press and Hemisphere, New York, NY, USA, 1977.

[16] R. Hino and T. Ueda, "Studies on heat transfer and flow characteristics in subcooled flow boiling—part 2: flow characteristics," *International Journal of Multiphase Flow*, vol. 11, no. 3, pp. 283–297, 1985.

[17] E. Janssen and S. Levy, "Burnout limit curves for boiling water reactors," Tech. Rep. APED-3892, General Electric, San Jose, Calif, USA, 1962.

Hindawi Publishing Corporation
Science and Technology of Nuclear Installations
Volume 2009, Article ID 583259, 13 pages
doi:10.1155/2009/583259

Project Report

An Overview of the Pressurized Thermal Shock Issue in the Context of the NURESIM Project

D. Lucas,[1] D. Bestion,[2] E. Bodèle,[1] P. Coste,[2] M. Scheuerer,[3] F. D'Auria,[4] D. Mazzini,[4] B. Smith,[5] I. Tiselj,[6] A. Martin,[7] D. Lakehal,[8] J.-M. Seynhaeve,[9] R. Kyrki-Rajamäki,[10] M. Ilvonen,[11] and J. Macek[12]

[1]*Forschungszentrum Dresden-Rossendorf, e.V. (FZD), Institute of Safety Reseach, P.O. Box 510 199, 01454 Dresden, Germany*
[2]*Commissariat à l'Énergie Atomique (CEA), Centre d'Études Nucléaires de Grenoble, 17 Rue des Martyrs, 38054 Grenoble, France*
[3]*Gesellschaft für Anlagen- und Reaktorsicherheit mbH(GRS), 85748 Garching, Germany*
[4]*Dipartmento di Ingengeria Meccanica, Nucleare e della produzione, Università di Pisa, Via Diotisalvi 2, 56126 Pisa, Italy*
[5]*Paul Scherrer Institute, 5232 Villigen-PSI, Switzerland*
[6]*Jožef Stefan Institute (JSI), 1000 Ljubljana, Slovenia*
[7]*Fluid Dynamics Power Generation Department, Recherche et Développement, Électricité de France (EDF), 6 quai Watier, 78400 Chatou, France*
[8]*ASCOMP GmbH, Technoparkstrass 1, 8005 Zurich, Switzerland*
[9]*Université Catholique de Louvain La Neuve (UCL), Place du levant.2, 1348 Louvain-La-Neuve, Belgium*
[10]*Lappeenranta University of Technology (LUT), Skinnarilankatu 34, 53851 Lappeenranta, Finland*
[11]*VTT Industrial Systems, PL 1000, 02044 VTT, Finland*
[12]*Nuclear Research Institute Rez plc (NRI), Husinec-Rez 130, 25068 Rez, Czech Republic*

Correspondence should be addressed to D. Lucas, d.lucas@fzd.de

Received 14 January 2008; Accepted 21 February 2008

Recommended by Yassin Hassan

Within the European Integrated Project NURESIM, the simulation of PTS is investigated. Some accident scenarios for Pressurized Water Reactors may cause Emergency Core Coolant injection into the cold leg leading to PTS situations. They imply the formation of temperature gradients in the thick vessel walls with consequent localized stresses and the potential for propagation of possible flaws present in the material. This paper focuses on two-phase conditions that are potentially at the origin of PTS. It summarizes recent advances in the understanding of the two-phase phenomena occurring within the geometric region of the nuclear reactor,that is, the cold leg and the downcomer, where the "PTS fluid-dynamics" is relevant. Available experimental data for validation of two-phase CFD simulation tools are reviewed and the capabilities of such tools to capture each basic phenomenon are discussed. Key conclusions show that several two-phase flow subphenomena are involved and can individually be simulated at least at a qualitative level, but the capability to simulate their interaction and the overall system performance is still limited. In the near term, one may envisage a simplified treatment of two-phase PTS transients by neglecting some effects which are not yet well controlled, leading to slightly conservative predictions.

1. Introduction

Pressurized thermal shock (PTS) in general denotes the occurrence of thermal loads on the reactor pressure vessel (RPV) under pressurized conditions. PTS was identified by the European project EUROFASTNET as one of the most important industrial needs related to nuclear reactor safety since the integrity of the RPV has to be assured throughout the reactor lifetime; it is one of the barriers against fission product release, and its replacement is not feasible. A very severe PTS scenario is cold water emergency core cooling (ECC) injection into the cold leg during a hypothetical small-break loss of coolant accident (SB-LOCA).The injected water mixes with the hot fluid present in the cold leg, and the mixture flows towards the downcomer where further mixing with the ambient fluid takes place (see Figure 1). High

thermal gradients may occur in the structural components while the primary circuit pressurisation is partially preserved. Therefore, the transient fluid temperature must be reliably assessed to predict the loads upon the RPV and the pressure wall toughness. The cooling fluid can either be in single-phase or in two-phase condition, depending on the leak size, its location, and on the operating conditions of the nuclear power plant considered. The PTS has been the objective of a number of international cooperative programmes in the past, for example, the OECD-ICAS as given by [1].

PTS-scenarios were considered in the NURESIM project for the French 900 MW CPY PWR, the German 1300 MW Konvoi reactor, the Loviisa 500 MW VVER, and the Russian VVER-1000. Typical diameters of the cold leg are between 700 mm and 850 mm while the sizes of the ECC injection nozzle vary between 170 mm and 225 mm. Loss of coolant accident (LOCA) scenarios, with different leak sizes and leak locations, are considered as initial events leading to ECC injection, which can create PTS situations. For all the scenarios, there is a high-pressure injection (HPI) into the cold leg. For some of the scenarios, the pressure can be stabilized to remain within single-phase flow conditions in the cold leg. However, for all reactor concepts, there are also scenarios that lead to two-phase flow situations in the cold leg. Injection from the hydroaccumulators needs to be considered in addition to the HPI. While the accumulators are connected to the cold leg for some PWR, the accumulators inject the cooling water into the downcomer and into the upper plenum in case of the VVER reactors. In the two-phase flow scenario, the cold leg is either partially uncovered or totally uncovered. Both situations have to be covered by two-phase flow simulations; in particular, stratified flow with a void fraction range from 0 to 100% needs to be considered for a partially filled cold leg.

In all the two-phase flow scenarios, the pressure is below 7.5 MPa. The liquid flow rates in the cold leg at the exit of the pumps are close to zero but may have fluctuations in the range from −100 kg/s to +100 kg/s. Maximum steam flow rates in the considered scenarios are up to 50 kg/s in case of a steam flow from the downcomer towards the steam generator and up to 15 kg/s for a flow from the steam generator towards the downcomer. Mass flow rates from the HPI are limited to a maximum value of 80 kg/s, while the temperatures are in the range between 283°C and 298°C. The maximum accumulator flow rates for the reactor designs with an injection into the cold leg are up to 30 kg/s. The temperature of the injected water is between 25°C and 60°C.

The PTS work package within the frame of the NURESIM Integrated project of the 6th Framework Programme focuses on a two-phase flow configuration resulting from a partially or fully uncovered cold leg. In the case of a partially uncovered cold leg, a stratification of cold water on the bottom of the cold leg with counter-current flow of hot water and steam on top of this cold-water layer may occur (see Figure 1). There is a mixing between hot and cold water. Condensation takes place at the free surfaces of the cooling water jet and of the stratified flow. The process is strongly dependent on the turbulence in the fluids. If the water level in the downcomer has dropped below the cold leg nozzle, cold water is injected into vapor with direct contact condensation on the steam-water interface and heating along walls of both the cold leg and the downcomer. Stripe cooling will occur in the downcomer. Direct contact condensation (DCC) is of prime importance in this situation since it is the main heat source for the cold water. Interfacial transfers (momentum—including turbulence—mass and energy) have then to be considered in the jet area as well as in the stratified flow.

As shown in Figure 1, different flow phenomena occur. There are flows with separated surfaces (jet interface, horizontal interface), but also dispersed flows occur due to bubble entrainment (at jet impingement and possibly also in the horizontal flow region by entrainment caused by waves). Since there is a strong thermal nonequilibrium at these interfaces, momentum transfer as well as heat and mass transfer have to be considered. The various two-phase phenomena taking place are strongly coupled, both within the fluids and in regard to the heat transfer to walls. The different phenomena depend on very different characteristic length-scales, from the size of the smallest eddy up to the system scale. Some of the involved phenomena are not yet well understood regarding their physics. The simulations of the whole system during the ECC injection process and then accurate reproduction of the thermal loads on the RPV are thus a considerable challenge.

In detail, the following "geometrical" flow regions or flow patterns connected with the listed single phenomena can be distinguished for the two-phase PTS situation (e.g., [2], see also Figure 1).

(i) Free liquid jet:
   (a) momentum transfer at the jet interface, including instabilities,
   (b) splitting of the jet,
   (c) condensation on the jet surface.

(ii) Zone of the impinging jet:
   (a) surface deformation by the jet including generation of waves,
   (b) steam bubble entrainment,
   (c) bubble migration and de-entrainment,
   (d) turbulence production below the jet.

(iii) Zone of horizontal flow:
   (a) momentum exchange at the gas-liquid interface, including generation of waves and growth or damping of these waves,
   (b) heat and mass transfer (condensation) at the gas-liquid interface including its influence on the momentum transfer,
   (c) heat transfer to the walls,
   (d) turbulence production at the interface,
   (e) turbulence production at the walls,
   (f) influence of the phase change on turbulence and on wave pattern,
   (g) mixing/stratification of hot and cold water streams.

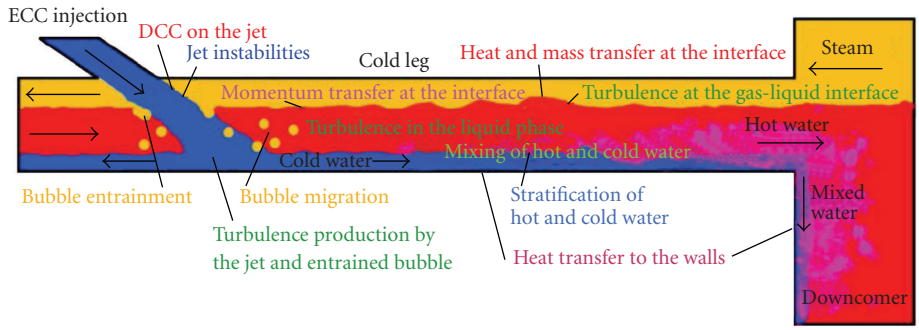

Figure 1: Most important flow phenomena during a PTS situation with partially filled cold leg.

(iv) Flow in the downcomer in the case of a partially filled cold leg:

  (a) turbulence production at the walls,
  (b) mixing/stratification of hot and cold water,
  (c) heat transfer to the walls.

(v) Flow in the downcomer in the case of the water level being below the cold leg nozzle:

  (a) separation of the incoming water jet from the downcomer wall or not,
  (b) momentum transfer at the jet interface, including instabilities,
  (c) splitting of the jet,
  (d) phase change at the jet surface,
  (e) heat transfer to the walls.

There are strong interactions between the listed flow regions and related flow patterns. The effect of noncondensable gases has to be considered due to nitrogen degassing from ECCS water.

It is not possible to reproduce experimentally in full scale, the whole ECC injection process, starting from the injection location to the inner downcomer, considering the various two-phase flow regimes. Reliable numerical simulations are required, and two-phase PTS constitutes one of the most challenging exercises for a computational fluid dynamics (CFD) simulation. Improvements of the two-phase modelling capabilities have to be undertaken to qualify the codes for the simulation of such flows. A really accurate simulation of all the phenomena that occur in the scenario will only be possible in the far future. To reach this aim, it is necessary to go step-by-step and to improve the quality of the forecasts. However, the use of CFD in industrial studies related to PTS is already possible, but with some limitations.

The main goal of the NURESIM project is the development of a common European multiscale and multidisciplinary platform for NUclear REactor SIMulation (NURESIM). During the current NURESIM project, the simulation of PTS, including DCC scenarios, should be enhanced beyond the current state of the art by improving substantially the two-phase flow modelling capabilities of current CFD-codes. The Neptune_CFD (see [3, 4]) code is used as the initial framework for the common platform, and both the CFX and FLUENT CFD tools are also used for PTS investigations.

Within the above framework, the objective of the paper is on the one hand to provide a critical evaluation on the present status in the simulation of thermal-hydraulic aspects of PTS and on the other hand to show how the NURESIM project uses available experimental data for improving and validating the models. A detailed presentation of scenarios leading to two-phase PTS situations as well as a discussion on the status of CFD capabilities for PTS at the beginning of the NURESIM was given by Lucas [5].

2. Experimental Data Basis

CFD methods use many turbulence and two-phase flow models which have a certain degree of empiricism. The accuracy and universal validity of these models have to be assessed by comparison of the numerical results with experimental data. Depending on the suitability of the data, test cases are used for validation and calibration of statistical models and for demonstration of model capabilities.

2.1. Validation Experiments. Validation cases focus on separate effects as they test different aspects of a CFD code and its physical models. The successful simulation of the single separated effects is a prerequisite for a complex industrial PTS flow simulation. In a validation test, the quality of the statistical model is checked for a given flow situation. Validation tests are the only method to minimize and quantify modelling errors and to ensure that new models are applicable with confidence to certain types of flows. In an ideal case, a validation test case gives sufficient details to allow for an improvement of the physical models. In NURESIM, validation data are also obtained from direct numerical simulation (DNS) studies.

In the NURESIM database [6], test cases were selected which clearly identify the main features of the CFD models that are to be tested and which are dominant in the validation case. In order to ensure completeness of information, all experiments are described according to the following template:

(i) general description and flow features,

(ii) description of measurements and geometry,

(iii) detailed information on boundary and initial conditions,

(iv) availability of experimental data,

(v) information on previous work and related experiments.

Next to the completeness of the data, their quality is of primary importance for a successful validation exercise. The quality of the data is mainly evaluated by error bounds provided by the experimentalists. Unfortunately, most experiments still do not provide this information. Moreover, even if error estimates are available, they cannot exclude systematic errors by the experimentalist. In addition to error bounds, it is therefore desirable to have an overlap of experimental data, which allow for testing of the consistency of the measurements. To this end, experiments have been gathered investigating the same or similar PTS phenomena but performed by different experimental groups in different facilities using different experimental techniques.

Experiments investigating jet impingement on a free surface and bubble entrainment were performed by Bonetto and Lahey [7] and Iguchi [8] as follows.

(i) The Bonetto and Lahey experiment investigates jet impingement on a free surface using an axisymmetric, turbulent jet impinging orthogonally on a free surface. The flow was statistically steady-state; the fluid was water in an air environment. A laser Doppler anemometer (LDA) system was used to measure the liquid gas velocities (both mean and fluctuations), and both a fiber phase-Doppler anemometer (FPDA) and an impedance probe were used to measure the void fraction, depending on the bubble size created by the impinging jet. The void fraction was measured at varying depths below the undisturbed surface.

(ii) A turbulent nonfragmented water jet impinging on a free surface in air environment was investigated by Iguchi et al. [8] at the University of Hokkaido. LDA was used to measure mean velocities and RMS values of the vertical and radial velocity below the free surface. However, no measurements of bubble entrainment were made.

Air water flows in horizontal channels were investigated at Forschungszentrum Dresden-Rossendorf (FZD) by Vallée et al. [9] and at INP Toulouse by Fabre et al. [10]:

(i) A horizontal channel with rectangular cross section was built at FZD for the investigation of co- and counter-current air water flow at atmospheric pressure. The measurements were focused on the behaviour of slug flow. Optical techniques, like video observation, were used to record the flow pattern and to determine the water level. Velocity-fields are measured using particle image velocimetry (PIV). Data is available for all NURESIM partners on the basis of bilateral agreements.

(ii) In the Fabre experiment, air-water turbulent stratified flow was investigated in a quasi horizontal (descending) rectangular channel. Systematic measurements of the components of the mean velocities and Reynolds stresses were performed with LDA and hot wire anemometry under carefully controlled inlet conditions. The data was used by [11] for validating the turbulence modelling near a free surface and below the free surface in the liquid including the interfacial production terms in adiabatic conditions. Selected data is made available to NURESIM partners by CEA.

Stratified steam water flows with condensation were investigated by Lim et al. [12] and Ruile [13] as follows.

(i) Lim investigated steam-water turbulent stratified flow with condensation in a horizontal channel with a rectangular cross-section. In the experiment, Pitot tubes were used to measure the local mean steam velocity, and conductivity probes to measure the water height at five locations. The data was used to validate interfacial condensation models by Yao et al. [14].

(ii) Ruile [13], Hein et al. [15], and Goldbrunner [16] investigated contact condensation in horizontal stratified flows of subcooled water and saturated steam in the LAOKOON test facility at the University of Munich. The experimental equipment was designed to set up co-current and counter-current flow conditions in a straight channel with adiabatic walls. Available measured data include the water and steam flow rates at the water feed cross section, the inlet water temperature, and the temperature distribution across the water layer at one location, where a vertical array of thermocouples was installed. The pressure level inside the channel and the water layer height were also measured. Data for selected test cases is available for NURESIM partners.

Water hammer in a horizontal section of a steam-line, induced by the injection of the cold water, was experimentally analysed at PMK-2 test facility of the Hungarian Atomic Energy Research Institute KFKI [17]. For the NURESIM project, mesh sensor data can be useful for the development and verification of the heat and mass transfer models in a horizontally stratified flow. However, it is well known that due to the Helmholtz instability measurement error can be as large as 50%.

Condensation pool studies were performed in the Nuclear Safety Research Unit at Lappeenranta University of Technology, LUT [18]. They were designed to correspond to the conditions of a postulated accident in BWRs in Finland. In the first tests, the formation, size, and distribution of noncondensable gas bubbles were studied in the condensation pool facility POOLEX. In the frame of the national SAFIR programme, steam instead of noncondensable gas was injected into the condensation pool test rig in order to study bubble dynamics issues such as bubble growth, upward acceleration, detachment, and breakup. The experiments

usually consisted of several individual steam blows, where the key parameters of the experiments (pool subcooling, steam mass flux) were varied. High-frequency instrumentation and a high-speed camera were used in the experiments. Structural loads were evaluated with the help of strain gauge measurements.

2.2. Demonstration Experiments. The purpose of a demonstration exercise is to build confidence in the ability of a CFD method to simulate complex flows. While validation studies show for a number of building block experiments that the physical models can cover the basic aspects of the PTS application, demonstration cases test the ability of the CFD methods to predict combined effects, including geometrical complexity. Typically, the level of completeness of the data for demonstration cases is much lower than for validation cases. Even though the density of data is usually lower, the NURESIM selection required that the quality satisfies the same criteria as for validation cases. Error estimates are desirable and so are independent measurements.

Suitable demonstration experiments were selected with complex flow phenomena for PTS-scenarios as follows.

(i) The 1 : 2 scaled HYBISCUS experiments where local temperature measurements were taken in the cold leg and in the downcomer of a PWR simulating ECC-injection. However, data is property of EDF and only available on special bilateral agreement.

(ii) The COSI experiments (see [19]) which provide temperature measurements for ECC injection scenarios in a cold leg with focus on direct contact condensation in the injection zone. The analysis of COSI tests data concluded that the jet-induced local turbulence in the water was the main phenomenon controlling the global condensation rate since most of the total condensation occurs close to the jet where this jet-induced turbulence enhances heat mixing below the free surface. Data is property of CEA and EDF, and there is no published data available.

(iii) Selected 1 : 1 scaled UPTF experiments where condensation and mixing phenomena during ECC injection were studied in the test series TRAM C1 and TRAM C2. Temperature measurements were taken in the cold legs, downcomer, lower, and upper plenum and in the core region. A detailed description of the geometry, the instrumentation, and selected data is made available in the frame of the NURESIM project.

(iv) The 1 : 48 volumetrically scaled ROSA test facility which was originally designed for the investigation of system behaviour. However, several spinoff experiments in the ROSA-IV and ROSA-V test programmes are focused on stratified flows. Data for temperature and concentration measurements are restricted to the ROSA group. Future experiments are planned with focus on the simulation of ECC injection and temperature stratification.

(v) Structural mechanics data resulting from thermal stresses assuming PTS conditions are also made available in the NURESIM database. They relate to thermal shock cryogenic experiments on steel plates which were performed at the University of Pisa, DIMNP.

Although there are a number of experiments available where flow phenomena are investigated as separate effects and as integral effects, there is still a need for well-instrumented validation data and demonstration experiments where experimental parameters are varied in order to investigate PTS phenomena. The data are required in a high resolution in space and time for the whole domain of interest and should include local and time-dependent information on interface between the phases, mean, and fluctuations (turbulence parameter) values for temperature and velocity.

For this purpose, the *TOPFLOW PTS experimental programme* has been conceived. Its objective is to provide a well-informed experimental database for both validation of CFD modelling of the two-phase flow in the cold leg and the downcomer including flow-wall heat transfer, and the improvement of the understanding of key thermal hydraulic (TH) phenomena involved. Besides the operational standard instrumentation (pressure, differential pressure, temperature, flow rates), the instrumentation will comprise thermocouples, heat-flux probes, wire-mesh sensors, local void probes equipped with a microthermocouple, high-speed camera observation, infrared camera observations and a local conductivity probe. It is planned to operate the test mockup in steady-state conditions with and without mass transfer due to condensation as well as in transient operation.

3. CFD Capabilities for the Simulation of Two-Phase PTS

3.1. Free Liquid Jet. The cold liquid jet injected into the horizontal cold leg pipe interacts first with the surrounding hot steam environment. These interactions are strongly dependent on the position and shape of the interface between the cold water and the hot gaseous environment. Interface tracking methods (ITM) are needed for a detailed description of these interactions. Depending on various characteristics of both the liquid and the gas, such as the relative velocity between the two phases or turbulence properties, instabilities at the surface of the jet can occur. Instabilities can also be directly generated by the condensation process [20]. They affect the heat and mass transfer. Models for DCC at the jet surface have to be applied. The instabilities also influence the gas entrainment at the jet impingement point on the liquid surface by capturing gas. Adequate modelling of the interface, in connection with a suitable coupling of the turbulence fields of the single phases and local mass and heat transfer, is needed.

Numerous theories relating to mechanisms on generation and growth of jet instabilities exist. Several numerical approaches have been used, such as DNS or large-eddy simulation (LES) for the prediction of their behaviour using various conditions [21, 22]. Even if the individual effects of some parameters, such as gravity or nozzle internal flow, have been separately studied, no computations exist

taking into account all these effects simultaneously. Actually, some models for the treatment of these instabilities are based on restrictive assumptions, which limit strongly their applicability. The LES approach seems the most suitable for the modelling of this specific flow situation, not presuming what would be the best choice for the simulation of the whole PTS.

DCC at the jet surface resulting from the temperature difference between the two phases is responsible for a non-negligible part of the total condensation in the considered flow domain of the cold leg [19]. For the condensation rate at the jet surface, correlations exist [19], but no representative experimental data are available to confirm this model. No special models were developed for DCC at the jet surface. The variations of the condensation rate along the jet and the effects of the noncondensable gases have been qualitatively reproduced [23], but the quantitative prediction was not fully mature.

3.2. Zone of the Impinging Jet. Appropriate modelling of the turbulence production below the jet is highly important, since turbulence is responsible for the mixing of the fluid. Gas entrainment caused by the jet impingement influences the characteristics of the turbulence below the free surface. The properties of the entrained gas (e.g., bubble size, penetration depth, horizontal migration, and total amount of entrained gas) are dependent on various properties of both phases and jet. The jet velocity is one of the most critical parameters. Depending on it, several scenarios for the gas entrainment below the free surface have already been experimentally identified [24, 25]. Most of the attempts for the development of theories able to reproduce the properties of the entrained gas below the free liquid surface have resulted in global correlations, which are limited to the corresponding operating conditions and geometric configuration. Several studies have highlighted the absence of theoretical approach and of valid correlations for the prediction of the minimal jet velocity at which the gas entrainment occurs. The modelling of the impinging jet zone requires simultaneous consideration of separated (surface) and dispersed (bubbles) flow within one flow domain.

Two issues have to be considered regarding turbulence production: the turbulence generated by the impingement of the jet itself and the influence of the bubbles on the turbulence. In the NURESIM project, investigations are done on the turbulence production below the jet by CEA and University of Pisa which simulated [8] tests of a plunging jet [26]. Together with Neptune_CFD standard models, a CEA/Grenoble modified k-ε model was tested. Quite good agreement with experimental data was achieved with best performing models: numerical predictions of the mean velocity field were always good, and turbulence was generally not bad but with significant underestimation far from the jet axis region.

In most simulations, the effect of the liquid turbulence on the bubbles is modelled, but the opposite effect (corresponding to the influence of the bubbles on the liquid turbulence field) is only considered in regards to the turbulent viscosity, for example, using the Sato model [27], despite this effect being important in the dense bubble region (near the impingement point). Some studies have thus to be conducted to improve understanding and modelling of the coupling between these various processes.Both LES and RANS models can be used for the simulation of the zone of the impinging jet. A more general investigation on the applicability of RANS and LES models for bubbly flow, including bubble plumes, was undertaken in the frame of the NURESIM project by PSI.

In the impinging jet zone, four different interface structures have to be considered: (1) the surface of the jet, (2) the free surface of the pool (i.e., liquid level in the cold leg), (3) the entrained bubbles, and (4) the complicated surface structure in the region where the jet impacts the surface. Separated (jet surface and pool surface) as well as dispersed (bubbles) flow regions exist simultaneously in one flow domain. The most difficult thing is to model the transitions between the two types of interfaces (i.e., bubble entrainment and de-entrainment). For the different interfacial structures, different closure models are needed, for example, for drag. The identification of the interfaces for separated flows is thus of crucial importance.

Some computations of the whole plunging jet process (starting from the jet, to the bubble de-entrainment, considering the impingement zone, the bubble migration below the free liquid surface and the free surface) have been performed with some success in the past [28]. These were able to reproduce the global behaviour for the free liquid surface (small waves at the free surface and shape at the impingement point), the gas entrainment, the bubble migration below the free surface, and the bubble de-entrainment at the free surface. Even if the entrainment process has been more or less well reproduced numerically (generation of entrained bubbles at the impingement point), the total volume flow rate of entrained gas has been largely overestimated. One of the most critical problems pointed out during these computations is the treatment of the liquid/gas interfaces. To overcome the discrepancies, the two kinds of interface mentioned above have to be modelled using two different models (or at least the same model with different values for the parameters). In the frame of the NURESIM project, investigations are done by FZD regarding these problems. This resulted in the suggestion to use so-called algebraic interfacial area density (AIAD) models which allow to apply two different drag coefficients for free surface and for bubbly flow. A blending function based on the gas void fraction is used to apply the adequate drag coefficient depending on the flow regime.

The behaviour of the entrained gas bubbles below the free liquid surface is determined by several forces acting on individual bubbles. The most important of these forces are buoyancy, drag, virtual mass force, lift force, and turbulent dispersion force. All these forces are strongly dependent on the bubble size (see, e.g., [29]). For bubbly flow in vertical pipes, a combination of Tomiyama lift- and wall force together with the Favre-averaged drag force [30] was found to reflect the experimental findings in poly-dispersed flows [31]. In the case of developing flows, some differences have been pointed out between calculations and experimental

data [32]. In the frame of the NURESIM project, the influence of the bubble forces on bubble migration is investigated by FZD for an impinging jet configuration.

In most computations, the bubble diameters are assumed to be constant. In principle, CFD models which allow consideration of a number of bubbles classes already exist [33], but calculations are then very time consuming. The bubbles size distribution is strongly influenced by bubble coalescence and breakup, for which various models exist in the literature (e.g., [34–36]). The models for bubble forces, as well as the models for bubble coalescence and breakup, have consequently to be validated for the plunging jet configuration.

There are also some attempts on a direct tracking of interfaces at zone of the jet impingement. Interface tracking techniques have indeed been applied, in combination with LES of the fields in each phase, to interfacial, sheared, two-phase flow [37, 38]. These authors incorporated the VOF approach to an LES simulation and applied it to the case of air/steam injection into a water pool, as investigated previously by Meier [39]. It is obvious that the available computational resources will not allow this approach to be used to capture the details of a dispersed bubbly flow; the routinely used two-fluid formulation remains much less demanding. Nevertheless, the LES/VOF combination may be a candidate future technique for tackling flows involving large interfacial inclusions. Novel analytical developments to the method have now been made by Liovic and Lakehal [38], namely, in the treatment of turbulence near sheared deformable interfaces.

3.3. Zone of Stratified Flow in the Cold Leg. In the horizontal cold leg pipe, a stratified flow has to be considered. In the context of PTS, the interface is characterised by intense heat, mass, momentum, and turbulence transfer. Heat transfer between the fluids and the wall of the cold leg pipe has also to be considered.

3.3.1. Momentum and Turbulence Transfer. Depending on the relative velocities of the gas and the liquid phases, the liquid/gas interface is strongly or mildly perturbed. For low relative velocities, the interface is quasistatic. For higher relative velocities, the interface is perturbed, and small waves are generated. Depending on the actual conditions, these waves can be amplified during their propagation in the horizontal pipe. The so-called *Kelvin-Helmholtz instability* can occur when a velocity shear is present within a continuous fluid or when there is sufficient velocity difference across the interface between two fluids. The CFD modelling of this instability was investigated in the frame of the NURESIM project by UCL. The classical theory can be used to predict the onset of instability in fluids of slightly different densities moving at various speeds. In the absence of surface tension, all wavelengths are unstable. The existence of surface tension stabilises the short wavelength condition; the theory then predicts stability until a velocity threshold is reached. For this reason, interface tracking methods or any method which includes surface tension effects have to be used [40, 41]. For cases with high-density differences, such as steam and water in the case of PTS, the situation is much more complicated (see [42]). It was found that either a single-fluid approach with VOF (FLUENT) or a two-fluid model with a large interface recognition (Neptune) could predict reasonably wave generation and growing and that condensation-induced instability could also be qualitatively predicted by Neptune and CFX.

In cases with high relative velocities in horizontal pipes, the waves are strongly amplified, and a *slug flow* with a complex system of interactions (presence of gas bubbles and liquid droplets) between the two phases can occur. The generated waves can, in certain cases of high relative velocity, entirely block the cold leg pipe. The slug flow regime is usually characterised by an acceleration of the gaseous phase and by the transition of fast liquid slugs carrying a significant amount of liquid with high-kinetic energy. The two-phase flow regimes in horizontal pipes are not only dependent on the local conditions but depend also on the characteristics of the free falling jet which may itself generate waves.

A systematic study of numerical simulation of slug flow in horizontal pipes using ANSYS CFX was carried out by Frank [9] and Vallée et al. [43]. It was shown that the formation of the slug flow regime strongly depends on the wall friction of the liquid phase. In simulations using inlet/outlet boundary conditions, it was found that the formation of slug flow regimes strongly depends on the agitation or perturbation of the inlet boundary conditions. Furthermore, Frank showed that the length of the computational domain also plays an important role in slug formation. Similar experimental data are being used in NURESIM for benchmarking the Neptune_CFD code by UCL, while University of Pisa and CEA do simulations of Fabre et al. [10]. A new modelling approach of large interfaces is developed considering an interfacial layer of 3 cells [44].

Momentum transfer is closely connected with turbulent transfer. In the case of the turbulence predicted by the k-ε model, the interfacial momentum can be modelled using several closure laws. The interfacial sublayer model (ISM, [14]) in the gas phase supposes, due to the significant difference between the gas and liquid densities, that the interface can be treated as a "moving solid wall" with a velocity equal to the liquid velocity. The gas region close to the interface is modelled with the two sublayer models, which is similar to the wall function concept. It is also possible to use the average viscosity assumption (AVM, [14]). This model is based on the simplified momentum equation in the case of a thin layer near a smooth interface without phase change, which permits the interfacial friction and velocity to be evaluated. Morel [45] has proposed a modification of the Taitel and Dukler model (TDM, [46]) for multidimensional calculations.

3.3.2. Turbulence Modelling. The mixing of hot and cold water is mainly determined by turbulence. The turbulence fields for both the liquid and the gas phases and the coupling between them play also important roles on the interfacial

transfer and on the two-phase flow regime in the cold leg, and for the transition between different regimes (i.e., smooth surface, wavy flow, slug flow). Close to the interface, three turbulence sources have been identified: turbulence diffused from wall boundaries, turbulence production by the interfacial friction, and turbulence induced by interfacial waves. Close to the interface, the anisotropy of the turbulence has to be considered. It is not reproduced by any classic model. In most of the cases, the turbulence is modelled using the k-ω or the k-ε (classic or modified) models, together with a specific hypothesis at the interface [47, 48]. Without any special treatment of the free surface, the high-velocity gradients at the free surface generate too high turbulence when using eddy viscosity models like the k-ε or the k-ω model. Therefore, a symmetric damping procedure for the solid wall-like damping of turbulence in both gas and liquid phases has been proposed by Egorov [28]. A numerical database obtained by DNS simulation of the interface was generated in the frame of NURESIM by ASCOMP [49, 50].

Vallée et al. [51] employed the shear stress transport (SST) turbulence model for each phase. The k-ω based SST model [52] accounts for the transport of the turbulent shear stress and gives good predictions of the onset and the amount of flow separation under adverse pressure gradients. The qualitative slug formation in the simulations (ANSYS-CFX) was in good agreement with the experiment.

3.3.3. Modelling of the Free Surface. According to Zwart [53], numerical models for free surface flow may be divided into three categories: surface adaptive methods, interface-capturing methods, and interface-tracking methods.

Surface-adaptive methods are typically single-phase approaches in which the kinematic condition is used to update the location of the free surface interface, and the mesh boundary conforms to this interface at all times. These methods inherently involve mesh motion. While these methods are successful for certain classes of flows, they are typically restricted to modest degrees of interface deformation. Methods of working around these limitations have been devised, including periodic remeshing and interpolation, characteristic streamline diffusion finite element methods [54], and the integrated space-time finite volume method [55]. Despite these advances in tracking significant interface deformation, it remains the case that surface adaptive methods are useful primarily when the interface topology is straightforward. Effects such as splashing, breaking, and colliding of waves remain difficult challenges. Moreover, the geometries themselves must be simple in order to calculate how to move the mesh at interface-wall intersections.

These limitations may be overcome by having a fixed mesh, which spans the interface location. The *interface is captured* within the mesh by specific algorithms. Most commonly, the algorithm makes use of the continuity equation for one of the phases, in which the dependent variable is the volume fraction of that phase; these methods are called volume-of-fluid (VOF) methods. They differ widely in their detailed implementation. Many of them are interface-capturing and solve the VOF equation using a continuum advection scheme. If standard techniques are used for the advection operator, numerical diffusion will lead to significant smearing of the interface. A variety of compressive advection schemes have been devised to minimize this diffusion. The compressivness is often obtained by using a controlled downwinding of the fluxes, as with the donor-acceptor [56] and CICSAM [57] schemes. Controlled downwinding schemes have compressive characteristics which depend upon the time-step and therefore require small time steps to retain sharp interfaces, even for steady-state free surface flows. More recently, a new scheme having compressive characteristics independent of the time step size has been developed [58].

Other VOF methods are *interface-tracking* and explicitly track the free surface interface. For a particular volume fraction field, the interface is reconstructed using a piecewise representation (constant, linear, or parabolic) in each cell. The volume fluxes may be calculated either geometrically or using an advection operator as described above. Further details of these algorithms can be found in [59, 60]. Another fixed grid strategy for free surface flow problems involves the use of level set method [61]. The level set strategy formulates and solves an equation representing the signed distance to the free surface interface; the interface itself is extracted as the zero-distance isosurface. This method has the advantage that the level set variable is smooth, rather than discontinuous across the interface, and is therefore easier to solve. Its disadvantage is that the level set needs to be reset periodically, and this process is not strictly mass-conservative.

Surface tension effects are important in many free surface flows as well, as mentioned above. The continuum surface force method [62] formulates the surface tension force as a volumetric force. A key ingredient of this method is evaluating the interface curvature; it is challenging because it in effect requires second derivatives of the discontinuous volume fraction field. Care must be used in order to avoid errors in this calculation. Further details are discussed by Kothe et al. [60].

In addition to the surface adaptive, interface-capturing, and interface-tracking methods, Coste has developed a method of large interface recognition in a two-fluid model [44]. This method allows to define the position of large interfaces (the characteristic length scale being larger than the mesh size) like a free surface or a surface of the jet in order to being able to model interfacial transfers by an extension of the wall function approach. The objective is to combine the merits of the two-fluid model which models statistically "small interfaces" (e.g., for bubbles and droplets) with the specific treatment of large interfaces required for PTS simulations.

3.3.4. Direct Contact Condensation. In the context of PTS, the gas-liquid interface is characterised by intense heat and mass transfer in addition to the effects discussed in the previous section. Some simulations exist on the safety analysis of a nuclear reactor in which rapid contact condensation of vapour occurs during the emergency injection of cold water [63–67]. The following condensation models were tested by

Yao et al. [14] in a turbulent stratified steam-water flow of Lim's experiment [12].

(i) Interfacial sublayer concept (ISM), using "wall function" approach to model the sublayer that exists at a gas-liquid interface. The modelling of the interfacial heat transfer is based on approaches similar to the interfacial friction transfer. Schiestel [68] and Jayatilleke [69] have proposed relations for the temperature profile and the Prandtl number, using a formulation similar to the interfacial sublayer model.

(ii) A model based on asymptotic behaviour of the eddy viscosity model (EVM) [70–72] describes the turbulent viscosity in the boundary layer with a Gaussian function.

(iii) A model based on surface renewal concept [63, 64, 73, 74] with small eddies (HDM) was proposed by Banerjee [75]. He has proposed a relation for the heat transfer, that was modified by Hughes and Duffey [64] by introducing the Kolmogorov time scale for the small eddies. The use of these models with the steam-water flow is theoretically questionable as discussed by Yao et al. [14].

An alternative model was then proposed [23] in order to avoid this question. The time scale in this model is built with the Kolmogorov length scale and the turbulent velocity (velocity fluctuations due to turbulence) which gives in the theoretical framework of surface renewal an acceptable domain of validity compatible with steam water flows. This model has been validated with SIMMER and Neptune_CFD codes calculations of eighteen COSI tests and a LAOKOON test [76]. It is being tested and used within the 3D two-fluid models for the stratified flow condensation during the PTS related transients.

Various experiments are being used to test these condensation models in the stratified flow with two-fluid models of various 3D CFD codes.

(i) Condensation of hot steam in the stratified flow of the LAOKOON test facility [77] at Technical University of Munich is being modelled in the frame of the NURESIM project by GRS, CEA, and University of Pisa with two-fluid models of the computer codes Neptune_CFD and CFX.

(ii) Condensation-induced water hammer experiment, where a cold liquid is slowly flooding a horizontal pipe filled with hot steam, has been performed at KFKI, Budapest [78, 79]. The first phase of the transient is another example of condensation of hot steam on a stratified cold liquid, that can lead to the slug formation and severe pressure peaks due to the condensation-induced slug acceleration. CFD simulations of this experiment for benchmarking Neptune_CFD and CFX are done in NURESIM project by JSI. The development and implementation of new models are planned.

(iii) Test STB-31 at the POOLEX experimental facility is the test case for the condensation modes in a different geometry of a stratified flow: steam is being introduced into the cold water pool through a vertical pipe, and the selected test case exhibits a condensation over a flat and stable gas-liquid interface in the vertical pipe. The experiment was done by LUT in the frame of the national SAFIR programme for the NURESIM project. Simulations of the experiment are done by LUT and VTT using Neptune_CFD.

The KFKI water hammer experiment and the POOLEX experiment of LUT might require conjugate heat transfer calculations that take into account heat transfer in the structure walls and thus present a test case also for that physical phenomenon relevant for the integral PTS simulations.

In the frame of the NURESIM project, a database generated by DNS simulations of a stratified air/steam water flow is used by ASCOMP to obtain new scaling laws for the normalized heat transfer coefficient for both the steam and liquid phases. The database has been initially developed to infer modelling approaches to turbulence transport at interfacial two-phase flows without phase change. In a second step, a thermal DNS database for the steam-water stratified flow has been exploited in order to understand the importance of the relative driving mechanisms for the condensation heat transfer in both phases [50]. New scaling laws for the normalized heat transfer coefficient have been derived for both the steam and liquid phases. On the gas side of the interface, condensation heat transfer was found to scale with the interfacial friction velocity and Prandtl number like in the passive heat transfer case studied by Lakehal et al. [49]. In the liquid phase, the DNS results produced a condensation heat transfer coefficient that remains roughly constant at a given total shear velocity. However, an augmentation of heat transfer due to the combined effects of mass exchange and interfacial waviness has been observed. The surface divergence model of Banerjee et al. [80] is found to apply in the liquid phase, with an excellent agreement in the low-to-mild interfacial shear regime in particular. Regarding the interfacial friction, the DNS data confirm that in the presence of condensation, the interfacial shear stress is influenced by the mass exchange, and a correction factor based on the rate of condensation is needed to correctly predict the variation of the friction coefficient.

3.4. Flow in the Downcomer and Wall Heat Transfer. In the case of a partially filled cold leg, the flow in the downcomer can be assumed to be single phase, and the temperature distribution of the fluid cooling the pressure vessel wall is mainly influenced by ECC injections, local mixing phenomena, and geometrical constraints. On the other hand, if the water level in the downcomer is below the nozzle of the cold leg, a complex two-phase flow regime occurs. Because of the low liquid level in the downcomer, another impingement region has to be considered. The same modelling approaches have to be applied as discussed for the impinging jet. Depending on the water velocity when entering the downcomer, a detachment of the flow from the walls is possible. If this detachment occurs, the heat transfer

between the water and the walls is decreased. Because of the variations in the flow regime and the presence of waves in the cold leg pipe, the velocity is not constant when the liquid enters the downcomer. The presence of the walls modifies the liquid flow behaviour by changing the turbulence properties, the liquid temperature, and the velocity field. Some calculations of the flow in the downcomer have been performed [81] and have been able to reproduce the water temperature oscillations in the downcomer.

The prediction of the transient and local heat transfer to the RPV wall is the final aim of the thermal fluid dynamic simulation of the PTS situation. However, the heat transfer to the cold leg wall has also to be considered, since there is a feedback from the wall temperatures on the flow. The various flow regimes taking place in the different regions influence the heat transfer at the walls. The numerical prediction of the transfer with the walls is strongly dependent on the accuracy with which the other phenomena are represented. The variations of the temperature fields for both the liquid and the gas phases are strongly dependent on the mixing between the phases, which results in the local phenomena. Conversely, the heat transfer at the walls influences the behaviour of the other phenomena by changing the temperature fields of the fluids.

As far as the simulation of the wall heat transfer is concerned, models valid for single phase should be sufficient. Various models exist and have been extensively studied. In most of the CFD codes, some heat transfer models with a solid wall are available. These models require the definition of the wall properties, depending on their composition. These models have already been used successfully in various configurations but not for the jet impingement where the local Nusselt number is not properly predicted [82].

3.5. Integral Simulation. The thermal-hydraulic phenomena at the origin of the two-phase PTS event have been split into several parts or subphenomena in the sections above. Each of those subphenomena, that is, Sections 3.1 to 3.4, actually implies the presence of inherent: (a) transient conditions, (b) thermo-dynamic non equilibrium, (c) mechanical nonequilibrium, (d) three-dimensional situation, and (e) nonfully-developed flow condition. Starting from this premise, any attempt to perform an integral simulation (i.e., considering all together the listed phenomena and the related interactions) of the PTS thermal-hydraulics phenomena are at worst meaningless, or more positively tainted by unreliable results, as also pointed out in the text before (e.g., attempts to consider together some of the identified subphenomena).

Three calculation types can be identified:

(A) licensing analysis accepted or acceptable by regulatory authorities;

(B) support (i.e., to licensing) calculations performed by "advanced" methods;

(C) scoping calculations by "advanced" methods to understand the phenomena or the use of the computational tools.

Advanced methods mean two-phase CFD in this case. Analyses of type (A) are performed by system thermal-hydraulic codes and typically based on conservative assumptions and do not fit with the content of the present paper (however, see below): there is no or limited consideration for phenomena, and the calculations are addressed to the estimate of the safety margins rather than to the prediction of the physical system transient evolution. At the basis of those analyses, there is the experience of safety technologists, including the consideration of experimental data and of deficiencies of the available computational tools. At the bottom end, comparison of expected conservative results from analyses of type (A), and results from methods discussed in this paper, when these will be available, will definitely prove the quality of the adequacy of the adopted conservatism. Analyses of type (B) are not accepted by licensing authorities nowadays. Therefore, only analyses of type (C) can be carried out. The analyses of type (C) suffer from all the limitations and the problems discussed in Sections 3.1 to 3.4.

In the frame of the NURESIM project, simulations are done by CEA for the COSI experiments (see Section 2) using the Neptune_CFD code. They found that some results are generally within a reasonable range, namely the water level, the liquid heat up in the cold water injection region, and the global condensation rate. Some other results are not satisfactory, for example, water temperature profiles upstream of the injection, and even in the downstream region in some cases. Simulations of UPTF TRAM experiments were done by EDF and GRS.

Further code improvements are required to allow reliable simulations of the two-phase PTS situation considering all the involved phenomena.In the near term, one may envisage a simplified treatment of two-phase PTS transients by neglecting some effects which are not yet controlled like the bubble entrainment and the possible effects of waves on the free surface. A better modelling of interfacial transfers of heat and mass at the free surface allowing convergence with a reasonable coarse mesh is still required to be able to predict the minimum liquid temperature entering the downcomer. It is very likely that neglecting entrained bubbles and interfacial waves leads to conservative predictions since both phenomena may increase condensation and mixing.

4. Conclusions

A comprehensive overview of the thermal-hydraulic phenomena (and subphenomena) connected with PTS in pressurized water reactors has been provided, with emphasis given to two-phase conditions.

The outline given in relation to single-phase phenomena shows that coupling techniques involving system thermal-hydraulics and CFD codes are mature enough to be used for technological purposes, with main reference to the evaluation of safety margins, though improvements are still needed (as expected when nuclear safety is part of the game) in the area of convection heat transfer.

The detailed analysis performed in relation to the two-phase flow phenomena shows the complexity of those phenomena. Computation techniques are capable to reproduce

qualitatively the individual aspects (also called subphenomena) but fail, so far, in the prediction of the interaction among the subphenomena and of the overall system behaviour.

The NURESIM EC project, that constitutes the key source of information for this paper, gave a unique possibility to a dozen EU institutions to cooperate and create a synergy for better understanding and modelling the overall thermal-hydraulic phenomena at the basis of PTS, and a continuation of the project is envisaged to address the open issues listed in Sections 3.1 to 3.5. Best practice guidelines [52] have to be applied for the integral simulations.

List of Abbreviations

AIAD:	Algebraic interfacial area density.
AVM:	Average viscosity model.
CFD:	Computational fluid dynamics.
DCC:	Direct contact condensation.
DNS:	Direct numerical simulation.
ECC:	Emergency core cooling.
EVM:	Eddy viscosity model.
FPDA:	Fiber-phase doppler anemometry.
HPI:	High pressure injection.
HDM:	Hughes &Duffey model.
ISM:	Interfacial sublayer model.
ITM:	Interface tracking methods.
LES:	Large eddy simulation.
LDA:	Laser Doppler anemometry.
LOCA:	Loss of coolant accident.
PIV:	Particle image velocimetry.
PTS:	Pressurized thermal shock.
PWR:	Pressurized water reactor.
RANS:	Reynolds-averaged Navier-stokes.
RMS:	Root mean square.
SB-LOCA:	Small break loss of coolant accident.
TDM:	Taitel and Dukler model.
VOF:	Volume of fluid.

Acknowledgment

The NURESIM project is partly funded by the European Commission in the framework of the Sixth Framework Programme (2004–2006).

References

[1] J. Sievers, C. Boyd, F. D'Auria, et al., "Thermal-hydraulic aspects of the international comparative assessment study on reactor pressure vessel under PTS loading (RPV PTS ICAS)," in *Proceedings of the OECD/CSNI Workshop on Advanced Thermal-Hydraulic and Neutronic Codes: Current and Future Applications*, Barcelona, Spain, April 2000.

[2] D. Bestion, H. Anglart, B. L. Smith, et al., "Extension of CFD codes to two-phase flow safety problems," Tech. Rep. NEA/SEN/SIN/AMA(2006)2, OECD Nuclear Energy Agency, Issy-les-Moulineaux, France, 2006.

[3] D. Bestion and A. Guelfi, "Status and perspective of two-phase flow modelling in the NEPTUNE multiscale thermal-hydraulic platform for nuclear reactor simulation," *Nuclear Engineering and Technology*, vol. 37, no. 6, pp. 511–524, 2005.

[4] A. Guelfi, D. Bestion, M. Boucker, et al., "NEPTUNE: a new software platform for advanced nuclear thermal hydraulics," *Nuclear Science and Engineering*, vol. 156, no. 3, pp. 281–324, 2007.

[5] D. Lucas, D. Bestion, E. Bodele, et al., "NURESIM-TH Deliverable D2.1.1: identification of relevant PTS-scenarios, state of the art of modelling and needs for model improvements," 6th Euratom Framework Program, 2005.

[6] "NURESIM-TH Deliverable D2.1.2: review of the existing data basis for the validation of models for PTS," 6th Euratom Framework Program, 2005.

[7] F. Bonetto and R. T. Lahey Jr., "An experimental study on air carry-under due to a plunging liquid jet," *International Journal of Multiphase Flow*, vol. 19, no. 2, pp. 281–294, 1993.

[8] M. Iguchi, K. Okita, and F. Yamamoto, "Mean velocity and turbulence characteristics of water flow in the bubble dispersion region induced by plunging water jet," *International Journal of Multiphase Flow*, vol. 24, no. 4, pp. 523–537, 1998.

[9] C. Vallée, T. Höhne, H.-M. Prasser, and T. Sühnel, "Experimental modelling and CFD simulation of air/water flow in a horizontal channel," in *Proceedings of the The 11th International Topical Meeting on Nuclear Reactor Thermal-Hydraulics (NURETH '05)*, Avignon, France, 2005.

[10] J. Fabre, L. Masbernat, and C. Suzanne, "Stratified flow, part I: local structure," *Multiphase Science and Technology*, vol. 3, no. 1–4, pp. 285–301, 1987.

[11] C. Suzanne, "Structure de l'écoulement stratifié de gaz et de liquide en canal rectangulaire," Thèse de Docteur es-Sciences, INP, Toulouse, France, 1985.

[12] I. S. Lim, R. S. Tankin, and M. C. Yuen, "Condensation measurement of horizontal cocurrent steam-water flow," *Journal of Heat Transfer*, vol. 106, pp. 425–432, 1984.

[13] H. Ruile, *Direktkontaktkondensation in Geschichteten Zweiphasenströmungen*, VDI-Fortschrittsbericht Reihe 19, VDI-Verlag, Düsseldorf, 1996, Germany.

[14] W. Yao, D. Bestion, P. Coste, and M. Boucker, "A three-dimensional two-fluid modeling of stratified flow with condensation for pressurized thermal shock investigations," *Nuclear Technology*, vol. 152, no. 1, pp. 129–142, 2005.

[15] D. Hein, H. Ruile, and J. Karl, "Kühlmittelerwärmung bei Direktkontaktkondensation an horizontalen Schichten und vertikalen Streifen zur Quantifizierung des druckbelasteten Thermoschocks," BMFT Forschungsvorhaben 1500906, Abschlußbericht, Lehrstuhl für Thermische Kraftanlagen, TU München, Germany, 1995.

[16] M. Goldbrunner, J. Karl, and D. Hein, "Experimental investigation of heat transfer phenomena during direct contact condensation in the presence of non condensable gas by means of linear raman spectroscopy," in *Proceedings of the 10th International Symposium on Laser Techniques Applied to Fluid Mechanics*, Lisbon, Portugal, July 2002.

[17] L. Szabados, G. Baranyai, A. Guba, et al., "PMK-2 handbook, technical specification of the Hungarian integral test facility for VVER-440/213 safety analysis and steam line water hammer equipment," WAHALoads project deliverable D12, KFKI Atomic Energy Research Institute, Budapest, Hungary, 2001.

[18] M. Puustinen, "Condensation Pool Experiments (POOLEX)," In Final Report of SAFIR, VTT Research Notes 2363, pp. 179–198. (VTT), 2006.

[19] A. Janicot and D. Bestion, "Condensation modelling for ECC injection," *Nuclear Engineering & Design*, vol. 145, pp. 37–45, 1993.

[20] P. Weiss, "UPTF experiment: principal full scale test results for enhanced knowledge of large break LOCA scenario in PWR's," in *Proceedings of the 4th International Topical Meeting on Nuclear Reactor Thermal-Hydraulics*, Karlsruhe, Germany, October 1989.

[21] Y. Pan and K. Suga, "Direct simulation of water jet into air," in *Proceedings of the 5th International Conference on Multiphase Flow (ICMF '04)*, Yokohama, Japan, 2004, Paper no. 377.

[22] A. O. Demuren and R. W. Wilson, "Streamwise vorticity generation in laminar and turbulent jets," NASA/CR-1999-209517. ICASE Report 99–33, NASA Langley Research Center, Hampton, Va, USA, 1999.

[23] P. Coste, "Computational simulation of multi-D liquid-vapour thermal shock with condensation," in *Proceedings of the 5th International Conference on Multiphase Flow (ICMF '04)*, pp. 1–17, Yokohama, Japan, September2004, Paper no. 392.

[24] A. K. Bin, "Gas entrainment by plunging liquid jets," *Chemical Engineering Science*, vol. 48, no. 21, pp. 3585–3630, 1993.

[25] L. Davoust, J. L. Achard, and M. El Hammoumi, "Air entrainment by a plunging jet: the dynamical roughness concept and its estimation by a light absorption technique," *International Journal of Multiphase Flow*, vol. 28, no. 9, pp. 1541–1564, 2002.

[26] M. C. Galassi, C. Morel, D. Bestion, J. Pouvreau, and F. D'Auria, "Validation of NEPTUNE CFD module with data of a plunging water jet entering a free surface," in *Proceedings of the 12th International Topical Meeting on Nuclear Reactor Thermal Hydraulics (NURETH '07)*, Pittsburgh, Pa, USA, September-October 2007.

[27] Y. Sato, M. Sadatomi, and K. Sekoguchi, "Momentum and heat transfer in two-phase bubble flow-I," *International Journal Of Multiphase Flow*, vol. 7, pp. 167–177, 1981.

[28] Y. Egorov, "Deliverable D2.1.2: review of the existing data basis for the validation of models for PTS," 5th Euratom Framework Programme ECORA Project WP4, EVOL-ECORA-D07, 2004.

[29] A. Tomiyama, "Struggle with computational bubble dynamics," in *Proceedings of the 3rd International Conference on Multiphase Flow (ICMF '98)*, pp. 1–18, Lyon, France, June 1998.

[30] A. D. Burns, T. Frank, I. Hamill, and J.-M. Shi, "The favre averaged drag model for turbulence dispersion in Eulerian multi-phase flows," in *Proceedings of the 5th International Conference on Multiphase Flow (ICMF '04)*, Yokohama, Japan, September2004.

[31] D. Lucas, J.-M. Shi, E. Krepper, and H.-M. Prasser, "Models for the forces acting on bubbles in comparison with experimental data for vertical pipe flow," in *Proceedings of the 3rd International Symposium on Two-Phase Flow Modelling and Experimentation*, Pisa, Italy, September 2004, Paper ha04.

[32] D. Lucas, E. Krepper, and H.-M. Prasser, "Modelling of the evolution of bubbly flow along a large vertical pipe," in *Proceedings of the 11th International Topical Meeting on Nuclear Reactor Thermal-Hydraulics (NURETH '05)*, Avignon, France, 2005.

[33] E. Krepper, D. Lucas, and H.-M. Prasser, "On the modelling of bubbly flow in vertical pipes," *Nuclear Engineering & Design*, vol. 235, no. 5, pp. 597–611, 2005.

[34] M.-J. Prince and H. W. Blanch, "Bubble coalescence and break-up in air-sparger bubble columns," *AIChE Journal*, vol. 36, no. 10, pp. 1485–1499, 1990.

[35] H. Luo and H. F. Svendsen, "Theoretical model for drop and bubble break-up in turbulent dispersions," *AIChE Journal*, vol. 42, no. 5, pp. 1225–1233, 1996.

[36] C. Martínez-Bazán, J. L. Montañés, and J. C. Lasheras, "On the break-up of an air bubble injected into a fully developed turbulent flow: part 2. Size PDF of the resulting daughter bubbles," *Journal of Fluid Mechanics*, vol. 401, pp. 183–207, 1999.

[37] P. Liovic and D. Lakehal, "Interface-turbulence interactions in large-scale bubbling processes," *International Journal of Heat & Fluid Flow*, vol. 28, no. 1, pp. 127–144, 2007.

[38] P. Liovic and D. Lakehal, "Multi-physics treatment in the vicinity of arbitrarily deformable gas-liquid interfaces," *Journal of Computational Physics*, vol. 222, no. 2, pp. 504–535, 2007.

[39] M. Meier, "Numerical and experimental study of large steam/air bubbles condensing in water," Doctoral dissertation, Swiss Federal Institute of Technology, Zurich, Switzerland, 1999.

[40] Y. Bartosiewicz and J.-M. Seynhaeve, "Numerical investigation on the Kelvin-Helmholtz instability in the case of immiscible fluids," in *Proceedings of the 13th International Conference on Fluid Flow Technologies*, Budapest, Hungary, September 2006.

[41] Y. Bartosiewicz and J.-M. Seynhaeve, "Assessment of the NEPTUNE CFD platform to model the occurrence of instabilities in a stratified flow," in *Proceedings of the10th International Conference on Multiphase Flow in Industrial Plan (MFIP '06)*, Tropea, Italy, September 2006.

[42] I. Tiselj, L. Strubelj, and I. Bajsic, "Test-case no 36: Kelvin-Helmholtz instability," *Multiphase Science and Technology*, vol. 16, no. 1–3, pp. 273–280, 2004.

[43] T. Frank, "Numerical simulations of multiphase flows using CFX-5," in *CFX Users Conference*, Garmisch-Partenkirchen, Germany, November 2003.

[44] P. Coste, J. Pouvreau, C. Morel, J. Laviéville, M. Boucker, and A. Martin, "Modelling turbulence and friction around a large interface in a three-dimension two-velocity Eulerian code," in *Proceedings of the 12th International Topical Meeting on Nuclear Reactor Thermal Hydraulics (NURETH '07)*, Pittsburgh, Pa, USA, May-June 2007.

[45] C. Morel, "Conditionnement numérique des équations de bilans supplémentaires. Premiers résultats de calculs de l'expérience Super Moby Dyck Horizontal," DTP/SMTH/LMDS/2002-010, 2002.

[46] Y. Taitel and A. E. Dukler, "A theoretical approach to the Lockhart-Martinelli correlation for stratified flow," *International Journal of Multiphase Flow*, vol. 2, no. 5-6, pp. 591–595, 1976.

[47] M. Akai, A. Inoue, S. Aoki, and K. Endo, "Co-current stratified air-mercury flow with wavy interface," *International Journal of Multiphase Flow*, vol. 6, no. 3, pp. 173–190, 1980.

[48] R. I. Issa, "Prediction of turbulent, stratified, two-phase flow in inclined pipes and channels," *International Journal of Multiphase Flow*, vol. 14, no. 2, pp. 141–154, 1988.

[49] D. Lakehal, M. Fulgosi, G. Yadigaroglu, and S. Banerjee, "Direct Numerical Simulation of heat transfer at different Prandtl numbers in counter-current gas-liquid flows," *Journal of Heat Transfer*, vol. 125, no. 6, pp. 1129–1140, 2003.

[50] D. Lakehal, M. Fulgosi, and G. Yadigaroglu, "Direct numerical simulation of condensing stratified flow," *Journal of Heat Transfer*, vol. 130, no. 2, Article ID 021501, 10 pages, 2008.

[51] C. Vallée, T. Höhne, H.-M. Prasser, and T. Sühnel, "Experimental investigation and CFD simulation of horizontal air/water slug flow," *Kerntechnik*, vol. 71, no. 3, pp. 95–103, 2006.

[52] F. Menter, "CFD best practice guidelines for CFD code validation for reactor-safety applications," EC-report EVOL-ECORA-D01, 2002.

[53] P. J. Zwart, "Industrial CFD applications of free surface and cavitating flows," VKI Lecture Series: Industrial Two-Phase Flow CFD, 2005.

[54] P. Hansbo, "Characteristic streamline diffusion method for the time-dependent incompressible Navier-Stokes equations," *Computer Methods in Applied Mechanics and Engineering*, vol. 99, no. 2-3, pp. 171–186, 1992.

[55] P. J. Zwart, G. D. Raithby, and M. J. Raw, "The integrated space-time finite volume method and its application to moving boundary problems," *Journal of Computational Physics*, vol. 154, no. 2, pp. 497–519, 1999.

[56] B. Hirt and B. Nichols, "Volume of fluid (VOF) method for the dynamics of free boundaries," *Journal of Computational Physics*, vol. 39, no. 1, pp. 201–225, 1981.

[57] O. Ubbink and R. I. Issa, "A method for capturing sharp fluid interfaces on arbitrary meshes," *Journal of Computational Physics*, vol. 153, no. 1, pp. 26–50, 1999.

[58] P. J. Zwart, M. Scheuerer, and M. Bogner, "Free surface flow modelling of an impinging jet," in *Proceedings of the ASTAR International Workshop on Advanced Numerical Methods for Multidimensional Simulation of Two-Phase Flows*, Garching, Germany, September 2003.

[59] M. Rudman, "Volume-tracking methods for interfacial flow calculations," *International Journal for Numerical Methods in Fluids*, vol. 24, no. 7, pp. 671–691, 1997.

[60] D. B. Kothe, W. J. Rider, S. J. Mosso, and J. S. Brock, "Volume tracking of interfaces having surface tension in two and three dimensions," AIAA Paper 96-0859, 1996.

[61] M. Sussman, E. Fatemi, P. Smereka, and S. Osher, "An improved level set method for incompressible two-phase flows," *Computers and Fluids*, vol. 27, no. 5-6, pp. 663–680, 1998.

[62] J. U. Brackbill, D. B. Kothe, and C. Zemach, "A continuum method for modelling surface tension," *Journal of Computational Physics*, vol. 110, no. 2, pp. 335–353, 1992.

[63] S. G. Bankoff, "Some condensation studies pertinent to LWR safety," *International Journal of Multiphase Flow*, vol. 6, no. 1-2, pp. 51–67, 1980.

[64] E. D. Hughes and R. B. Duffey, "Direct contact condensation and momentum transfer in turbulent separated flows," *International Journal of Multiphase Flow*, vol. 17, no. 5, pp. 599–619, 1991.

[65] A. Murata, E. Hihara, and T. Saito, "Prediction of heat transfer by direct contact condensation at a steam-subcooled water interface," *International Journal of Heat and Mass Transfer*, vol. 35, no. 1, pp. 101–109, 1992.

[66] Q. Zhang, G. F. Hewitt, and D. C. Leslie, "Nuclear safety code modelling of condensation in stratified flow," *Nuclear Engineering & Design*, vol. 139, pp. 1–15, 1993.

[67] I.-C. Chu, M. K. Chung, S.-O. Yu, and M.-H. Chun, "Interfacial condensation heat transfer for counter-current steam-water stratified flow in a circular pipe," *Journal of the Korean Nuclear Society*, vol. 32, no. 2, pp. 142–156, 2000.

[68] R. Schiestel, *Modélisation et simulation des écoulements turbulents*, Hermès, Paris, France, 1993.

[69] C. L. V. Jayatilleke, "The influence of Prandtl number and surface roughness on the resistance of the laminar sub-layer to momentum and heat transfer," *Progress in Heat and Mass Transfer*, vol. 1, p. 193, 1969.

[70] P. V. Danckwerts, "Significance of thin film coefficient in gas absorption," *Industrial & Engineering Chemistry*, vol. 43, no. 6, pp. 1460–1467, 1951.

[71] L. Shen, G. S. Triantafyllou, and D. K. P. Yue, "Turbulent diffusion near a free surface," *Journal of Fluid Mechanics*, vol. 407, pp. 145–166, 2000.

[72] Y. Yamamoto, T. Kunugi, and A. Serizawa, "Turbulence statistics and scalar transport in an open-channel flow," *Journal of Turbulence*, vol. 2, no. 10, pp. 1–16, 2001.

[73] H. Higbie, "The rate of absorption of a pure gas into a still liquid during short periods of exposure," *Transaction of the AIChE*, vol. 31, pp. 365–388, 1935.

[74] M. Rashidi, G. Hetsroni, and S. Banerjee, "Mechanisms of heat and mass transport at gas-liquid interfaces," *International Journal of Heat and Mass Transfer*, vol. 34, no. 7, pp. 1799–1810, 1991.

[75] S. Banerjee, "A surface renewal model for interfacial heat and mass transfer in transient two-phase flow," *International Journal of Multiphase Flow*, vol. 4, no. 5-6, pp. 571–573, 1978.

[76] M. Scheuerer, M. C. Galassi, P. Coste, and F. D'Auria, "Numerical simulation of free surface flows with heat and mass transfer," in *Proceedings of the 12th International Topical Meeting on Nuclear Reactor Thermal Hydraulics (NURETH '07)*, Pittsburgh, Pa, USA, Septembre-Octobre 2007.

[77] D. Hein, J. Karl, and H. Ruile, "Transport phenomena and heat transfer with direct contact condensation," *Kerntechnik*, vol. 63, no. 1-2, pp. 51–56, 1998.

[78] H.-M. Prasser, G. Ezsol, and G. Baranyai, "PMK-2 water hammer tests, condensation caused by cold water injection into main steam-line of VVER-440-type PWR—data evaluation report (DER)," *WAHALOADS project deliverable D51*, 2004.

[79] I. Tiselj, L. Štrubelj, and A. Prošek, "Direct contact condensation in horizontally stratified flow of AEKI PMK-2 device," 6th Euratom Framework Programm NURESIM, Deliverable D2.1.13.1, 2006.

[80] S. Banerjee, D. Lakehal, and M. Fulgosi, "Surface divergence models for scalar exchange between turbulent streams," *International Journal of Multiphase Flow*, vol. 30, no. 7-8, pp. 963–977, 2004.

[81] S. M. Willemsen and E. M. J. Komen, "Assessment of RANS CFD modelling for pressurized thermal shock analysis," in *Proceedings of the 11th International Topical Meeting on Nuclear Reactor Thermal-Hydraulics (NURETH '05)*, Avignon, France, 2005.

[82] T. J. Craft, L. J. W. Graham, and B. E. Launder, "Impinging jet studies for turbulence model assessment—II: an examination of the performance of four turbulence models," *International Journal of Heat and Mass Transfer*, vol. 36, no. 10, pp. 2685–2697, 1993.

Hindawi Publishing Corporation
Science and Technology of Nuclear Installations
Volume 2009, Article ID 148436, 12 pages
doi:10.1155/2009/148436

Research Article

CFD Approaches for Modelling Bubble Entrainment by an Impinging Jet

Martin Schmidtke and Dirk Lucas

Forschungszentrum Dresden-Rossendorf, Institute of Safety Research, P.O. Box 510119, 01314 Dresden, Germany

Correspondence should be addressed to Martin Schmidtke, m.schmidtke@fzd.de

Received 31 March 2008; Accepted 25 June 2008

Recommended by Fabio Moretti

This contribution presents different approaches for the modeling of gas entrainment under water by a plunging jet. Since the generation of bubbles happens on a scale which is smaller than the bubbles, this process cannot be resolved in meso-scale simulations, which include the full length of the jet and its environment. This is why the gas entrainment has to be modeled in meso-scale simulations. In the frame of a Euler-Euler simulation, the local morphology of the phases has to be considered in the drag model. For example, the gas is a continuous phase above the water level but bubbly below the water level. Various drag models are tested and their influence on the gas void fraction below the water level is discussed. The algebraic interface area density (AIAD) model applies a drag coefficient for bubbles and a different drag coefficient for the free surface. If the AIAD model is used for the simulation of impinging jets, the gas entrainment depends on the free parameters included in this model. The calculated gas entrainment can be adapted via these parameters. Therefore, an advanced AIAD approach could be used in future for the implementation of models (e.g., correlations) for the gas entrainment.

1. Introduction

This work concerns the evaluation of the capabilities of the CFX-11 software for the numerical predictions of gas entrainment in the case of a plunging jet configuration. The configuration of an impinging jet occurs in different scenarios of reactor safety analysis.

In the scenario of an emergency core cooling (ECC), water is injected into the cold leg. The pipe may only be partially filled with hot water, if a loss of coolant accident occurs. In this case, the injected cold water impinges as a jet on the surface of the hot water. Depending on the velocity of the jet, steam bubbles may be entrained below the surface by the impinging jet. These bubbles contribute to heat exchanged and mixing of the fluids. Heat transfer between cold and hot water and mixing in the cold leg play an important role since the mixed water enters the reactor pressure vessel and may cause high temperature gradients at the wall of the vessel. These gradients cause mechanical stress in the wall due to thermal shock, which can have a negative effect on the durability of the reactor vessel.

An impinging jet may also occur, when an emergency coolant tank is filled up with water and the initial water level is below the inlet. Here, the mixing of the injected water and the water in the tank is a point of interest if the temperatures or the boron concentrations are different.

Another scenario for the occurrence of plunging jet phenomena can be found in the case of a break, when insulation material of components is released by the break. The fibrous material is transported into the reactor sump and might there perturb the core cooling system. During this situation, the reactor sump is partially filled with water. The jet from the break impinges at the sump water surface and causes a fluid flow in the sump, which influences the transport of the fibrous insulation material towards the sump strainers. The gas entrainment and its influence on the fluid flow field and the transport of the fibrous insulation are of particular interest.

Generally for the CFD modeling of large hydrodynamic configurations with multiphase flow, the Euler-Euler approach is used. The physical process of bubble generation near a plunging jet occurs on a very small scale, which cannot

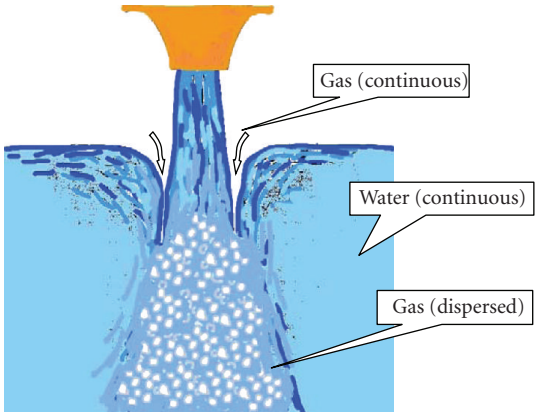

Figure 1: Morphologies of the phases near an impinging jet.

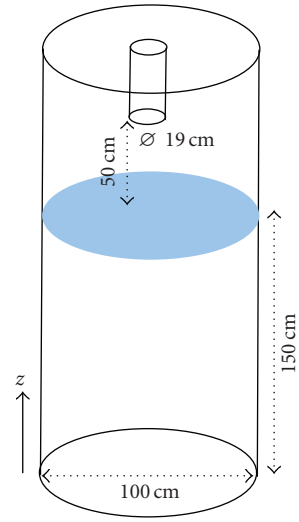

Figure 2: Geometry of a cylindrical tank filled with water through a nozzle above the free surface.

be resolved in a mesoscale simulation. Therefore, the gas entrainment has to be physically modeled in simulations of plunging jets. The aim of this study is to find an approach for the simulation of plunging jet, where the gas entrainment can be deliberately tuned to some extent (e.g., in terms adjusting free parameters), in order for a physical model or correlation of the entrainment process to be implemented into future simulations.

In the plunging jet configuration, gas has two different morphologies (see Figure 1). The gas above the water level is a continuous phase, whereas the gas below the water level is bubbly, that is, a dispersed phase. The water can be regarded as a continuous phase everywhere. For modelling this with the Euler-Euler method, two approaches are possible.

One can use two different phases for the two morphologies of gas. Then, water is treated as a third phase. Gas entrainment near the jet and degassing at the water surface has to be modelled with sources and sink terms that describe the conversion of gas from a continuous to a dispersed (bubbly) morphology and vice versa. This requires algorithms that identify the regions of entrainment and of degassing.

The other approach uses only two phases, one for water and one for gas. The different morphologies of the gas then have to be reflected by different coefficients in the closures for the momentum transfer between the gas and water phases.

The first simulations presented here are performed with water as a continuous phase and gas as a dispersed phase. Thus, the gas is assumed bubbly everywhere in the domain, and a constant drag coefficient is applied. The influence of the magnitude of the drag coefficient is investigated. Then, a more complex drag model is tested, which take into account the different morphologies of the gas phase.

2. Definition of the Test Case

2.1. Geometry and Mesh. A cylindrical tank with a diameter of 100 cm is filled through a nozzle. The water level is 50 cm below the nozzle and 150 cm above the bottom of the tank. The nozzle diameter is 19 cm (see Figure 2). To reduce the costs of computation time, only a section of five degrees is used for the simulation to be performed as 2D axisymmetric calculation (see Figure 3).

Table 1: Fluid properties.

Property	Water	Gas: air
Viscosity ($kg \cdot m^{-1} \cdot s^{-1}$)	0.0008899	1.831e-05
Density ($kg \cdot m^{-3}$)	997	1.185

The structured mesh has 125 uniform cells for the total height of the domain. For the radius of the water inlet, seven uniform cells are used and 30 uniform cells for the opening (see Figure 3). The tank is quite small compared to the jet diameter and the height of the nozzle above the water level is small enough for physicality of the result to be influenced significantly by the walls. This disadvantage is accepted, since we concentrate here on the gas entrainment, which takes place where the jet hits the water surface. It can be assumed that effects far away from this area do not influence the gas entrainment. The limitations of the geometry and the low mesh resolution are meant to reduce the computational costs. This is important for parametric studies. The simplicity of the geometry is accepted here since this investigation is meant to study concepts for modelling the gas entrainment. For some of the cases, the grid is refined by reducing the cell size by a factor two in each dimension.

2.2. Fluid Properties, Initial Conditions, and Boundary Conditions and Turbulence. During the calculations, the fluids are water for the continuous phase and gas for the dispersed bubbly phase. The main properties (25°C and atmospheric pressure) for water and gas are summarized in Table 1.

The domain is partially filled with water up to a level of 150 cm above the bottom. The distance between the free surface and the water nozzle is then equal to 50 cm. The initial velocity for both water and gas in the computational domain is taken equal to 0 m/s in each direction. The

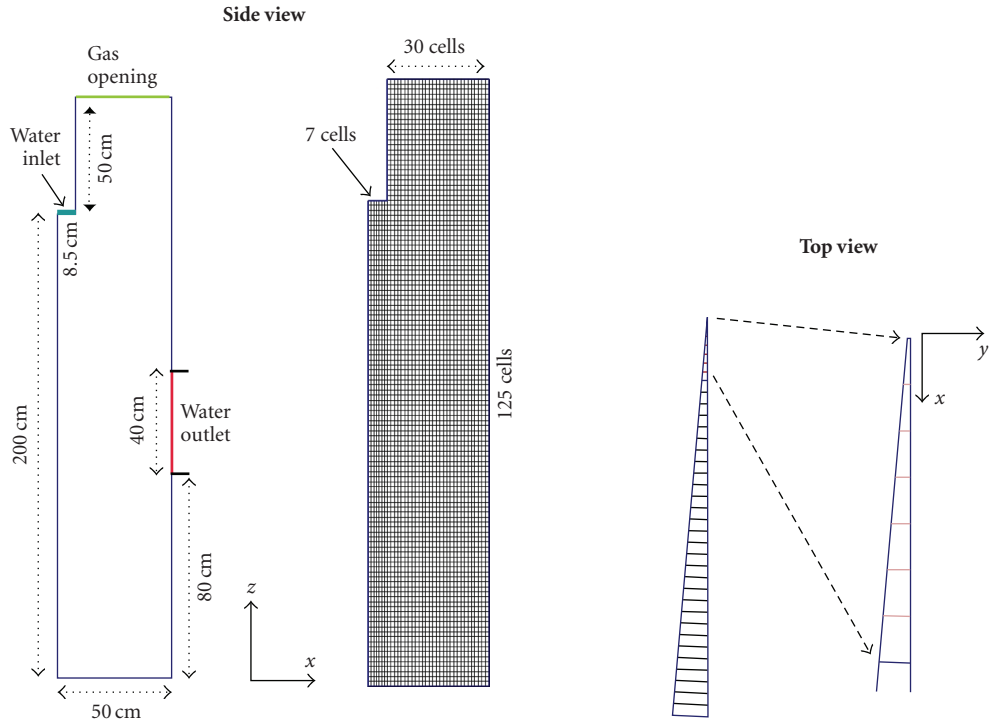

Figure 3: Section (five degrees) of the cylindrical tank; geometry and mesh.

hydrostatic pressure is initialized accordingly to the water level in the domain.

Liquid Inlet. The jet is injected through the nozzle with a velocity of 3 m/s. The volume fraction is 1 for water and 0 for gas.

Gas Outlet. For the gas outlet, an opening condition is used. The volume fraction is 1 for gas and 0 for water. Aconstant relative pressure equal to 0 Pa is assumed. For the fluid, a velocity normal to the boundary condition is considered.

Liquid Outlet. For the liquid outlet, an outlet condition is used. The volume fraction is 1 for water and 0 for gas. Therefore, the gas mass flow rate is equal to 0 kg/s at this boundary condition. For the maintenance of a constant liquid level, the liquid mass flow rate leaving the domain is defined equal to the liquid mass flow rate introduced by the injector.

Walls. Outer walls are adiabatic walls and are defined using a no slip boundary condition. For the "inner walls" caused by limiting the domain to a section, a symmetry boundary condition is applied. In the case of stratified flows, the buoyancy force causes a separation of gas and water.

Turbulence Model. The homogeneous shear stress turbulence (SST) model is applied (i.e., no separate calculation of the turbulence for both phases). In the ANSYS CFX-Solver modelling guide [1], a homogeneous turbulence model is recommended for separate flow and stratified flow, whereas for dilute dispersed two-phase flow (e.g., bubbly flow), the manual recommends using separate turbulence model for each phase. In the plunging jet, separate flow and bubbly flow coexist in one domain, so none of the turbulence approaches is suitable everywhere in the domain. The calculations presented below are calculated with a homogeneous SST model by default. For comparison, some calculations are repeated with an inhomogeneous turbulence model, which is the SST model for the liquid phase and a laminar assumption for the gaseous phase (see Section 3.3).

3. Dispersed Phase Model for Gas

The simplest approach for modelling the plunging jet is achieved if the water is treated as continuous phase and the gas is a dispersed phase with a constant particle diameter ($d = 2$ mm). This approach neglects the fact that the particle model is not appropriate for the gas above the water level.

3.1. Drag Model. For the bubbles, a constant drag coefficient is used. The default value used here is $C_D = 0.44$, which is the drag coefficient for solid spheres in the Newton range. To study the effect of the particle drag coefficient on the gas entrainment, the simulations are performed with the drag coefficient $C_D = 0.44$ and with a reduced value $C_D = 0.05$ for comparison.

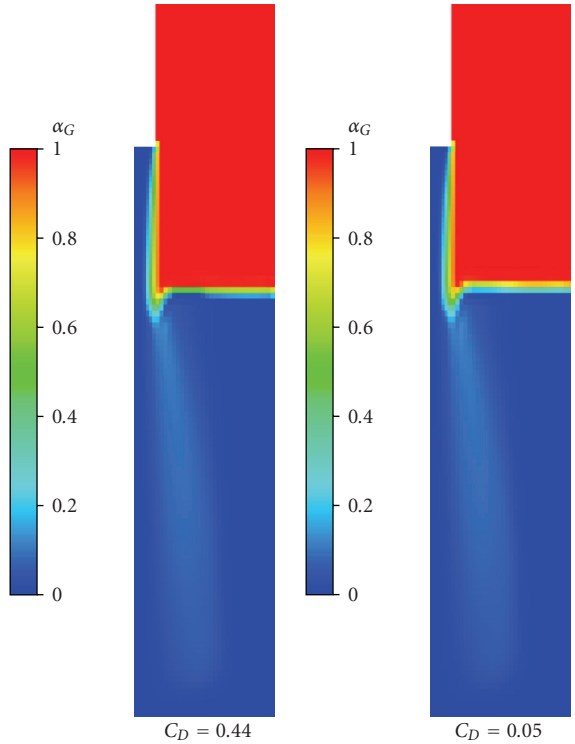

FIGURE 4: Gas void fraction fields for a simulation using a dispersed phase model for gas homogenous SST turbulence for both phases.

3.2. Nondrag Forces. Since the focus of this study is on the gas entrainment at the surface, nondrag forces (lift force and turbulent dispersion force) are neglected here. It is expected that the turbulent dispersion force causes an increase of the horizontal extension of the bubble plume. Nevertheless, an application of nondrag forces above the water level is meaningless. Therefore, nondrag forces are not modelled here.

3.3. Results for the Simulations with Gas as Dispersed Phase. A few seconds after the jet release from the nozzle the interface becomes stable and the gas void fraction field also becomes steady (see Figure 4). A reduction of the drag coefficient from $C_D = 0.44$ to $C_D = 0.05$ has no significant effect on the gas void fraction field. Thus, the drag coefficient cannot be used as a parameter that influences the gas entrainment in the simulation. If the SST model is applied for the liquid phase and the turbulence of the gas is neglected (laminar assumption), the gas void fractions are similar to those in Figure 4 which have been calculated with a homogenous SST model. Therefore, the coupling of both phases by sharing the same turbulence field does not contribute to gas entrainment. In the subsequent simulations, only the homogenous SST model is used.

3.4. Vertical Gas Fluxes below the Water Level. For a characterization of the gas entrainment, it is advantageous to use integral quantities for the intensity and the geometry of the gas plume. By performing an extensive survey of experimental studies Bin [2] obtained correlations for the penetration depth and the entrainment rate. The penetration depth h_p is the vertical extension of the gas plume below the water level. Bin's correlation [2] for the penetration depth in meter is

$$h_p = 2.1 w_j^{0.775} d_0^{0.67}, \tag{1}$$

where d_0 is the nozzle diameter in meter and w_j is the vertical jet velocity at the water level (in m/s). Due to gravitational acceleration, the velocity of a free falling jet is increasing until it hits the surface. If h_j is the height of the nozzle above the surface and w_0 is the liquid velocity at the nozzle, w_j can be calculated as

$$w_j = \sqrt{w_0^2 + 2gh_j}. \tag{2}$$

For the height of $h_j = 0.5$ and $w_0 = 3.0$ m/s, one obtains $w_j = 4.3$ m/s for the jet velocity at the water level and a penetration depth of 215 cm according to (1). The predicted value for the penetration depth is larger then the depth of the water in the tank. Therefore, the length of the gas plume might be restricted artificially by the geometry. In fact, according to Figure 4 the gas plumes almost reach the bottom of the tank. For a better quantification of the vertical distribution of the gas, the gas void fraction α_G is integrated on horizontal planes:

$$A_G = \int_A \alpha_G \, dA. \tag{3}$$

Since the gas void fraction is dimensionless, the integral (3) yields the dimension of an area for A_G. This can be interpreted as the area occupied by gas on the horizontal plane A. In Figure 5, A_G is plotted versus the depth below the water level. Here, A_G is normalized by the area of the jet cross-section at the inlet. There is only a little difference between the values for $C_D = 0.44$ and $C_D = 0.05$ (see also Figure 4).

The depth at which the normalized gas area is zero can be used to define a penetration depth for jets. According to Figure 5, the penetration depth is 150 m which means that the plumes reach the tank bottom. This is in accordance with the prediction of (1).

The entrainment rate is the ratio of the gas flux Q_G entrained below the water by the impinging jet and the water flux Q_L of the jet. The correlation for the entrainment rate suggested by Bin [2] is

$$\frac{Q_G}{Q_L} = 0.04 \, \mathrm{Fr}^{0.28} \left(\frac{h_j}{d_0}\right)^{0.4}, \quad \text{with } \mathrm{Fr} = \frac{w_j^2}{g d_0}, \tag{4}$$

where h_j is the jet height above the water level and g is the gravity. For the boundary conditions used in the simulations, this correlation yields an entrainment rate of 0.08. Another correlation was obtained by Ohkawa et al. [3]:

$$\frac{Q_G}{Q_L} = 0.016 \left[\mathrm{Fr}^{0.28} \left(\frac{h_j}{d_0}\right)^{0.4}\right]^{1.17}. \tag{5}$$

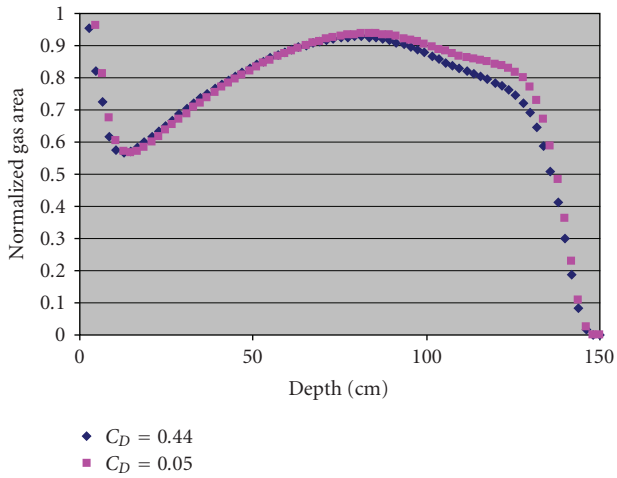

FIGURE 5: Normalized gas area as a function of the depth below the water surface.

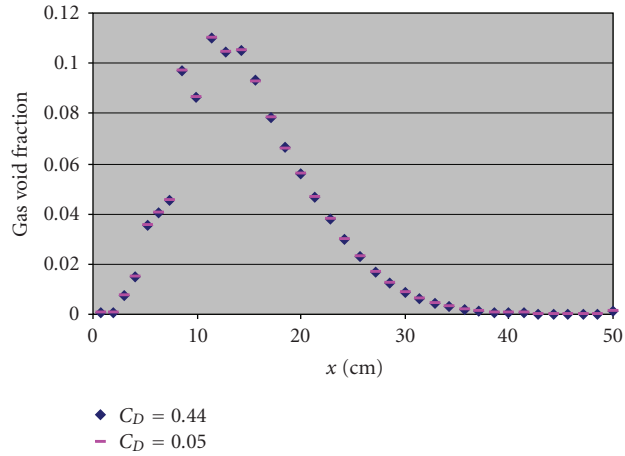

FIGURE 6: Gas void fraction as a function of the horizontal distance to the jet axis, 30 cm below the water level. The values for $C_D = 0.44$ (blue) and $C_D = 0.95$ (mangenta) differ hardly.

This correlation yields an entrainment rate of 0.036 for the boundary conditions used here.

To compare the simulation results in terms of entrainment rate with the predictions given by correlations (4) and (5), the gas fluxes below the water have to be investigated more closely. The product of the gas void fraction α_G and the vertical velocity of the gas w_G defines a vertical gas flux density q_G:

$$q_G = \alpha_G w_G. \tag{6}$$

The upward and the downward fluxes can be distinguished by the definition of

$$q_G^+ = \begin{cases} q_G, & \text{if } q_G > 0, \\ 0, & \text{else}, \end{cases}$$
$$q_G^- = \begin{cases} q_G, & \text{if } q_G < 0, \\ 0, & \text{else}. \end{cases} \tag{7}$$

So the total downward flux at a certain level below the surface is

$$Q_G^- = \int_A q_G^- \, dA, \tag{8}$$

where A is the horizontal cross-section of the domain at a certain level below the surface. The total upward flux Q_G^+ is calculated in the same way. Figures 6–8 show the gas void faction, the vertical velocities, and the vertical gas flux density at a depth of 30 cm below the water level.

In Figure 9, the total upward and downward gas fluxes are shown for the two jets modelled with the drag coefficients $C_D = 0.44$ and $C_D = 0.05$. The gas fluxes below the water level are normalized by the water flux of the jet $Q_{L,0}$ at the nozzle and plotted as function of the depth below the water level. For $C_D = 0.44$, the upward and downward gas fluxes are similar which means that the solution is steady.

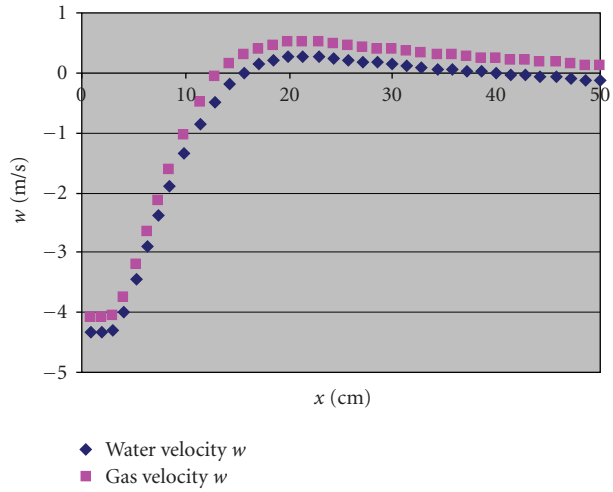

FIGURE 7: Vertical velocities as a function of the horizontal distance to the jet axis, 30 cm below the water level ($C_D = 0.44$).

At each level, the same amount is transported upwards and downwards. For the different drag coefficients, the gas downward fluxes are also similar. Thus, the drag hardly contributes to gas entrainment. The carry-under of gas therefore seems to be mainly caused by numerical effects within the solver. The curves for the normalized gas fluxes show a local minimum ca. 10 cm below the water level. This is the depth of the deformed water surface ("trumpet") near the jet. At a depth of 60 cm, all the curves have a local maximum. This can be explained by the re-entrainment of bubbles, which are trapped in the vortex caused by the jet. At the depth of 20 cm, the normalized gas fluxes are about 0.06 which is just between the predictions for the entrainment rate by Bin (see (4)) and by Ohkawa (see (5)). Since the entrainment is mainly caused by numerical effects in this setup, we can expect the value to be sensitive to the geometry and resolution of the grid. This must be studied in future.

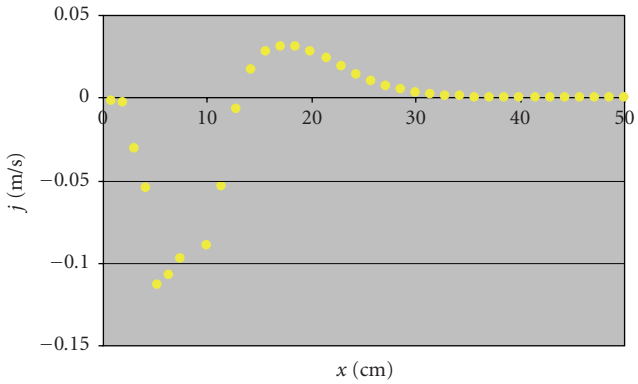

Figure 8: Vertical gas flux density as a function of the horizontal distance to the jet axis, 30 cm below the water level ($C_D = 0.44$).

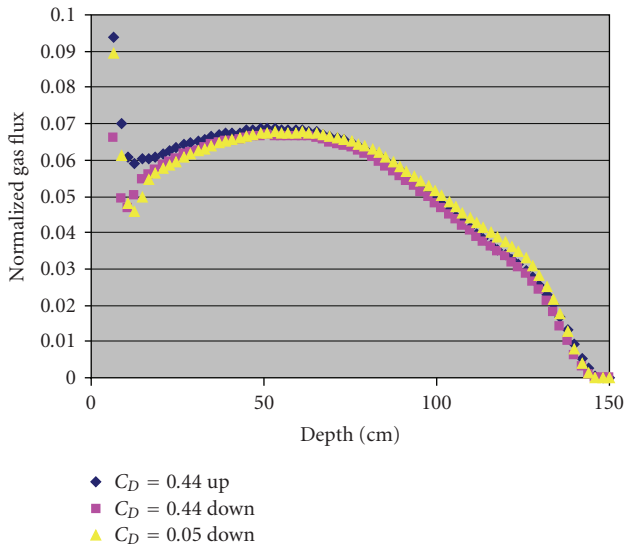

Figure 9: Normalized gas fluxes as function of the depth below the water level. Blue symbols: upward gas flux ($C_D = 0.44$). Red symbols: downward gas flux ($C_D = 0.44$). Yellow: downward gas flux ($C_D = 0.05$).

However, it seems to be a coincidence that the simulated entrainment rate in this simulation is in the range predicted by empirical correlations.

4. The Simmer-Drag Model

In the previous simulations, the gas was treated as a dispersed phase everywhere in the domain. However, the SIMMER model, first introduced into the SIMMER-code [4], takes into account the distinction in morphology that phases can have in the domain. The morphology of the phases has to be reflected by appropriate parameters in the drag force. The magnitude of the force density for the drag is

$$|D| = C_D\, a\, \frac{1}{2}\rho\, |\mathbf{V_R}|^2, \tag{9}$$

where C_D is the drag coefficient, a is the interfacial area density, and ρ is the density of the continuous phase (if the other phase is a dispersed phase). $\mathbf{V_R}$ is the relative velocity between the two phases.

In the SIMMER model, the drag force depends on the gas void fraction α_G. The gas is assumed to have the morphology of bubbles where the gas void fraction is low, that is, $\alpha_G < 0.3$. Where the gas void fraction is high ($\alpha_G > 0.7$), droplets are supposed to be present in gas. In the intermediate range ($0.3 < \alpha_G < 0.7$), a linear interpolation between bubble drag and droplet drag is performed. This means that the interfacial area density a and the continuous phase density ρ depend on the gas void fraction, which is used as indicator for the morphology of both phases.

4.1. The Continuous Phase Density. If the gas void fraction is low, the liquid phase is the continuous phase ($\rho = \rho_L$). For high gas void fractions, the gas is the continuous phase ($\rho = \rho_G$). In the intermediate range, the density ρ is interpolated:

$$\rho = \begin{cases} \rho_L, & \text{for } \alpha_G \le 0.3, \\ \rho_G, & \text{for } \alpha_G \ge 0.7, \\ \rho_L + (\rho_G - \rho_L)\dfrac{\alpha_G - 0.3}{0.7 - 0.3}, & \text{else.} \end{cases} \tag{10}$$

4.2. The Area Density. The total area density for a spherical particle is

$$a_P = 6\frac{\alpha_P}{d_P}, \tag{11}$$

where α_P is the particle void fraction. The drag coefficients for particles are related to projected areas. The projected area of a sphere is 1/4th of its total area. Therefore, the so-called *projected* area densities for spherical bubbles and droplets are calculated as

$$a_B = \frac{3}{2}\frac{\alpha_G}{d_B}, \qquad a_D = \frac{3}{2}\frac{\alpha_L}{d_D}, \tag{12}$$

where d_B und d_D are the bubble diameter and the droplet diameter, respectively. In the simulations for simplicity, the same particle diameters are applied for droplets ($d = d_B = d_D$). Similar to the continuous phase density, the global area density a is defined as

$$a = \begin{cases} a_B, & \text{for } \alpha_G \le 0.3, \\ a_D, & \text{for } \alpha_G \ge 0.7, \\ a_B^* + (a_D^* - a_D^*)\dfrac{\alpha_G - 0.3}{0.7 - 0.3}, & \text{else,} \end{cases}$$
$$\text{where} a_B^* = a_B(\alpha_G = 0.3), \quad a_D^* = a_D(\alpha_G = 0.7). \tag{13}$$

4.3. The Drag Coefficient. Bubbles are assumed spherical, where the drag coefficient that has a constant value of 0.44 is applied. As an alternative, the Schiller-Naumann drag correlation is used which reads

$$C_D = \frac{24}{\mathrm{Re}}(1 + 0.15\mathrm{Re}^{0.687}). \tag{14}$$

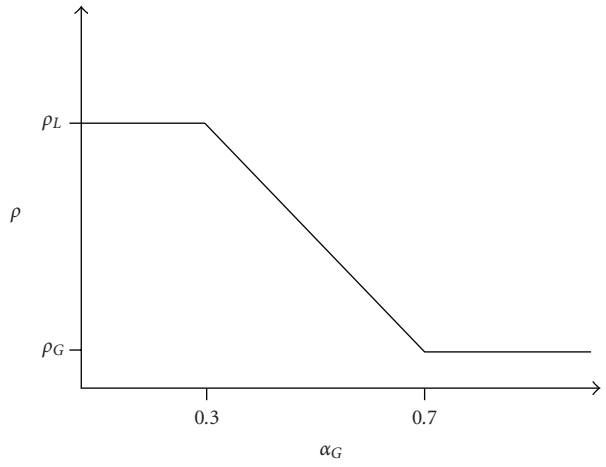

Figure 10: The continuous phase density as a function of the gas void fraction.

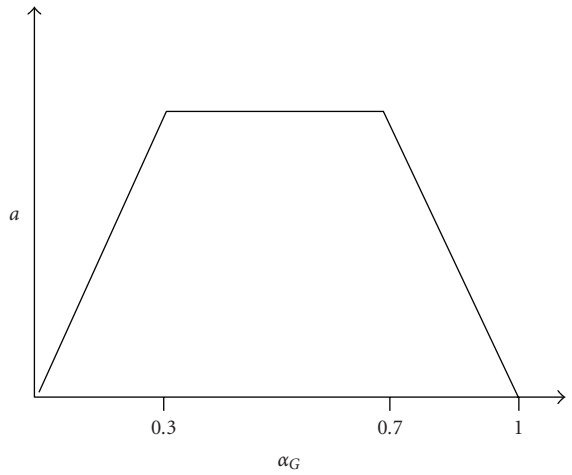

Figure 11: The area density as a function of the gas void fraction.

Since the material properties of the continuous phase are included in the Reynolds number, this equation yields two drag coefficients: $C_{D,B}$ for bubbles and $C_{D,D}$ for droplets. The drag coefficient C_D at a position in the domain is calculated according to the local gas void fraction in the same way as it is done for the continuous phase density and the area density:

$$C_D = \begin{cases} C_{D,B}, & \text{for } \alpha_G \le 0.3, \\ C_{D,D}, & \text{for } \alpha_G \ge 0.7, \\ C_{D,B} + (C_{D,D} - C_{D,B}) \dfrac{\alpha_G - 0.3}{0.7 - 0.3}, & \text{else.} \end{cases} \tag{15}$$

If a constant drag is used, a case differentiation is not necessary. Then $C_D = 0.44$ is applied everywhere.

4.4. Results. The development of the gas void fraction near the jet is studied using transient calculations. The drag is modified by applying either a constant drag coefficient or the Schiller-Naumann drag correlation. The calculations show a steady behaviour after a few seconds (see Figure 12).

The influence of the drag model (constant drag versus Schiller-Naumann drag) and of the particle diameter is very low. The gas entrainment seems to be always overestimated, since gas void fractions higher than 60% occur below the surface in all simulations.

There is no free parameter inside the SIMMER drag model, which could be used to adjust the entrainment according to an empirical correlation or another physical entrainment model. The effect of modified drag coefficients has not been studied yet. However, using arbitrary drag coefficients causes unphysical velocities for buoyant particles (e.g., bubbles) and it is therefore meaningless.

5. The Algebraic Interfacial Area Density (AIAD) Model

5.1. Drag Model. The algebraic interfacial area density model applies two different drag coefficients, $C_{D,B}$ for bubbles and $C_{D,S}$ for free surface. The interfacial area density a also depends on the morphology of the phases. For bubbles, the projected interfacial area density is

$$a_B = \frac{1}{4} \frac{6}{d_B} \alpha_G, \tag{16}$$

where d_B is the bubble diameter and α_G is the gas void fraction. For a free surface, the interfacial area density is

$$a_S = |\nabla \alpha_G|. \tag{17}$$

Since the concept of a continuous phase is not meaningful in the range of medium gas void fractions, instead of a continuous phase density, an average density is applied in (9). The average density is defined as

$$\rho = \rho_G \alpha_G + \rho_L (1 - \alpha_G), \tag{18}$$

where ρ_L and ρ_G are the liquid and the gas phase densities, respectively. In the bubbly regime, where α_G is low, the average density according to (18) is close to the liquid phase density ρ_L, which is the continuous phase density in this case. According to the flow regime (bubbly flow or stratified flow with a free surface), the corresponding drag coefficients and interfacial area densities have to be applied. This can be done by introducing a blending function f which is 1 for bubbly flow and 0 for stratified flow. Then, the area density and the drag coefficient are well defined everywhere in the domain by

$$a = f a_B + (1 - f) a_S, \tag{19}$$

$$C_D = f C_{D,B} + (1 - f) C_{D,S}. \tag{20}$$

It is not easy to find an algorithm that recognizes the flow regime of course. A very simple approach identifies the flow regime by using a gas void fraction limit α_0. Bubbly flow is assumed, where $\alpha_G < \alpha_0$, and stratified flow everywhere else. This would mean that blending function f is a step function. To avoid numerical problems, a continuous blending function is preferred (see Figure 13):

$$f = \frac{1}{1 + \exp\left(-100(\alpha_G - \alpha_0)\right)}. \tag{21}$$

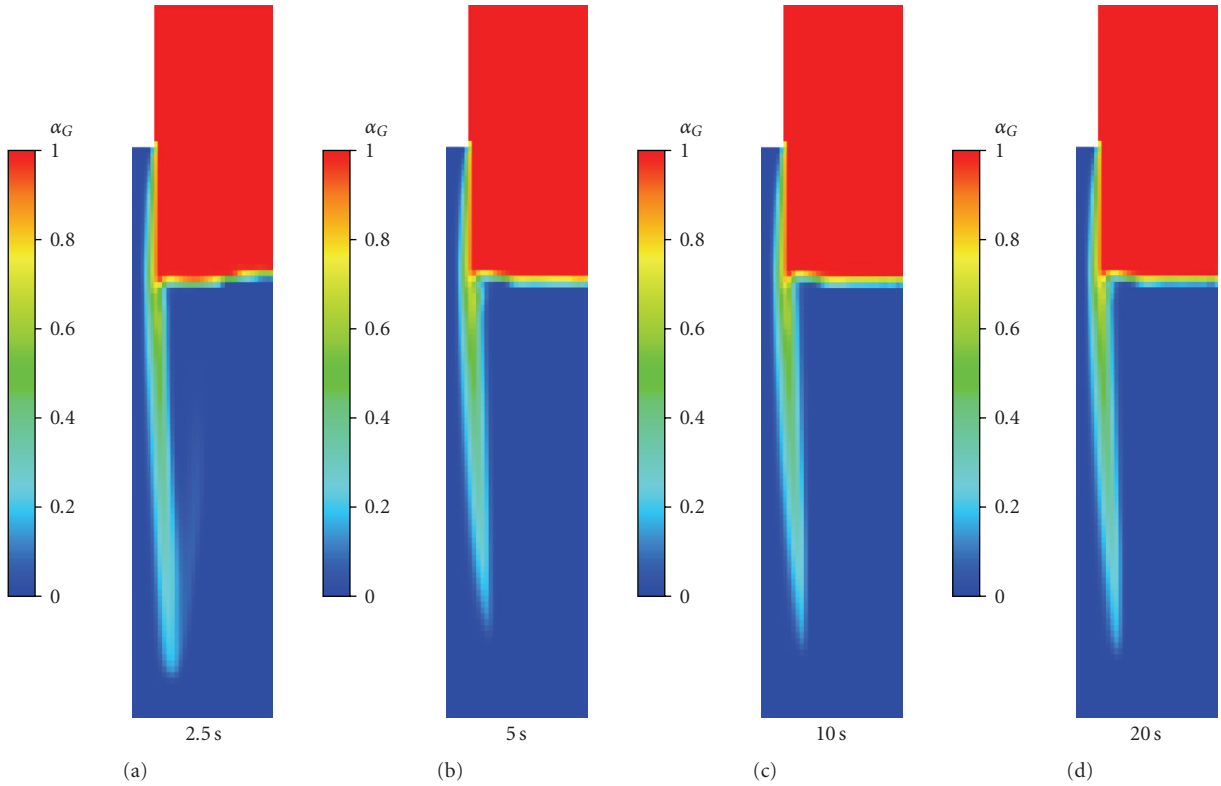

FIGURE 12: Gas void fraction for a constant drag ($C_D = 0.44$) and particle diameter $d = 2$ mm.

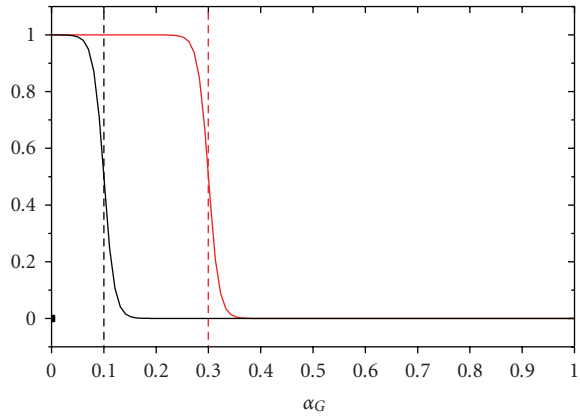

FIGURE 13: Blending function f according to (21) for $\alpha_0 = 0.1$ (black curve) and $\alpha_0 = 0.3$ (red).

For a first judgement, the gas entrainment is quantified by the gas void fractions just below the liquid interface. These are investigated for various values of the free surface drag coefficient $C_{D,S}$ and gas void fraction limits α_0. For the bubble drag coefficient, a constant value of $C_{D,B} = 0.44$ is taken, based on the drag of rigid spheres at the medium to high Reynolds number regime. As bubble diameter $d_B = 2$ mm is chosen.

5.2. Variation of the Surface Drag Coefficient. It is not clear which surface drag coefficient is appropriate for the situation of the impinging jet. The value of $C_{D,S}$ has to include subgrid information of the free surface structure ("rough" or "smooth"), and this certainly depends on the grid resolution, since with a finer mesh more details of the surface structure are resolved. Therefore, the free surface drag coefficient $C_{D,S}$ is varied over several orders of magnitude. Its influence on the gas void fraction below the water surface is studied while keeping the gas void fraction limit constant at $\alpha_0 = 0.1$. Note that the vertical water velocity at the nozzle is kept constant at $w_0 = 3$ m/s. The simulation is performed in the transient mode, but the result is almost in a steady state 10 seconds after the start when the jet is released from the nozzle.

Figure 14 shows the gas void fraction for $C_{D,S} = 10$. The gas entrainment seems to be overestimated here, since even at a depth of 50 cm below the water surface gas void fractions of 0.5 appear. In Figure 15(a), the corresponding bubble area density a_B is displayed. Note that a_B is proportional to the gas void fraction in (16), where it is greatest at $\alpha_G = 1$. Of course bubbles are not assumed to be present where $\alpha_G = 1$. According to (19) and (20), the blending function switches to free surface area density a_S at high gas void fractions. The free surface area density a_S for this case is shown in Figure 15(b). In Figure 16, the total area density a according to (19), the total drag coefficient C_D according to (20), and the product of a and C_D are shown.

As one can see from Figure 17 that the gas entrainment below the surface decreases if the surface drag coefficient is reduced. Note that the solver does not converge when $C_{D,S} = 0$. Since the maximal gas void fraction below

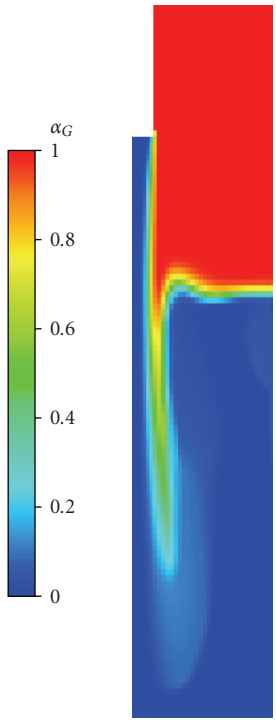

Figure 14: Gas void fraction α_G for the free surface drag coefficient $C_D = 10$.

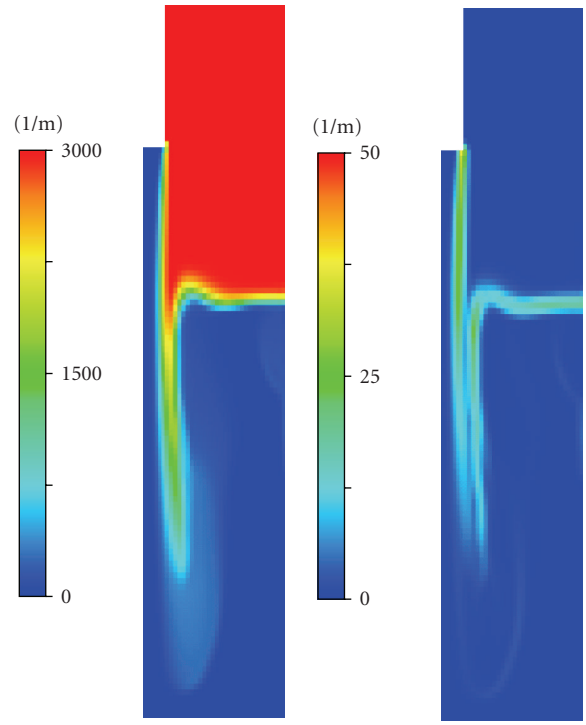

Figure 15: (a) Bubble projected area density a_B. (b) Free surface area density a_S.

the water surface is similar for $C_{D,S} = 0.1$ and $C_{D,S} = 0.01$, it is obvious that entrainment cannot be suppressed by further reducing $C_{D,S}$. Even for a very small bubble drag coefficient ($C_{D,B} = 0.044$), the gas entrainment is not negligible (see Figure 18). This indicates that numerical diffusion contributes to entrainment.

5.3. Variation of the Blending Function. By changing the gas void fraction limit α_0 the blending function can be modified. The value of α_0 has a significant influence on the gas entrainment (see Figure 19). It is not clear which value is appropriate since α_0 has no physical meaning. The definition of the blending function in general and of α_0 in particular is arbitrary to some extent. Note that in this case, the gas void fraction α_G is used as criterion to identify the location of the surface. This is a quite simple approach of course and a more sophisticated blending function could use the gradient of α_G to identify the surface since this gradient is high near the surface.

5.4. Grid Resolution. To check the influence of the grid resolution on the numerical solution, one calculation ($C_D = 0.1$) is repeated with a doubled spatial resolution. The gas void fraction fields are similar (see Figure 20).

Figure 20 shows that the gas plume is narrower in the calculation with the higher resolution. By an integration of the vertical flux density at this level according to (8) and by normalizing the result with the water flux at the nozzle $Q_{L,0}$, the dimensionless entrainment rate is obtained. For the coarse mesh, the entrainment rate is 3.5% and for the fine mesh it is about 6.4%. Of course the results of a CFD model should not depend on the grid resolution (see [5]). However, in a simulation of an impinging jet with increasing resolution more details of the complex surface geometry at the impinging zone is resolved. In the borderline case of an infinite resolution, the real bubble generation process could be captured. With a decreasing resolution, the geometry of the impinging zone is further simplified. This is the reason why the resolution has an effect on the simulated entrainment.

6. Conclusion

Generally for the CFD modelling of large hydrodynamic configurations with multiphase flow, the Euler-Euler approach is used. This is the reason why the capabilities of the Euler-Euler approach for the modelling of the impinging jet are investigated in this contribution. The physical process of bubble generation near the jet occurs on a very small scale, which cannot be resolved in a large-scale simulation. Therefore, the gas entrainment has to be described by a model, which represents the physics of the entrainment (e.g., a correlation). For the implementation of such a physical model in the frame of a CFD code, a mechanism is required that allows the adjustment of the gas entrained in the simulation according to the correlation. Since the gas and liquid phases tend to separate due to the buoyancy force, it is an obvious choice to use its counterpart—the drag force—to

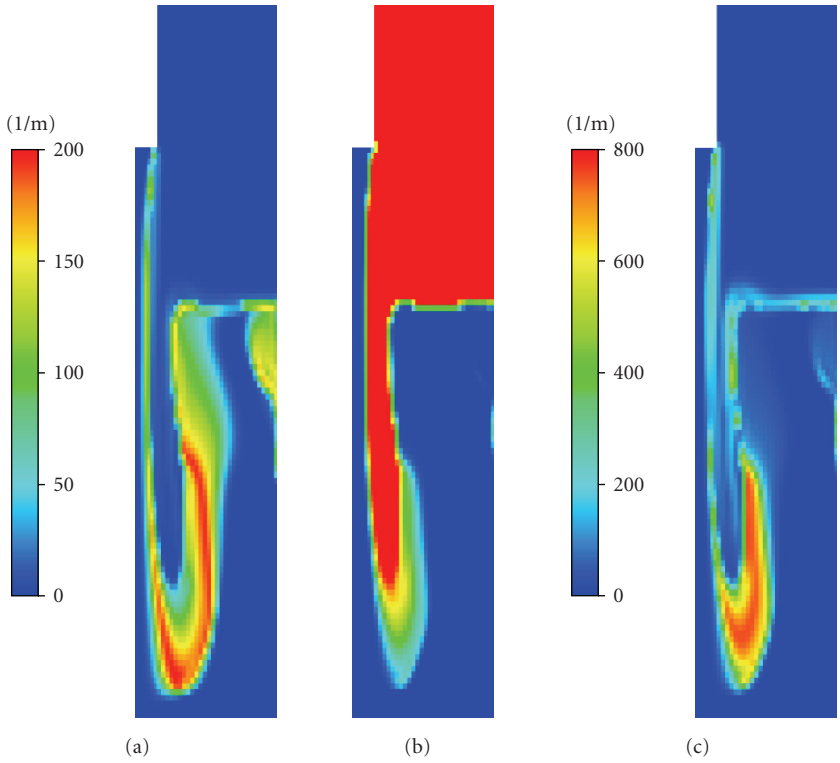

Figure 16: (a) Total area density a. (b) Total drag coefficient C_D. (c) Product $a\ C_D$.

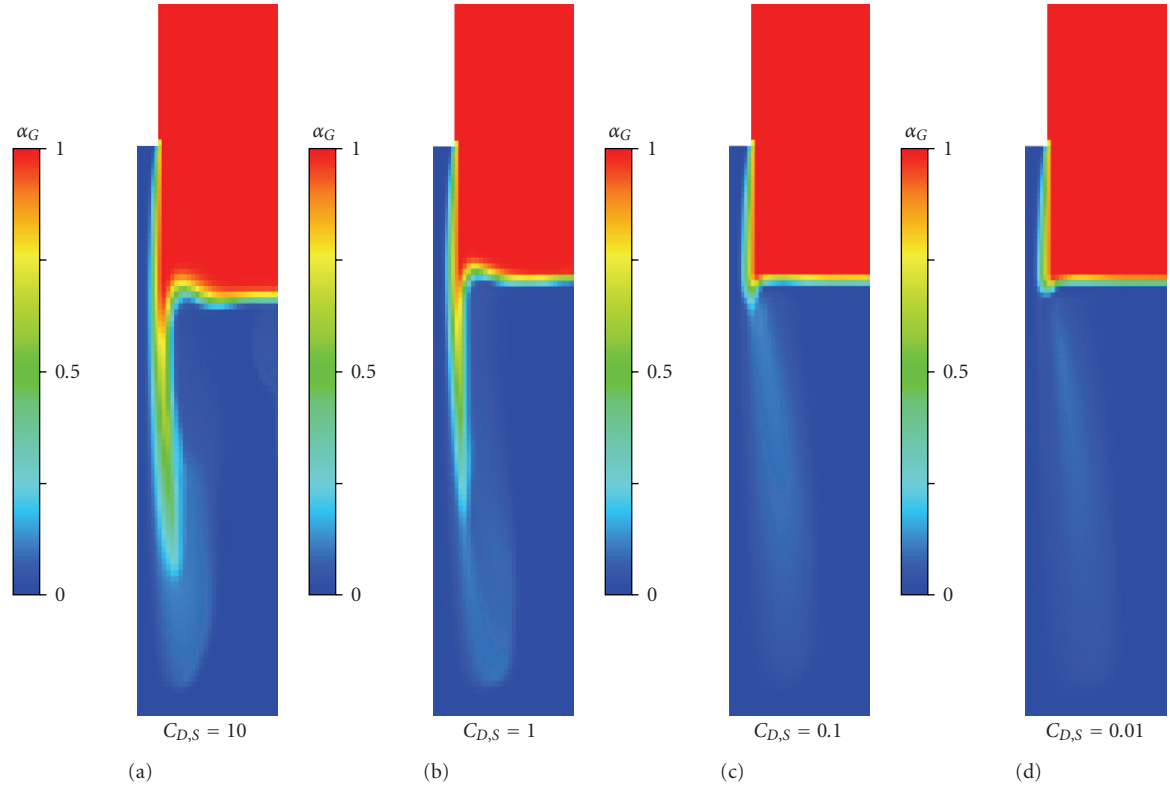

Figure 17: Gas void fraction for various surface drag coefficients. Representative plots at time $t > 10$ seconds.

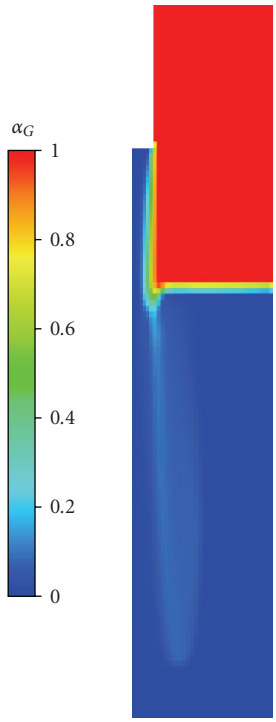

FIGURE 18: Gas void fraction for a very small bubble drag coefficient.

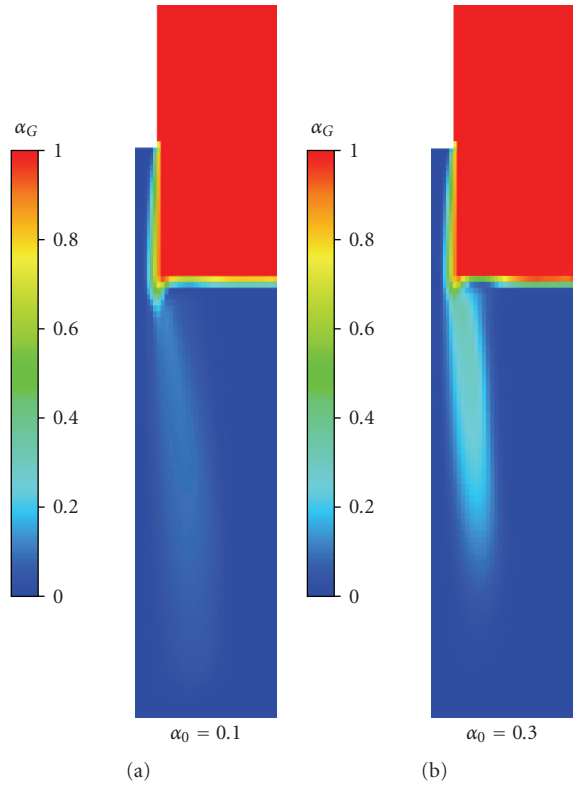

(a) (b)

FIGURE 19: Gas void fraction for $C_{D,S} = 0.1$ and various α_0.

obtain gas entrainment below the surface. However, if the gas is modelled as dispersed phase in an Euler-Euler simulation, the entrainment barely depends on the magnitude of drag coefficient, and it is obviously caused by numerical effects. Thus, this approach is not suitable for the implementation of a physical model for gas entrainment.

The SIMMER model assumes bubbly flow, where the gas void fraction is low and it assumes droplet flow, and droplets in gas, where the gas void fraction is high. A variation of the drag force—either by modification of the assumed particle diameter for bubbles and drops or by using different correlations for the drag coefficients of spherical particles—does not have a significant effect on the gas entrainment in the simulations performed with the SIMMER model. The gas entrainment is overestimated in all simulations, and there is no free parameter inside the SIMMER model, which allows the modification of the amount of gas entrainment in the simulation.

The algebraic interfacial area density (AIAD) model was found to be a suitable approach to adjust the entrainment. There are two free parameters inside the AIAD model that have a strong influence on the suction of gas across the liquid interface. These parameters are a drag coefficient for the free surface and the shape of the blending function. The blending function is used to identify regions of stratified flow (free surface flow) and regions of dispersed phase flow (bubbly flow) in order to apply the appropriate drag model.

Nevertheless, the gas entrainment calculated with the AIAD model is arbitrary, as the model does not realistically

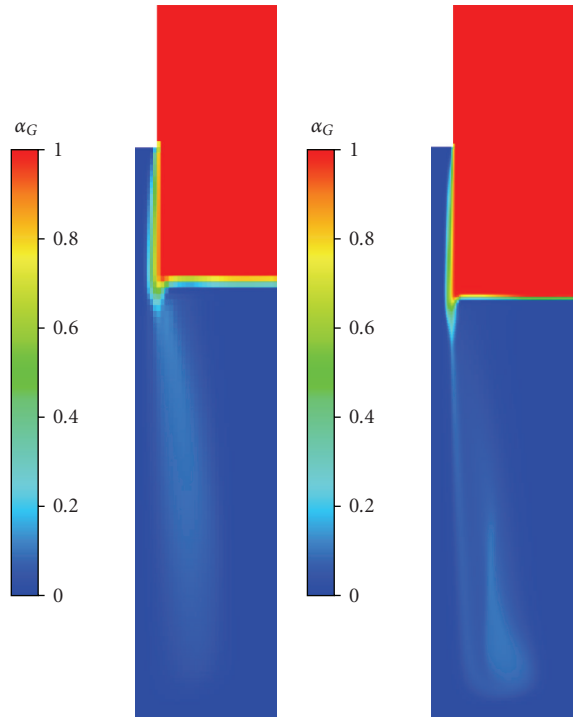

(a) (b)

FIGURE 20: Gas void fraction for two different grid resolutions, $C_D = 0.1$, representative plots.

reflect physics of the bubble entrainment. Further investigations will be performed to improve the parameterization in terms of the AIAD model.

(i) In the AIAD model, only the magnitude of the gas void fraction is evaluated by the blending function to identify the location of the free surface. In a more sophisticated approach, more criteria could be evaluated such as the gradient of the gas void fraction.

(ii) It is not clear which drag coefficients for the free surface are appropriate. The drag coefficient should also reflect the roughness of the jet surface, for example.

(iii) Up to now, the blending function is meant to identify the location of the free surface. With a more complex algorithm, it might be possible to identify the region where the jet entrains gas. This would allow applying special closure models (e.g., drag forces) to obtain a more controlled gas entrainment there.

(iv) The parameters for a realistic entrainment probably depend on the grid resolution.

(v) Up to now, the literature about gas entrainment near impinging jets is rather fragmentary. More experimental data are necessary to adjust the CFD models and obtain realistic entrainment in simulations. The Forschungszentrum Dresden-Rossendorf (FZD) is planning to perform new experiments with impinging jets. New sensors for multiphase flow measurements, which have been developed at the FZD, will also be used.

Nomenclature

Symbols

α: [-] Void fraction
α_0: [-] Gas void fraction limit
a: [1/m] Interfacial area density
C_D: [-] Drag coefficient
d: [m] Equivalent diameter
D: [N/m^3] Force density
d_0: [m] Nozzle diameter
g: [m/s^2] Gravity
h: [m] Height
h_j: [m] Jet height above water level
h_p: [m] Penetration depth
q: [m/s] Vertical flux density
Q: [m^3/s] Vertical flux
$Q_{L,0}$: [m^3/s] Liquid flux at the jet nozzle
ρ: [kg/m^3] Density of the continuous phase
$\mathbf{V_R}$: [m/s] Relative velocity
w: [m/s] Vertical velocity
w_0: [m/s] Jet velocity at the nozzle
w_j: [m/s] Jet velocity at water level.

Indices

G: Gas
L: Liquid
B: Bubble
S: Surface
+: Upward
−: Downward.

Acknowledgment

The NURESIM project is partly funded by the European Commission in the framework of the Sixth Framework Program (2004–2006).

References

[1] ANSYS CFX-Solver Modeling Guide, ANSYS CFX Release 11.0.
[2] A. K. Biń, "Gas entrainment by plunging liquid jets," *Chemical Engineering Science*, vol. 48, no. 21, pp. 3585–3630, 1993.
[3] A. Ohkawa, D. Kusabiraki, Y. Kawai, N. Sakai, and K. Endoh, "Some flow characteristics of a vertical liquid jet system having downcomers," *Chemical Engineering Science*, vol. 41, no. 9, pp. 2347–2361, 1986.
[4] S. Kondo, Y. Tobita, K. Morita, D.J. Brear, K. Kamiyama, H. Yamano, S. Fujita, W. Maschek, E.A. Fischer, E. Kiefhaber, G. Buckel, E. Hesselschwerdt, P. Coste, and S. Pigny, "Current status and validation of the SIMMER-III LMFR safety analysis code," in *Proceedings of the 7th International Conference on Nuclear Engineering (ICONE '07)*, vol. 1, pp. 19–23, Kyoto, Japan, April 1999.
[5] F. R. Menter, "CFD best practice guidelines for CFD code validation for reactor-safety applications," Deliverable Report EVOL-ECORA-D01, ECORA, 2002.

Hindawi Publishing Corporation
Science and Technology of Nuclear Installations
Volume 2009, Article ID 953527, 8 pages
doi:10.1155/2009/953527

Research Article

Modeling of Multisize Bubbly Flow and Application to the Simulation of Boiling Flows with the Neptune_CFD Code

Christophe Morel[1] and Jérôme M. Laviéville[2]

[1] *Commissariat à l'Energie Atomique, DEN/DER/SSTH/LMDL, 17 Rue des Martyrs, 38054 Grenoble Cedex 9, France*
[2] *R&D Division, Electricité de France, 6 Quai Watier, 78400 Chatou, France*

Correspondence should be addressed to Christophe Morel, christophe.morel@cea.fr

Received 19 December 2007; Accepted 9 June 2008

Recommended by Fabio Moretti

This paper describes the modeling of boiling multisize bubbly flows and its application to the simulation of the DEBORA experiment. We follow the method proposed originally by Kamp, assuming a given mathematical expression for the bubble diameter pdf. The original model is completed by the addition of some new terms for vapor compressibility and phase change. The liquid-to-interface heat transfer term, which essentially determines the bubbles condensation rate in the DEBORA experiment, is also modeled with care. First numerical results realized with the Neptune_CFD code are presented and discussed.

1. Introduction

This paper describes the modeling of boiling multisize bubbly flows and its application to the simulation of the DEBORA experiment (see [1]). First of all, the two-fluid model we use for the calculation of boiling bubbly flows is presented (see [2, 3]). In its first version, this two-fluid model assumed that the bubbles can be characterized by a single bubble diameter which is the classical Sauter mean diameter. Of course, this diameter is not a constant, but is determined as a function of the bubbles interfacial area concentration and the void fraction. As a consequence, the mean bubble diameter evolves according to several physical phenomena: bubble coalescence and breakup, but also phase change phenomena, including bubble nucleation and vapor compressibility inside the bubbles. All these phenomena are taken into account as different source terms in the interfacial area concentration balance equation.

In real flows, a bubble diameter spectrum is often observed, rather than a single bubble diameter. In order to take this diameter spectrum into account, Kamp et al. (see [4–6]) introduced a log-normal law in order to mathematically describe the bubble probability density function (pdf). As a consequence, the bubble diameter pdf is a function of only two parameters which can be analytically expressed as functions of two particular moments of the bubble diameter distribution function. The interfacial area concentration is one of these two moments. Therefore, only one additional moment transport equation is necessary in order to be able to reconstruct the bubble diameter distribution function, hence extending our previous models to the multisize effects appearing in boiling bubbly flows. The original work of Kamp was devoted to the study of bubble coalescence in adiabatic flows under microgravity. Here, we extend his model ability to boiling bubbly flows by taking into account the vapor compressibility as well as phase change terms in the different balance equations.

The outline of the paper is the following. The classical two-fluid model for boiling bubbly flows is summarized in Section 2. In Section 3, the original model of Kamp is briefly recalled. This model is extended in Section 4 in order to take into account the vapor compressibility as well as the phase change effects, including wall nucleation, into the different balance equations. Section 5 is devoted to the modeling of the liquid-to-interface heat transfer term including the multisize effect of the bubbles. Numerical simulations of one DEBORA experimental test realized with the Neptune_CFD code are illustrated in Section 6, before concluding and

making some perspectives for future work in Section 7. This activity was realized in the context of the European NURESIM project.

2. Two-Fluid Model for Boiling Bubbly Flow

The two-fluid model we use for our boiling bubbly flow calculations is constituted of the following six balance equations (e.g., [3]):

(i) two mass balance equations:

$$\frac{\partial \alpha_k \rho_k}{\partial t} + \nabla \cdot (\alpha_k \rho_k \underline{V}_k) = \Gamma_k \quad k = L, G, \tag{1}$$

where t is the time, α_k, ρ_k, $\underline{V}_k$ denote the volumetric fraction of phase k, its averaged density and velocity and Γ_k is the interfacial mass transfer per unit volume and unit time; the phase index k takes the values L for the liquid phase and G for the gas phase;

(ii) two momentum balance equations:

$$\frac{\partial \alpha_k \rho_k \underline{V}_k}{\partial t} + \nabla \cdot (\alpha_k \rho_k \underline{V}_k \underline{V}_k) = -\alpha_k \underline{\nabla} p + \underline{M}_k + \alpha_k \rho_k \underline{g} + \nabla \cdot [\alpha_k (\underline{\underline{\tau}}_k + \underline{\underline{\tau}}_k^T)] \quad k = L, G, \tag{2}$$

where p is the pressure, g is the gravity acceleration, $\underline{M}_k$ is the interfacial momentum transfer per unit volume and unit time, and $\underline{\underline{\tau}}_k$ and $\underline{\underline{\tau}}_k^T$ denote the molecular and turbulent stress tensors, the latter being also called the Reynolds stress tensor;

(iii) two total enthalpy balance equations:

$$\frac{\partial}{\partial t}\left[\alpha_k \rho_k \left(h_k + \frac{V_k^2}{2}\right)\right] + \nabla \cdot \left(\alpha_k \rho_k \left(h_k + \frac{V_k^2}{2}\right) \underline{V}_k\right) = \alpha_k \frac{\partial p}{\partial t} + \alpha_k \rho_k \underline{g} \cdot \underline{V}_k + \Gamma_k \left(h_{ki} + \frac{V_k^2}{2}\right) + q_{ki}'' a_i + q_{wk}''' - \nabla \cdot [\alpha_k (\underline{q}_k + \underline{q}_k^T)] \quad k = L, G, \tag{3}$$

where h_k is the phase-averaged enthalpy for phase k and h_{ki} is the interfacial-averaged enthalpy. We have assumed that the two phases are governed by the same averaged pressure field p and we make no distinction between the pressures in the two phases or between the bulk pressure and the interface pressure for simplicity. The three terms Γ_k, M_k, and $q_{ki}'' a_i$ denote the interfacial transfer terms of mass, momentum, and heat, the quantity a_i being the interfacial area concentration. The terms q_{wk}''' denote the wall-to-fluid heat transfer per unit volume and unit time for each phase. The heterogeneous (wall) nucleation of bubbles is included as a part of the term Γ_k (the bubble heterogeneous nucleation corresponds to an interfacial transfer of mass between phases, even if it is located onto the heated wall surface). The two terms $\underline{q}_k$ and $\underline{q}_k^T$ denote the molecular and turbulent heat fluxes inside phase k. Except for the liquid-to-interface heat transfer term $q_{Li}'' a_i$ (see Section 5), the modeling of the different averaged transfer terms (interfacial, turbulent, and wall transfer terms) is largely discussed in our previous papers (see [2, 3, 7]). Here, we only present what has been changed through the introduction of the bubble multisize modeling.

3. Kamp's Model for the Coalescence of Multisize Bubbles

Kamp et al. (see [4–6]) propose to model the bubble size distribution function by a log-normal law. The bubbles are assumed to remain spherical and are characterized by their diameter d. The γ's moment of the bubble distribution function and the log-normal law for the bubble diameter pdf are given by

$$S_\gamma \hat{=} n \int P(d) d^\gamma \delta d, \qquad P(d) = \frac{1}{\sqrt{2\pi}\hat{\sigma} d} e^{-\{\ln(d/d_{00})\}^2/2\hat{\sigma}^2}, \tag{4}$$

where $P(d)$ denotes the bubble diameter pdf and the function $f = nP$ is the bubble diameter distribution function, n being the total number of bubbles per unit volume of the two-phase mixture. It should be noted that n and $P(d)$ are local instantaneous quantities (defined in the sense of the ensemble average). In fact, n and $P(d)$ should be noted as $n(\underline{x}, t)$ and $P(d; \underline{x}, t)$ but we have omitted their dependence in the position $\underline{x}$ and time t for simplicity. The diameter pdf P depends on $(\underline{x}, t)$ through the dependence of the two parameters $d_{00}(\underline{x}, t)$ and $\hat{\sigma}(\underline{x}, t)$. It should be noted that d, $\underline{x}$, and t are independent variables. The first four remarkable moments of the bubble diameter distribution function are related to more usual quantities by the following relations:

$$n \hat{=} S_0, \qquad d_{10} \hat{=} \frac{S_1}{n} \qquad , a_i \hat{=} \pi S_2, \qquad \alpha \hat{=} \frac{\pi S_3}{6}, \tag{5}$$

where d_{10} is a mean bubble diameter, a_i is the interfacial area concentration, and α is the void fraction (vapor volumetric fraction). An infinity of mean diameters can be constructed by using the following definition:

$$d_{\gamma\delta} \hat{=} \left(\frac{S_\gamma}{S_\delta}\right)^{1/(\gamma-\delta)}. \tag{6}$$

The diameter d_{10} is one of them, the Sauter mean diameter d_{32} constructed with the second and third moments is another one. The two parameters of the diameter pdf are analytically expressed by the following functions of the particular moments S_1 and S_2 and of the void fraction α (see [5]):

$$\hat{\sigma} = \sqrt{\ln\left(\frac{6\alpha S_1}{\pi S_2^2}\right)}, \qquad d_{00} = \frac{6\alpha}{\pi S_2} e^{-5\hat{\sigma}^2/2}. \tag{7}$$

Then, with these two parameters being determined, any moment defined by the first relation (4) can be expressed analytically by the following relation:

$$S_\gamma = \frac{6\alpha}{\pi} d_{00}^{\gamma-3} e^{\hat{\sigma}^2/2(\gamma^2-9)}. \tag{8}$$

With the void fraction field α being part of the solution of the equations of the two-fluid model (1)–(3), it is sufficient then to use two additional balance equations for the two particular moments S_1 and S_2 to completely close the geometrical quantities (provided that these two equations are themselves closed). The departure point is the so-called Liouville equation for the bubble diameter distribution function which can be derived in a very general manner as

$$\frac{\partial nP(d)}{\partial t} + \nabla\cdot[nP(d)\underline{v}(d)] = -\frac{\partial}{\partial d}[GnP(d)] + \varphi(d,\underline{x},t), \tag{9}$$

where $\underline{v}(d)$ is the velocity of a bubble having a diameter d, the quantity $G(d;\underline{x},t)$ is the Lagrangian derivative of the bubble diameter measured along the bubble path. It represents the continuous bubble size variation due to vapor compressibility and phase change. The last term $\varphi(d,\underline{x},t)$ represents all phenomena which are responsible for discontinuous bubble diameter changes, namely the bubble coalescence and breakup as well as bubble nucleation and collapse. Multiplying (9) by d^γ and integrating the resulting equation with respect to d from zero to infinity, the following balance equation for the γ's moment is obtained:

$$\frac{\partial S_\gamma}{\partial t} + \nabla\cdot(S_\gamma \underline{v}_\gamma) = \gamma G_{\gamma-1} S_{\gamma-1} + \varphi_\gamma, \tag{10}$$

which is used for $\gamma = 1, 2$. In this equation, $\underline{v}_\gamma$, G_γ, and φ_γ are defined by the following relations:

$$\begin{aligned}
\underline{v}_\gamma &\hat{=} \frac{\int_0^\infty \underline{v}(d)d^\gamma P(d)\delta d}{\int_0^\infty d^\gamma P(d)\delta d},\\
G_\gamma &\hat{=} \frac{\int_0^\infty G(d)d^\gamma P(d)\delta d}{\int_0^\infty d^\gamma P(d)\delta d},\\
\varphi_\gamma &\hat{=} \int_0^\infty \varphi(d)d^\gamma \delta d.
\end{aligned} \tag{11}$$

In the original model of Kamp, the term proportional to $G_{\gamma-1}$ is neglected and the coalescence is the only effect taken into account in the modeling of φ_γ. At the end, the modeled equations for S_1 and S_2 read (see [5])

$$\begin{aligned}
&\frac{\partial S_1}{\partial t} + \nabla\cdot(S_1\underline{v}_G)\\
&\quad = \sqrt{\frac{8\pi}{3}}\left(\frac{6\alpha}{\pi}\right)^{2/3}\frac{C_t\varepsilon_L^{1/3}}{\sqrt{1.61}}(2^{1/3}-2)S_1^{4/3}f(1,\hat{\sigma},P_{00}),\\
&\frac{\partial S_2}{\partial t} + \nabla\cdot(S_2\underline{v}_G)\\
&\quad = \sqrt{\frac{8\pi}{3}}\left(\frac{6\alpha}{\pi}\right)^{1/3}\frac{C_t\varepsilon_L^{1/3}}{\sqrt{1.61}}(2^{2/3}-2)S_2^{5/3}f(2,\hat{\sigma},P_{00}),
\end{aligned} \tag{12}$$

where the two velocities $\underline{v}_1$ and $\underline{v}_2$ have been assumed to be equal to the averaged gas velocity $\underline{v}_G$. In the right-hand side of (12), ε_L is the dissipation rate of liquid turbulence, C_t is the ratio of the dispersed phase turbulent fluctuations by the continuous phase turbulent fluctuations, and $f(1,\hat{\sigma},P_{00})$ and $f(2,\hat{\sigma},P_{00})$ are numerical functions of the width parameter $\hat{\sigma}$ and the coalescence probability (based on the molecular chaos assumption) P_{00} of two bubbles having a diameter d_{00} (see the original work of Kamp for more information).

4. Extension of Kamp's Model to Vapor Compressibility and Phase Change

In the original work of Kamp, the term G in (9) was neglected. Here we calculate the corresponding terms $G_{\gamma-1}$ appearing in (10) when G is due to the vapor compressibility (Section 4.1) and to phase change (Section 4.2).

4.1. Vapor Compressibility. Let $D(\underline{x},t)$ be the bubble diameter in physical space (the notation d stands for the bubble diameter in phase space). In the absence of phase change, the bubble mass is conserved along its trajectory. As a consequence, the bubble diameter variation and the vapor density variation measured along the bubble path are related through

$$\frac{D_G D}{Dt} \hat{=} \frac{\partial D}{\partial t} + \underline{v}\cdot\nabla D = -\frac{D}{3\rho}\left(\frac{\partial\rho}{\partial t} + \underline{v}\cdot\nabla\rho\right), \tag{13}$$

where ρ denotes the vapor density and $\underline{v}$ the bubble velocity. The quantity G appearing in (9) is the conditional expectation of the Lagrangian derivative given by (13) conditioned by the equality $D(\underline{x},t) = d$:

$$\begin{aligned}
G &= \left\langle \frac{D_G D}{Dt} \mid D = d \right\rangle\\
&= -\frac{d}{3}\left\langle \frac{1}{\rho}\left(\frac{\partial\rho}{\partial t} + \underline{v}\cdot\nabla\rho\right) \mid D = d \right\rangle\\
&\cong -\frac{d}{3}\frac{1}{\rho_G}\left(\frac{\partial\rho_G}{\partial t} + \underline{v}_G\cdot\nabla\rho_G\right).
\end{aligned} \tag{14}$$

If we assume that the vapor density ρ and the bubble velocity $\underline{v}$ do not depend on the bubble diameter D, the conditional average appearing in the second expression of (14) can be replaced by the unconditional one. The last equality in (14) simply assumes that we neglect nonlinear effect when we average the term under the brackets, therefore keeping only first order effects. This is clearly an approximation where the microscopic quantities ρ and $\underline{v}$ characterizing the bubble are replaced by the macroscopic (averaged) ones ρ_G and $\underline{v}_G$.

Substituting the expression (14) into (10) and (11) gives the following expressions for the effect of the vapor compressibility on the two particular moments considered:

$$\begin{aligned}
\left[\frac{\partial S_1}{\partial t} + \nabla\cdot(S_1\underline{v}_G)\right]_{\text{compressibility}} &= G_0 S_0\\
&= -\frac{S_1}{3\rho_G}\left(\frac{\partial\rho_G}{\partial t} + \underline{v}_G\cdot\nabla\rho_G\right),
\end{aligned}$$

$$\left[\frac{\partial S_2}{\partial t}+\nabla\cdot(S_2\underline{v}_G)\right]_{\text{compressibility}}=2G_1S_1=-\frac{2}{3}\frac{S_2}{\rho_G}\left(\frac{\partial\rho_G}{\partial t}+\underline{v}_G\cdot\nabla\rho_G\right). \tag{15}$$

4.2. Phase Change. In the previous paragraph, we made the assumption of no phase change in order to derive the compressibility terms in the equations for $S_{1,2}$. Here we assume a constant vapor density $\rho=\rho_G$ in order to derive the phase change terms in the same equations. At the end, the two effects are taken into account simultaneously by assuming that the corresponding terms can be linearly superimposed into the $S_{1,2}$ balance equations. For a constant vapor density, the bubble diameter variation in physical space is simply given by

$$\frac{D_GD}{Dt}\hat{=}\frac{\partial D}{\partial t}+\underline{v}.\nabla D=\frac{2\dot{m}}{\rho_G}, \tag{16}$$

where $\dot{m}$ denotes the bubble mass gain per unit surface per unit time due to vaporization or condensation through the bubble surface. Substituting (16) into (14) gives

$$G=\left\langle\frac{D_GD}{Dt}\mid D=d\right\rangle=\left\langle\frac{2\dot{m}}{\rho_G}\mid D=d\right\rangle=\frac{2}{\rho_G}\langle\dot{m}\mid D=d\rangle. \tag{17}$$

The closure issue consists to propose an expression for the conditional expectation $\langle\dot{m}\mid D=d\rangle$. The simplest choice is to assume that $\langle\dot{m}\mid D=d\rangle$ is simply given by the ratio $(\Gamma_G-\Gamma_N)/a_I$, where Γ_G is the vapor source per unit volume per unit time and Γ_N is the part of this source due to newly nucleated bubbles, therefore $\Gamma_G-\Gamma_N$ is the part of the phase change through the surfaces of the already existing bubbles. Making this simple choice, we obtain the following expressions for the effect of the phase change on the two particular moments considered:

$$\left[\frac{\partial S_1}{\partial t}+\nabla\cdot(S_1\underline{v}_G)\right]_{\text{phase change}}=G_0S_0=\frac{2}{\rho_G}\frac{\Gamma_G-\Gamma_N}{a_I}S_0,$$
$$\left[\frac{\partial S_2}{\partial t}+\nabla\cdot(S_2\underline{v}_G)\right]_{\text{phase change}}=2G_1S_1=\frac{4}{\rho_G}\frac{\Gamma_G-\Gamma_N}{a_I}S_1, \tag{18}$$

where S_0 is the volumetric number of bubbles n obtained by making $\gamma=0$ into the relation (8). A more sophisticated model taking into account the dependence of $\langle\dot{m}\mid D=d\rangle$ on the diameter d will be presented in the next section.

4.3. A Few Words on Nucleation. In subcooled boiling flows, as this is the case for the DEBORA experiment, vapor bubbles are essentially nucleated onto the heated wall surface (heterogeneous nucleation) rather than in the liquid bulk, because the liquid is subcooled in the major part of the flow. Therefore, we can neglect a possible homogeneous nucleation in comparison to the heterogeneous nucleation. The newly nucleated bubbles are supposed to be generated with a unique size: the so-called detachment diameter d_d. In our model, this detachment diameter is calculated with the help of Ünal's correlation (see [8]), used together with the model of Kurul and Podowski [9] for the active nucleation site density. These models are used to estimate the vapor produced in the meshes adjacent to the wall due to nucleation Γ_N. Dividing Γ_N by the mass of a nucleated bubble $\rho_G\pi d_d^3/6$, the volumetric number of bubbles source term is obtained. The corresponding source terms in the S_1 and S_2 equations are simply obtained by multiplying this volumetric number of bubbles source term by the diameter d_d or by its square d_d^2, according to the order of the moment considered.

5. Heat and Mass Transfers through the Surface of the Existing Bubbles

For a relatively low speed flow, the local instantaneous interfacial balance of total energy (see [10, 11]) can be simplified:

$$(\underline{q}_G-\underline{q}_L)\cdot\underline{n}_G-\dot{m}(h_{GI}-h_{LI})\cong 0. \tag{19}$$

In this relation, $\underline{q}_G\cdot\underline{n}_G$ and $\underline{q}_L\cdot\underline{n}_G$ are the heat flux densities on the two sides of the interface, $\underline{n}_G$ being the unit vector normal to the interface directed towards the exterior of the bubble. The relation (19) is valid at each point of the bubble interface. The quantities h_{GI} and h_{LI} are the vapor and liquid enthalpies at the bubble interface, they are generally assumed to be equal to the saturation enthalpies. The relation (19) gives the link between the rate of phase change $\dot{m}$ and the two heat flux densities between the two phases and the interface. In a bubbly flow with relatively small bubbles, the temperature of the vapor inside the bubbles is generally close to the saturation temperature. In subcooled liquid, the rate of bubble condensation is essentially determined by the heat exchange on the liquid side, rather than the one on the vapor side. Neglecting $\underline{q}_G\cdot\underline{n}_G$ in comparison to $\underline{q}_L\cdot\underline{n}_G$ in the previous equation and introducing a Nusselt number Nu_L to characterize the liquid-to-interface heat transfer, (19) becomes

$$\dot{m}\cong\frac{\underline{q}_L\cdot\underline{n}_L}{h_{GI}-h_{LI}}=\frac{\mathrm{Nu}_L\lambda_L}{(h_{GI}-h_{LI})D}(\theta_L-\theta_{\text{sat}}), \tag{20}$$

where λ_L is the liquid thermal conductivity and θ_L and θ_{sat} represent the liquid and saturation temperatures, respectively. The Nusselt number is given by the Ranz-Marschall law [12]

$$\mathrm{Nu}_L=2+0.55\mathrm{Re}^{1/2}\mathrm{Pr}_L^{1/3}, \tag{21}$$

where Re and Pr_L are the bubble Reynolds number and the liquid Prandtl number, respectively. Neglecting the fluctuations of the enthalpies h_{GI} and h_{LI}, the averaging of the first relation (20) gives

$$q''_{LI}a_I\hat{=}\Gamma_G(h_{GI}-h_{LI})\ \text{with}$$
$$\Gamma_G\hat{=}\int\langle\dot{m}\mid D=d\rangle\pi d^2nP(d)\delta d, \tag{22}$$
$$q''_{LI}a_I\hat{=}\int\langle\underline{q}_L\cdot\underline{n}_L\mid D=d\rangle\pi d^2nP(d)\delta d,$$

where Γ_G and $q''_{LI}a_I$ are the average interfacial mass and heat transfer terms appearing in (1) and (3). The term Γ_G is related to the vapor phase because $\dot{m}$ is the bubble mass gain and $q''_{LI}a_I$ is the liquid-to-interface heat transfer per unit volume per unit time, the heat transfer density q''_{LI} being expressed per unit area per unit time, a_I being the interfacial area concentration. Equation (22) is very useful because it directly relates the mass transfer rate to the liquid-to-interface heat transfer rate (under the assumption of a nearly saturated vapor inside the bubbles). The averaging of the second relation (20) gives

$$q''_{LI}a_I \mathrel{\hat{=}} \int \left\langle \frac{\mathrm{Nu}_L\lambda_L}{D}(\theta_L - \theta_{\mathrm{sat}}) \mid D = d \right\rangle \pi d^2 nP(d)\delta d. \tag{23}$$

The relations (21) and (23) are the basic tools to calculate the average interfacial liquid-to-interface heat transfer. In what follows, we give three different approximated expressions for this term. The first one is a single-size approximation of the liquid-to-interface heat flux, it is given by

$$\begin{aligned} q''_{LI}a_I &\cong \int \pi d\mathrm{Nu}_L\lambda_L(\theta_L - \theta_{\mathrm{sat}})nP(d)\delta d \\ &\cong a_I \frac{\mathrm{Nu}_L(d_{32})}{d_{32}}\lambda_L(\Theta_L - \Theta_{\mathrm{sat}}). \end{aligned} \tag{24}$$

In this expression, it is implicitly assumed that all the bubbles have the same diameter which is given by the Sauter mean diameter $d_{32} = 6\alpha/a_I$ (single-size approximation). The relation (21) is directly calculated as a function of the Sauter mean diameter and the average relative velocity of the bubbles into the Reynolds number. The second (more precise) approximation consists in using the log-normal law for the bubble diameter pdf (4). The result is

$$\begin{aligned} q''_{LI}a_I = &\left[2\pi\lambda_L S_1 + 0.55\pi\lambda_L \frac{\mathrm{Pr}_L^{1/3}}{\nu_L^{1/2}}|v_r|^{1/2} n d_{00}^{3/2} \exp\left(\frac{9}{8}\hat{\sigma}^2\right)\right] \\ &\times (\Theta_L - \Theta_{\mathrm{sat}}). \end{aligned} \tag{25}$$

The dependence of the bubble Reynolds number Re on the bubble diameter d has been taken into account in the derivation of (25), but not the variation of the relative velocity $|v_r|$, also appearing in the Reynolds number, as a function of the bubble size. When using (25), the norm of the relative velocity is assumed to be given by the averaged fields. In order to alleviate this approximation, a third model has been constructed by assuming that the norm of the relative velocity can be accurately given by the terminal velocity

$$|v_r| \approx v_T = \sqrt{\frac{4}{3}\frac{\Delta\rho g d}{\rho_L C_D}}, \tag{26}$$

where $\Delta\rho$ is the absolute value of the density difference $|\rho_L - \rho_G|$ and C_D is the drag coefficient, which can be given for spherical bubbles by (e.g., [13])

$$C_D = \frac{24}{\mathrm{Re}}(1 + 0.1\mathrm{Re}^{3/4}). \tag{27}$$

Assuming that the bubble Reynolds number is sufficiently high in order to approximate the preceding relation by $C_D = 2.4/\mathrm{Re}^{1/4}$, we obtain the following relation for the square root of the terminal velocity:

$$v_T^{1/2} = \left(\frac{\Delta\rho g}{1.8\rho_c \nu_c^{1/4}}\right)^{2/7} d^{5/14}. \tag{28}$$

Reevaluating the liquid-to-interface heat transfer from (4), (21), (23), and (28) gives a third model:

$$\begin{aligned} q''_{LI}a_I = &\left[2\pi\lambda_L S_1 + 0.55\pi\lambda_L \frac{\mathrm{Pr}_L^{1/3}}{\nu_L^{1/2}}\left(\frac{\Delta\rho g}{1.8\rho_L \nu_L^{1/4}}\right)^{2/7}\right. \\ &\left.\times n d_{00}^{13/7} \exp\left(\frac{169}{98}\hat{\sigma}^2\right)\right](\Theta_L - \Theta_{\mathrm{sat}}). \end{aligned} \tag{29}$$

Now, having the model given by (20)-(21) for the bubble mass gain $\dot{m}$, we can evaluate more precisely the corresponding terms in the equations for the two moments S_1 and S_2, namely the terms G_0 and G_1 with G given from (17). The results are the following:

$$\begin{aligned} &\left[\frac{\partial S_1}{\partial t} + \nabla\cdot(S_1\underline{v}_G)\right]_{\text{phase change}} \\ &\quad = \begin{bmatrix} \dfrac{4}{\rho_G}\dfrac{\lambda_L}{h_{GI} - h_{LI}}\dfrac{n}{d_{00}}\exp\left(\dfrac{\hat{\sigma}^2}{2}\right) \\ +\dfrac{1.1}{\rho_G}\dfrac{\lambda_L}{h_{GI} - h_{LI}}\dfrac{\mathrm{Pr}_L^{1/3}}{\nu_L^{1/2}}\left(\dfrac{\Delta\rho g}{1.8\rho_L\nu_L^{1/4}}\right)^{2/7}\dfrac{n}{d_{00}^{1/7}}\exp\left(\dfrac{\hat{\sigma}^2}{98}\right) \end{bmatrix} \\ &\qquad \times (\Theta_L - \Theta_{\mathrm{sat}}), \\ &\left[\frac{\partial S_2}{\partial t} + \nabla\cdot(S_2\underline{v}_G)\right]_{\text{phase change}} \\ &\quad = \frac{8}{\rho_G}\frac{\lambda_L}{h_{GI} - h_{LI}} n(\Theta_L - \Theta_{\mathrm{sat}}) \\ &\qquad + \frac{2.2}{\rho_G}\frac{\lambda_L}{h_{GI} - h_{LI}}\frac{\mathrm{Pr}_L^{1/3}}{\nu_L^{1/2}}\left(\frac{\Delta\rho g}{1.8\rho_L\nu_L^{1/4}}\right)^{2/7} n d_{00}^{6/7}\exp\left(\frac{18}{49}\hat{\sigma}^2\right) \\ &\qquad \times (\Theta_L - \Theta_{\mathrm{sat}}). \end{aligned} \tag{30}$$

To conclude the modeling sections, we can summarize the complete modeling of boiling bubbly flows with multisize bubbles in its present state. The basic equations are the mass, momentum and total enthalpy balance equations written for the two phases, they are given by (1)–(3). A multisize model is used in conjunction with the two-fluid model to evaluate the evolution of the bubble diameter spectrum under several physical effects: coalescence, vapor compressibility, and phase-change. It should be noted that a bubble breakup term is removed in the present state of the model. A log-normal law is used to describe the bubble diameter pdf. This law involves two parameters d_{00} and $\hat{\sigma}$ which are analytically determined from two particular moments of the bubble diameter pdf (7). Therefore, a set of two additional transport equations are written for these two moments. These moments balance equations have the

general form (10) with their right-hand side including a coalescence model (12), a vapor compressibility model (15), and two possible phase change models (18) or (30). The model also includes wall nucleation source terms which are not presented here (see [2]). At the end, we have proposed several expressions for the liquid-to-interface heat transfer term appearing in the liquid enthalpy balance (3). This term is responsible for the bubble condensation in the core of the flow. The first one (24) is the classical expression used in usual (single size) bubbly flow models. The two others (25) and (29) take into account the bubble diameter spectrum as modeled by the log-normal law. The last one (29) also takes into account the dependence of the bubble relative velocity on the bubble diameter. All these models should be tested. In the following section, we give the results of a comparison of Neptune_CFD simulations with an experimental test of the DEBORA database.

6. Numerical Simulations of a Boiling Bubbly Flow

The DEBORA experiment, carried out at the French Commissariat à l'Energie Atomique (see [1]), has been chosen to evaluate our model. In this experiment, the R-12 has been adopted as the working fluid to simulate the PWR (pressurized water reactor) conditions under low pressure. Some liquid R-12 flows upwardly inside a vertical pipe having an internal diameter equal to 19.2 mm. A part of the tube wall of 3.5 m long is electrically heated. Numerous vapor bubbles are nucleated onto the heated wall surface, and condense in the core of the flow, where the liquid is subcooled. At the end of the heated section, the radial profiles of the void fraction, bubble diameter, and vertical bubble velocity are measured by means of an optical probe and the liquid temperature is measured by means of a thermocouple.

Here we evaluate the different models presented above on a particular DEBORA experimental test. The controlling parameters of this test are the following.

(i) Test pressure: 14.59 bar.

(ii) Inlet mass flux density (liquid only): 2027 kg/m^{2}s.

(iii) Liquid inlet temperature: 28.52°C.

(iv) Wall to fluid heat flux density: 76200 W/m^2.

All the models have been implemented in the multiphase Neptune_CFD code. With the flow being axi-symmetric, we use a two-dimensional axi-symmetric calculation grid. This grid is characterized by 80 axial meshes and 10 radial meshes. We assume that this relatively coarse grid is sufficient for a first test of the different models. The models tested are the three expressions of the liquid-to-interface heat flux (24), (25), and (29) and the multisize model for bubbly flows with the two different expressions (18) and (30) for the phase change terms. The compared quantities are the void fraction (Figure 1), the vapor mean velocity (Figure 2), the liquid temperature (Figure 3), the interfacial area concentration (Figure 4), the Sauter mean diameter d_{32} (Figure 5), and the mean diameter d_{20} defined by (6) (Figure 6). All the radial

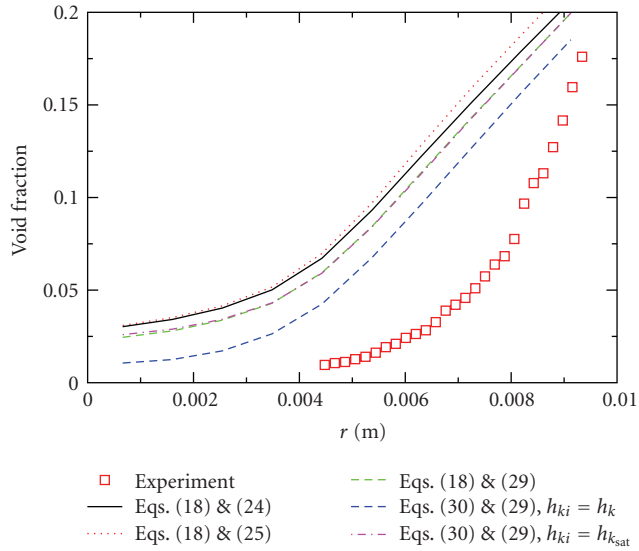

Figure 1: comparison of the different models on the void fraction profile.

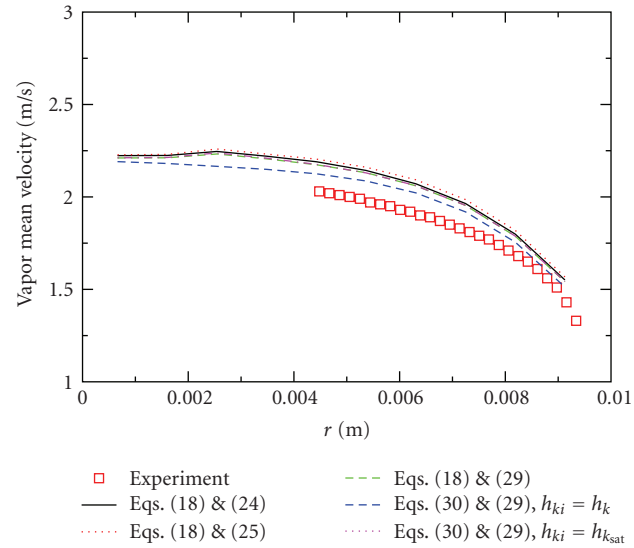

Figure 2: comparison of the different models on the vapor velocity profile.

profiles (experimental and calculated) have been taken at the end of the heated length.

Each figure compares the results of five calculations together with the experimental values.

According to these comparisons, the model giving better results on the void fraction, the vapor mean velocity, the liquid temperature, and the interfacial area concentration seems to be the one using (29) and (30) with the interfacial averaged enthalpies being equal to the phase averaged ones. It can also be seen that the void fraction is strongly overestimated for all the models tested, but the interfacial area concentration is overestimated too, therefore giving approximately the right values for the bubble Sauter mean diameter and the mean diameter d_{20}. The overestimation of

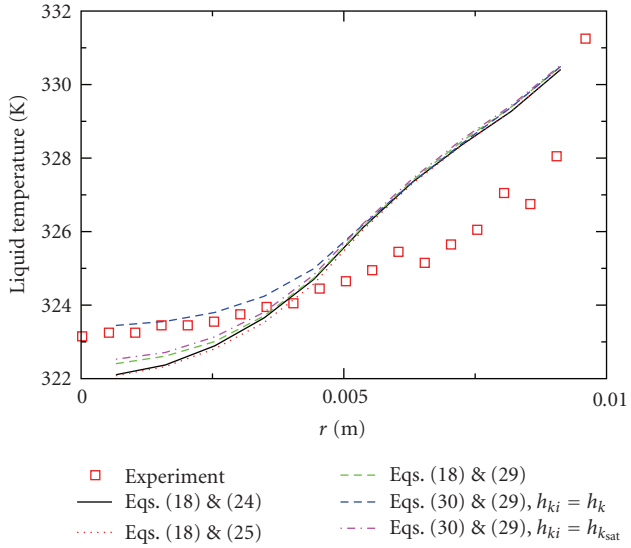

FIGURE 3: comparison of the different models on the liquid temperature profile.

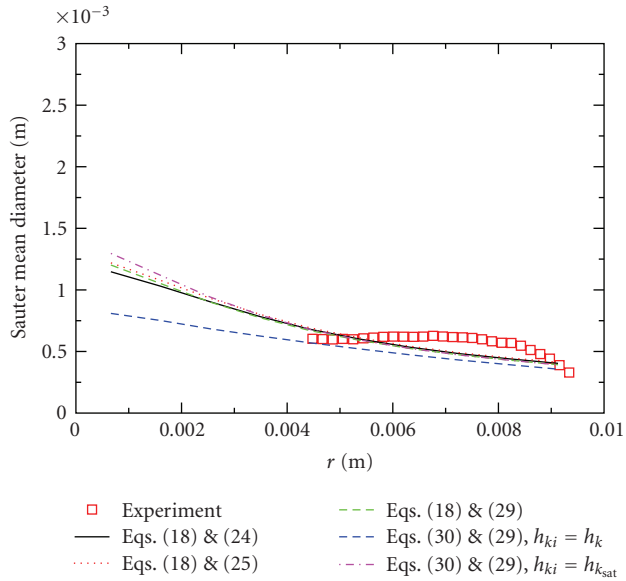

FIGURE 5: comparison of the different models on the Sauter mean diameter profile.

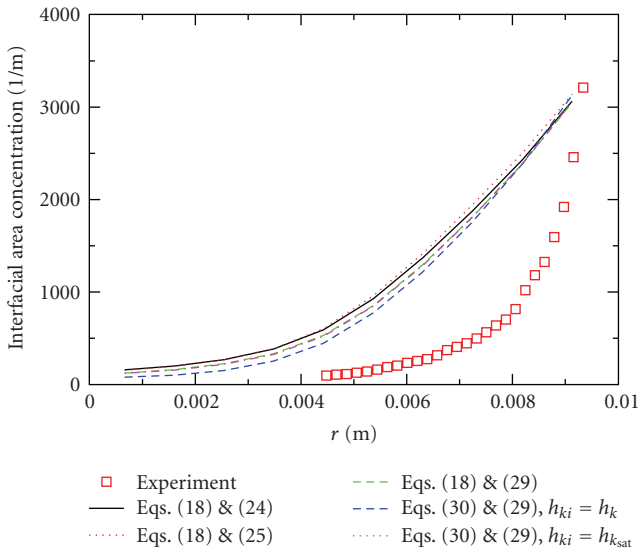

FIGURE 4: comparison of the different models on the interfacial area profile.

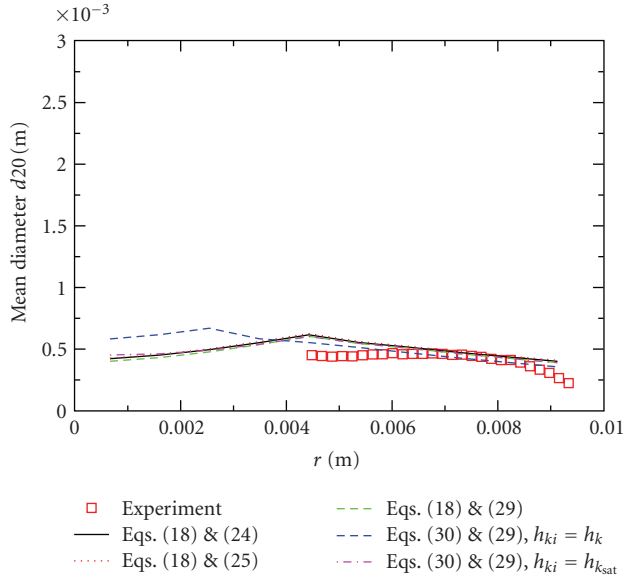

FIGURE 6: comparison of the different models on the mean diameter d_{20} profile.

the void fraction could be attributed to the inadequacy of the Ranz and Marschall law (21) to describe the condensation of bubbles in a subcooled liquid. This issue will be studied in future work.

7. Conclusions

A multisize model for boiling bubbly flows has been presented in detail. This model is not completely achieved (e.g., a bubble breakup term is missing in the equations). Nevertheless, we made first calculations to evaluate the capabilities of this model in its present state. Five different calculations have been done and compared to a single experimental test of the DEBORA experiment. It has been shown that the results are sensitive to the expressions used for the liquid-to-interface heat transfer (24), (25), or (29) and to the phase change terms in the geometrical equations (18) or (30). The model using the particular expressions (29) and (30), with the interfacial averaged enthalpies being given by the phase averaged ones, gives better results. Unfortunately, the void fraction and the interfacial area density are strongly overestimated. Further investigations are needed to clarify these questions.

Several issues can be raised for future developments:

(i) a bubble breakup model should be added for completeness of the model;

(ii) a bubble collapse model is missing too;

(iii) the physical model given by Ranz and Marschall [12] (21) could not be adapted for condensing bubbles

in subcooled liquid. The validity of this model should be evaluated first (perhaps by using DNS calculations).

Acknowledgments

Neptune_CFD is a three-dimensional two-fluid code developed more especially for nuclear reactor applications within the framework of the Neptune project, financially supported by CEA (Commissariat à l'Energie Atomique), EDF (Electricité de France), IRSN (Institut de Radioprotection et de Sûreté Nucléaire), and AREVA-NP. This activity was realized in the context of the NURESIM project financed by the European Union.

References

[1] J. Garnier, E. Manon, and G. Cubizolles, "Local measurements on flow boiling of refrigerant 12 in a vertical tube," *Multiphase Science and Technology*, vol. 13, no. 1-2, pp. 1–111, 2001.

[2] W. Yao and C. Morel, "Volumetric interfacial area prediction in upward bubbly two-phase flow," *International Journal of Heat and Mass Transfer*, vol. 47, no. 2, pp. 307–328, 2004.

[3] C. Morel, S. Mimouni, J. M. Laviéville, and M. Boucker, "R113 boiling bubbly flow in an annular geometry simulated with the NEPTUNE code," in *Proceedings of the 11th International Topical Meeting on Nuclear Reactor Thermalhydraulics (NURETH-11)*, Avignon, France, October 2005, paper: 248.

[4] A. M. Kamp, *Ecoulements turbulents à bulles dans une conduite en micropesanteur*, Ph.D. thesis, Institut National Polytechnique de Toulouse, Toulouse, France, 1996.

[5] A. M. Kamp, A. K. Chesters, C. Colin, and J. Fabre, "Bubble coalescence in turbulent flows: a mechanistic model for turbulence-induced coalescene applied to microgravity bubbly pipe flow," *International Journal of Multiphase Flow*, vol. 27, no. 8, pp. 1363–1396, 2001.

[6] C. Colin, X. Riou, and J. Fabre, "Turbulence and shear-induced coalescence in gas-liquid pipe flows," in *Proceedings of the 5th International Conference on Multiphase Flow (ICMF '04)*, Yokohama, Japan, May-June 2004, paper no. 425.

[7] C. Morel, J. Pouvreau, J. M. Laviéville, and M. Boucker, "Numerical simulations of a bubbly flow in a sudden expansion with the NEPTUNE code," in *Proceedings of the 3rd International Symposium on Two-Phase Flow Modeling and Experimentation*, Pisa, Italy, September 2004.

[8] H. C. Ünal, "Maximum bubble diameter, maximum bubble-growth time and bubble-growth rate during the subcooled nucleate flow boiling of water up to 17.7 MN/m^2," *International Journal of Heat and Mass Transfer*, vol. 19, no. 6, pp. 643–649, 1976.

[9] N. Kurul and M. Z. Podowski, "Multidimensional effects in forced convection subcooled boiling," in *Proceedings of the 9th International Heat Transfer Conference*, vol. 1, pp. 21–26, Jerusalem, Israel, August 1990, paper no.-04.

[10] J. M. Delhaye, *Thermohydraulics of Two-Phase Systems for Industrial Design and Nuclear Engineering*, McGraw-Hill, New York, NY, USA, 1981.

[11] M. Ishii and T. Hibiki, *Thermo-Fluid Dynamics of Two-Phase Flow*, Springer, New York, NY, USA, 2006.

[12] W. E. Ranz and W. R. Marschall, "Evaporation from drops," *Chemical Engineering Progress*, vol. 48, pp. 173–180, 1952.

[13] M. Ishii, "Two-fluid model for two-phase flow," *Multiphase Science and Technology*, vol. 5, no. 1–4, pp. 1–63, 1990.

Hindawi Publishing Corporation
Science and Technology of Nuclear Installations
Volume 2009, Article ID 436218, 12 pages
doi:10.1155/2009/436218

Research Article

CFD Analysis of a Slug Mixing Experiment Conducted on a VVER-1000 Model

F. Moretti,[1] D. Melideo,[1] A. Del Nevo,[1] F. D'Auria,[1] T. Höhne,[2] and E. Lisenkov[3]

[1] *Dipartimento di Ingegneria Meccanica, Nucleare e della Produzione, Università di Pisa (UNIPI), 2 Via Diotisalvi, 56100 Pisa, Italy*
[2] *Forschungszentrum Dresden-Rossendorf (FZD) Institute of Safety Research, P.O. Box 51 01 19, 01314 Dresden, Germany*
[3] *Experimental Thermal Hydraulics Department, OKB Gidropress, Ordshonikidize 21, 142103 Podolsk, Moscow district, Russia*

Correspondence should be addressed to F. Moretti, f.moretti@ing.unipi.it

Received 13 June 2008; Accepted 3 November 2008

Recommended by Dirk Lucas

A commercial CFD code was applied, for validation purposes, to the simulation of a slug mixing experiment carried out at OKB "Gidropress" scaled facility in the framework of EC TACIS project R2.02/02: "Development of safety analysis capabilities for VVER-1000 transients involving spatial variations of coolant properties (temperature or boron concentration) at core inlet." Such experimental model reproduces a VVER-1000 nuclear reactor and is aimed at investigating the in-vessel mixing phenomena. The addressed experiment involves the start-up of one of the four reactor coolant pumps (the other three remaining idle), and the presence of a tracer slug on the starting loop, which is thus transported to the reactor pressure vessel where it mixes with the clear water. Such conditions may occur in a boron dilution scenario, hence the relevance of the addressed phenomena for nuclear reactor safety. Both a pretest and a posttest CFD simulations of the mentioned experiment were performed, which differ in the definition of the boundary conditions (based either on nominal quantities or on measured quantities, resp.). The numerical results are qualitatively and quantitatively analyzed and compared against the measured data in terms of space and time tracer distribution at the core inlet. The improvement of the results due to the optimization of the boundary conditions is evidenced, and a quantification of the simulation accuracy is proposed.

1. Introduction

In a pressurized water reactor (PWR) several transient scenarios can be hypothesized leading to a perturbation of the coolant time and space distribution at the core inlet (such as temperature and boron concentration), which in turn can induce positive reactivity insertion and power excursion. Transients leading to Boron dilution as well as main steam line break (MSLB) transients are examples of such scenarios.

The perturbation is influenced by the turbulent mixing phenomena occurring inside the reactor pressure vessel (RPV), that is, a perfect mixing between the perturbed coolant (e.g., a deborated slug coming from a loop) and the nonperturbed coolant is expected to lead to the smallest core response, while the absence of mixing is likely to induce a stronger and localized reactivity insertion. Obviously a quantitative assessment of the relationship between the mixing effects and their consequences in terms of reactivity is needed for demonstrating the reactor safety.

The mixing phenomena are inherently three-dimensional, therefore they can be properly analyzed and predicted by means of numerical tools having 3D capabilities, in particular the computational fluid dynamic (CFD) codes (and, to a certain extent, by system codes embedding 3D modules and mixing models).

Several international projects and experimental campaigns have been conducted in the past to investigate the in-vessel mixing phenomena and the code capabilities to predict them. Examples are the experiments carried out at Forschungszentrum Dresden-Rossendorf (FZD) ROCOM facility [1], University of Maryland [2], Vattenfall [3], while as far as the code assessment is concerned, the OECD/NEA International Standard Problem (ISP) no. 43 [4], the EC FLOMIX-R project [5], and the EC ECORA project [6] can be mentioned.

Recently, these issues have been addressed in the framework of the EC-funded TACIS project R2.02/02 "Development of safety analysis capabilities for VVER-1000 transients

involving spatial variations of coolant properties (temperature or boron concentration) at core inlet" [7]. An extensive experimental campaign was conducted at the OKB "Gidropress" mixing facility (a 1 : 5 scaled model of a VVER-1000 reactor) to study fluid mixing scenarios featured by different flow conditions, such as symmetric and asymmetric steady pump operation at nominal flowrates in presence of tracer injection (5 experiments), and pump start-up scenarios in presence of tracer slugs (5 more experiments). All the measured data collected have been utilized for the validation of mixing models implemented in a set of Russian thermo-hydraulics system codes, with CFD being used as a valuable support to the phenomena understanding, and results interpretation, and being object of validation itself.

One of the experimental tests performed consisted in a main coolant pump (MCP) start-up, with the other three pumps switched-off and a tracer slug (simulating deborated water) accumulated in the cold leg of the starting loop. Such experiment was then simulated both with system codes and CFD codes. In particular, pretest and posttest simulations were run using the commercial CFD code ANSYS-CFX and the results obtained were compared against the measured data. Such CFD code validation activity is described in the present paper.

As explained above, the present work is a part of a wider and more comprehensive activity, which included the CFD grid generation, the pretest and posttest simulations of all the experiment performed, the execution of sensitivity analyses on the main modelling parameters, in compliance with the requirements of the Best Practice Guidelines (BPG, [8, 9]). Description of the entire work is beyond the scope of the paper and is not reported, but some additional information can be found for instance in [10, 11].

This work is connected to the CFD code validation activity in progress at the University of Pisa, related to single-phase in-vessel flows. Analogous analyses were performed, for instance, for some experiments carried out on the above-mentioned ROCOM facility [12].

It is also worth mentioning that CFD validation activities [13] had been carried out in the recent past on a previous version of the same Gidropress mixing facility in the framework of the above-mentioned FLOMIX-R project.

2. Description of the Experiment

The experimental facility basically consists of an RPV model, connected with four circulating loops. The RPV model (Figure 1(a)) is made of steel and reproduces, at a 1 : 5 scale, practically all the geometrical features of the RPV of a VVER-1000 reactor (namely, Novovoronezh NPP reactor, Unit no. 5) which are affecting the in-vessel mixing phenomena up to the core inlet, particularly the internal components such as the barrel, the lower ellipsoidal perforated shell (with more than 1300 drillings of two different diameters), the core support columns (one for each of the 151 fuel assemblies) and the core lower plate (which separates the core region from the lower plenum region). The core region is actually not modelled; rather a structure is present made of perforated plates and guide tubes supporting 90 conductivity probes which are located just above the lower core plate.

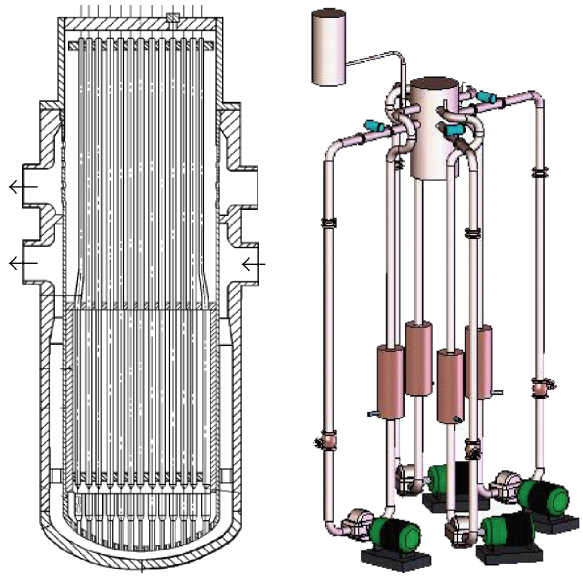

Figure 1: (a) Vertical cross-section of the RPV model; (b) 3D isometric sketch of the facility.

Each loop is equipped with an independent computer-controlled circulation pump, which permits to simulate a wide range of flow conditions. An expansion tank is connected to one of the loops in lieu of the pressurizer; atmospheric conditions reign above the water level in the tank, while higher pressures (although still in the range 1 to 2 atm) occur in the RPV model due to the hydrostatic effect and to the pumps head. The experiments are conducted at ambient temperature. The circulating loops (Figure 1(b)) do not exactly reproduce the real piping layout; however the related volumes are such that the $1 : 5^3$ volume scale is kept.

Some auxiliary systems are present for the tracer injection, consisting in injection pumps, fast acting valves, a tracer tank, and pipelines connecting all such components to the main loops. For instance, such systems can be operated for accumulating a tracer slug in the ascending section of one loop while the pumps are at rest, with such section being "isolated" by two fast acting valves (Figure 2). Furthermore, a continuous tracer injection can also be performed into the volume compensation tank located upstream of a circulation pump.

The tracer utilized is sodium chloride, which alters the water electrical conductivity. Through a calibration procedure, the conductivity can be easily correlated to the salt concentration. The facility is equipped with a number of conductivity probes, providing high-frequency measurements of the local tracer concentration. As mentioned above, 90 of such probes are located above the lower core plate, each being aligned with the centreline of one coolant channel. This means that experimental information is available for 60% of the coolant channels (90 out of 151), which is obviously not an "ideal" configuration (as it would be if all the

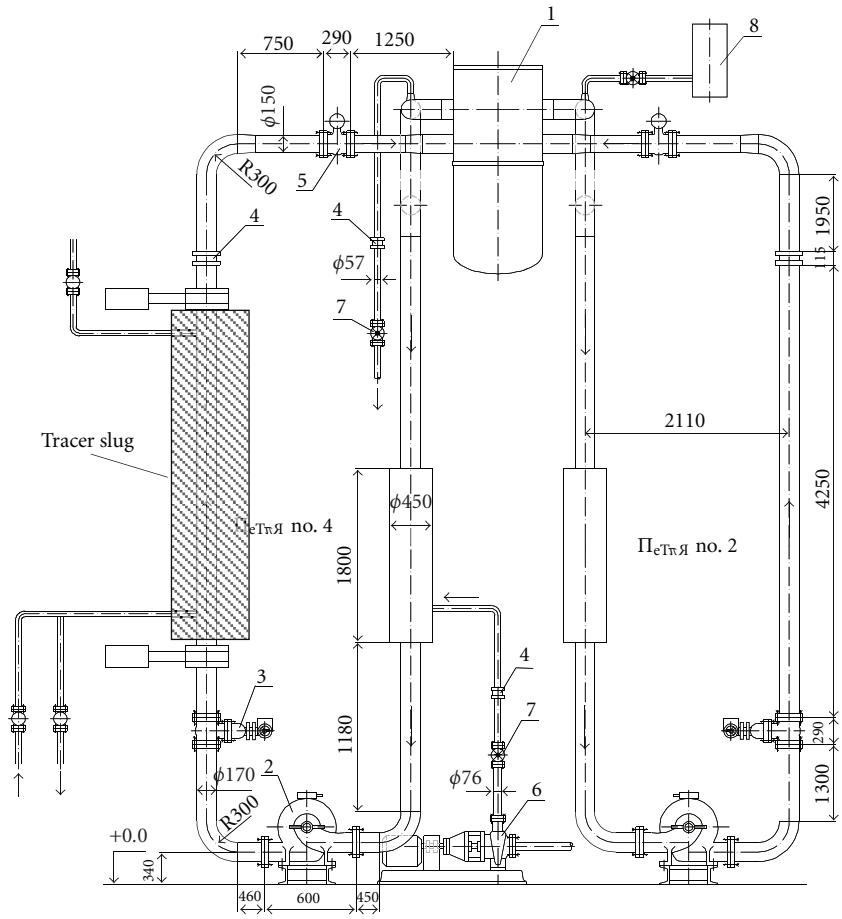

Figure 2: Location of the tracer slug.

channels were instrumented); however such measurement equipment still permits to gather valuable information of the perturbation at the core inlet. A conductivity probe is located also at each inlet and outlet nozzle; some probes are present in the tracer tank.

The loop flowrates are measured by electromagnetic flow meters located close to each inlet nozzle.

As can be understood from the description above, the facility can be operated such as to simulate a wide spectrum of operation conditions and accidental scenarios involving the perturbation of the coolant properties distribution at the core inlet. The experiment addressed in the present work was intended to reproduce the start-up of one reactor coolant pump (the other pumps remaining at rest) assuming that a "deborated slug" had previously been accumulated in the starting loop. The slug is thus transported inside the RPV, where it partially mixes with the normally borated water before reaching the core inlet and then introducing a positive reactivity in the reactor core.

Namely, the deborated slug is here represented by a salted water slug (0.072 m^3 volume, which roughly corresponds to the scaled volume of the loop seal, where a deborated slug would most probably accumulate).

The starting pump is run, via the numerical control, such as to achieve an exponential growth for the flowrate, according to (1) (the target flowrate being $Q_0 = 220\,m^3/h$); 10 seconds are enough to reach ~98% of the target flowrate:

$$Q = Q_0 \cdot \left(1 - e^{-0{,}25 \cdot \tau}\right). \quad (1)$$

The isolation valves of the idle loops are left open; therefore inverse flows develop which are expected to strongly affect the flow field in the RPV model as well as the tracer distribution. The inverse flowrates are not known before the execution of the experiments, and thus constitute the main unknown parameters in the pretest phase of the numerical analysis.

3. Description of the Computational Model

3.1. Computational Grid. The computational domain selected for the in-vessel mixing simulations (shaded region in Figure 3) includes the following coolant regions: cold legs, inlet nozzles, downcomer (DC), lower plenum (LP). The reactor core region and the upper plenum are not modelled because they are not expected to influence the coolant flow upstream of the core inlet. However, a dummy outlet volume is defined corresponding to a fraction of the core region, to permit the easy application of pressure-controlled outlet boundary conditions.

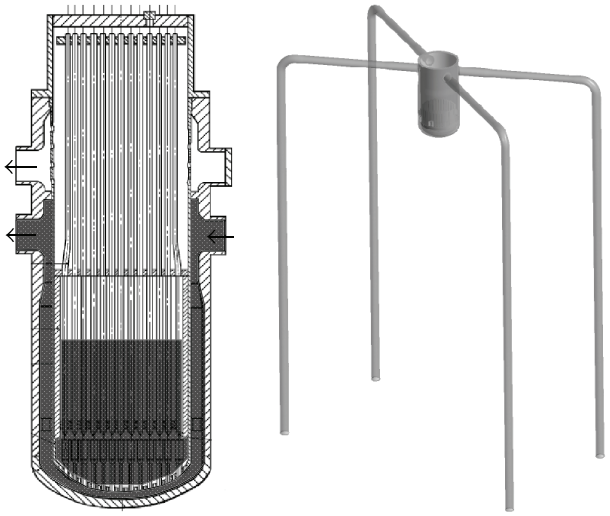

(a) (b)

Figure 3: Sketch of the computational domain chosen for CFD simulations.

The identified computational domain is defined and bounded by the following solid parts.

(i) Inner wall of the cold legs and inlet nozzles (including round surface at connection with vessel wall).

(ii) Inner wall of the vessel (including cylindrical regions, diameter variations, elliptical bottom).

(iii) Consoles, located in the lower part of the DC.

(iv) Outer wall of the barrel (including elliptical bottom).

(v) Inner wall of the barrel (including elliptical bottom), only up to the core inlet.

(vi) Holes through the barrel bottom (also referred to as "perforated shell" in the following).

(vii) Support columns, located in the region between the inner wall of the barrel bottom and the lower side of the core support plate; each column includes a "solid column" part (14 mm diameter) on the bottom and a "perforated column" part on the top (a tube, 38 mm outer diameter, connected to the solid columns through a conic region, and having perforations on its wall allowing the fluid to pass from the LP to the core support plate holes and then to the core region).

(viii) Core support plate.

(ix) Baffle inner wall.

The presence of such a large number of small geometric details (consoles, perforations through the barrel bottom, support columns, etc.) makes the achievement of a high-quality and accurate computational grid quite a tough task.

The mesh has been developed with the package ANSYS ICEM-CFD 10.0 (see [14]), following a modular approach, that is, the domain has been subdivided into several subdomains which have been meshed separately. Then the submeshes obtained have been connected together by means of "interfaces" (one-to-one interfaces were used for conformal subgrids and general grid interfaces for nonconformal subgrids; see [15]). This approach allowed adopting different mesh types in different subdomains, namely the DC was meshed with hexahedral elements, while tetrahedrons were used to model LP region (where the complexity of the geometry would make impracticable the hexahedral meshing), including the ellipsoidal perforated shell with its ~1300 holes. The result is a so-called hybrid grid.

For a proper treatment of the near-wall turbulence, based on logarithmic wall functions, the grid spacing was refined close to the walls in the hexahedral submeshes, while prism layers were inflated in the tetrahedral submeshes. The adopted spacing yielded an average value of about 110 for the nondimensional distance $y+$ of the first nodes from the walls.

Several grids were generated and assembled based on different meshing approaches (e.g., tetrahedral versus hexahedral elements) and sizes adopted in some submeshes. Grid sensitivity analyses are described in [11]. They helped selecting a reference grid (the same used for the present calculations; see Table 1) as the one providing the better convergence, and show that an improvement of the results could be expected from finer meshes.

It is worth remarking that the reference grid is to be considered as a "production grid," in the sense that its size results from a compromise between the need of achieving a high numerical accuracy and mesh-converged results (as recommended by the BPG) on one side, and the computational resources limitations on the other side. It was not possible to demonstrate that the grid is able to provide grid-independent results, as usually happens when addressing CFD problems having the same degree of complexity. However, it is believed to be a state-of-the-art grid, suitable for CFD simulation of turbulent flows, at least as far as the Reynolds-Averaged Navier-Stokes turbulence modelling is adopted. Some pictures of the reference grid are shown in Figure 4.

3.2. Simulations Setup. The simulations have been performed with the commercial, multipurpose CFD code ANSYS CFX-10.0 (see [15]), using 8 processors of a Linux-cluster available at the University of Pisa. The main features of the simulations setup are as follows:

(i) working fluid: water (incompressible) at 1 atm, 25°C,

(ii) density: 997 kg/m^3,

(iii) dynamic viscosity: 8.899×10^{-4} kg m^{-1} s^{-1},

(iv) turbulence accounted for with SST model.

The following field equations have been solved:

(i) mass balance (continuity),

(ii) momentum balance (Navier-Stokes),

(iii) transport of turbulent kinetic energy (k),

(iv) transport of turbulent eddy frequency,

(v) transport of an additional, user-defined, scalar variable simulating the tracer.

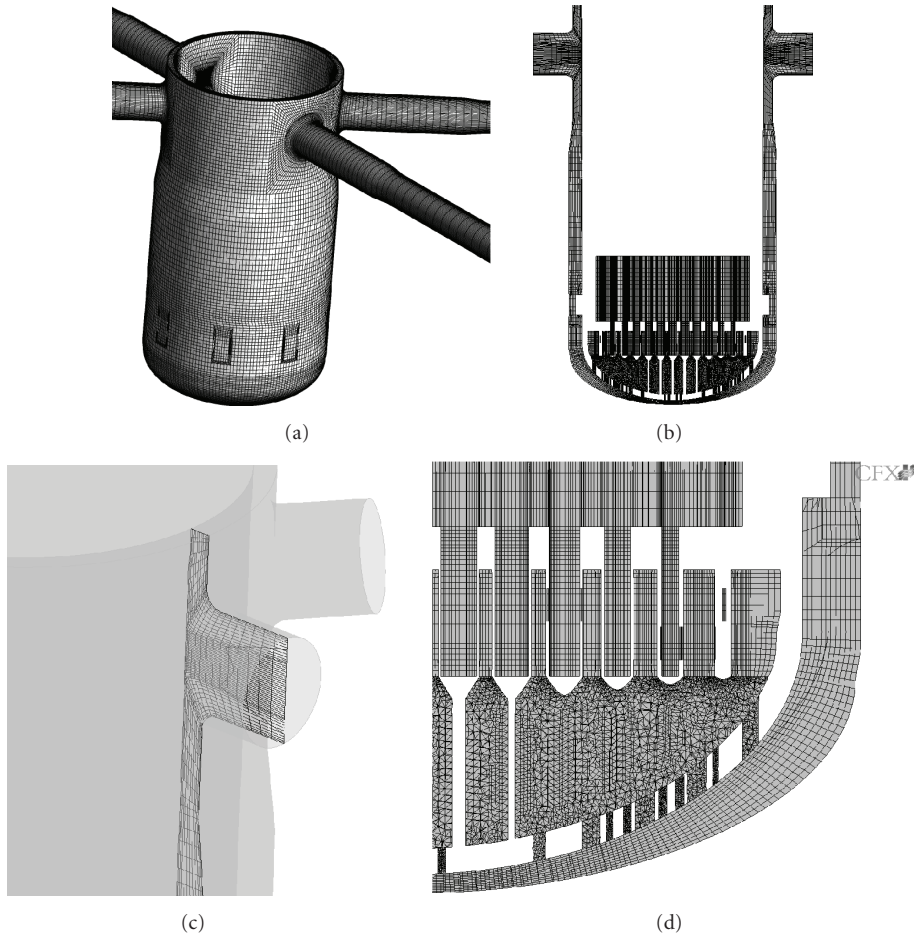

Figure 4: Reference grid.

Table 1: Size of reference grid ($M = 10^6$).

	No. of nodes	No. of tetrahedra	No. of wedges	No. of pyramids	No. of hexahedra	Total no. of elements
Reference grid	**4.3 M**	3 M	630 000	32 000	2.75 M	**6.46 M**

The tracer concentration is handled in terms of normalized concentration (also referred to as the mixing scalar or MS). Normalization is such that the mixing scalar ranges between the values 0 and 1, which correspond respectively to absence of tracer (i.e., full boron concentration in a hypothetical real plant transient) and initial concentration in the tracer slug (i.e., lowest boron concentration).

Since the addressed flow is dominated by turbulent diffusion, the molecular diffusion of the tracer provides a negligible contribution to the effective diffusion and was then neglected. Sensitivity analyses on the tracer diffusivity performed within the FLOMIX-R project (see [5]) support this assumption.

The transient solver available in CFX was used for both calculations, and the second-order backward Euler time advancement scheme was adopted. A constant time-step equal to 0.05 second was used, which made most time-steps converge with only two internal iterations, and allowed obtaining the results in a reasonable time (about 10 days computation on 8 CPUs of a AMD Opteron Linux cluster, for simulating 25 seconds). Sensitivity analyses on the time-step size are envisaged for the future.

The upwind scheme for the discretization of the advection terms was selected; adopting higher-order schemes is generally recommended (see, e.g., the Best Practice Guidelines [8]), because they are less prone to numerical diffusion than first-order schemes (such as upwind), however previous sensitivity calculations performed using the same grid had shown some nonsatisfactory performance (local nonphysical oscillations, bad convergence) when a higher-order scheme was used, therefore it was decided to stay with the upwind scheme.

The initial conditions (for both the pretest and the posttest calculations) consisted in zero-velocity flow over the whole domain, and zero-concentration everywhere except for the volume corresponding to the tracer slug, which was marked with mixing scalar equal to 1. The following boundary conditions were set for the pretest calculation.

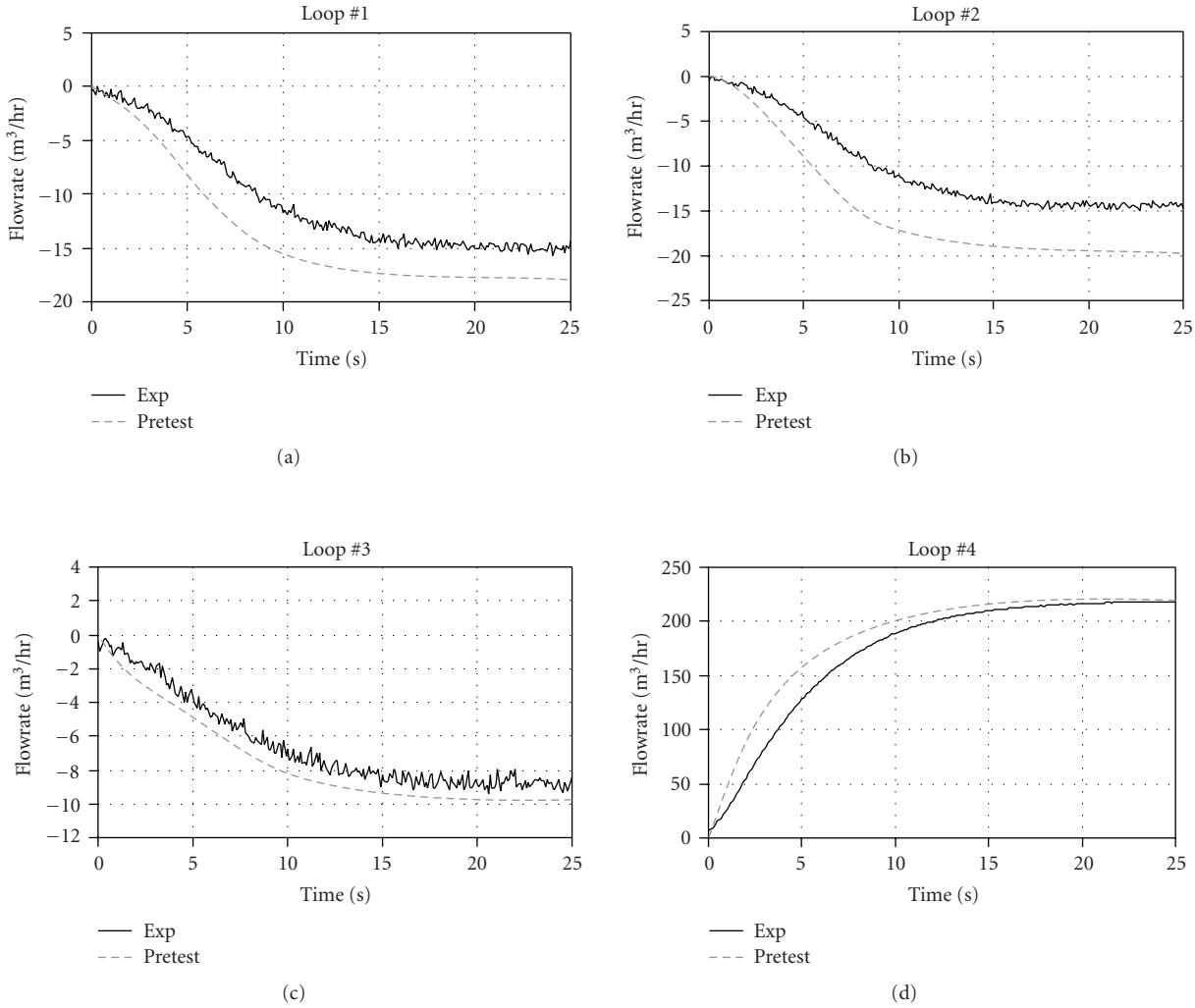

Figure 5: Loop flowrates (posttest values coincide with experimental values).

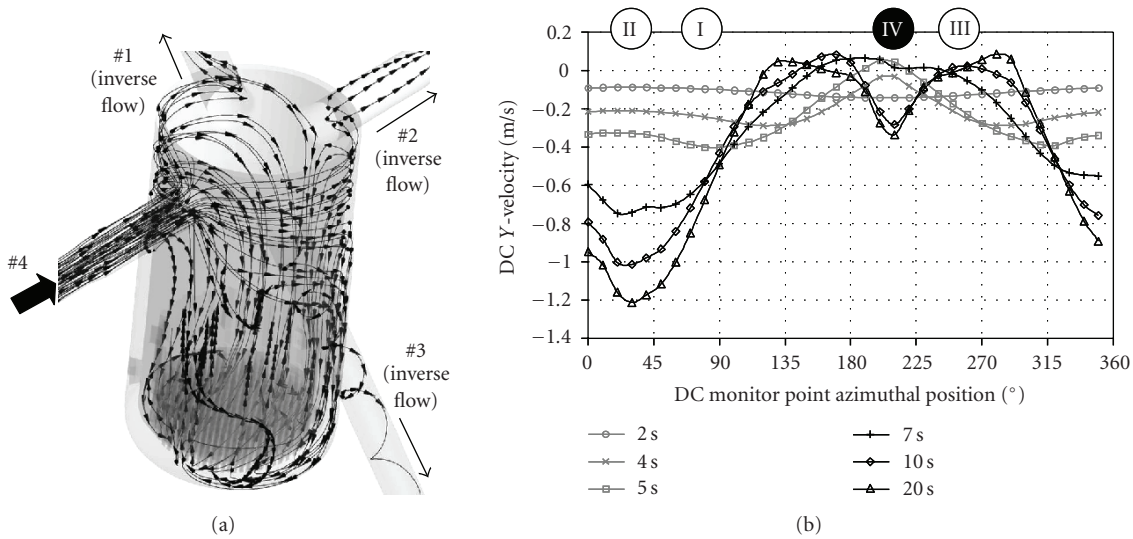

Figure 6: Numerical results: (a) velocity field (streamlines from loop 4); (b) azimuthal velocity profile in DC.

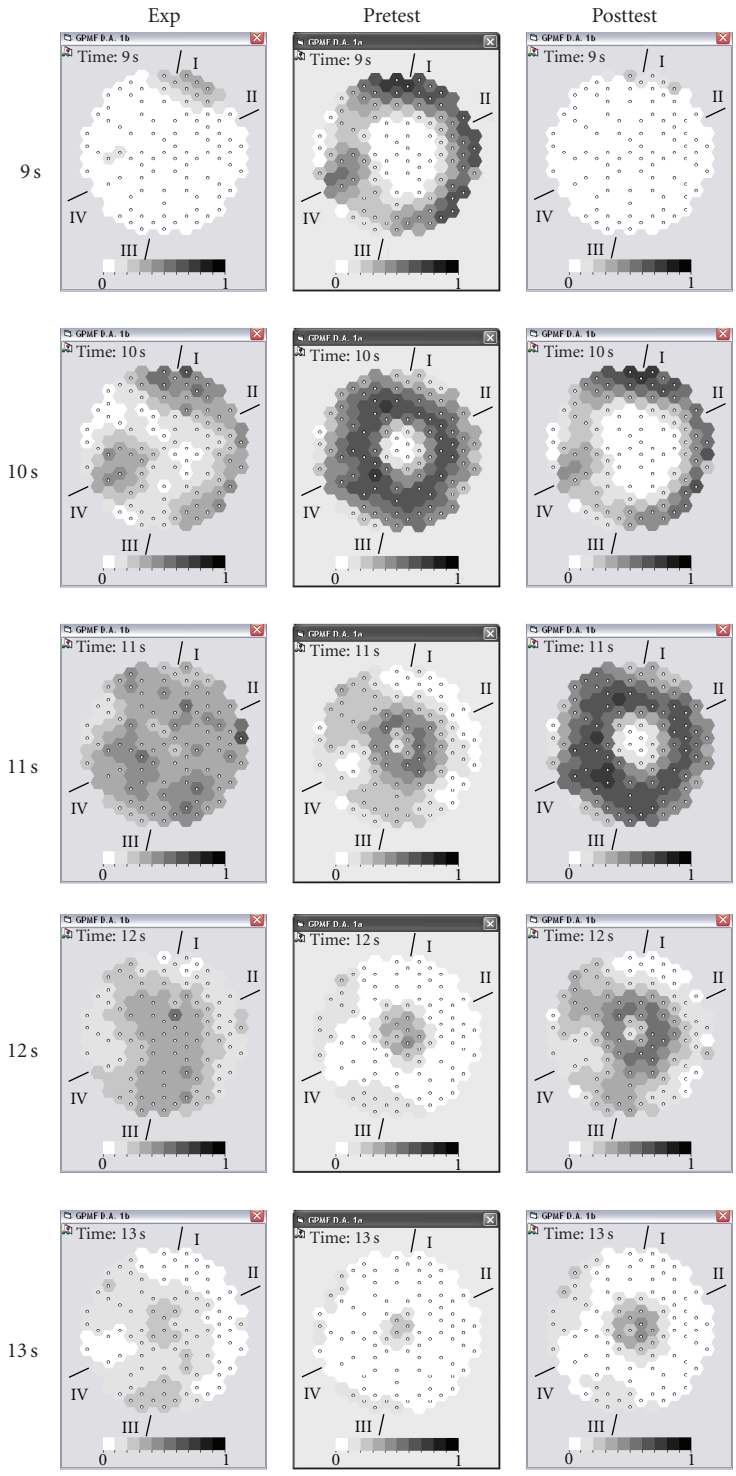

Figure 7: Comparison of mixing scalar distribution at core inlet during slug passage.

(i) Time-dependent flowrate at loop #4 inlet nozzle, according the theoretical law (see (1) above).

(ii) 5% turbulence intensity at loop #4 inlet nozzle.

(iii) Pressure-controlled "Opening" at inlet nozzles #1, 2 and 3 (to permit inverse flows), with additional concentrated pressure losses to account for the overall flow resistance of the idle loops (the pressure loss coefficients have been roughly estimated based on sensitivity calculations and experimental information on the inverse flowrates, which were known not to exceed 10% of the nominal flowrate).

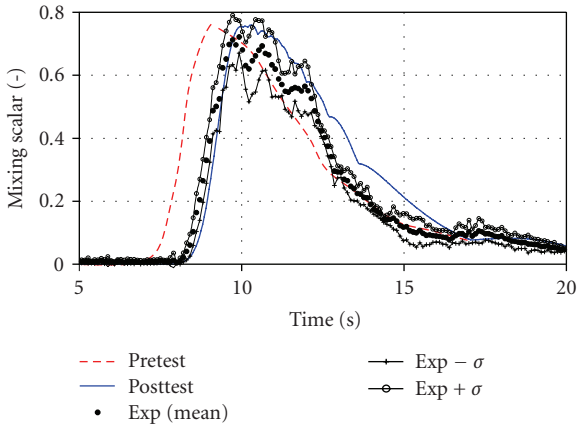

Figure 8: Maximum mixing scalar at core inlet.

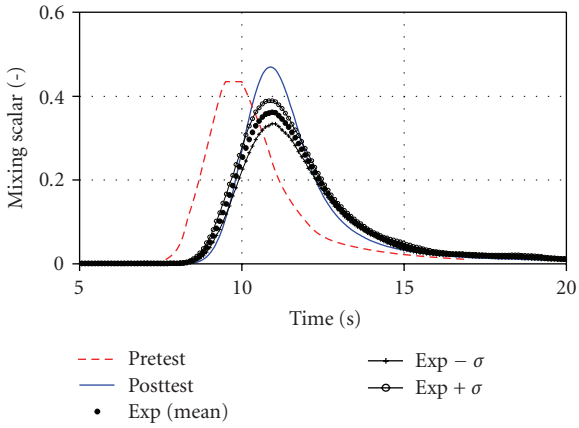

Figure 9: Core-averaged mixing scalar.

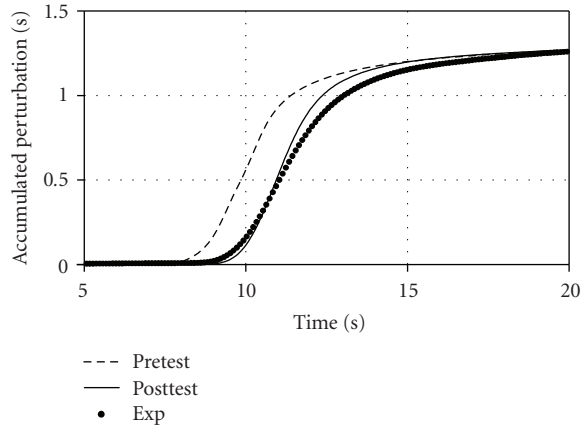

Figure 10: Accumulated perturbation at core inlet.

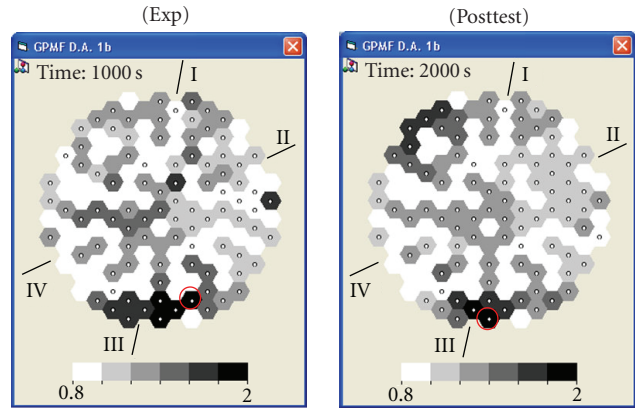

Figure 11: Maps of channel-by-channel accumulated perturbation at 25 seconds.

(iv) Pressure-controlled "Outlet" at the top boundary of the dummy outlet volume replacing the core region.

(v) No-slip condition at all walls (i.e., all boundaries not mentioned above).

(vi) Near-wall treatment of turbulence based on logarithmic law.

The posttest calculation setup is identical to the pretest, except for the boundary conditions at the cold legs. In this case, in fact, all the flowrates (including the inverse ones) were imposed based on the measured values. The experimental flowrates are plotted in Figure 5, along with those resulting from the pretest calculation.

4. Results

All results and experimental data are reported (and compared) in terms of normalized concentration (mixing scalar) at the core inlet, in particular at the 90 instrumented channels locations.

Figure 6(a) provides a picture of the flow pattern developing in the RPV model, by means of streamlines entering from the starting loop. The entering flow keeps a dominant horizontal component and tends to reach the opposite side before moving downwards (towards the lower plenum). Besides, a portion of the flow leaves the RPV model through the idle loops (the related valves being kept open): such inverse flows are shown by some streamlines in the picture, and are expected to affect the amount of tracer that will reach the core inlet (since part of the tracer will exit through the idle loops). Furthermore, a stagnation region appears below the starting loop. This is also shown by the azimuthal profile of the velocity in the DC (at different instants) plotted in Figure 6(b).

Such a qualitative behaviour of the flow is highly dominated by three-dimensional features, so that it would be hardly described by system codes (even if with 3D capabilities). CFD codes represent the "natural" approach to deal with such behaviour, although an accurate modelling of the turbulence may still be a challenging task due to the high anisotropy of the turbulence parameters expected in a strongly bounded flow.

The correct description of the flow field developing in the downcomer is important because it determines the space

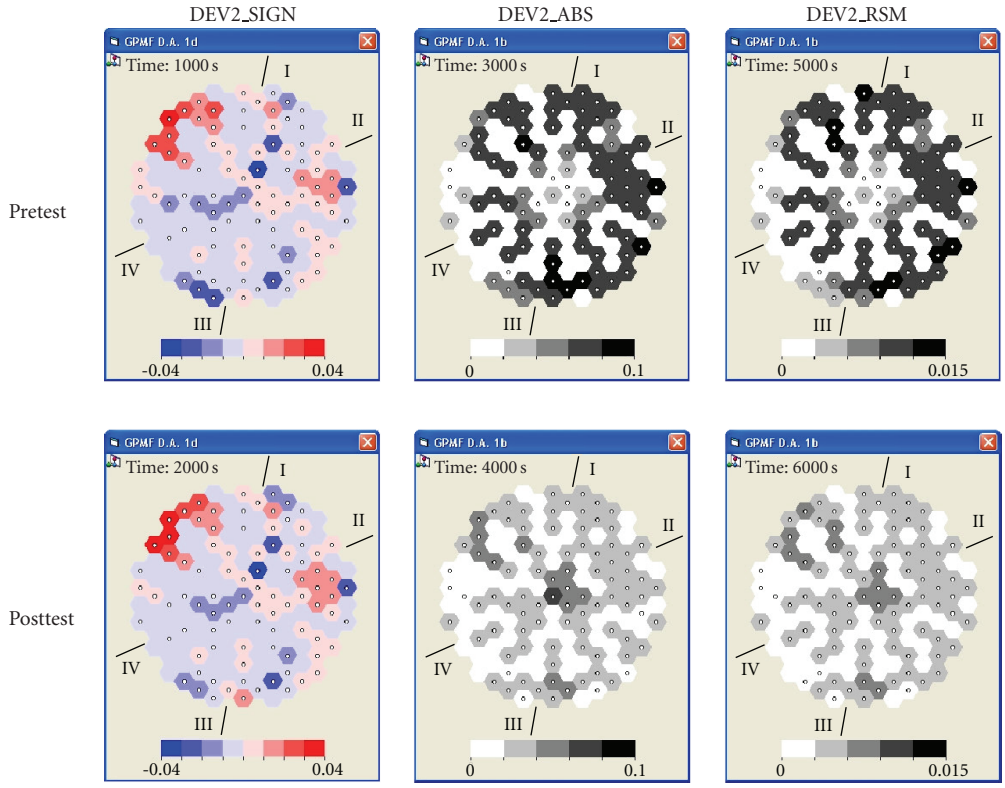

Figure 12: Maps of DEV2 deviations.

distribution of the perturbation at the core inlet, particularly the location and the shape of the perturbation.

Figure 7 shows a qualitative code-to-experiment comparison of the mixing scalar at the core inlet at several selected instants during the slug passage. As from the experimental measurements, the first perturbation appears at the core inlet at around 9 seconds and is located below loop no. 1, that is, on the opposite side to the starting loop (i.e., no. 4). Then the perturbation extends to other peripheral channels in the clockwise direction; furthermore, a secondary perturbation spot appears just below loop no. 2. After a couple of seconds from the first perturbation appearance, almost all channels are affected, and the mixing scalar distribution has become relatively uniform. In a few more seconds, the perturbation disappears from the core inlet.

The pretest results show the same results, from a qualitative point of view. In particular, the appearance of a primary perturbation on the opposite side with respect to the starting loop and a secondary perturbation spot below the same loop is correctly described, although with a small discrepancy in timing (1 second ahead) and somewhat larger spatial gradients. Moreover, when most of the perturbation is crossing the core inlet, the spatial distribution is quite less uniform than observed in the experiment.

As can be observed in Figure 5, the pretest calculation overestimated all the inverse flowrates in idle loops. In addition, also the direct flowrate in the starting loop is larger that the measured value (as the experiment is not exactly behaving according to the theoretical law), and this explains why the perturbation reaches the core inlet in advance with respect to the test. Such time shift disappears in the posttest calculation, where the experimental loop flowrates are imposed as boundary conditions. The perturbations appearance now appears aligned with the experiment.

It is evident how the morphology of the perturbation affecting the core inlet is determined by the flow distribution in the downcomer (described above).

It is also evident that the predicted spatial distribution of the perturbation is quite less uniform than observed in the experiment. In other words, a less effective mixing is predicted, as it has previously been observed in similar works (see [12]), and this behaviour is most probably related to limitations of the RANS turbulence modelling.

A key parameter affecting the core neutron kinetics response is the maximum perturbation (e.g., the lowest boron concentration, in a boron dilution scenario) reached at the core inlet. The related code predictions are plotted in Figure 8, where they are compared with the corresponding experimental trend. As mentioned before, five runs were conducted for this experiment, and the measured values were averaged over such data sets. The mean value of the maximum perturbation is reported in the figure, along with the two curves defining a confidence interval of one standard deviation around the mean value. It is observed that both calculations slightly overpredicted the peak of the mean value curve, although still within the confidence interval. The pretest results show a time shift of 1 second in advance (as already observed from Figure 7), which is related to

the nonoptimized boundary conditions. The posttest results show instead an accurate timing for the peak occurrence, as well as for the first appearance of the perturbation (around 8 seconds). Later, the code prediction shows a slight delay in the maximum perturbation decrease: at 15 seconds the predicted value for the maximum perturbation is around 0.2, while the experimental value is a little above 0.1. The posttest results, although they are generally outside the confidence interval, look pretty close to the experimental behaviour.

Another key parameter is the core-averaged perturbation, and the related results comparison is shown in Figure 9 (the averaging is made on the 90 instrumented locations, both for measured and calculated data). The pretest results show the same time shift observed above. The posttest results show a correct timing, and a less smooth behaviour than the experimental trend, which indicates that a less "diffused" slug is passing through the core inlet.

A time integration of the core-averaged perturbation provides a measure of the "accumulated perturbation"; this is shown in Figure 10. Again, the posttest results show a less diffusive trend (indicated by a steeper gradient); in other words, the most amount of perturbation takes—according to the code prediction—a smaller time to cross the core inlet than in the experiment. Quite surprisingly, at the end of the slug passage both calculations predicted the same accumulated perturbation as the experiment, thta is, the same amount of tracer has reached the core inlet despite the nonaccurate boundary conditions in the pretest.

The accumulated perturbation at 25 seconds for both the experiment and the posttest results is shown in Figure 11 for each instrumented channel. Those maps evidence that the code tends to underpredict the overall perturbation in the central region and to overpredict it in the peripheral region between loops I and IV.

The measured maximum local accumulated perturbation is 2.02 (s/−), while the predicted value is 2.07 (s/−). The locations of those two maxima are indicated by red circles in Figure 11.

Table 2 summarizes the results obtained for some key parameters such as the timing of perturbation appearance (defined as MS = 0.1), timing and value of the maximum perturbation, and timing and value of the core-averaged perturbation peak. As observed before, the appearance of the perturbation is predicted 1 second in advance by the pretest calculation, and with a 0.2 second delay by the posttest calculation. Similar time discrepancies (−0.9 second and +0.4 second, resp.) appear for the prediction of maximum. The maximum value is predicted quite satisfactorily in both cases (with a 5% overestimation, which is, however, within the $\pm\sigma$ confidence interval).

Similar time discrepancies (−0.9 second and +0.1 second, resp.) also appear for the prediction of core-averaged peak, while the related peak value is noticeably overpredicted in both cases (27% and 35%, resp.). This seems to indicate a less effective mixing.

A quantitative analysis of the agreement between code predictions and measured data requires taking into account the results channel by channel, in addition to the core-averaged and maximum perturbations discussed above.

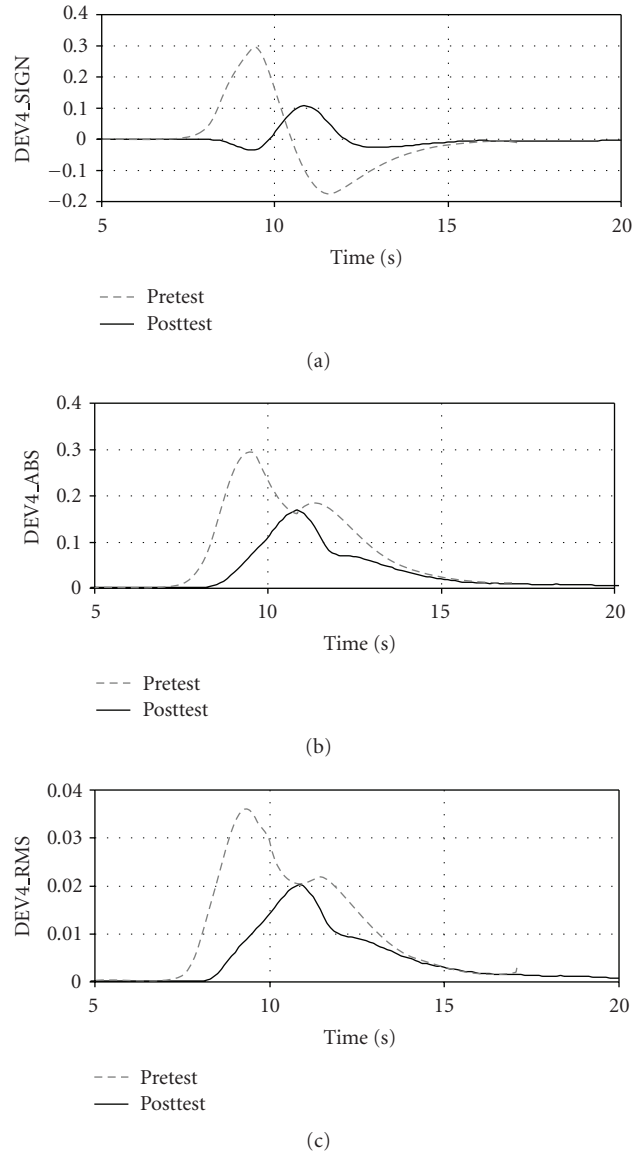

Figure 13: Core-averaged deviations (DEV4): sign, abs. value, root mean square.

However, as easily expected from the quantitative analysis shown before, an excellent agreement would be observed at some locations while at the other locations the perturbation will be either overpredicted or underpredicted by the calculations. This does not allow an easy judgement on the overall quality of the code prediction, unless some general, synthetic accuracy parameter is defined.

A local instantaneous code-to-experiment deviation can be defined as follows (based on the same approach adopted within the FLOMIX-R project [1]):

$$\mathrm{DEV1}_{i,t} = c_{i,t} - e_{i,t}, \tag{2}$$

where $c_{i,t}$ and $e_{i,t}$, respectively, represent the calculated and experimental values at ith location and tth time-step.

Table 2: Comparison of results (perturbation appearance; max. perturbation; core-average).

	Exp − σ	Exp	Exp + σ	Pretest	Posttest
Time for MS > 0.1 (s)	—	8.5	—	7.5	8.7
Time of Max. MS (s)	—	9.9	—	9	10.3
Max. MS [−]	0.670	0.721	0.773	0.755	0.758
Time of max. Ave. MS (s)	—	10.9	—	10	11.0
Max. Ave. MS (90 ch.) (−)	0.334	0.362	0.389	0.460	0.489

The deviation DEV1 can be averaged over a time interval of interest (e.g., 0–17 seconds, corresponding to the slug passage through the core inlet). The following three deviations are thus obtained (based, resp., on relative and absolute values of DEV1 deviations, and on a root mean square averaging approach):

$$\begin{aligned}
\mathrm{DEV2_SIGN}_i &= \frac{1}{t_N - t_0} \cdot \sum_{k=1}^{N} \mathrm{DEV1}_{i,t} \cdot (t_k - t_{k-1}), \\
\mathrm{DEV2_ABS}_i &= \frac{1}{t_N - t_0} \cdot \sum_{k=1}^{N} |\mathrm{DEV1}_{i,t}| \cdot (t_k - t_{k-1}), \\
\mathrm{DEV2_RMS}_i &= \frac{1}{t_N - t_0} \cdot \sqrt{\sum_{k=1}^{N} (\mathrm{DEV1}_{i,t})^2 \cdot (t_k - t_{k-1})^2},
\end{aligned} \tag{3}$$

where N is the number of time-steps within the selected time period, and t_k is the time value at kth time-step.

Maps of the DEV2 deviations for both calculations are plotted in Figure 12, obviously for the 90 instrumented channels only (the others being represented by white colour). Concerning the deviations with their sign, they approximately range between −0.04 and 0.04, and no evident change is observed from pre- to posttest: this is because the two calculations actually behave similarly, except for the time shift, and thus errors with opposite sign during the transient partly compensate. Some locations are evidenced, in both cases, where the perturbation is systematically overpredicted (red) or underpredicted (blue).

Concerning the absolute deviations, it is not possible to identify specific patterns on the map of pretest results, while on posttest map it is observed that the largest discrepancies occur in the central region and in the peripheral region around 90° away from loop #4 (on both directions); moreover, a noticeable improvement is noticed from pretest to posttest. The same behaviour is observed for the root mean square deviations.

If the DEV2 deviations are averaged over the instrumented locations, then the results in Table 3 are obtained (deviations DEV3), which represent a measure of the overall accumulated deviations. Again, the higher accuracy of the posttest predictions is evidenced. Only the DEV3SIGN deviation is increased.

The local instantaneous deviations can also be directly averaged over the instrumented locations, so as to obtain time-dependent deviations (DEV4), according to the following equations:

Table 3: Core- and time-averaged deviations (DEV3).

	Pretest	Posttest
DEV3_SIGN	0.0011	0.0020
DEV3_ABS	0.0620	0.0311
DEV3_RMS	0.0092	0.0049

$$\begin{aligned}
\mathrm{DEV4_SIGN}_t &= \frac{1}{M} \cdot \sum_{k=1}^{M} \mathrm{DEV1}_{i,t}, \\
\mathrm{DEV4_ABS}_t &= \frac{1}{M} \cdot \sum_{k=1}^{M} |\mathrm{DEV1}_{i,t}|, \\
\mathrm{DEV4_RMS}_t &= \frac{1}{M} \cdot \sqrt{\sum_{k=1}^{M} (\mathrm{DEV1}_{i,t})^2}.
\end{aligned} \tag{4}$$

The resulting plots are shown in Figure 13. The first plot clearly indicates that the pretest results first over predict the perturbation (until 11 seconds), then the under prediction prevails; this is related to the time shift. The posttest results show an opposite behaviour, and generally the discrepancy is much reduced.

The second and the third plots show the same qualitative behaviour; in both cases the noticeable improvement of posttest results is evident.

5. Conclusions

A pump start-up experiment with the presence of a tracer slug, conducted on a Gidropress mixing facility in the framework of TACIS project R2.02/02, was simulated with the CFD code ANSYS CFX. Both a pretest and a posttest calculation were run, differing by the boundary conditions imposed in terms of loop flowrates. The numerical results were compared against the experimental data available, which consist in tracer concentration measurements at several locations at the core inlet.

The results of both calculations showed quite a good agreement with the experiment from the qualitative point of view: in particular, the morphology of the tracer concentration distribution at the core inlet was correctly

described, including the appearance of two different perturbation patterns (one on the opposite side with respect to the starting loop, and a secondary one on the same side). The only noticeable difference between the pretest and the posttest—confirmed also by the quantitative analysis—is a time shift (in advance) of the former, due to an imposed loop flowrate which was little higher than actually obtained in the experiment. This qualitative agreement is quite an important achievement, since the addressed scenario is featured by a complex, highly three-dimensional, flow distribution in the downcomer, and its accurate numerical prediction is not a trivial task, due to the well-known limitations of the turbulence modelling based on the Reynolds-Averaged Navier-Stokes approach and particularly on the eddy viscosity concept (i.e., the difficulties in dealing with turbulence anisotropy, unsteady flows, separation phenomena, secondary motions), and typical of most industrial-scale CFD applications.

From a quantitative point of view, the results in terms of maximum perturbation (and related timing), core-averaged perturbation, and accumulated perturbation are also satisfactory. The perturbation peak is overpredicted by 5%, which is comparable with the experimental uncertainty. The predicted time history of the core-averaged perturbation shows a less smooth trend than the experiment, which seems to indicate a less effective mixing (this would be consistent with results from previous CFD validation studies against symmetric loop operation experiments, which had shown a tendency to underpredict the turbulent mixing by the CFD/2-equation turbulence modelling approach).

A further quantitative analysis of the results was done based on a set of "deviations" defined according to a similar approach to that adopted within the FLOMIX-R project. This kind of analysis of the agreement between code predictions and experiment provides a valuable tool to compare the accuracy of different code results. However, a real judgement on the results accuracy cannot be given because it would require a sort of "acceptance thresholds" (in relation to the nuclear reactor safety), which however have not been proposed yet. This is certainly an important matter for future research.

Possible future developments of the present work involve developing finer grids (as far as allowed by the available computing resources), running further sensitivity analyses (e.g., with respect to time discretization, wall roughness) and switching to large eddy simulation (LES) or LES/RANS hybrid approaches for a more accurate prediction of turbulence.

Acknowledgment

The work reported about in this paper was supported by the EU TACIS project R2.02/02, "Development of safety analysis capabilities for VVER-1000 transients involving spatial variations of coolant properties (temperature or boron concentration at core inlet)."

References

[1] U. Rohde, T. Höhne, S. Kliem, et al., "Fluid mixing and flow distribution in a primary circuit of a nuclear pressurized water reactor—Validation of CFD codes," *Nuclear Engineering and Design*, vol. 237, no. 15–17, pp. 1639–1655, 2007.

[2] K. T. Kiger and F. Gavelli, "Boron mixing in complex geometries: flow structure details," *Nuclear Engineering and Design*, vol. 208, no. 1, pp. 67–85, 2001.

[3] B. Hemstroem and N.-G. Andersson, "Physical modelling of a rapid boron dilution transient—II: study of the Ringhals case, using a more complete model," Report US 97:20, Vattenfall, Sweden, 1997.

[4] M. Gavrilas and K. Kiger, "OECD/CSNI ISP Nr. 43 Rapid Boron-Dilution Transient Tests for Code Verification," September 2000.

[5] U. Rohde, T. Höhne, S. Kliem, et al., "FLOMIX-R Project—Final Summary Report," European Commission.

[6] M. Scheuerer, M. Andreani, D. Bestion, et al., "ECORA Project—Condensed Final Summary Report," European Commission, March 2005.

[7] European Commission—Europeaid Cooperation Office, TACIS Project R2.02/02, "Development of safety analysis capabilities for VVER-1000 transients involving spatial variations of coolant properties (temperature or boron concentration at core inlet)," Terms of Reference.

[8] F. Menter, "Evaluation of computational fluid dynamic methods for reactor safety analysis," CFD Best Practice Guidelines for CFD Code Validation for Reactor-Safety Applications, EU/FP5 ECORA Project, EVOL-ECORA-D01, Germany, February 2002.

[9] J. Mahaffy, B. Chung, F. Dubois, et al., "Best practice guidelines for the use of CFD in nuclear reactor safety applications," NEA/CSNI/R(2007)5, May 2007.

[10] T. Höhne, U. Rohde, D. Melideo, et al., "Pre-test CFD simulations of gidropress mixing facility experiments using ANSYS CFX," in *Proceeding of the 17th AER Symposium on VVER Reactor Physics and Reactor Safety*, Yalta, Crimea, Ukraine, September 2007.

[11] T. Höhne, U. Rohde, D. Melideo, et al., "CFD simulations of gidropress mixing facility experiments in the framework of TACIS project R2.02/02," in *Proceedings of TOPSAFE Conference*, Dubrovnik, Croatia, September-October 2008.

[12] F. Moretti, D. Melideo, F. D'Auria, T. Höhne, and S. Kliem, "CFX simulations of ROCOM slug mixing experiments," *Journal of Power and Energy Systems*, vol. 2, no. 2, pp. 720–733, 2008.

[13] L. Vyskocil, "CFD simulation of slug mixing in VVER-1000 reactor," in *Proceedings of the 14th International Conference on Nuclear Engineering (ICONE-14)*, p. 10, Miami, Fla, USA, July 2006.

[14] ANSYS ICEM-CFD 10.0 User Manual, (embedded in the software package), 2005.

[15] ANSYS CFX-10.0 User Manual, (embedded in the software package), 2005.